120 Springer Series in Solid-State Sciences
Edited by H.-J. Queisser

Springer-Verlag Berlin Heidelberg GmbH

Springer Series in Solid-State Sciences

Editors: M. Cardona P. Fulde K. von Klitzing H.-J. Queisser

Managing Editor: H. K.V. Lotsch

Volumes 1–89 are listed at the end of the book

90 **Earlier and Recent Aspects of Superconductivity**
Editors: J. G. Bednorz and K. A. Müller

91 **Electronic Properties of Conjugated Polymers III** Basic Models and Applications
Editors: H. Kuzmany, M. Mehring, and S. Roth

92 **Physics and Engineering Applications of Magnetism** Editors: Y. Ishikawa and N. Miura

93 **Quasicrystals** Editors: T. Fujiwara and T. Ogawa

94 **Electronic Conduction in Oxides**
By N. Tsuda, K. Nasu, A. Yanase, and K. Siratori

95 **Electronic Materials**
A New Era in Materials Science
Editors: J. R. Chelikowsky and A. Franciosi

96 **Electron Liquids** By A. Isihara

97 **Localization and Confinement of Electrons in Semiconductors**
Editors: F. Kuchar, H. Heinrich, and G. Bauer

98 **Magnetism and the Electronic Structure of Crystals** By V.A. Gubanov, A.I. Liechtenstein, and A.V. Postnikov

99 **Electronic Properties of High-T_c Superconductors and Related Compounds**
Editors: H. Kuzmany, M. Mehring, and J. Fink

100 **Electron Correlations in Molecules and Solids** 3rd Edition By P. Fulde

101 **High Magnetic Fields in Semiconductor Physics III** Quantum Hall Effect, Transport and Optics By G. Landwehr

102 **Conjugated Conducting Polymers**
Editor: H. Kiess

103 **Molecular Dynamics Simulations**
Editor: F. Yonezawa

104 **Products of Random Matrices** in Statistical Physics By A. Crisanti, G. Paladin, and A. Vulpiani

105 **Self-Trapped Excitons**
By K. S. Song and R. T. Williams

106 **Physics of High-Temperature Superconductors**
Editors: S. Maekawa and M. Sato

107 **Electronic Properties of Polymers**
Orientation and Dimensionality of Conjugated Systems Editors: H. Kuzmany, M. Mehring, and S. Roth

108 **Site Symmetry in Crystals** Theory and Applications By R. A. Evarestov and V. P. Smirnov

109 **Transport Phenomena in Mesoscopic Systems** Editors: H. Fukuyama and T. Ando

110 **Superlattices and Other Heterostructures**
Symmetry and Optical Phenomena
By E. L. Ivchenko and G. E. Pikus

111 **Low-Dimensional Electronic Systems**
New Concepts
Editors: G. Bauer, F. Kuchar, and H. Heinrich

112 **Phonon Scattering in Condensed Matter VII**
Editors: M. Meissner and R. O. Pohl

113 **Electronic Properties of High-T_c Superconductors**
Editors: H. Kuzmany, M. Mehring, and J. Fink

114 **Interatomic Potential and Structural Stability**
Editors: K. Terakura and H. Akai

115 **Ultrafast Spectroscopy of Semiconductors and Semiconductor Nanostructures** By J. Shah

116 **Electron Spectrum of Gapless Semiconductors**
By J. M. Tsidilovski

117 **Electronic Properties of Fullerenes**
Editors: H. Kuzmany, J. Fink, M. Mehring, and S. Roth

118 **Correlation Effects in Low-Dimensional Electron Systems**
Editors: A. Okiji and N. Kawakami

119 **Spectroscopy of Mott Insulators and Correlated Metals**
Editors: A. Fujimori and Y. Tokura

120 **Optical Properties of III-V Semiconductors**
The Influence of Multi-Valley Band Structures
By H. Kalt

Heinz Kalt

Optical Properties of III-V Semiconductors

The Influence of Multi-Valley Band Structures

With 143 Figures

Springer

Professor Dr. Heinz Kalt
Institut für Angewandte Physik, Universität Karlsruhe, Postfach 6980
D-76128 Karlsruhe, Germany

Series Editors:

Professor Dr., Dres. h. c. Manuel Cardona
Professor Dr., Dres. h. c. Peter Fulde
Professor Dr., Dres. h. c. Klaus von Klitzing
Professor Dr., Dres. h. c. Hans-Joachim Queisser

Max-Planck-Institut für Festkörperforschung, Heisenbergstrasse 1
D-70569 Stuttgart, Germany

Managing Editor:

Dr. Helmut K.V. Lotsch

Springer-Verlag, Tiergartenstrasse 17, D-69121 Heidelberg, Germany

Library of Congress Cataloging-in-Publication Data

Kalt, H. (Heinz), 1957-
Optical propeties of III-V semiconductors : the influence of multi-valley bandstructures / H. Kalt.
p. cm. -- (Springer series in solid-state sceince ; 120)
Includes index.
ISBN 978-3-642-63527-4 ISBN 978-3-642-58284-4 (eBook)
DOI 10.1007/978-3-642-58284-4
1. Many-valley semiconductors--Optical properties. 2. Conduction band. I. Title. II. Series.
QC611.8.M27K35 1995
539.6'226--dc20 95-24949
CIP

ISBN 978-3-642-63527-4

This work is subject to copyright. All rights are reserved, whether the whole or part of the material is concerned, specifically the rights of translation, reprinting, reuse of illustrations, recitation, broadcasting, reproduction on microfilm or in any other way, and storage in data banks. Duplication of this publication or parts thereof is permitted only under the provisions of the German Copyright Law of September 9, 1965, in its current version, and permission for use must always be obtained from Springer-Verlag. Violations are liable for prosecution under the German Copyright Law.

© Springer-Verlag Berlin Heidelberg 1996
Originally published by Springer-Verlag Berlin Heidelberg New York in 1996
Softcover reprint of the hardcover 1st edition 1996
The use of general descriptive names, registered names, trademarks, etc. in this publication does not imply, even in the absence of a specific statement, that such names are exempt from the relevant protective laws and regulations and therefore free for general use.

Typesetting: Data conversion by Kurt Mattes, Heidelberg
SPIN: 10120412 54/3144 – 5 4 3 2 1 0 – Printed on acid-free paper.

To Lissi, Patrick, and Sebastian

Preface

Semiconductor compounds consisting of elements of the third and fifth row of the periodic system, i.e., the so-called III-V semiconductors such as GaAs, InP, or $Al_xGa_{1-x}As$, are frequently used in modern (electro)-optical devices such as Light-Emitting Diodes (LEDs), semiconductor lasers, electro-optic modulators, or light detectors. The reason for using these materials in optics rather than the most widely employed semiconductor Si is the difference in band structure: Many III-V semiconductors have a direct band gap resulting in efficient optical absorption or emission. Silicon is an indirect band-gap semiconductor which in its crystalline form has only few optical applications.

The specific optical properties of III-V semiconductors are given by their band-structure characteristics. The wavelength of luminescence (e.g., the color of the LED or laser emission) is determined by the width of the forbidden gap between the valence and conduction bands. The efficiency of such devices is strongly related to the effective mass or density of states for the carriers in each band.

The band structure of semiconductors can be rather complex even within the small range of energies around the band gap that is interesting for optical applications. Device performance is often not only determined by the character and specific parameters of the fundamental gap, but further details can be most important such as the presence of additional extrema in the bands at various points of the Brillouin zone. Such a multi-valley band structure is the reason for severe restrictions of the efficiency of semiconductor lasers based on GaAs-related alloys. The latter materials are used to bring the emission wavelength of lasers and LEDs into the visible spectral range. But a multi-valley band structure can also have its merits, as is demonstrated by the Gunn oscillators used in microwave generation. The Gunn device relies on current oscillations due to the distribution of electrons among conduction-band minima with different effective masses.

In this monograph I want to review recent experimental research on the properties of III-V semiconductors with multi-valley band structures using optical methods. This research has been especially fruitful in the last decade due to the development of ultrafast, high-power lasers which can time-resolve fast relaxation processes of carriers within the multi-valley band structure as

well as generate high carrier densities resulting, e.g., in optical nonlinearities or laser emission. Another most interesting development was the progress in epitaxial sample growth which brought about low-dimensional semiconductor structures, for example, quantum wells, superlattices, quantum wires, and quantum dots. In particular, the optical properties of two-dimensional structures are meanwhile well understood and used in optical devices. The implications of both laser and material developments on semiconductor optics will be extensively discussed.

The intention of this book is to give scientists, engineers, and graduate students a comprehensive dicussion of the latest scientific results alongside a short introduction to basic concepts of semiconductor optics. A fair number of references have been cited, but such a listing is far from complete. The focus of the text will, of course, be on complex multi-valley band structures, but I will always start with a description of the properties of a simple two-band system. The extension to multi-valley systems is then not necessarily a complication but can even result in a better understanding of the two-band case. This monograph is written from the perspective of an experimental physicist and will thus treat mainly the basic physics underlying optical devices rather than engineering problems. But exactly this basic physics is essential to understand the actual device performance and to generate new ideas for the development of optical devices. The variety of III-V materials and structures which are currently being studied is enormous and a complete review of all specific features is impossible. Most of the basic ideas, however, can be illustrated via results concerning GaAs, AlAs, and their related alloys and heterostructures, which comprise the most widely investigated class of III-V semiconductors.

The first chapter gives an introduction to semiconductor band structures, methods for their calculation, symmetry considerations, and special features of the band structure of III-V compounds. It will further describe the motivation for research on multi-valley semiconductors. The optics of semiconductors under low-excitation conditions is mainly related to excitons, which are the quasiparticles of the energetically lowest excitations of intrinsic semiconductors. Their basic properties in the bulk and in low-dimensional systems and the modifications at the crossover from a direct-gap to an indirect-gap semiconductor, which occurs in several III-V systems, will be the topic of Chap. 2. The properties of laser diodes or electro-optical modulators can only be understood by consideration of many-body effects occurring at high carrier densities. In particular, the consequences of screening such as gap shrinkage, enhancement of the strength of optical transitions, and the formation of a liquid phase and the resulting optical nonlinearities will be discussed in Chap. 3. The dynamics of carriers in multi-valley systems and the spectroscopy of intervalley coupling processes will be treated in Chap. 4. I shall illustrate the importance of various mechanisms leading to a transfer of carriers between different band extrema or resulting in (sometimes even stimulated) indirect recombination. I shall close with a short summary and outlook in Chap. 5.

A large number of the results described are based on the experimental research of the author. This research was only possible due to the most fruitful collaboration with K. Bohnert, W. Rühle, M. Rinker, C.I. Harris, K. Reimann, and R. Cingolani. Further valuable contributions came from T.F. Boggess, H. Gießen, S. Haacke, K. Leo, B. Monemar, and D.P. Noorwood. Excellent samples were provided by E. Bauser, P. Ganser, I.J. D'Haennens, H. Lage, K. Köhler, Y.-C. Lu, R. Nötzel, and K. Ploog. I am very grateful for the continuous support and the hospitality of A.L. Smirl of the Center for Applied Quantum Electronics in Denton, USA (now University of Iowa), H.-J. Queisser of the Max-Planck-Institut für Festkörperforschung in Stuttgart, Germany, and C. Klingshirn of the Fachbereich Physik der Universität Kaiserslautern, Germany (now Universität Karlsruhe).

I finally want to thank I. Wollscheidt and U. Bolz, who drew most of the figures, and the staff at Springer Verlag for many suggestions for improvement of the text and expert editorial support.

Karlsruhe, August 1995 *Heinz Kalt*

Table of Contents

1. Introduction to Semiconductor Band Structures 1
1.1 Electronic States in Crystalline Solids 1
1.1.1 The One-Electron Approximation 1
1.1.2 Bloch Waves and the Band Structure Model 3
1.2 Band Structure of III–V Semiconductors 6
1.3 Some General Properties of Multi-Valley Band Structures . . . 11

2. Excitons in Multi-Valley Semiconductors 17
2.1 Basic Properties of Three-Dimensional Excitons 17
2.2 Direct-to-Indirect Crossover in Bulk Semiconductors 19
2.3 Exciton Dynamics in $Al_xGa_{1-x}As$ Near Crossover 25
2.4 Excitons in Low-Dimensional Structures 33
2.5 Direct-to-Indirect Transitions in 2D and 1D Structures 36

3. Many-Body Effects in Multi-Valley Scenarios 41
3.1 Introduction to Screening in Highly Excited Semiconductors . 41
3.2 Band-Gap Renormalization in Bulk Semiconductors 47
3.2.1 Time-Resolved Electron–Hole Plasma Luminescence . . 49
3.2.2 The Multi-Valley Model for Band-Gap Renormalization 55
3.2.3 Differential Gap Renormalization 65
3.3 Gap Renormalization in Low-Dimensional Systems 72
3.3.1 Subband Renormalization in Quantum Wells 72
3.3.2 Band-Gap Narrowing in Quantum Wires 81
3.4 Screening in One-Component Plasmas 83
3.5 Electron–Hole Droplet Formation 101
3.5.1 Picosecond Electron–Hole Droplet Formation in Indirect-Gap $Al_xGa_{1-x}As$ 103
3.5.2 Quantum-Confined Electron–Hole Droplets 112
3.6 Optical Nonlinearities at the Direct Gap of Indirect-Gap Semiconductors 119

4. Intervalley Coupling 125
4.1 Theoretical Considerations 126
4.1.1 Transfer Between Real Band States and Scattering Potentials 126
4.1.2 Transitions Involving Virtual Intermediate States . . . 133
4.2 Optical Spectroscopy of Intervalley Coupling 134
4.2.1 Timescales of Carrier Dynamics in Semiconductors . . 134
4.2.2 Deformation-Potential Scattering 136
4.2.3 Alloy-Disorder-Induced Intervalley Coupling 144
4.2.4 Real-Space Transfer in Type-II Heterostructures 158
4.3 Indirect Stimulated Emission 166

5. Summary and Outlook 173

References 179

Index 195

1. Introduction to Semiconductor Band Structures

This introductory chapter is intended to give some background on band structures in semiconductors. The reasons for the occurrence of electronic bands and forbidden gaps in solids are described, and some basic ideas for the theoretical treatment of the band structure including consideration of the crystal symmetry are discussed. The specific features of the band structure in zincblende-type III–V semiconductors and some general properties of multi-valley scenarios are introduced.

1.1 Electronic States in Crystalline Solids

1.1.1 The One-Electron Approximation

The description of the electronic properties of solids [1.1–3] is at first sight a difficult task. In most cases, the solid can be considered to be composed of ions sitting at the lattice sites with a density on the order of $10^{23}\,\mathrm{cm}^{-3}$. Most electrons in the solid are tightly bound to the ion cores while only the outer-shell electrons, the so-called *valence electrons*, contribute to the solid-state properties such as chemical binding, conductivity, and optical transitions. The Hamiltonian describing the collective properties of such a huge many-particle system would have to include the interactions of all valence electrons, of all ions, as well as interactions between electrons and ions. It is obvious that this problem requires some approximations in order to be manageable.

The first of these is the *adiabatic approximation* which relies on the significantly different masses of ions and electrons. The electron will follow adiabatically any motion of the ions while the ions themselves react rather slowly to changes in the spatial electron distribution. The electronic properties can thus be described in the framework of a rigid lattice. The interactions of the electrons with the elementary vibrational excitations of the lattice ions (i.e., with phonons) are treated as a perturbation. The description of the ions can be decoupled from the electrons in a similar way. In this book we will focus only on the electronic properties of solids.

The next simplification results from the *one-electron approximation.* Each electron reacts not only to the periodically modulated potential of the lattice ions but also to the Coulomb repulsion from the other $N-1$ electrons. It is desirable to combine the latter interactions into an effective potential so that one can treat a single-particle problem. This is done in the *Hartree–Fock approximation* which will be briefly outlined in the following.

The simplest solution of the overall Schrödinger equation

$$\mathcal{H}\Phi = E\Phi \tag{1.1}$$

would be a product wave function

$$\Phi(\mathbf{r}_1 \dots \mathbf{r}_N) = \phi_1(\mathbf{r}_1)\,\phi_2(\mathbf{r}_2) \dots \phi_N(\mathbf{r}_N) \tag{1.2}$$

which allows one to separate (1.1) into single-electron equations and to obtain the overall energy by summing over all energy eigenvalues. But the Hamiltonian $\mathcal{H}$ includes a Coulomb-interaction term which depends on the space coordinates $\mathbf{r}_i$ of two particles. If one still inserts ansatz (1.2) into (1.1) and determines the wave functions $\phi_i(\mathbf{r}_i)$ using a variational calculation to minimize the eigenenergies the result is:

$$\left[-\frac{\hbar^2}{2m}\Delta + V_{\text{lat}}(\mathbf{r}_j) + e^2 \sum_{i\neq j} \int \frac{|\phi_i(\mathbf{r}_i)|^2}{|\mathbf{r}_i - \mathbf{r}_j|}\,d\tau\right] \phi_j(\mathbf{r}_j) = E_j\,\phi_j(\mathbf{r}_j) \quad . \tag{1.3}$$

This one-electron equation, called the *Hartree equation*, includes the lattice potential as well as an average Coulomb interaction.

To account for the Pauli principle one must extend the ansatz (1.2) to a determinant (the *Slater determinant*):

$$\Phi = \frac{1}{\sqrt{N!}} \begin{vmatrix} \phi_1(\mathbf{q}_1) & \dots & \phi_N(\mathbf{q}_1) \\ \vdots & & \vdots \\ \phi_1(\mathbf{q}_N) & \dots & \phi_N(\mathbf{q}_N) \end{vmatrix} \tag{1.4}$$

which vanishes if two electrons have the same coordinates $\mathbf{q}$ (including the space coordinate $\mathbf{r}$ and the spin coordinate), i.e., if two columns are equal. Repeating the variational calculation with this new determinantal wave function and diagonalizing the Hamiltonian leads finally to the *Hartree–Fock* equation:

$$\begin{aligned} &\left[-\frac{\hbar^2}{2m}\Delta + V_{\text{lat}}(\mathbf{r}_j) + e^2 \sum_{i\neq j} \int \frac{|\phi_i(\mathbf{r}_i)|^2}{|\mathbf{r}_i - \mathbf{r}_j|}\,d\tau\right] \phi_j(\mathbf{r}_j) \\ &\quad - e^2 \sum_{i\neq j} \int \frac{\phi_i^*(\mathbf{r}_i)\,\phi_j(\mathbf{r}_i)}{|\mathbf{r}_i - \mathbf{r}_j|}\,d\tau\,\phi_i(\mathbf{r}_j) \\ &\quad = E_j\,\phi_j(\mathbf{r}_j) \quad , \end{aligned} \tag{1.5}$$

where the summation in the last term on the l.h.s. runs only over states with parallel spin. This term is the *exchange interaction* which leads to a correlated behavior of electrons having parallel spin alignment.

1.1.2 Bloch Waves and the Band Structure Model

Most important for the properties of electrons in a crystalline solid is the periodicity of the potential or rather the invariance of the Hamiltonian under translations by lattice vectors $\mathbf{R}_l$. This invariance becomes obvious when one considers the simplified version of the Hartree–Fock equation:

$$\mathcal{H}\,\psi(\mathbf{r}) = \left[-\frac{\hbar^2}{2m}\Delta + V(\mathbf{r})\right]\psi(\mathbf{r}) = E\,\psi(\mathbf{r}) \quad , \tag{1.6}$$

where $V(\mathbf{r})$ includes the potential of the ions as well as the average Coulomb and exchange terms of (1.5). This potential is invariant under primitive lattice translations as is the whole Hamiltonian, i.e., the translation operators $T_{\mathbf{R}_l}$ and $\mathcal{H}$ commute:

$$\mathcal{H}(T_{\mathbf{R}_l}\psi_n) = T_{\mathbf{R}_l}(\mathcal{H}\psi_n) = T_{\mathbf{R}_l}(E_n\psi_n) = E_n(T_{\mathbf{R}_l}\psi_n) \quad . \tag{1.7}$$

The wave functions ψ_n and $T_{\mathbf{R}_l}\psi_n$ are simultaneous eigenfunctions of $\mathcal{H}$ with the same eigenvalue E_n. These two functions are thus equal except for a factor of magnitude one: $\mathrm{e}^{\mathrm{i}\mathbf{k}\cdot\mathbf{R}_l}$. The eigenfunctions are now classified by a wavevector $\mathbf{k}$ and the eigenvalues are also a function of $\mathbf{k}$: $E_n = E_n(\mathbf{k})$. Consequently, electrons in a periodic potential are described by *Bloch waves*, i.e., plane waves which are modulated with the lattice period by a function $u_n(\mathbf{k},\mathbf{r})$:

$$\psi_n(\mathbf{k},\mathbf{r}) = \mathrm{e}^{\mathrm{i}\mathbf{k}\cdot\mathbf{r}}\,u_n(\mathbf{k},\mathbf{r}) \tag{1.8}$$

with

$$u_n(\mathbf{k},\mathbf{r}+\mathbf{R}_l) = u_n(\mathbf{k},\mathbf{r}) \quad . \tag{1.9}$$

Bloch wave functions are periodic not only in real but also in reciprocal space. A translation of $\psi(\mathbf{k},\mathbf{r})$ by a reciprocal lattice vector $\mathbf{G}$ leads to the same function:

$$\psi_n(\mathbf{k}+\mathbf{G},\mathbf{r}) = \psi_n(\mathbf{k},\mathbf{r}) \quad . \tag{1.10}$$

Therefore, it is only necessary to consider the function $E_n(\mathbf{k})$ within the first Brillouin zone. The complete dispersion can be projected into this zone by translations through reciprocal lattice vectors. This leads to a reduced zone diagram, as shown in Fig. 1.1, for the dispersion of free and nearly free electrons. The dispersion of free electrons is parabolic in $\mathbf{k}$ because it is simply given by their kinetic energy $E(\mathbf{k}) = \hbar^2\mathbf{k}^2/2m_0$ with m_0 being the electron rest mass.

The occurrence of energy gaps at the edges of the Brillouin zones for the case of nearly free electrons – these are electrons in crystalline solids for which the lattice potential can be viewed as a small perturbation – is a further direct consequence of the lattice periodicity. Electrons with wave vectors equal to the zone-edge wave vectors fulfill the conditions for Bragg reflection. Such electrons form standing waves due to superposition of forward and backward

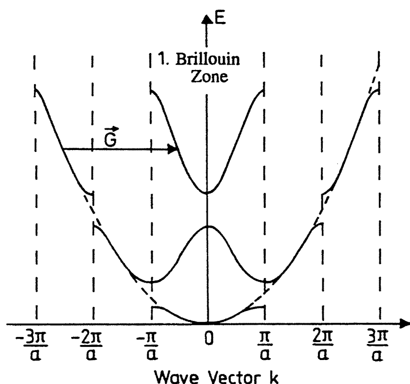

Fig. 1.1. Dispersion of free (dashed line) and nearly free electrons (solid lines) in a periodic potential for the first three Brillouin zones

scattered waves resulting in a vanishing group velocity $\partial\omega/\partial k$ at the zone edge. The degeneracy of the dispersion branches at the zone edge is lifted by the presence of the lattice potential: Standing waves having their maxima at the positions of the lattice ions have a different potential energy to those with their maxima between the ions. Thus, electrons in a periodic potential have a dispersion $E(\mathbf{k})$ which is split into various energy bands separated by forbidden gaps. This dispersion is called *band structure.*

It is obvious that in such a band structure the physical quantities momentum, given for free electrons by the first derivative of the energy with respect to k, and mass, given by the inverse of the second derivative, lose their meaning. The expectation value of the momentum is not equal to $\hbar\mathbf{k}$ in a solid, so the latter quantity is called *quasi-momentum.* The reaction of the crystal electron to external forces is described by the effective mass defined by

$$\frac{1}{m_{\text{eff}}} = \frac{1}{\hbar}\frac{d^2 E}{d k^2} \quad . \tag{1.11}$$

The effective mass is not constant for all wave vectors, as is evident from Fig. 1.1. It can even be negative, which means that the electron group velocity decreases when a field is applied, as a result of the rising superposition of backscattered waves close to the zone edge. Parabolic dispersion, i.e., a constant effective mass, is often found close to the band extrema. These regions are most important for optical and transport properties allowing, in many cases, the use of a fixed mass (*effective-mass approximation*). In semiconductors these masses are typically smaller than the electron rest mass.

Some general properties of the band structure arise from the *symmetry* of the semiconductor crystal [1.1, 2]. We already discussed some implications of translational symmetry leading to periodicity in reciprocal space. The electron dispersion is further invariant under the time-reversal operation (1.13) and the whole Brillouin zone has the full symmetry of the crystal point group, which comprises all symmetry operators α transforming the crystal into itself. The general symmetry properties are summarized by

$$E_n(\mathbf{k}) = E_n(\mathbf{k}+\mathbf{G}) \quad , \tag{1.12}$$
$$E_n(\mathbf{k}) = E_n(-\mathbf{k}) \quad , \tag{1.13}$$
$$E_n(\mathbf{k}) = E_n(\alpha\mathbf{k}) \quad . \tag{1.14}$$

More implications of the crystal symmetry will be dicussed in the next subsection for the example of zincblende-type semiconductors.

Because the electron Bloch wave functions are separable into plane-wave and lattice-periodic parts, calculations of band structures typically center on one of these parts [1.3]. They treat the crystal electrons as plane waves with the periodic potential being only a small perturbation (*nearly-free-electron approximation*, NFE) or they view the electrons as tightly bound to the ions (*tight-binding approximation*). The NFE was the basis of the discussion concerning Fig. 1.1. An example of tight-binding method is the method using a linear combination of atomic orbitals (LCAO). Here, one sums up over atomic wave functions of the original ions forming the lattice multiplied by phase factors to obey the Bloch theorem (1.7). N isolated ions have well defined atomic states. The ensemble thereof then has corresponding energy eigenvalues which are N-fold degenerate. The overlap of the wave functions, if one arranges the ions closely spaced in a lattice, leads to the splitting of the degenerate levels into bands with N nondegenerate states. Therefore, both types of calculation, NFE and LCAO result in the formation of energy bands separated by forbidden gaps.

The NFE and LCAO methods are only useful to calculate extreme situations in the band structure: either strongly delocalized or tightly bound states, respectively. To achieve good descriptions of realistic band structures one can use combinations of the two methods such as the orthogonalized plane wave (OPW), the augmented plane wave (APW), or the Korringa, Kohn, Rostocker (KKR) methods. The wave functions of nearly free electrons in OPW are modified such that they are orthogonal to the atomic core states to account for the screening of the ion Coulomb potential by deep states. The APW method uses a so-called muffin-tin potential which is constant between the ion potentials. The wave functions here are superpositions of plane-wave and radially symmetric functions, while in the KKR calculations structural Green's functions are used which include the symmetry of the lattice. The best results for band structure calculations are achieved by the use of pseudopotentials in the above described methods. Here, the deep ion potentials are replaced by flat, non-local (i.e., k-dependent) potentials which give the same scattering amplitudes for the electrons.

Finally, the electron dispersion close to the center of the Brillouin zone can be easily calculated by the $\mathbf{k}\cdot\mathbf{p}$ method [1.4]. Using the Bloch wave ansatz (1.8) in the Schrödinger equation (1.6) leads to a term $(-i\hbar/m)\,\mathbf{k}\cdot\nabla = (\hbar/m)\,\mathbf{k}\cdot\mathbf{p}$ which describes the deviation from parabolicity. This term is treated for small $\mathbf{k}$ as an additional perturbation. This method does not

require any explicit band structure calculation and is useful e.g. for the treatment of the spin–orbit coupling.

1.2 Band Structure of III–V Semiconductors

In this section we want to illustrate the details of the band structure of III–V compounds [1.5, 6]. These semiconductors crystallize in the zincblende structure which corresponds to the space group T_d. The point lattice is face-centered cubic (fcc) with a basis of two atoms similar to the diamond lattice. The III–V semiconductors therefore have band-structure features similar to one of the elemental semiconductors Si or Ge.

The Brillouin zone of the fcc lattice is shown in Fig. 1.2. The most important symmetry points in this structure are: the Γ-point at (0,0,0), the X point at (0,0,1) and its two equivalent points at (0,1,0) and (1,0,0), and the L points at $(\frac{1}{2},\frac{1}{2},\frac{1}{2})$ and the three equivalent points $(-\frac{1}{2},\frac{1}{2},\frac{1}{2})$, $(-\frac{1}{2},-\frac{1}{2},\frac{1}{2})$, and $(\frac{1}{2},-\frac{1}{2},\frac{1}{2})$. The K and U points (Fig. 1.2) are of minor importance for the optical properties. Also given in the figure are the main symmetry lines, e.g., Δ between Γ and X and Λ between Γ and L. Band structures are usually calculated along these main symmetry lines.

The band structures of two typical representatives of the III–V compounds, namely GaAs and AlAs, are depicted in Figs. 1.3 and 1.4. These compounds have a tetrahedrally oriented binding between the period-III and period-V elements mediated by eight electrons per basis from the uppermost s and p shells. The binding character is partly ionic, i.e., a mixture between full transfer of the three period-III element valence electrons to the empty period-V element valence states (ionic binding) and a distribution of the eight electrons among sp^3-hybrid states. Consequently, the upper three valence bands (VB) of the III–V band structure originate from the six atomic p orbitals while the lowest conduction band stems from the two atomic s orbitals. Each band has a two-fold degeneracy related to the electron spin. A general feature of the III–V compounds is that the maxima of the uppermost valence bands are situated at the Γ point (Figs. 1.3 and 1.4).

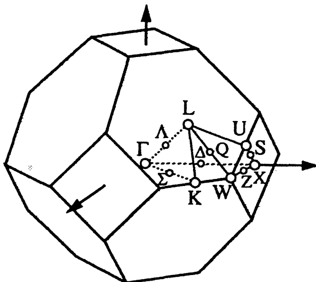

Fig. 1.2. First Brillouin zone and main symmetry points and lines for the fcc lattice

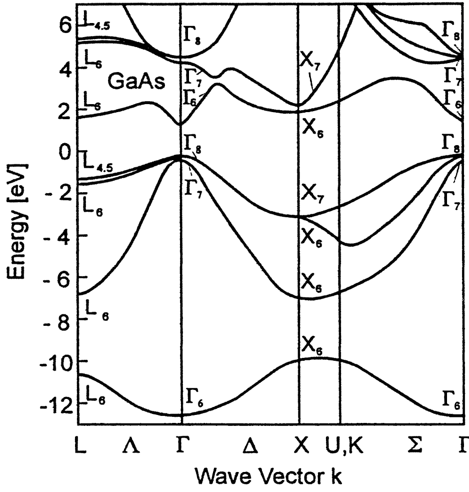

Fig. 1.3. Band structure $E(\mathbf{k})$ along the main symmetry lines calculated for the direct-gap semiconductor GaAs [1.5]

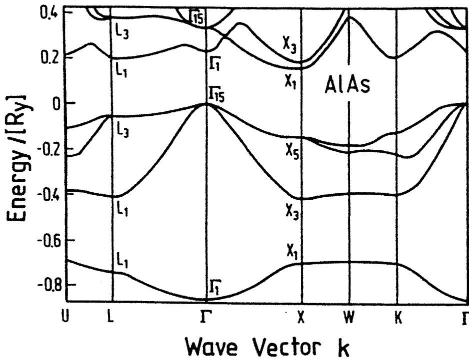

Fig. 1.4. Band structure of the indirect-gap semiconductor AlAs. The spin–orbit interaction is not included in this calculation [1.5]

The conduction band always has three minima: one each at the Γ, at the L, and close to the X point on the Δ line. The relative arrangement of these minima determines the character of the fundamental gap: For example, GaAs, InAs, and InP each have a direct fundamental gap between the Γ_8 VB maximum and the Γ_6 CB minimum, while the gaps of AlAs and GaP involve the CB minimum at (or rather close to) the X_6 minimum. The latter gaps are called indirect because optical transitions of electrons across these gaps are only possible with the assistance of a scattering process (e.g., the emission or absorption of a phonon or disorder scattering) providing the necessary quasi-momentum. The momentum of the photon involved is negligible compared to the electron $\mathbf{k}$ so that direct optical transitions are always vertical in reciprocal space.

Before we continue with more details of the band structure in the first Brillouin zone of III–V compounds, we briefly summarize the influence of the point symmetry of the lattice on the band structure. The main considerations

of group theory [1.8] will be outlined here using the example of GaAs band structure.

Each state $E_n(\mathbf{k})$ of the band structure can be classified by an irreducible representation (examples are Γ_8, X_6, or Δ_5 etc. in Figs. 1.3–5) having the same transformation properties under symmetry operations as the related wave function $\psi_n(\mathbf{k}, \mathbf{r})$. A representation is a complete set of matrices which fulfills the multiplication table of the space group. The latter table lists the results of multiplying (here sequential application of operators) the elements of the space group. These elements are the basic symmetry operations projecting the lattice onto itself. The space group T_d has eight classes of elements which are the symmetry operators transforming a tetrahedron onto itself (e.g., rotations by 120°) plus the rotations around the face diagonals of a cube. The number of irreducible representations equals the number of classes in a group. The representations of the T_d space group at $\mathbf{k} = 0$ are called $\Gamma_1 \dots \Gamma_8$, at $\mathbf{k} = (0, 0, 1)\pi/a$ $X_1 \dots X_8$ and so on.

A representation is called irreducible if it is not possible by a unitary matrix transformation to split the matrix into a direct sum of matrices of lower dimension. The dimension of an irreducible matrix gives the degeneracy of the corresponding energy eigenvalue. If one proceeds from a state $\mathbf{k}$ at a high symmetry point to a state with lower symmetry, the representation can usually be further reduced and the degeneracy of the energy eigenvalue is lifted.

An example for the latter behavior is given in the valence-band structure of III–V semiconductors at $\mathbf{k} = 0$ (Fig. 1.5). The highest valence band has a four-fold degeneracy, i.e., the corresponding representation (Γ_8) has a dimension of four. If one proceeds to a $\mathbf{k}$ point on the symmetry line between Γ and X points, the symmetry of the state is reduced considerably. The procedure is now to find the compatibility of the representation Γ_8 with the symme-

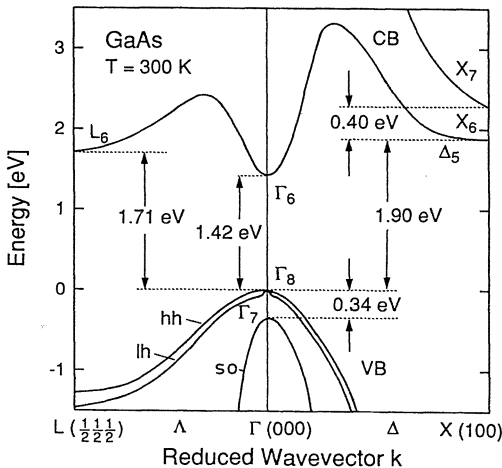

Fig. 1.5. Plot of the band structure of GaAs, including the features relevant for optoelectronic properties. The energy scale is chosen to be zero at the top of the uppermost valence band (VB). CB: conduction band; lh: light-hole; hh: heavy-hole; so: split-off VB. After [1.7]

try elements transforming the eigenfunction related to eigenvalue $E(\mathbf{k})$ into itself. Reference [1.9] gives an extensive compilation of compatibility tables. The representation is here found to split into a direct sum of two irreducible representations of dimension 2. The band is thus found to split into a light-hole and a heavy-hole valence band. The remaining degeneracy is due to the electron spin and can be lifted by further symmetry reduction, e.g., by the application of a magnetic field.

The original representations at the high symmetry points, e.g., Γ_6 for the CB and Γ_7 and Γ_8 for the VBs are found from the compatibility of the symmetry of the atomic wave functions with the symmetry elements of the T_d space group. The CB functions stem from the s orbitals while the VB states result from the p orbitals. The splitting of the VB into a four-fold degenerate and a two-fold degenerate band at $\mathbf{k} = 0$ is due to the spin–orbit coupling. The latter is called the split-off (so) band. Note that the calculated band structure of AlAs in Fig. 1.4 does not account for the spin–orbit interaction. Its consideration would lead to a reduction of the irreducible representations used in Fig. 1.4 to the ones used in Fig. 1.3 for the example of GaAs. Further, some corrections of the dispersions would result, such as the lifting of the degeneracy of the valence bands at the Γ point.

These symmetry considerations within group theory not only influence the shape of the band structure: They also determine whether transitions of electrons between different eigenstates $E_n(\mathbf{k})$ are allowed. Such transitions are mediated by interactions, e.g., with photons or phonons. The product of the representations of the eigenfunction and the scattering operator (e.g., the dipole operator), which is a direct sum of some (ir-)reducible representations as can be found from multiplication tables [1.9], has to include the representations of the final state of the transition. For example, the dipole operator transforms like the translation operators along the main crystal axes. The latter are classified in a crystal with T_d symmetry by the representation Γ_5. The direct product of the representations of the VB and the dipole operator $\Gamma_8 \otimes \Gamma_5 = \Gamma_6 + \Gamma_7 + 2\Gamma_8$ includes the representation Γ_6 of the CB. Consequently, the transition VB(Γ_8) – CB(Γ_6) is dipole-allowed.

We now return to the details of the band structure of III–V semiconductors exemplified by GaAs (Fig. 1.5). This semiconductor and its related compounds and alloys have a *multi-valley band structure*. We will use this nomenclature to describe a scenario in which several non-equivalent valleys in the conduction band are important for the properties of the material. Here, these are the minima at the Γ, L, and X points. We want to point out that this scenario is different from a *many-valley band structure* which applies in the cases of Si, Ge, AlAs, etc. in which several equivalent valleys are found at the global conduction-band minimum. But before we detail some of the general properties related to multi-valley band structures (Sect. 1.3), a few additional features like warping, terms linear in k, non-parabolicity of the dispersion, and the various definitions of effective mass [1.7] must be discussed.

Although a cubic lattice such as the fcc lattice of GaAs has the highest symmetry possible in a solid, it does not, of course, have full spherical symmetry. Electrons moving in different lattice directions respond to slightly different periodic potentials. In other words, the surface of constant energy in reciprocal space $E(\mathbf{k})$ = constant close to the Γ point reflects the symmetry of the fcc lattice but has some deviations from the surface of a sphere. This phenomenon is called band-structure *warping*. It plays only a minor role in GaAs because the influence of band non-parabolicity, which will be discussed below, is much stronger. Effective masses at the Γ point given in this book are always spherically averaged masses.

Also typically neglected is the presence of dispersion terms linear in k. Due to the lack of inversion symmetry in the zincblende structures, the Kramer theorem (1.13), which implies that only even powers of $\mathbf{k}$ occur in an expansion of $E(\mathbf{k})$, can be violated. Terms linear in k can be present shifting the maximum of the uppermost VB away from $k = 0$ as indicated in Fig. 1.6. This effect however is found to be only of the order of a few meV.

Deviations from the parabolic dispersion are far more pronounced (Fig. 1.6). They originate from interactions between different bands and can be calculated within the $\mathbf{k} \cdot \mathbf{p}$ approximation. The Γ_6 conduction-band minimum has a steadily increasing effective mass and the light-hole band has a small mass only close to the zone center. The split-off band, on the other hand, shows with increasing k first a steadily decreasing mass and then the reverse behavior at larger quasi-momentum. Consequently, the k-dependence of the effective masses of these bands has to be accounted for in transport studies and in some optical experiments (Sect. 3.2.1).

The effective masses at the L and X points of the Brillouin zone are highly anisotropic. Constant-energy surfaces are given here by rotation ellipsoids with the rotation axes along the Λ and Δ directions, respectively. The band effective mass along these axes, the longitudinal mass m_l, is larger than the

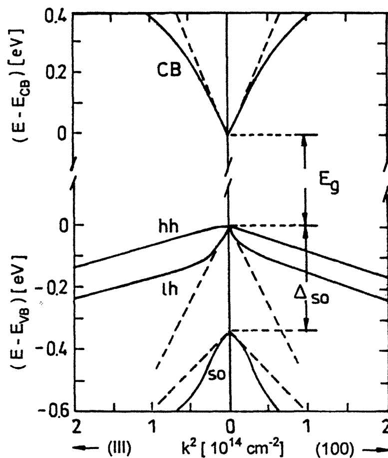

Fig. 1.6. Band structure E as as function of $(\mathbf{k}^2)$ close to the center of the first Brillouin zone in GaAs reflecting the deviations from parabolic dispersion (dashed lines). After [1.7]

two equivalent perpendicular masses, the transverse masses m_t (Table 5.1 at end of Chap. 5).

In order to simplify the description of optical or transport properties in such cases of anisotropy or of degenerate bands, the relevant band extrema are characterized by averaged effective masses. Here, one has to distinguish between the *density-of-states effective mass* (or curvature mass) m_d used for carrier statistics and the *optical mass* (or slope effective mass) m_{opt} relevant for optical and magnetic properties such as in the binding energy of excitons. As a result of the dependence between the carrier density and m_d in semiconductor statistics [1.6, 9] one chooses an average effective density-of-states mass for the combined hh and lh VB of:

$$m_d^{VB} = (m_{lh}^{3/2} + m_{hh}^{3/2})^{2/3} \quad . \tag{1.15}$$

The density-of-states mass in anisotropic bands is given by the geometrical average over the transverse and longitudinal masses:

$$m_d = (m_l m_t^2)^{1/3} \nu_e^{2/3} \tag{1.16}$$

with ν_e being the number of equivalent valleys. This case is trivial for the (nearly) isotropic Γ_6 minimum where $\nu_e = 1$ and $m_l = m_t$ and thus m_d is simply the curvature mass. Averages for the optical masses are achieved by calculating the harmonic average:

$$\frac{1}{m_{opt}^{CB}} = \frac{1}{3}\left(\frac{2}{m_t} + \frac{1}{m_l}\right) \tag{1.17}$$

$$\frac{1}{m_{opt}^{VB}} = \frac{1}{2}\left(\frac{1}{m_{hh}} + \frac{1}{m_{lh}}\right) \tag{1.18}$$

The band structure details described above are accounted for in the subsequent discussions of the optical properties of III–V compounds (Sect. 3.2.1).

1.3 Some General Properties of Multi-Valley Band Structures

The properties of modern semiconductor devices in electronics and optoelectronics are largely determined by the above-described characteristic details of the band structure of the materials employed [1.9–11]. The energy of the fundamental gap, E_g, determines e.g. the thermal population of the conduction band in intrinsic materials or the emission wavelength of laser diodes, while the carrier mobility and the density of states are directly related to the carrier effective mass, m_{eff}, at the relevant band-structure extrema. The character of the fundamental gap, either direct as in GaAs or indirect as in Si and Ge, dictates the mechanism and strength of optical transitions, and

thus determines the applicability of these semiconductors for light-emitting or light-detecting devices.

An important feature of semiconductor band structure is the presence of nonequivalent valleys at energies higher than the global minimum which determines the fundamental gap, i.e., a multi-valley band structure. The presence of these side valleys severely restricts the performance of III–V semiconductor devices, but also provides a big opportunity for device applications and novel physical phenomena.

Electrons with sufficient kinetic energy are able to transfer to states in the side valleys on a subpicosecond timescale [1.13]. The required kinetic energies for such an *intervalley transfer* are easily achieved in the GaAs system by application of high electric fields [1.14], or generation of carriers at high excess energy by optical excitation [1.13], or direct injection such as in hot-electron transistors [1.15]. In the related alloys such as $Al_xGa_{1-x}As$ or $GaAs_xP_{1-x}$, the decreasing energetic separation of central and side valleys with mole fraction x leads to large populations in the L and X minima at room temperature simply due to Boltzmann statistics. The electron transfer process requires in any case a scattering mechanism which provides the large change of quasi-momentum between the electronic states at the center and the edge of the Brillouin zone. The possible mechanisms are scattering by large wave vector phonons, by disorder-related lattice-potential fluctuations, or by periodic modulations of the band structure as are realized in superlattices. These processes can be extremely efficient on the above-mentioned timescale as already indicated.

The first electronic device to exploit the carrier transfer into the side valleys was the *Gunn oscillator* [1.16]. This microwave device relies on electrons in the side valleys of GaAs which have a much higher effective mass than those in the central minimum (Table 5.1). The application of high electric fields accelerates the electrons in the Γ minimum such that a significant number of them will transfer to the L valley. Once transferred, these carriers have a strongly reduced mobility due to the change in effective mass. The direct result is that the drift velocity of the electrons starts to decrease as a function of applied field above a critical field. This effect is demonstrated in Fig. 1.7, which compares the drift behavior in GaAs and Si. While GaAs shows the described negative differential mobility, the drift velocity in Si is a steadily increasing function until saturation occurs. The low-field drift velocity is of course much lower in Si, because the electrons are already in a high effective-mass valley at the zone edge (X_6), while the saturation velocities are similar in both materials. The described negative differential mobility or resistance (NDR) leads to the occurrence of current instabilities because deviations from avarage properties do not decay within a characteristic relaxation time but rather are amplified [1.10]. The result in GaAs is periodic oscillations of the

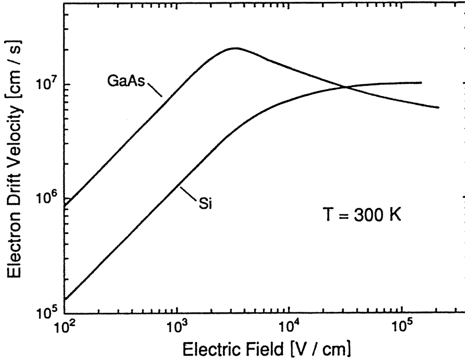

Fig. 1.7. Electron drift velocity in GaAs and Si as a function of applied field at room temperature. The negative differential velocity for GaAs results from intervalley transfer of the electrons [1.10]

resistance and thus emission of electromagetic radiation with frequencies in the microwave regime [1.17].

The NDR effect and the resulting heterogeneous electrical properties of the semiconductor material are still highly topical subjects of research. Its manifestations in space-charge instabilities or high-current-filament formation are currently being explored for nonlinear dynamic and chaotic behavior [1.18]. It is interesting to note that such effects do not require the presence of multiple nonequivalent valleys but can also occur in the standard semiconductor material Si. The anisotropy of the effective mass in the X valleys with a large longitudinal and much smaller transverse masses results in an anisotropic distribution of electrons among equivalent valleys for certain directions of the electric current with respect to the crystal orientation. The resulting spontaneous breaking of symmetry of the electron population and related instabilities [1.19] are only possible due to efficient electron transfer mechanisms between the different (but here equivalent) valleys.

The intervalley transfer of electrons also puts some strong limitations on the performance of electronic devices. One of the major goals in semiconductor device development today is to obtain ultrafast switching elements or oscillators (e.g. *ballistic hot-electron transfer devices* [1.15]). One way to achieve this aim is the miniaturization of the devices and thus the reduction of the transfer times of the electrons through them. The other is the increase of the electron drift velocity. However, as already mentioned above, the drift velocities achievable by application of high electric fields or by direct injection with high kinetic energy from an adjacent layer with a larger band gap are restricted by the intervalley scattering.

The dependence of the electron Hall mobility on the x-value or on the hydrostatic pressure in $Al_xGa_{1-x}As$ as shown in Figs. 1.8, 9 [1.20] nicely demonstrates that the observed effects of reduced mobility really stem from the transfer to the side valleys. This ternary alloy has a crossover from a direct to an indirect-gap semiconductor due to a large increase of the direct Γ_8–Γ_6 gap and a comparably small increase (or even reduction, respectively) of the indirect Γ_8–X_6 gap as a function of composition [1.21] or pressure [1.22]. An

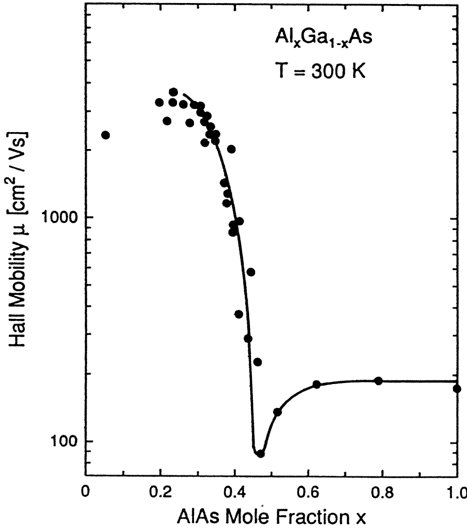

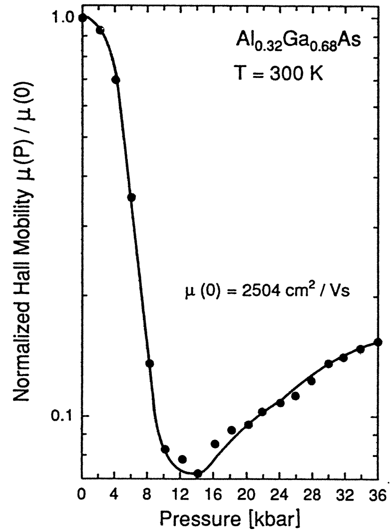

Fig. 1.8. Electron Hall mobility as a function of composition in $Al_xGa_{1-x}As$. The direct-to-indirect crossover occurs for $x = 0.45$ at room temperature [1.20]

Fig. 1.9. Electron Hall mobility as a function of applied hydrostatic pressure $Al_{0.36}Ga_{0.64}As$. The direct-to-indirect crossover occurs around 14.6 kbar [1.20]

increasing fraction of the electron population is transferred into the X and also the L valleys leading to the rapid decrease in mobility. The minimum mobility is reached around the crossover point in both cases and the mobility of the high-effective-mass side valleys is aquired far above the crossover. The similar behavior of both the composition and pressure dependence of the mobility proves directly that the observed effects are indeed induced by the intervalley transfer and not by disorder-related intravalley scattering.

However, not only the mobility of the electrons is affected by intervalley transfer: The latter mechanism also limits the emission efficiency of *semiconductor lasers* or *light emitting diodes* (LEDs) [1.10, 11]. The electrons in the side valleys of direct-gap $Al_xGa_{1-x}As$ do not contribute to the emission process. An increasing AlAs-mole content x leads to a larger relative population of the L and X minima and thus to a drastic reduction of the internal quantum efficiency for increasing bandgap, i.e., decreasing emission wavelength (Fig. 1.10). All efforts to shift the emission wavelength into the visible emission range by the choice of higher x-values resulting in a larger band-gap energy are thus truncated at about 680 nm (or $x = 0.33$) for direct-gap $Al_xGa_{1-x}As$ lasers and about 630 nm for LEDs. A further shift to shorter wavelengths would be highly desirable because the response of the human eye increases towards the blue-green range as is demonstrated in Fig. 1.10. [1.23]

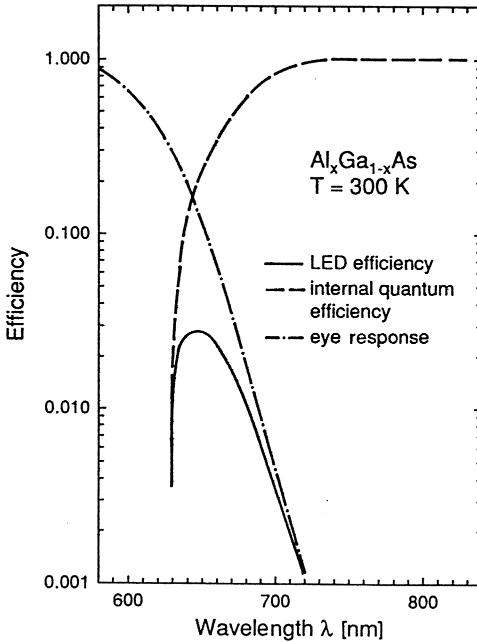

Fig. 1.10. Efficiency of $Al_xGa_{1-x}As$ LEDs as a function of wavelength. The efficiency is determined by the internal quantum efficiency (dashed) and corrected for the response of the human eye (dashed-dotted) [1.23]

The current enormous interest in intervalley transfer processes is largely triggered by the above discussed implications on device performance. No less stimulating is the direct access to such fast relaxation processes, which is now possible due to the development of *ultrafast laser spectroscopy* in the past decade [1.24]. It is possible with these methods to study fundamental relaxation processes of hot carriers in semiconductors from the temporal evolution of the optical properties such as transmission, reflection, or luminescence after generation of the electron–hole pairs by a short laser pulse [1.25].

An equally important aspect of semiconductors having a multi-valley band structure is the possibility to test many-body theories describing the dense electron–hole system which has been optically or electrically generated [1.25–27]. The *many-body effects* such as band-gap narrowing or phase transitions of the electron–hole system are significantly affected by the precise arrangement of the multi-valley scenario [1.29]. This is nicely demonstrated by the effect of differential gap narrowing in a given highly excited material which depends on the actual population of the related conduction band minima [1.29, 30]. Such many-body effects in turn strongly rearrange the band structure: the relative energetic positions of the individual valleys are shifted and even a density-induced crossover from a direct-gap to an indirect-gap semiconductor can be achieved [1.30]. It is evident that these effects have a significant impact on the intervalley-transfer processes. They also determine the performance of semiconductor devices, influencing such things as the emission wavelength or the efficiency of semiconductor lasers.

A model system well suited to study the impact of a multi-valley band structure on the optical properties of semiconductors is the alloy system $Al_xGa_{1-x}As$ including pure GaAs and AlAs, and related heterostructures. The advantages of this model system lie in the possibility to tune its band structure by changing the alloy composition [1.21] or by applying hydrostatic pressure [1.22] to these materials as was already demonstrated in Figs. 1.8, 9. For the case of low-dimensional semiconductor structures, such as short-period superlattices (SPSL), the relative position of various conduction-band minima and the character of the fundamental gap can be tailored by the choice of the compositions and thicknesses of well and barrier layers [1.32]. It is thus possible in this model system to study systematically the intervalley transfer processes as a function of the relative energy separation of the valleys involved. Another important property is that various conduction-band minima can be populated simultaneously after optical excitation. One is thus able to determine the interaction between carriers situated in different regions of the band structure.

In the first part of this work (Chap. 2) we will review optical studies on excitons in multi-valley III–V semiconductors. The properties of these excitons such as binding energy and dynamics are very sensitive to the details of the semiconductor band structure. They directly reflect the character of the related band gap and the coupling between different minima of the conduction band. The optical properties of semiconductors under intense laser excitation or high electrically injected carrier densities are governed by many-body phenomena. In Chap. 3 we will describe these many-body effects such as screening, band-gap renormalization, and the relaxation of the electron–hole plasma into a liquid phase and the modification of these effects in a multi-valley scenario. The influence of dimensionality will be illustrated as well as the differences between one- and two-component plasmas. Examples of the application of many-body effects will be given in the discussion of the optical nonlinearities at the direct gap of indirect-gap semiconductors. Our model of optical properties will then be used in Chap. 4 to deduce the mechanisms and strengths of intervalley coupling from both time-resolved and steady-state optical spectroscopy. Indirect stimulated emission in $Al_xGa_{1-x}As$ is finally discussed as a rather unusual application of efficient disorder-induced intervalley coupling in combination with a band alignment just above the crossover to an indirect-gap semiconductor [1.33]. This mechanism shows some promising features for device applications: the wavelength of stimulated emission in the $Al_xGa_{1-x}As$ system is pushed into the orange spectral region at room temperature and its threshold is much less sensitive to the lattice temperature than is the usual direct emission [1.33, 34]. We will close with a summary and a short outlook to future developments in semiconductor optics.

2. Excitons in Multi-Valley Semiconductors

Excitons are the quasi-particles of the lowest electronic excitations in intrinsic semiconductors. This chapter summarizes the basic optical properties related to excitons in both bulk and low-dimensional semiconductors. We specially emphazise the situation in semiconductors close to the transition from a direct to an indirect-gap band structure. The dynamics of excitons in $Al_xGa_{1-x}As$ at the crossover point illustrate the consequences of such a multi-valley scenario. Excitonic transitions which are indirect in reciprocal as well as in real space are found in type-II superlattices. The crossover from type-I to type-II band alignment in quasi one- and two-dimensional structures can be deduced from exciton spectroscopy.

2.1 Basic Properties of Three-Dimensional Excitons

The optical properties of semiconductors in the regime of low excitation are largely determined by *excitons*, i.e., by the bound and continuum states of electron–hole pairs [2.1–3]. The Coulomb attraction between an electron and a hole leads to a hydrogen-like resonance spectrum below the band-gap energy E_g and a Sommerfeld enhancement of the band-to-band transitions. The exciton eigenfunctions $\Psi^{n,\mathbf{K}}$ in bulk (3D) materials are given in the effective-mass approximation by a product of the conduction- and valence-band functions $u_{c,v}(\mathbf{r}_{e,h})$ and a modulation function $\phi^{n,\mathbf{K}}(\mathbf{r}_e, \mathbf{r}_h)$: [2.4]

$$\Psi^{n,\mathbf{K}}(\mathbf{r}_e, \mathbf{r}_h) = \Omega\, \phi^{n,\mathbf{K}}(\mathbf{r}_e, \mathbf{r}_h)\, u_c(\mathbf{r}_e)\, u_v(\mathbf{r}_h) \quad , \tag{2.1}$$

where $\mathbf{r}_{e,h}$ are the electron and hole coordinates, Ω is the unit-cell volume and $\mathbf{K} = \mathbf{k}_e + \mathbf{k}_h$ is the total exciton wave vector. The modulation function is a solution of a Schrödinger equation which is separated into a center-of-mass translation and a relative motion of the electron and hole in their attractive Coulomb potential:

$$\phi^{n,\mathbf{K}}(\mathbf{r}, \mathbf{R}) = \frac{1}{\sqrt{V}}\, e^{i\mathbf{K}\cdot\mathbf{R}}\, \psi^n(\mathbf{r}) \quad , \tag{2.2}$$

with $\mathbf{r}$ and $\mathbf{R}$ being the relative and center-of-mass coordinates, respectively; V is the crystal volume, and the envelope functions $\psi^n(\mathbf{r})$ are solutions of a

modified hydrogen problem. The exciton eigenenergy E_n is characterized by a principal quantum number n and has a dispersion related to the motion of the center of mass ($M = m_e + m_h$):

$$E_n^{3D}(k) = E_g - \frac{Ry^*}{n_B^2} + \frac{\hbar^2 K^2}{2M} \quad . \tag{2.3}$$

The excitonic Rydberg energy is calculated in analogy to the hydrogen model, but accounting for the exciton reduced mass μ_{ex} and the modified strength of the Coulomb interaction in the solid by the real part of the dielectric function ϵ_1:

$$Ry^* = \frac{e^2 \mu_{ex} m_0}{2(4\pi \epsilon_0)^2 \epsilon_1^2 \hbar^2} \quad . \tag{2.4}$$

The natural constants e (unit charge), m_0 (electron rest mass), ϵ_0 (permittivity of vacuum) and $\hbar$ (Planck's constant) are used here in SI units. The excitonic Bohr radius is found from minimizing the total energy to be:

$$a_B^* = \frac{4\pi\epsilon_0 \epsilon_1 \hbar^2}{m_0 \mu e^2} \quad . \tag{2.5}$$

The exciton dispersion and the optical absorption of a semiconductor in the region of the exciton resonances are schematically shown in Fig. 2.1. Exciton absorption (or luminescence) is governed by the fact that creation (annihilation) of an exciton is only possible close to $K = 0$ due to the negligible momentum of the photon involved. The width of the absorption (emission) lines is related to homgeneous and/or inhomogeneous broadening.

Besides these free excitons, excitons bound to shallow impurities play an important role for the optical properties close to the band edge of semiconductors [2.5, 6]. The theoretical description of these bound excitons is a rather complex many-body problem, which will not be detailed here. A rough estimate of the binding energies of bound excitons is given by Haynes' rule, $E_b^{BE} \approx E_i/10$ [2.7]. The ionization energy E_i of the impurity can also be approximated by the hydrogen model by replacing μ_{ex} in (2.4) with the effective

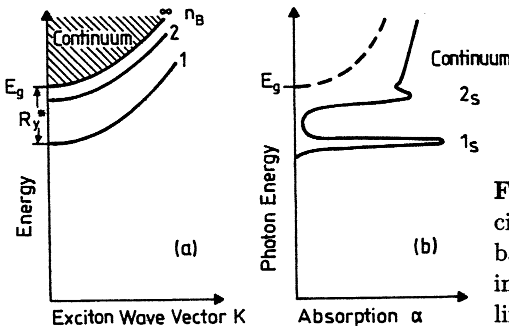

Fig. 2.1. (**a**) Dispersion of free excitons. (**b**) Absorption close to the band edge of a semiconductor including (solid line) and neglecting (dashed line) excitonic effects

mass of the electron or hole for the case of neutral donors or acceptors, respectively.

Excitonic binding is generally found between holes and electrons at critical points of the band structure provided both carrier types have equal group velocities. A coupling to an electromagnetic field, i.e., a nonvanishing oscillator strength of these excitons, is subject to group-theoretical selection rules. In the multi-valley scenario of GaAs (Fig. 1.5), strong excitonic resonances are found close to all direct and indirect band gaps related to the lowest conduction band. The only stable quasiparticle, however, is generally the exciton at the fundamental gap. The lifetimes of all excitonic resonances at higher energies are extremely short resulting from a strong coupling between the different valleys in the bands. The electron bound to the hole in the exciton typically scatters to the lowest conduction band minimum on a subpicosecond timescale. The relevant scattering mechanisms and their respective strengths will be discussed in detail in Chap. 4. Similar scattering mechanisms are also found when a lower-energy valence-band maximum is considered [2.8]. An exception to the behavior just decribed are the excitons in $Al_xGa_{1-x}As$ close to the crossover point, where stable direct and indirect excitons exist simultaneously. The dynamics of these excitons will be described in Sect. 2.3. But first we will outline in general terms how the transition from a direct to an indirect-gap semiconductor and the relative energy separation of various conduction-band minima influence the properties of the excitons (Sect. 2.2). The properties of excitons in low-dimensional semiconductor structures will be treated in Sect. 2.4, and the effect of the additional separation of electron and hole in an exciton as given in type-II structures will be discussed in Sect. 2.5.

2.2 Direct-to-Indirect Crossover in Bulk Semiconductors

Many basic properties of excitons are influenced by the nature of the band gap to which they are related. A nice way to illustrate these effects is to induce a transition from a direct to an indirect gap in a III-V compound semiconductor. The most obvious way to achieve such a transition is to form alloys of direct-gap semiconductors like GaAs or InP with indirect-gap materials such as AlAs or GaP. This transition is shown in Fig. 2.2 for the case of $Al_xGa_{1-x}As$ at low lattice temperature ($T_L = 5\,K$) [2.9]. The energies of the band gaps between the Γ_8 valence band and the Γ_6, L_6, and X_6 conduction bands depend differently on the AlAs mole fraction x resulting in a smooth transition between the $\Gamma - L - X$ ordering in GaAs and the $X - L - \Gamma$ ordering in AlAs. The actual direct-to-indirect crossover occurs at $x_c = 0.43$ at low lattice temperature. The crossover composition x_c shifts to 0.45 at room temperature [2.10] as a result of different Varshni coefficients [2.11] for the

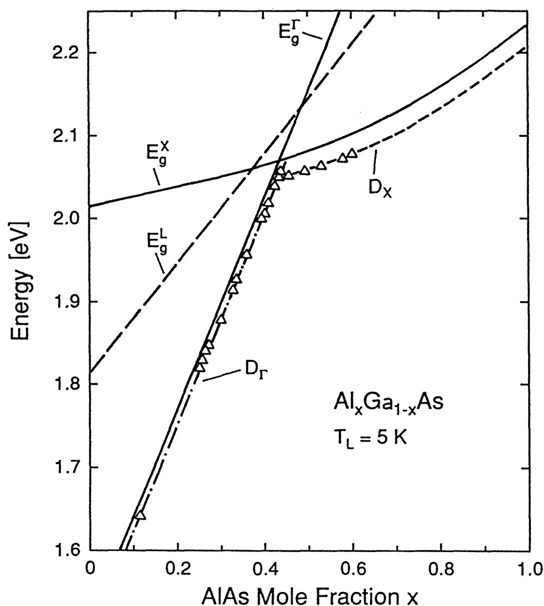

Fig. 2.2. Energy of the band gaps and of the donor-bound exciton as a function of composition in $Al_xGa_{1-x}As$. The direct-to-indirect crossover occurs at $x_c = 0.43$ for $T_L = 5$ K according to [2.9]

various gaps. We will return to this effect and its consequences for stimulated emission in Sect. 4.3. The composition dependence of the band gaps at room temperature is summarized in Table 5.1 at end of Chap. 5.

It is necessary at this point to comment on the variety of conflicting reports in the literature on the composition (x) dependence of the band gaps and the crossover composition in $Al_xGa_{1-x}As$. Recent publications applying new techniques such as electron microprobe analysis [2.12, 13] or nuclear reaction analysis [2.14, 15] for the determination of the absolute x value reported a steeper slope of $E_g^\Gamma(x)$ than measured in Ref. [2.9] and a crossover composition around $x = 0.38$. Measurements based on high-resolution x-ray diffraction [2.16, 17], on the other hand, seem to confirm the results of *Casey* et al. [2.10] and *Wolford* et al. [2.9]. One problem with these $E_g(x)$ calibrations is that either the determination of the composition [2.9, 10, 12, 13, 16, 17] and/or the optical determination of the band gaps [2.12, 15] rely on an approximate model of the results. Even the values of the excitonic binding energies needed to determine the gap energy from excitonic luminescence differ by a factor of 4 depending on whether a simple interpolation between GaAs and AlAs [2.9, 13, 14, 17] or the disorder-enhanced values of Ref. [2.18] are used as in [2.16]. In any case, most of the phenomena reported in this work do not depend critically on the absolute x-value but rather on the relative energy position of the conduction-band minima. These relative positions can be reliably extracted from the data of *Wolford* et al. [2.9] (Fig. 2.2) once the direct gap of a given sample has been determined. The x-value is then understood not as an absolute quantity but only as a label to calibrate the gap energies.

The exciton bound to shallow donors follows the energy dependence of the fundamental gap. This can easily be demonstrated by comparison of emission and absorption spectra (see also Figs. 2.7, 8). The change in binding energy of bound and free excitons at the crossover is then a direct result of the drastic change in effective mass of the electrons involved (2.4). Very similar effects are observed when the direct-to-indirect transition is achieved by application of hydrostatic pressure to initially direct-gap samples. The most attractive feature of such pressure dependence studies is that some selected properties such as the gap energies can be modified systematically without having to change the sample. The pressure dependence of the gaps in GaAs is illustrated in Fig. 2.3. Here, both the Γ_8–Γ_6 and Γ_8–L_6 gap increase as a function of pressure with pressure coefficients of 10.73 meV/kbar [2.19] and 2.8 meV/kbar [2.20], respectively, while the Γ_8–X_6 gap decreases with −1.34 meV/kbar [2.19]. Again, the change of effective mass is directly reflected in the excitonic binding energies. Note that close to the crossover point donor-bound excitons related to both the direct (D_Γ, X) and the indirect gap (D_X, X) are observed as long as the former is not yet resonant with the excitonic continuum related to the latter. We will demonstrate a similar effect for free excitons in Sect. 2.3.

The lifetime of the bound excitons strongly depends on the nature of the fundamental gap as well as on the energey separation between the Γ and X minima in the indirect regime as a result of the so-called *band-structure effect* [2.21, 22] Indirect recombination of the X-point electron and Γ-point hole in the excitons requires a mechanism to provide the necessary momentum

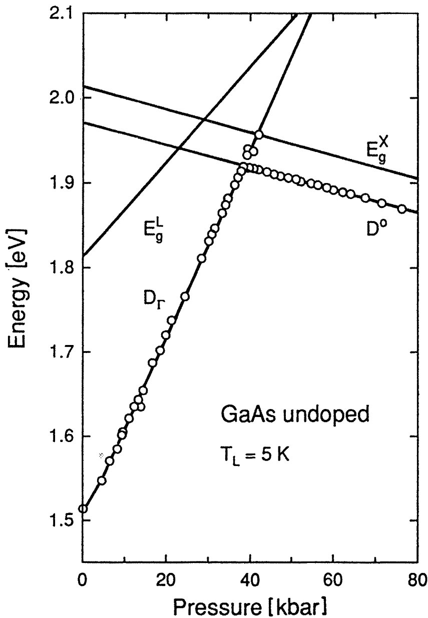

Fig. 2.3. Energy of the band gaps and of the donor-bound exciton as a function of pressure in GaAs. The direct-to-indirect crossover occurs at $P_c = 41.3$ kbar for $T_L = 5$ K according to [2.19]

change. This mechanism is given for the case of bound excitons by the fact that the electron wave function in this localized quasiparticle is a linear combination of wave functions of the whole first Brillouin zone with amplitudes at each k vector varying inversely with the energy separation between the bound state and the conduction band energy at that specific k vector. The increase of Γ–X separation, e.g. by raising the pressure, reduces the admixture of $k = 0$ states to the electron wave function and thus the overlap of electron and hole wave functions. The resulting reduction of the oscillator strength is reflected in a decrease of luminescence efficiency or an increase in radiative lifetime. The related theory and early measurements in $GaAs_{1-x}P_x$ and $Ga_xIn_{1-x}P$ are reviewed by *Pikhtin* [2.22], the properties of bound excitons in these materials are discussed by *Nelson* [2.23], while the case of excitons $Al_xGa_{1-x}As$ is treated by *Sturge* et al. [2.24]. Time-resolved experiments in GaAs were performed by *Mariette* et al. [2.25] (Fig. 2.4) and demonstrated the band-structure effect for hydrostatic pressures above P_c. The lifetime of the bound exciton is roughly 1 ns independent of pressure below the crossover pressure P_c. This finding is theoretically expected since direct optical transitions are a first-order perturbation process and thus only weakly dependent on the transition energy. Above P_c the lifetime suddenly changes to 20 ns and rises continually with increasing pressure. The latter results also indicate the rather strong oscillator strength of the indirect bound excitons close to the crossover point as reflected in the lifetime, which is only one order of magitude longer than in the direct-gap case. This large transition strength is exploited in visible LEDs which are based on the recombination of excitons bound to isoelectronic impurities as in GaP:N and $GaAs_xP_{1-x}$:N [2.10].

Not only the spatial confinement brings about a coupling between the conduction-band minima at different points of the Brilloiun zone but also the

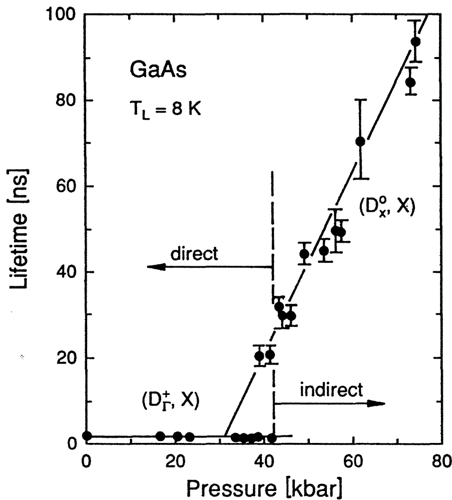

Fig. 2.4. Lifetime of donor-bound excitons in GaAs as a function of hydrostatic pressure [2.25]

periodic or random fluctuations in the lattice potential related to phonons, structural superperiodicity or disorder. Such fluctuations, as long as they occur on length scales comparable to the lattice constant, lead to mixtures of electronic wave functions with large wave-vector differences. The fluctuations can often be treated as small perturbations because the measured quantities such as carrier path length or the excitonic Bohr radius are significantly larger than the length scale of the fluctuation [2.22]. The consequence is that the usual band-structure picture as derived from the strict lattice periodicity is still applicable to a good approximation. The consequences of the mixing are detected in the excitonic optical properties of these materials which will be reviewed shortly. The determination of the absolute and relative coupling strength is left for the discussion in Chap. 4.

An example for such intervalley coupling is given by the luminescence spectrum in indirect-gap $Al_xGa_{1-x}As$ (Fig. 2.5). The emission shows the previously described zero-phonon recombination of the bound exciton as well as phonon-assisted and disorder-assisted recombination channels. Here the disorder mechanism is the *alloy disorder* resulting from the random substitution of Ga by Al atoms in the lattice. The phonons involved are zone-edge (i.e. large k vector) longitudinal optical (LO) vibration modes of the GaAs and AlAs sublattices [2.24]. It is important that the zero-phonon line and the phonon sidebands of the free exciton emission (FE) have similar intensities while the additional spatial-confinement effect strongly enhances the zero-phonon recombination of the bound exciton. The relative intensities of the bound and free excitons are mainly determined by capture and reemission

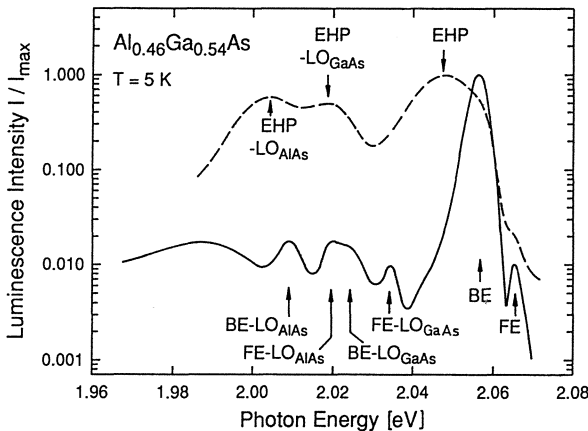

Fig. 2.5. Time-integrated luminescence in indirect-gap $Al_xGa_{1-x}As$ for low (solid line) and high optical excitation (dashed line) displaying zero-phonon and phonon-assisted recombination for free (FE) and bound excitons (BE) as well as for the electron–hole plasma (EHP)

processes between them (Sect. 2.3). Note that the same recombination mechanisms found for the FE also determine the emission in the high excitation case as is demonstrated by the time-integrated luminescence spectrum of an electron–hole plasma (dashed line in Fig. 2.5).

Up to now, we have only been concerned with the coupling of nonresonant states in different valleys. The same coupling mechanisms also lead to a transfer of carriers between real states. The exciton-related properties of a semiconductor are affected by such transfer in the case of excitons resonant with continuum states of a different minimum. This occurs e.g. for the Γ_8–Γ_6 gap exciton in indirect-gap $Al_xGa_{1-x}As$ [2.26], in GaP [2.27], and in GaAs, which is an indirect-gap material induced by hydrostatic pressure [2.28]. The electron state in the conduction band for these cases is resonant with states in the X or L minima, which imposes an extermely short lifetime on the related exciton due to a resulting intervalley scattering of the electron. This lifetime (discussed in conjunction with intervalley-scattering times in Chap. 4) leads to a significant broadening of the homogeneous linewidth of the excitonic resonance as was demonstrated by *Goñi* et al. [2.28] for excitonic absorption in GaAs under hydrostatic pressure (Fig. 2.6). In emission these excitons are visible, if at all, in time-resolved experiments in form of a flash-like, spectrally broad luminescence signal following the temporal evolution of the picosecond excitation pulse, although it remains unclear whether the observed emission really stems from electron–hole pairs, that have had enough time to form a bound excitonic state before recombination.

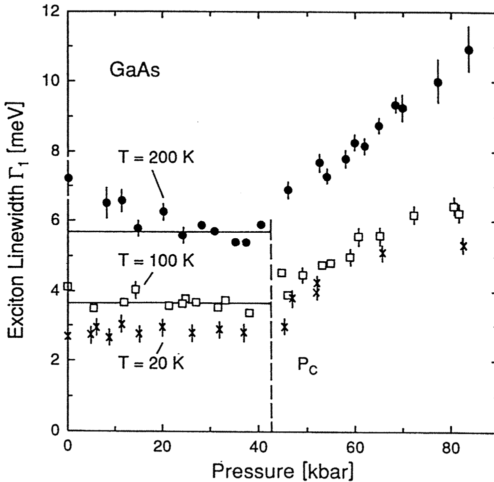

Fig. 2.6. Linewidth of the direct exciton in GaAs as a function of hydrostatic pressure. The linewidth stays about constant up to the crossover pressure P_c and then increases as a result of the intervalley transfer [2.28]

2.3 Exciton Dynamics in $Al_xGa_{1-x}As$ Near Crossover

An exception to the above described behavior are excitons in semiconductors close to the direct-to-indirect crossover. Stable excitons are formed once the related electron and hole states are not isoenergetic to continuum states at other wavevectors, e.g., at other subsidiary extrema of the band structure. Consequently, direct and indirect free excitons (FE_Γ and FE_X) are observed simultaneously in near crossover $Al_xGa_{1-x}As$. We will describe in the following the identification of and the interaction between the exciton states in a scenario where the semiconductor sample has a direct fundamental gap in the picture of the one-electron approximation, but is an indirect-gap material once many-particle states like excitons or an electron–hole plasma are excited.

The difference between a clearly indirect-gap material and a sample with the scenario just described can be demonstrated by comparison of the optical properties in absorption and emission. Low-excitation photoluminescence excitation (PLE) spectroscopy is used to determine the direct and indirect absorption edges. Only the direct absorption edge is observed in $Al_{0.42}Ga_{0.58}As$ without any additional step due to the indirect gap (Fig. 2.7). This is in contrast to what is found in clearly indirect samples like $Al_{0.44}Ga_{0.56}As$. Here, two steps related to the indirect and direct gaps are detected (Fig. 2.8). The indirect step is easily identified from the position of the zero-phonon line

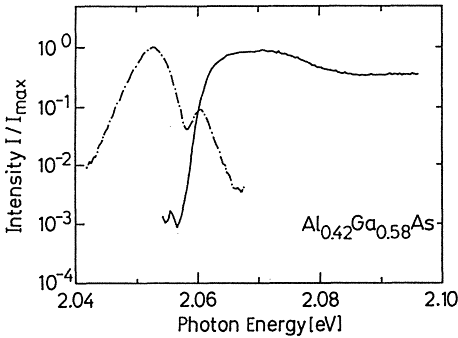

Fig. 2.7. Photoluminescence excitation (PLE) spectrum (solid line) and time-integrated luminescence (dashed-dotted line) in $Al_{0.42}Ga_{0.58}As$ [2.29]

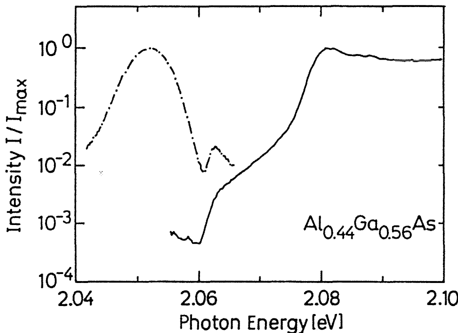

Fig. 2.8. Photoluminescence excitation spectrum and time-integrated luminescence in a sample well above the crossover composition [2.29]

related to the free X-point exciton FE_X, which exactly coincides with the indirect absorption edge. The broader line at lower energies is due to impurity-bound excitons (most likely donor-bound excitons). The same luminescence feature is, however, found in the $Al_{0.42}Ga_{0.58}As$ sample in the time-integrated spectrum at low excitation (Fig. 2.7). This demonstrates that the direct and indirect gaps must be very close in energy in the latter sample.

The actual ordering of the direct and indirect gaps can be concluded from the observation of the direct free exciton FE_Γ, an additional line in time resolved luminescence. This exciton is observed 2 meV above the FE_X in $Al_{0.42}Ga_{0.58}As$ (luminescence at short delay times in Fig. 2.9) and at slightly higher energies and well separated from the FE_X luminescence in a sample with slightly higher x-value (Fig. 2.10). The binding energy of the two excitons, as calculated from (2.4), is different by almost a factor of two, namely 6.8 meV for the FE_Γ and 11.4 meV for the FE_X. Extrapolation from the position of the exciton lines places the direct gap in the $Al_{0.42}Ga_{0.58}As$ sample at 2.068 eV and the indirect slightly higher at 2.071 eV (compare also Fig. 2.15).

The assignment of the additional line to the FE_Γ is supported by the pressure dependence of this line. The same emission line is observed in a $Al_{0.38}Ga_{0.62}As$ sample which is indirect due to hydrostatic pressure. We show in Fig. 2.11 two spectra at short delay times after excitation with a picosecond pulse at different pressures. The nominal crossover pressure for this sample would be at $P_c = 7.5$ kbar, i.e., a pressure of 6.9 kbar corresponds to a similar situation for the above described $x = 0.42$ sample just below the crossover. The scenario for 8 kbar is such that the lowest conduction-band minimum is at the X_6 point, but the direct-exciton energy is still lower than the indirect-gap energy. The bound-exciton line remains nearly unaffected by the increase in pressure which again confirms its assignment to the indirect gap. Increasing the pressure leads to a shift of the high-energy line

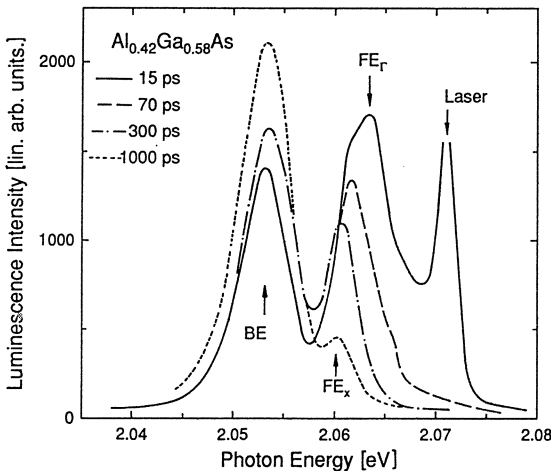

Fig. 2.9. Time-resolved luminescence spectra in $Al_{0.42}Ga_{0.58}As$ after picosecond excitation

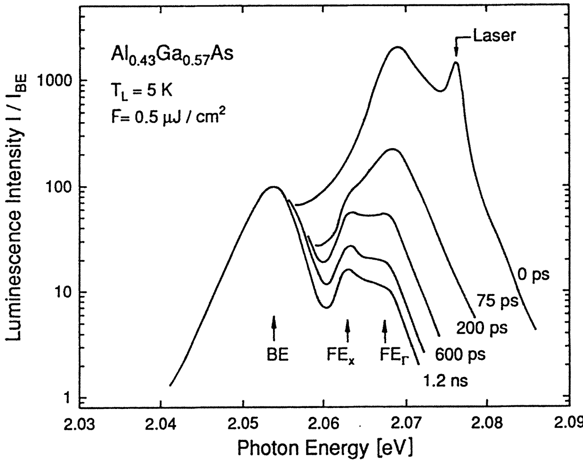

Fig. 2.10. Time-resolved luminescence spectra in $Al_{0.43}Ga_{0.57}As$ after picosecond excitation

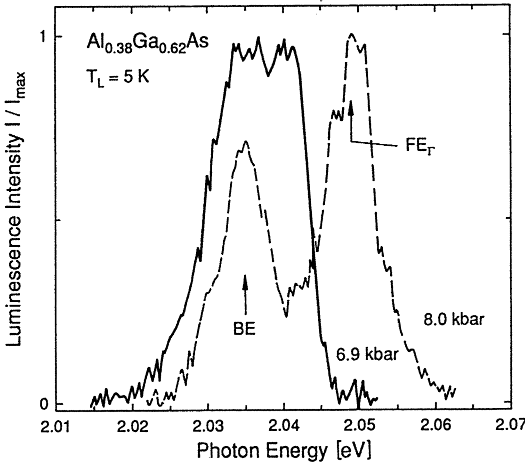

Fig. 2.11. Luminescence spectra taken at $t = 50$ ps in $Al_{0.38}Ga_{0.62}As$ just below (6.9 kbar) and above (8 kbar) the crossover pressure

in the spectra of Fig. 2.11 according to the pressure coefficient of the direct gap in $Al_{0.38}Ga_{0.62}As$ (9.9 meV/kbar [2.30]) as is evident from comparison of the 6.9-kbar and the 8-kbar spectra. The direct free exciton (FE_Γ) disappears as time progresses for $P = 8$ kbar (Fig. 2.12) similar to the behavior found in the $x = 0.42$ and $x = 0.43$ samples (Figs. 2.9, 10). For $P = 6.9$ kbar, the direct and indirect excitons are calculated from the pressure coefficients and binding energies and are found to be almost degenerate. Consistently, no separate lines and related dynamics are observed. The above-mentioned flash-like emission related to the direct gap is seen for further increases of pressure above 8.5 kbar, demonstrating the degeneracy of the FE_Γ with the continuum of the FE_X. The exciton is then very rapidly dissociated due to the fast intervalley scattering of the electron into the X minima.

More information on the identity of the observed exciton lines is gained from systematic studies of the temperature dependence of the luminescence

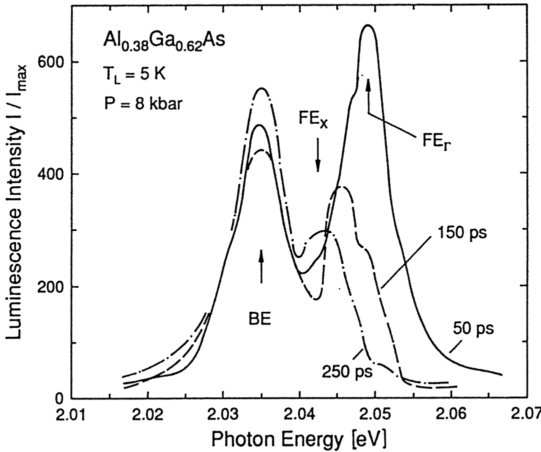

Fig. 2.12. Temporal evolution of the direct- and indirect-exciton luminescence in $Al_{0.38}Ga_{0.62}As$ above the crossover pressure

(Fig. 2.13). Both free and bound exciton emissions related to the indirect gap are rapidly quenched by increasing the temperature and have disappeared completely above a lattice temperature of $T = 50\,K$. This simultaneous quenching is consistent with the assignment of the emission lines already performed in connection with the PLE spectra (Figs. 2.7, 8). The direct exciton emission broadens on the high-energy side as a function of temperature according to the Boltzmann distribution of the excitons.

A final important experiment for the identification of the luminescence lines is the resonant excitation into the excitonic resonances. This experiment allows one to separate *free excitons* from those *localized* in potential fluctuations. These potential fluctuations arise in ternary semiconductors from alloy disorder resulting from the random distribution of the alloy constituents at the lattice sites. We will treat the implications of alloy disorder in more detail in Chap. 4. It is possible in the case of localization to resonantly excite excitons at a certain energy position in the tail of localized states. The resulting exciton distribution is then initially as narrow as the spectral linewidth of the laser. The distribution only broadens or shifts to lower energies when the excitons are able to relax within these tail states via hopping or multiple trapping with the assistance of acoustic phonons [2.31–34]. We observe such a line narrowing of the emission from the inhomogeneous linewidth to the spectral width of the laser (or rather, the spectral resolution of the experiment as given by the spectrometer) when tuning the laser to the low-energy side of the FE_X emission. This effect is demonstrated in Fig. 2.14 where three spectra taken for different excitation energies $h\nu_{exc}$ are displayed. These spectra show that localization is rather weak in the case of indirect excitons in $Al_xGa_{1-x}As$ as was already evident from the nearly negligible Stokes shift of the luminescence line with respect to the indirect excitonic absorption edge (Figs. 2.7, 8).

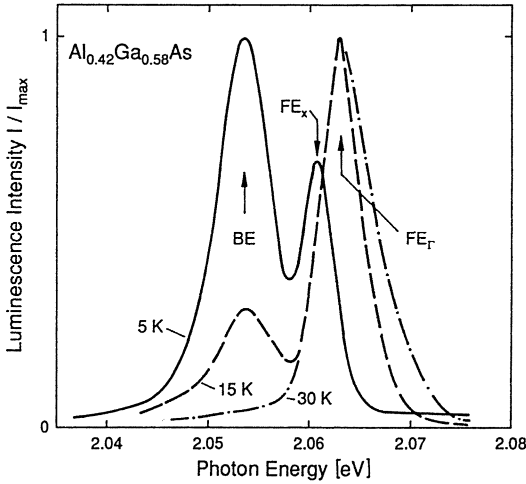

Fig. 2.13. Luminescence spectra in $Al_{0.42}Ga_{0.58}As$ as a function of lattice temperature

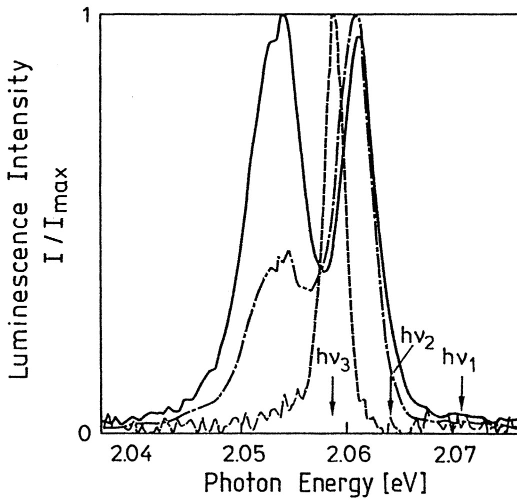

Fig. 2.14. Luminescence spectra in $Al_{0.42}Ga_{0.58}As$ as a function of excitation photon energy $h\nu$

These results on the localization of the indirect excitons confirm the findings of *Sturge* et al. [2.24]. They report on the zero-phonon decay of excitons in indirect-gap $Al_xGa_{1-x}As$ which they find to be nonexponential for the case of localized excitons. This behavior is explained in the model of *Klein* et al. [2.35] as resulting from the localization-depth dependent recombination rate of indirect excitons in semiconductor alloys (discussed in relation to alloy scattering in Chap. 4). The change of the exciton decay from nonexponential to exponential behavior with temperature demonstrates that the excitons are mobile above a lattice temperature of 8 K and partially mobile even at 2 K.

The clear distinction of excitons related to different gaps demonstrates that alloy disorder in $Al_xGa_{1-x}As$ does not significantly alter the band struc-

ture features resulting from the lattice periodicity. Strongly affected by the additional perturbation are, however, the optical matrix elements and the exciton dynamics. In the following we will focus more closely on the dynamics resulting from the interactions between the now clearly identified excitonic states. The actual interaction channels are obvious from the above-discussed properties of the excitonic emission. Trapping of excitons into states bound to shallow impurities is thus only efficient for free indirect excitons. That the excitons have to be mobile is proven by the disappearance of the bound-exciton emission when only localized excitons are excited (Fig. 2.14). Thus, there is no spatial correlation between localized and bound excitons, in contrast to the findings for excitons localized in well-width fluctuations in narrow quantum wells [2.36, 37]. The quenching of the BE emission at elevated lattice temperatures, where the indirect excitons are also lost, demonstrates that the direct excitons are not directly trapped at the impurities. Such a quenching of a BE emission with rising temperature is usually attributed to the thermal re-emission of the BE to the FE states following detailed-balance arguments [2.38]. The energy separation between BE and FE_Γ (11 meV) is here too large in comparison to the thermal energy to allow a significant re-emission to FE_Γ. The thermal energy $k_B T$, however, corresponds to the energy difference between the indirect and direct free excitons (3 meV). We can conclude that the FE_X are thermally scattered within their dispersion to states where they recombine via alloy-disorder scattering to the resonant FE_Γ states. The BE is lost simultaneously because these states are predominantly fed by FE_Xs.

This behavior is not surprising, because the trapping of an FE_Γ to the donor site requires a change of the electron wave funtion from Γ to X type and a simultaneous transfer of energy to the phonon system. The selection rules for electron–phonon interaction in this particular alloy, however, allow only a Γ–X scattering of electrons with assistance of zone-edge longitudinal optical phonons [2.40]. This transfer process is not possible because the energy separation between FE_Γ and BE or FE_X is too small. Scattering via alloy disorder, on the other hand, is an elastic process and thus also not suitable for the direct trapping of the direct exciton at the impurity site. The only interaction channel between direct and indirect excitons is then alloy scattering between FE_Γ states and resonant states of the FE_X with some excess kinetic energy above the minimum of the indirect-gap exciton dispersion. The exciton interactions in the crossover scenario are summarized in Fig. 2.15.

The resulting exciton dynamics is reflected in the above-discussed luminescence spectra and the decay of the individual luminescence lines (Fig. 2.16). The generation of the excitons proceeds mainly via direct absorption and direct excitons are dominant for a short period of time after the excitation (Figs. 2.9, 10, 12). For excitation above the band gap, as in Fig. 2.10, even a spectrally very broad, flash-type emission related to the Γ minimum is ob-

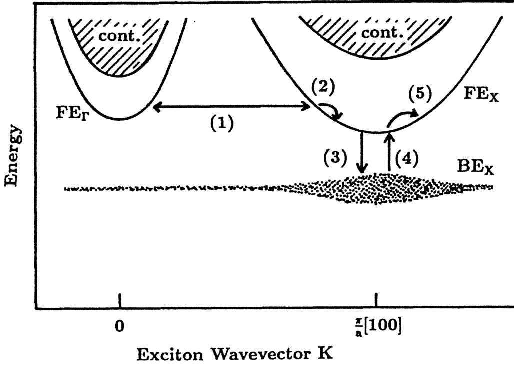

Fig. 2.15. Interaction channels between direct and indirect excitons in $Al_xGa_{1-x}As$ at the crossover point: (1) intervalley alloy scattering, (2) phonon emission, (3) trapping to impurity, (4) thermal re-emission, and (5) phonon absorption

served. This emission follows the temporal development of the laser pulse and reflects the initial fast transfer of electrons to the X valleys (Chap. 4). The FE_Γ decays extremely fast and reaches thermal equilibrium with the indirect exciton within about 300 ps, which is reflected by their common decay time of 1.5 ns. The indirect exciton emission shows a fast rise time which is covered by the flash-type direct emission during the excitation. The decay of the FE_X is single exponential during the observation time of 1.4 ns which is consistent with the expected behavior for mobile excitons. The bound exciton on the other hand displays a rather slow rise of the luminescence due to the trapping of mobile, indirect excitons at the shallow donor sites. We can exclude an influence of elevated temperature after the picosecond excitation. The excitons have cooled to temperatures slightly above the lattice temperature within 50 ps, as can be deduced from their luminescence line shape. The slow rise of the BE emission thus reflects the trapping efficiency. Note that the lifetime of the BE is of the order of the repetition time of the laser excitation (12.5 ns), leading to a strong residual BE population already present before each excitation pulse.

The dynamics of the direct and indirect excitons can be modelled by the following procedure which incorporates the above-mentioned experimental observations. The model is based on four coupled differential equations for the populations of the free X-point exciton n_X, of the bound excitons n_D, of the excitons with energies high enough to be resonantly coupled to the central valley n_{xX} and the direct excitons n_Γ:

$$\frac{dn_\Gamma}{dt} = G(t) - \frac{n_\Gamma}{\tau_\Gamma} - \frac{n_\Gamma}{\gamma} + \frac{n_{xX}}{\delta} \tag{2.6}$$

$$\frac{dn_X}{dt} = -\frac{n_X}{\tau_X} - \alpha n_X(n_0 - n_\mathrm{D}) + \Delta_X n_{xX} + \beta n_\mathrm{D} - \theta n_x \tag{2.7}$$

$$\frac{dn_\mathrm{D}}{dt} = -\frac{n_\mathrm{D}}{\tau_\mathrm{D}} + \alpha n_X(n_0 - n_\mathrm{D}) + \alpha n_{xX}(n_0 - n_\mathrm{D}) - \beta n_\mathrm{D} \tag{2.8}$$

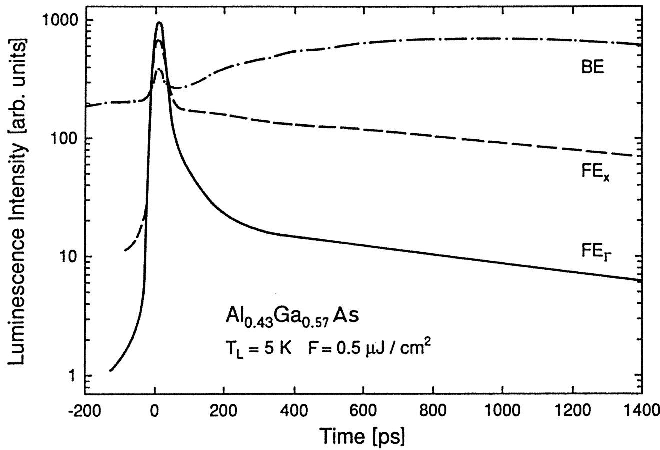

Fig. 2.16. Luminescence decay of free and bound excitons in $Al_{0.43}Ga_{0.57}As$ at low temperature

$$\frac{d\,n_{xX}}{d\,t} = -\frac{n_{xX}}{\tau_X} + \theta n_x - \Delta_X n_{xX} - \frac{n_{xX}}{\delta} - \alpha n_{xX}(n_0 - n_D) + \frac{n_\Gamma}{\gamma} \quad . \tag{2.9}$$

In these equations we use the following parameters: $G(t)$, generation term reflecting the laser pulse width and the total excited density, τ_Γ, τ_X and τ_D are the respective radiative decay times, γ is the Γ–X scattering efficiency, δ is the reversed process, α is the capture rate of the X excitons to the impurity,

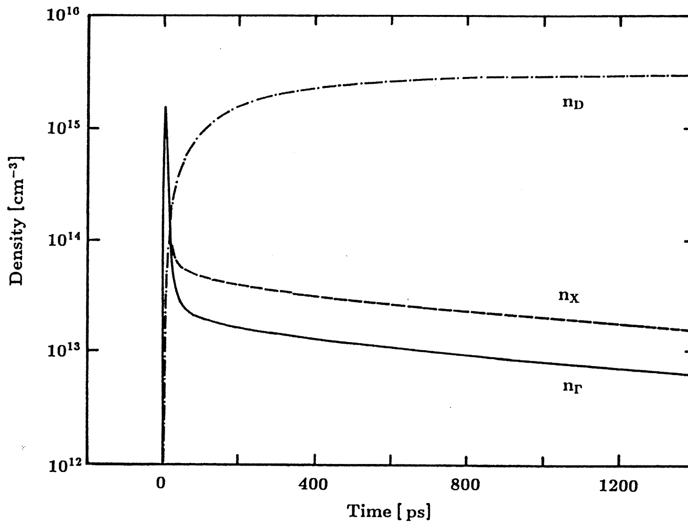

Fig. 2.17. Fit to decay curves of Fig. 2.16 calculated from (2.6–9)

β is the thermalization from bound to free excitons, Δ is the relaxation time within the indirect free exciton dispersion, θ is the reversed thermalization process and finally, n_0 is the density of impurity sites. This model (Fig. 2.17) is able to reproduce the overall decay dynamics of Fig. 2.16.

These studies of the exciton dynamics close to the direct-to-indirect crossover reflect a rather unique configuration of the direct and indirect excitons and continuum states. The interaction of these states is determined not only by the usual capture and thermalization dynamics between the free and bound excitons, but also by the coupling between the Γ and X valleys via the alloy disorder.

2.4 Excitons in Low-Dimensional Structures

Modern semiconductor technology allows the preparation of micro-structured materials where the motion of the carriers is inhibited in one, two or even all three directions [2.39–44]. The confinement of the carriers in so-called *quantum wells*, *quantum wires*, or *quantum dots* leads to a quantization of the eigenenergies in the direction of the restriction and a parabolic dispersion due to free motion in all remaining directions. The energies and dispersion of such subbands in a two-dimensional (2D) system are illustrated in Fig. 2.18 for the case of a GaAs/AlGaAs quantum well. The wells and barriers are formed here by the different energies of the direct gaps in these materials. The overall gap offset is distributed 60%/40%, respectively, between the conduction and valence bands [2.45], so that both electrons and holes are confined. The subband energies are shifted with respect to the bulk band gap by the confinement energies $E_{n_z,q}$ ($q = \mathrm{e, h}$) of the electrons and holes which are given for an infinite-height 2D quantum well of well width L_z by [2.46]:

$$E_{n_z,q} = \frac{\hbar^2 n_z^2 \pi^2}{2m_q L_z^2} \quad . \tag{2.10}$$

The in-plane dispersion of the valence subbands is rather complicated as indicated in Fig. 2.18. The degeneracy of the heavy-hole (hh) and light-hole (lh) valence bands is lifted due to the reduced translational symmetry. These bands are strongly mixed and anticross somewhere in the Brillouin zone [2.47].

The carrier confinement strongly modifies the properties of excitons in these low-dimensional structures with respect to bulk. The Schrödinger equation for the exciton problem can be solved for the exact two-dimensional case [2.48]. The eigenenergies of the exciton Hamltonian:

$$E_{n_\mathrm{B}}^{2D} = E_\mathrm{g} + E_{n_z,\mathrm{e}} + E_{n_z,\mathrm{h}} - \frac{Ry^*}{(n_\mathrm{B} - 1/2)^2} + \frac{\hbar^2 \left(K_x^2 + K_y^2\right)}{2M} \tag{2.11}$$

are shifted here by the confinement energies. The subband indexes n_z are chosen to be equal for electrons and holes reflecting the fact that optical

transitions are only symmetry-allowed for such combinations [2.49]. Note the restriction of the exciton motion to the x-y plane and the modification of the hydrogen problem in two dimensions in (2.11).

Some important consequences of the exciton confinement in one direction are illustrated by comparison to 3D excitons [2.39, 50]. For the binding energy E_{bind} and the radius a_1 of the lowest exciton state one finds from

$$(a_1^{3D})^2 \cdot E_{\text{bind}}^{3D} = \hbar^2/2m_0 = (a_1^{2D})^2 \cdot E_{\text{bind}}^{2D} \tag{2.12}$$

that the relations in bulk (3D) and quantum wells (2D) are

$$E_{\text{bind}}^{3D} = Ry^* \qquad a_1^{3D} = a_B \tag{2.13}$$

$$E_{\text{bind}}^{2D} = 4Ry^* \qquad a_1^{2D} = a_B/2, \tag{2.14}$$

i.e., the excitonic effects are strongly enhanced in lowered dimensions.

Quasi two-dimensional excitons are realized in semiconductor quantum wells and superlattices grown by epitaxial methods [2.39, 41]. Their properties, however, are not those of ideal 2D systems. The finite height of the potential wells (i.e., the offsets between the conduction and valence bands of the barrier and well materials, respectively) leads to a penetration of the electron and hole wave functions into the barriers. The limit for $L_z \to 0$ are not ideal 2D excitons but rather 3D excitons with properties determined by the barrier material [2.51]. Nonetheless, excitonic effects are much stronger in quantum wells than in 3D, which is reflected in the observation of excitonic effects up to room temperature [2.52, 53].

Typical absorption spectra of GaAs/AlGaAs quantum well systems are shown in Fig. 2.19. The absorption follows the step-like density of states in a two-dimensional system with distinct hh and lh exciton resonances at each

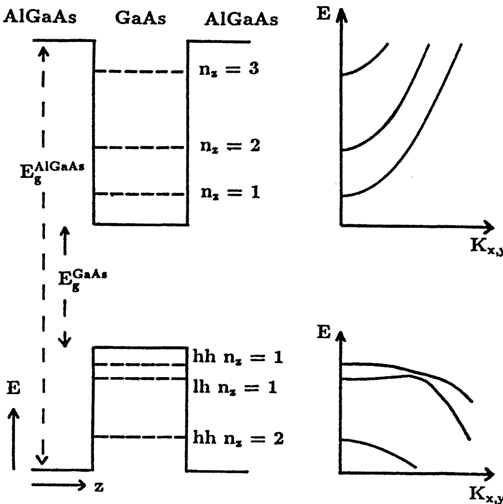

Fig. 2.18. Gap energies, confined electron and hole energy levels, and subband dispersion in the x-y plane for a GaAs/AlGaAs quantum well

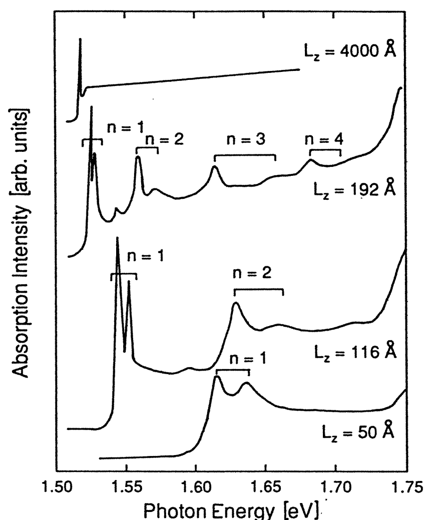

Fig. 2.19. Optical absorption in GaAs/$Al_{0.25}Ga_{0.75}As$ quantum wells with various well thicknesses demonstrating the strong excitonic resonances, the confinement dependence of the subband energies, the lh–hh splitting, and the step-like density of states. The absorption in a thick GaAs layer (uppermost trace) shows in comparison no confinement effects [2.41]

step. The increasing broadening of the absorption lines with index number can be partly attributed to the fast dissociation of the excitons, which are isoenergetic with continuum states of the lower-energy resonances. This degeneracy is further illustrated in the photoluminescence excitation (PLE) spectrum (Fig. 2.20) taken in a GaAs/AlAs QW [2.54]. The lh exciton absorption is found here superimposed on the continuum of the hh exciton, which sets in at an energy of 1.592 eV. Also clearly observable is the onset of the lh exciton continuum around 1.612 eV. The smaller, but distinct, peaks just below the continua are identified as 2*s* exciton states.

The properties of excitons or electron–hole pairs in 1D and 0D semiconductor structures, i.e., in quantum wires and dots, are relatively little known as yet. Such structures are technically realized by a variety of methods: spatially selective ion implantation [2.55], various etching techniques applied to quantum-well structures [2.42–44, 56], field-induced quantum confinement us-

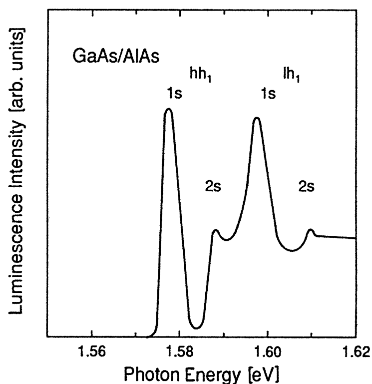

Fig. 2.20. PLE spectrum of a 85 Å GaAs/AlAs QW showing 1 s, 2 s, and continuum transitions for both $n_z = 1$ hh and lh excitons [2.54]

ing micro-structured surface contacts [2.43, 47], strain-induced lateral confinement [2.58], direct growth on tilted or high-surface-energy substrates [2.59, 60] or, in the case of quantum dots, also by incorporation of semiconductor microcrystallites into dielectric matrices [2.61–65]. All of these methods are, however, technologically rather difficult and well-defined low-dimensional structures are not easy to achieve. Still, confinement of electrons and holes into 1D and 0D and the occurrence of multiple subbands has been demonstrated for these systems [2.55–69].

Besides the growth-related difficulties, problems are encountered in the theoretical description of the exciton-related properties. The Coulomb interaction between electron and hole diverges, and thus the exciton binding energy also diverges in the exact 1D and 0D limits [2.70]. The divergence is, however, suppressed due to the finite barrier height and well width in realistic systems. The 1D exciton binding energy is expected to be significantly enhanced with respect to the 2D case, but approaches the value of the barrier material in the limit of vanishing wire radius. For quantum dots the confinement energies of the carriers are the dominant contribution to the energy shifts of optical transitions with respect to bulk material. The influence of excitonic binding is relatively small [2.71] but affects the optical absorption via the selection rules [2.67]. The role of 0D excitons in recombination is still debated but seems to be unimportant in comparison to strong surface-related effects [2.62–64, 71–73].

2.5 Direct-to-Indirect Transitions in 2D and 1D Structures

A crossover from a direct to an indirect fundamental subband gap, similar to the crossover in bulk, is achievable in 2D and 1D structures. The most common example is the crossover from *type-I* to *type-II band alignment* [2.74]. The nature of the lowest gap in (Al,Ga)As/AlAs type-II structures is indirect in both real and reciprocal space (inset in Fig. 2.23). The transition to such staggered band alignment (i.e., the top of the highest valence band and the lowest minimum in the conduction band are situated in different layers) is realized, for example, by a reduction of the well and barrier widths in $(\mathrm{GaAs})_n(\mathrm{AlAs})_m$ short period superlattices (SPSL) [2.75–77]. The labels n and m indicate here the average number of monolayers of each material in the SPSL. The strong dependence of the carrier confinement energy on the effective mass (2.10) leads to a larger, thickness-related shift for the Γ subbands in the GaAs wells than for the X subbands in the AlAs barriers. The transition to a type-II alignment occurs for symmetric $(\mathrm{GaAs})_m(\mathrm{AlAs})_m$ SPSL close to $m = 12$ as is demonstrated in Figs. 2.21, 22 [2.78]. Both the absorption edge and the emission in type-I SLs and quantum wells is dominated by the excitons at the lowest subbband. In type-II structures, on the other hand, one finds a strong

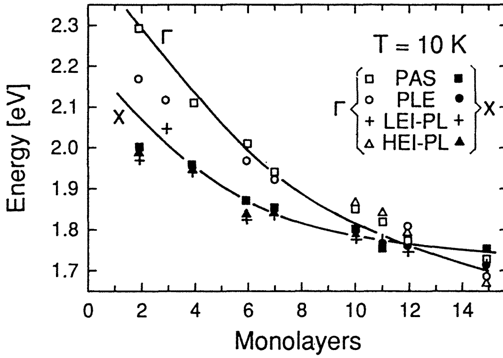

Fig. 2.21. Type-I to type-II crossover in $(GaAs)_m(AlAs)_m$ SPSLs as determined from various experiments [2.78]

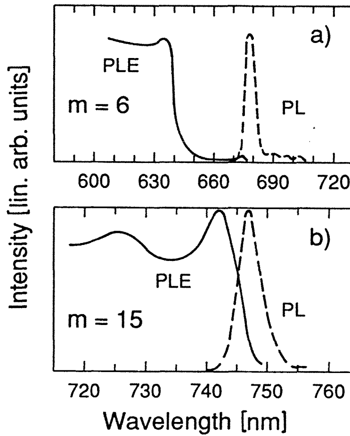

Fig. 2.22. Comparison of excitonic absorption (PLE) and emission (PL) in type-II (a) and type-I (b) SPSLs according to [2.78]

absorption edge at the direct gap in the GaAs well, while the emission is related to the excitons at the indirect $\Gamma_{(\mathrm{GaAs})} - X_{(\mathrm{AlAs})}$ gap.

Absorption and emission in the type-II scenario are further detailed in Fig. 2.23. The low-excitation photoluminescence displays a series of lines related to the indirect exciton. Their origin is attributed to a zero-phonon recombination, an impurity-bound exciton and two LO-phonon sidebands [2.77] very similar to the case of indirect-gap bulk $Al_xGa_{1-x}As$ (compare to Fig. 2.5). A different interpretation of luminescence lines in terms of recombination related to AlAs TA, LA and LO phonon emission as well as the zero-phonon line is given in [2.79, 80] In any case, all emission lines stem from recombination processes involving a coupling of the AlAs X minima to the Γ minima in the GaAs well. The additional superperiodicity introduced by the layer sequence actually leads to a splitting of the energy band related to the X_z (i.e., the X point states with k vectors in the growth direction) and to the $X_{x,y}$ minima. The corresponding wave functions couple via different processes to the central valley in the (Al,Ga)As layers as we will detail in Chap. 4. The same coupling is evident from the properties of type-I emission in these type-II SPSL. Similar to the direct emission in indirect-gap $Al_xGa_{1-x}As$, this luminescence is

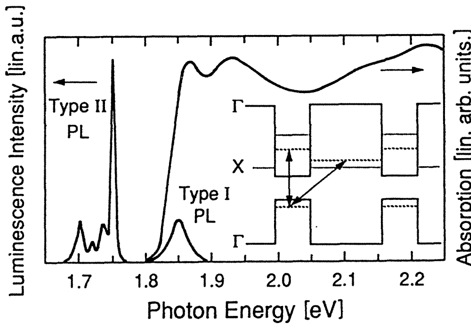

Fig. 2.23. Absorption and emission spectra of a type-II GaAs/AlAs SPSL. The inset shows the subband alignment and optical transitions for this scenario [2.82]

strongly lifetime broadened and only present during the picosecond generation process [2.81].

The spatial separation of the electrons and holes in type-II structures reduces their wave function overlap and thus their exciton binding energy. Recent variational calculations show that the exciton binding energy is of the order of 8–10 meV for a 30Å/30Å GaAs/AlAs SPSL and decreases monotonically with increasing layer thickness [2.80, 83, 84].

Type-II band alignment was also found recently in a SL of GaAs/AlAs quantum wires [2.60]. These quantum wires were directly grown on a high-index (311)A GaAs surface. The high-surface energy leads to a facet-type corrugation of the surface and a subsequent growth of well ordered thicker and thinner GaAs and AlAs channels (Fig. 2.24). The whole structure forms an array of quantum-well wires (QWW) aligned along the $[\bar{2}33]$ direction. These QWW SLs show some coupling of the wires in the (311) planes but also some significant 1D anisotropies of the optical and electrical properties. The excitons in these structures couple strongly to the optical phonons as a result of the confinement in the wires. An important feature for applications is the high luminescence efficiency up to room temperature of the QWW SLs. Similar to the case of the SPSLs, the band alignment was found to be of type I for average layer thicknesses above 35 Å and of type II below. An example of type-II emission displaying a zero-phonon line and two phonon side bands as well as a PLE spectrum reflecting the type-I absorption in such a QWW is given in Fig. 2.25. The first realization of a quantum-confined electron–hole liquid phase obtained in this material system will be discussed below (Sect. 3.5.2).

We finally want to refer to some further possibilities for achieving a direct to indirect transition in low dimensions. A type-II to type-I crossover was found for a type-II SPLS as a function of applied electric field [2.86]. The quantum-confined Stark effect induces a red shift of the direct exciton while the spatially indirect exciton is blue shifted due to the drop of field strength between adjacent layers. The crossing to staggered alignment is also achievable by the application of hydrostatic pressure to SPSL [2.87], quantum wells

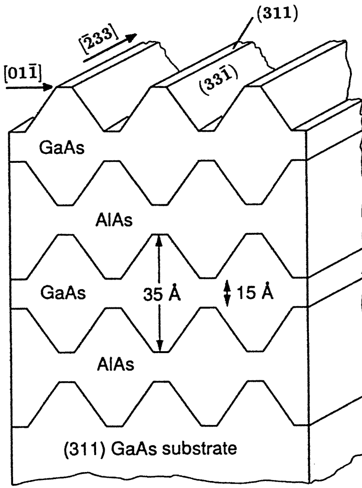

Fig. 2.24. Schematic picture of wire arrangement in QWW SL directly grown on a (311) GaAs substrate surface

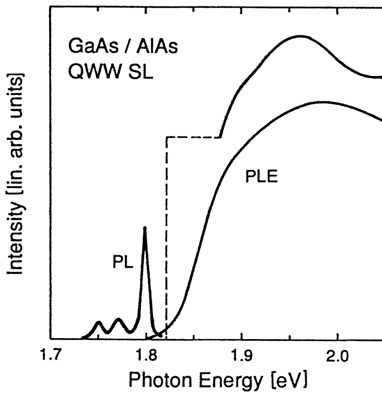

Fig. 2.25. Luminescence excitation (PLE) and emission (PL) spectra of a type-II GaAs/AlAs QWW SL [2.60]

[2.88] or (311) QWW SLs [2.89] exploiting the differential pressure coefficients of the direct and indirect gaps in adjacent layers.

The direct-to-indirect transition in low-dimensional systems does not necessarily result in structures that are indirect in both real as well as in k space. Spatially indirect excitons are, for example, found in coupled quantum wells. Here, the electron and the hole sit in different wells separated by a barrier layer. These excitons, however, are direct in k-space because both carrier types are related to the Γ point [2.90, 91]. The reverse case is found in GaSb/AlSb quantum wells, where the direct and indirect gaps of the same well cross as a function of well width [2.92]. These excitons are spatially direct but indirect in reciprocal space. Similar to the case of bulk $Al_xGa_{1-x}As$ is the pressure-induced Γ–X crossing in the wells of GaAs/AlGaAs quantum wells [2.93].

Such Γ–X or Γ–L crossover experiments are extremely useful for the determination of the intervalley-coupling strengths related to various mechanisms. Conclusions about the intervalley coupling can be drawn from the

dependence of optical properties on the energy separation between the conduction band minima at different points of the Brillouin zone. The methods described above are used to systematically tune this energy separation. We will review the results of these studies in Chap. 4.

3. Many-Body Effects in Multi-Valley Scenarios

The generation of a dense electron–hole system in semiconductors, e.g., by optical pumping, brings about significant modifications in the excitonic spectrum and the electronic band structure. The reasons are screening – i.e., the collective response of the electron–hole system to interactions resulting from Coulomb and exchange effects – and the removal of oscillator strength by occupation of states in phase space. These many-particle effects are accompanied by large optical nonlinearities close to the energies of the band gaps with most interesting prospects for applications in communication technology. After a general review of screening effects in semiconductors, we illustrate the influence of multi-valley band structures on the properties of electron–hole plasmas and degenerate carrier gases. The narrowing of various band or subband gaps in bulk material, or quantum wells and quantum wires, respectively are dicussed in the framework of multi-valley models. A laser-induced crossover from a direct- to an indirect-gap semiconductor is found as a result of a differential renormalization of various conduction-band minima. The role of screening is analyzed not only in electron–hole plasmas of different dimensions but also in one-component plasmas, where the Fermi-edge singularity is its most important consequence. A further result of screening is the condensation of the electron–hole plasma into a liquid phase. The disorder-related dynamics of droplet formation in $Al_xGa_{1-x}As$ as well as the observation of quantum-confined droplets are presented. The chapter closes with a discussion of optical nonlinearities at the direct gap of indirect semiconductors as direct applications of screening in multi-valley semiconductors.

3.1 Introduction to Screening in Highly Excited Semiconductors

The consequences of *screening* between carriers in semiconductors are manifold. For one, the formation of bound and continuum excitonic states and the related high oscillator strength are themselves results of the response of the electron–hole pair to the Coulomb interaction. This two-particle effect has its

many-particle equivalent in the so-called *Mahan exciton* or *Fermi-edge singularity* (FES) [3.1–3]. The reaction of a Fermi sea of electrons (or holes) to the presence of a single carrier of opposite charge is a colletive movement of this sea to accommodate the single hole (electron) at a minimum-energy site. This screening of the Coulomb attraction is performed by the carriers close to the quasi-Fermi energy, which are the only ones able to scatter. A direct consequence is the strong enhancement of oscillator strength (also called Coulomb or *excitonic enhancement* [3.4, 5]) for optical transitions close to the chemical potential.

Screening also leads to a renormalization of the single-particle energies [3.4–9]. In particular, each carrier in the electron–hole system repels all others with the same charge via the Coulomb force. This results in a local decrease of the average charge density at the position of any carrier, which can be described by an induced virtual charge of opposite sign. The repulsion is counterbalanced by the build-up of this virtual charge such that each carrier sustains a free space around itself, the so-called correlation hole. A similar effect is induced by the Pauli exclusion principle which prohibits fermions in the same spin state from occupying the same position. The separation of the carriers is thus larger than classically expected, leading to a reduction of the Coulomb repulsion. These rearrangements in the dense electron–hole system induced by *correlation* and *exchange effects* lower the energies of the carriers significantly. The result is a narrowing of the band gaps in the highly excited semiconductor with respect to the unexcited case [3.4–20]. Due to this *band-gap renormalization*, the low-energy onset of intrinsic luminescence or gain is shifted to the red, with important consequences for the performance of electro-optic devices such as semiconductor lasers [3.13].

Increasing the carrier density starting from the low-excitation case results in a *Mott transition*, which is here the transition from an excitonic insulator to a metallic *electron–hole plasma* (EHP) [3.6, 18]. This transition is brought about by the reduction of the excitonic binding energy and the simultaneous renormalization of the excitonic continuum (or the band-gap energy). Both effects in 3D semiconductors are of exactly the same magnitude so that the energy position of the excitonic resonance remains unshifted with increasing density and only loses oscillator strength [3.4, 5, 19]. The Mott transition occurs for $n_{\mathrm{M}} \approx 10^{15}$–$10^{16}\,\mathrm{cm}^{-3}$ in GaAs when the energy of the continuum states crosses below the excitonic ground state. This transition is demonstrated for example in the experiments of *Fehrenbach* et al. (Fig. 3.1), where the absorption in the region of the excitonic resonances is monitored as a function of additionally generated free electron–hole pairs or resonantly excited excitons, respectively. It is important to note that the transition to an electron–hole plasma occurs at higher pair densities in an excitonic gas than for the excitation of free carriers, reflecting the superior efficiency of screening by the latter species [3.19, 20]. The different screening behavior of the plasma and the exciton gas can be understood from the Bose-like charac-

ter of the excitons. The exciton is composed of two fermions with opposite charges and spin orientations (at least for the singlet exciton which is optically active in III-V semiconductors). Thus, the interactions between excitons stem only from the microscopic deviations from charge neutrality due to the different spatial extent of the electron and hole wave functions. Even a *Bose condensation* of the excitons was proposed by theory [3.5], but never realized unambiguously in III-V or elemental semiconductors. Only recently has some evidence been presented for such a phase transition in Cu_2O [3.21]. The Bose condensation is typically prohibited by the short exciton lifetime in direct-gap semiconductors or covered by a phase transition of the exciton gas to an *electron–hole liquid* (EHL) [3.6, 18, 22]. This phase transition is a direct result of the correlation and exchange effects. Section 3.5 is devoted to a detailed discussion of the condensation into a 'fog' of electron–hole droplets (EHDs) in GaAs-related systems.

Screening in low-dimensional systems turns out to be significantly different to that in bulk [3.23, 24]. The effect of screening between electron–hole pairs is rather inefficient due to their restricted mobility. The screening further saturates, for example in 2D systems, with rising pair density as a result of the constant density of states. The number of carriers contributing to the screening (i.e., the number of carriers close to the quasi-Fermi level) does not increase with pair density, in contrast to the bulk case where the DOS increases monotonically with energy. Moreover, even a weak 2D potential always has one bound state and the excitonic binding is greatly enhanced as a result of the spatial confinement of the electron–hole pair and hence the enhanced overlap of the wave functions.

The modified properties of the two-dimensional systems have some important consequences for their nonlinear optical response. The removal of the excitonic resonance as a function of pair density is here rather a consequence of *phase-space filling* and and the weakening of the Coulomb attraction by exchange effects than a result of Coulomb screening. The phase-space filling is in this context a population-induced Pauli blocking of the conduction-

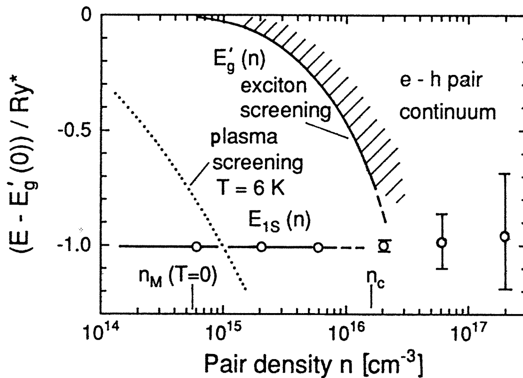

Fig. 3.1. Dependence of the band gap $E'_g(n)$ and the energy of the $n_B = 1$ exciton resonance on the density of free electron–hole pairs (plasma) or excitons, respectively [3.19]

and valence-band states contributing to the overall excitonic wave functions which leads to a reduction of the oscillator strength of the related excitonic transitions [3.23–25]. The relative strength of screening in comparison to the effects of the Pauli exclusion principle are illustrated by a fs time-resolved transmission experiment by *Knox* et al. (Fig. 3.2) [3.26]. A non-equilibrium electron–hole distribution is injected by a 100-fs laser pulse at some excess energy above the $n_z = 1$ exciton resonances. This distribution burns a spectral hole in the transmission spectrum which relaxes towards the $n_z = 1$ excitonic states on a timescale of 200 fs. The inefficiency of screening is evident from the differential transmission spectra by the rather small changes at the $n_z = 1$ (around 1.46 eV) and $n_z = 2$ exciton (around 1.58 eV) absorption at short delay times. The absorption at the $n_z = 1$ hh and lh excitons is strongly reduced once these states are occupied by the then thermalized injected carriers and the exchange and filling effects are turned on. The transmission at the higher-energy $n_z = 2$ excitons, however, remains unchanged reflecting the negligible change in screening during the relaxation of the carriers.

Schmitt-Rink et al. [3.23] proposed that the saturation of the excitonic oscillator strength by an excitonic gas is less efficient than by cold free-carrier pairs but much stronger than by hot free-carrier pairs. This was experimentelly verified by *Knox* et al. [3.27] in room temperature differential transmission spectra following resonant excitation of $n_z = 1$ excitons by a fs pulse. The initially strong absorption bleaching by the resonantly excited and thus cold excitons recovers partially in 300 fs when the excitons ionize to form a hot (300 K) electron–hole plasma.

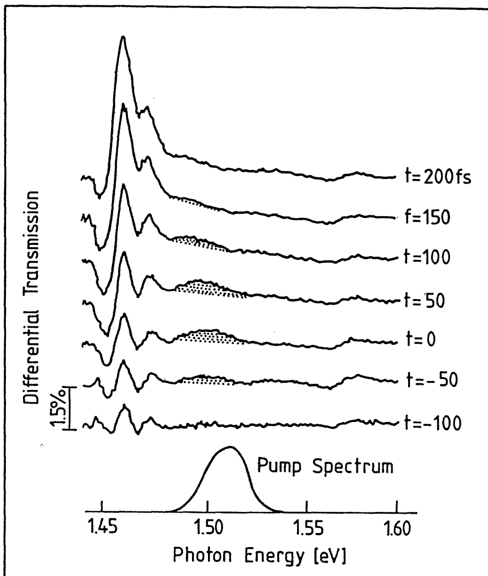

Fig. 3.2. Differential transmission spectra at room temperature of a GaAs/AlGaAs MQW measured with a broad-band 50-fs probe pulse at various times before and after injection of non-equilibrium e-h pairs by a narrow-band 100-fs pulse [3.26]

There are further differences between the screening in bulk and in two-dimensional semiconductors. The interactions in a two-dimensional excitonic gas lead to a slight blue shift of the exciton resonance [3.23, 28, 29]. This blue shift stems from the short-range exchange interaction ('hard-core repulsion') between the excitons which reduces their binding energy. This reduction is not compensated for by a screening-induced red shift of the single-particle states as in the 3D case (compare to Fig. 3.1). The weaker screening in low-dimensional systems also gives rise to larger exciton–exciton and exciton–free carrier scattering rates and thus shorter dephasing times for same average interparticle spacings in comparison to bulk material [3.30]. The actual implication of lowered dimensionality for band-gap renormalization is that the shift is smaller in reduced units, but stronger on an absolute scale due to the larger excitonic Rydberg state [3.5]. We will give more details about this topic below.

Little information is currently available on screening in quantum-wire structures. Calculations on the plasma-induced band-gap renormalization show that the contribution of correlation effects is insignificant due to the small Coulomb-screening ability of one-dimensional carriers [3.31]. Renormalizations of about 25 meV for $n\, a_{\mathrm{B}}^{3\mathrm{D}} = 1$ and of 10–20 meV for typical densities have been calculated for the cases of optically generated electron–hole plasmas and a one-component electron Fermi liquid, respectively [3.31, 150]. Preliminary experimental results of time-resolved studies of the band-filling luminescence in GaAs/AlGaAs quantum-well wires demonstrate renormalizations in this energy range (Sect. 3.3) [3.33, 35].

The question of how screening influences the *thermalization* of carrier distributions injected by ultra-short laser pulses has recently become a topic of intense research. The development of time-resolved optical measurement techniques, such as time-resolved differential transmission [3.27, 36, 37] and luminescence up-conversion [3.38, 39] or the analysis of band–acceptor luminescence [3.40, 42], provide the possibility to study athermal carrier distributions. These types of experiments give insight into basic interaction mechanisms in fermion gases. The thermalization process is found to be determined by carrier–phonon as well as carrier–carrier scattering [3.43, 46]. The efficiency of the latter mechanism is strongly influenced by the strength of the Coulomb interaction between the carriers, i.e., by screening. The reduction of the Coulomb interaction by screening in high-density systems reduces the scattering cross section with an important impact on the temporal evolution of the carrier distribution towards thermalization [3.47].

Especially interesting is the transition of nearly unscreened interactions in low-density distributions to efficient screening in the high-density case. Both extremal situations have been realized in recent experiments. For the case of high electron–hole pair densities in bulk GaAs or $\mathrm{Al}_x\mathrm{Ga}_{1-x}\mathrm{As}$, one finds a thermalisation of the individual carrier distributions within less than 200 fs [3.26, 39, 48, 49] The screening is quite efficient at densities typical for these

type of experiments. The screening length is on the order of the interparticle distances, which reduces the interaction to scattering only between nearest-neighbor carriers [3.50, 51]. The thermalization is nonetheless fast due to the enhanced probability of inelastic scattering events with large energy exchange at high densities [3.46]. Band-gap renormalization was measured from differential transmission in the region of the exciton resonances of CdSe to occur within 80 fs of interband excitation with 60-fs pulses [3.52]. The low-density case was recently examined in time-resolved studies of the band–acceptor luminescence in p-doped GaAs by *Snoke* et al. [3.42]. They report thermalization times of 50 ps independent of carrier density at densities of less than $10^{14}\,\mathrm{cm}^{-3}$. The main scattering mechanism is identified as spatially correlated electron–hole scattering in a weakly screened limit.

The theoretical description of the temporal evolution in such athermal carrier systems is a difficult task. Particularly poorly understood is the evolution of screening in such situations. One approach used in theoretical models is to calculate time-dependent carrier distribution functions from a Boltzmann equation but to incorporate the screening in its usual form developed for thermalized systems [3.42, 47, 48, 52]. A second approach is given by ensemble Monte Carlo simulations describing the plasma by the real-space dynamics of a classical gas of a few thousand particles [3.39, 43–45]. The Coulomb interaction is treated by simultaneous calculations with methods of molecular dynamics [3.43]. These simulations give good agreement with experiments mainly in the low-density limit. For the description of the high-density case, the exchange interaction has to be incorporated [3.53].

We finally want to address the screening related to elementary excitations which are still coherent with the driving laser field. Much attention was recently attracted by the interactions between virtually excited electron–hole states resulting in the so-called *optical Stark effect.* Nonresonant pumping of any electronic system with small detuning of the pump frequency with respect to an optically active resonance leads to a mixing of the ground and excited state of the system by the dipole interaction. The result is a pronounced blue shift of the resonance which lasts exactly as long as the pump pulse is present. Directly linked to this blue shift is a strong optical nonlinearity, the rise and decay of which are extemely fast (effectively instantaneous) when ps or fs laser pulses are used for the exitation. Such effects were extensively studied for the case of virtually excited excitons in MQWs [3.54–56] and were applied in an ultrafast optical gate to achieve subpicosecond switching times [3.57]. The problem with this fast transient nonlinearity is the extremely high pump power required for its observation. A good review of the experimental studies and the rather elaborate theory is given in [3.58].

In the following section we will detail the consequences of screening due to thermalized electron–hole plasmas in semiconductors with the focus on multi-valley scenarios. Particularly, the influence of carriers in highly populated minima of the conduction band on empty or only slightly occupied (sub)bands

at higher energies will be illuminated. We will start with the band-gap renormalization in bulk (Sect. 3.2), followed by the discussion of screening in low-dimensional systems (Sect. 3.3) and in one-component plasmas (Sect. 3.4). Then the potential-fluctuation enhanced formation of electron–hole droplets in both bulk $Al_xGa_{1-x}As$ and type-II GaAs/AlAs quantum-well wire superlattices (Sect. 3.5) will be discussed. We will finally indicate out some possible applications of these many-body effects in the form of fast optical nonlinearities at the direct gaps in indirect or type-II materials (Sect. 3.6).

3.2 Band-Gap Renormalization in Bulk Semiconductors with Multiple Non-Equivalent Valleys

A thorough understanding of band-gap renormalization (BGR) has been obtained in the last two decades for the case of a simple band structure with one minimum in the conduction band and one maximum in the valence band, including the modifications due to degeneracy and anisotropy of the band extrema [3.4–9, 18]. A frequent approach to the treatment of the many-particle system is the *random-phase approximation* (RPA) [3.4, 5]. The corrections to the single-particle self-energy are split here into two contributions: the *Coulomb-hole* and the *screened-exchange* terms. The latter term takes into account the fact that the exchange interaction is reduced because the Coulomb repulsion prohibits the close encounter of any two carriers with the same charge, which is necessary for the Pauli principle to be satisfied. *Vashishta* and *Kalia* (VK) demonstrated, by applying a self-consistent mean-field theory to several model systems, that the sum of the correlation and exchange energy can be approximated by a universal formula, once the selfenergy corrections and the carrier density are expressed in reduced units of the excitonic Rydberg and a normalized interparticle distance, respectively [3.8, 9]. This *universal formula* was experimentally proven to apply to nondrifting electron–hole plasmas or liquids in nonpolar semiconductors such as Si or GaAs [3.14, 59], but has to be corrected for polaron effects in polar compounds like CdS [3.20].

The description of many-particle effects in a dense EHP gets significantly more complicated when not only the fundamental band gap but also gaps or subband transitions at higher energies are considered. Great efforts are being made nowadays to solve the problems of intersubband screening and exchange effects in two-dimensional (2D) systems (e.g. [3.29, 60–62]). We will focus first on the many-particle interactions between non-equivalent minima in bulk semiconductors. The main differences between the bulk and the 2D case lie, for one, in the fact that Coulomb screening is very inefficient in 2D [3.26]. Furthermore, interband exchange in 2D [3.62] has to be considered be-

tween quantized levels of the same conduction-band minimum rather than for minima at different points of the Brillouin zone as in the bulk case (Sect. 3.3).

The treatment of the BGR in a multi-valley situation in bulk material is essentially reduced to the correct evaluation of the electron-exchange effects [3.12, 14–17]. Based on the fact that exchange between carriers in minima at different points of the Brillouin zone is negligible [3.63], we describe a model which accounts for the exchange in each individual minimum of the conduction band. This model applies a simple formalism relying on the high-density limits of the many-body theories of Refs. [3.5, 8, 9, 63]. The population and renormalization of each gap are calculated self-consistently. This formalism does not require any many-particle calculations and is thus easily applicable for practical purposes. The main effect of a multi-valley scenario as incorporated in this model is that different populations in the conduction-band minima lead, owing to the different effective masses, to differential renormalizations of all minima.

The model system for studying band-gap renormalization is again the semiconductor alloy $Al_xGa_{1-x}As$. The results of the investigations bear some important consequences for the exploitation of semicoductor alloys for laser and light-emitting diodes. We will show in the discussion below that the performance of these devices is strongly affected by the BGR. The tunability of the band structure by a systematic change in the AlAs mole content x of $Al_xGa_{1-x}As$ is again used to tune the energy separation of the conduction band minima. Two typical configurations of the band structure close to the crossover for the case of high excitation are depicted in Fig. 3.3. It is easy to simultaneously populate the minima at different points in the Brillouin zone by optical pumping and thus to study the interaction between carriers residing in non-equivalent minima.

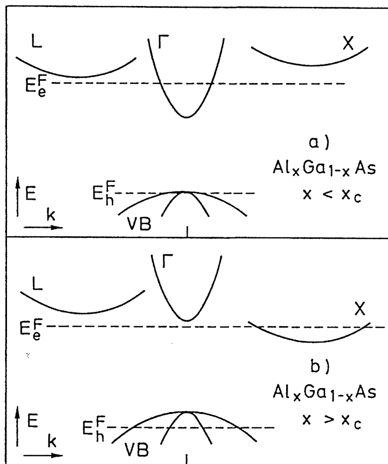

Fig. 3.3. Schematic picture of the band structure of direct-gap (**a**) and indirect-gap (**b**) $Al_xGa_{1-x}As$ close to the crossover. The positions of the quasi-Fermi levels are shown for typical excitation conditions. The higher threshold for the onset of stimulated emission in case (**b**) allows it to reach higher carrier densities (and thus a larger degeneracy of the valence band)

We will first outline how to extract the essential parameters for the study of BGR from a line-shape analysis of time-resolved luminescence (Sect. 3.2.1). In Sect. 3.2.2 we will introduce the theoretical model for BGR in a multi-valley scenario; it is an extension of the two-band model and the universal (VK) formula. The extended model is first tested for the case of indirect-gap $Al_xGa_{1-x}As$, where the higher-energy Γ minimum is nearly empty and thus electron-exchange contributions to the BGR of the direct gap are negligible. The influence of significant population of side valleys on the BGR of the fundamental gap is then demonstrated for direct-gap $Al_xGa_{1-x}As$. The next section (Sect. 3.2.3) deals with the ordering of the conduction-band minima in highly excited $Al_xGa_{1-x}As$ and its practical consequences. We will demonstrate a laser-induced changeover of a direct-gap semiconductor material to an indirect-gap one as a result of differential BGR of the gaps and prove the existence of further minima crossings by the properties of stimulated-emission processes.

3.2.1 Time-Resolved Electron–Hole Plasma Luminescence and Lineshape Analysis

A powerful tool for studying many-body effects in semiconductors is *time-resolved photoluminescence.* The samples are excited by a picosecond laser pulse, typically from a frequency-doubled, amplified, mode-locked Nd:YAG laser, to achieve high carrier densities or a synchronously pumped dye laser for medium excitation levels. With the picosecond pulse one prepares a high density electron–hole system whose temporal evolution is then monitored by both temporal and spectral dispersion of the luminescence signal stemming from the electron–hole pair recombination in the plasma. The detection system is typically a combination of a spectrometer and a streak camera with a 2D read out.

The picosecond temporal resolution of the experiments is essential in order to identify the observed luminescence bands. First, one is able to separate the recombination processes involving different conduction-band minima. This is important in the case of indirect-gap materials when the generation of the EHP occurs mainly via direct absorption. The electrons excited typically with some excess energy in the central Γ valley are transferred into the side-valleys at the X or L points on a subpicosecond timescale as will be extensively discussed in a latter section. But the intravalley relaxation of the electrons within the central valley occurs on an even faster timescale. This fast process which results mainly from electron–electron scattering is reflected in the observation of direct luminescence in the indirect-gap materials. This luminescence is not detected close to the excitation photon energy, but rather at photon energies corresponding to the direct gap in this highly excited materials. A significant number of the electrons are able to recombine with holes in the valence

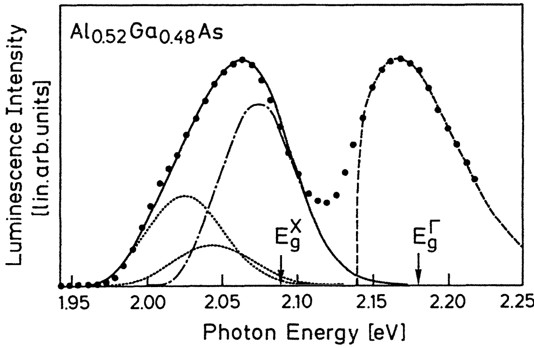

Fig. 3.4. Luminescence signal (dots) of an indirect-gap sample while the picosecond excitation pulse at 2.33 eV ($F = 8\,\mathrm{mJ/cm^2}$) is present. The indirect emission is modelled (solid line) by a superposition of a zero-phonon line (dashed-dotted) and two phonon side bands (dotted). The dashed line is a fit to the direct recombination signal neglecting the broadening at the low-energy tail. The arrows mark the unrenormalized direct and indirect band gaps [3.11]

band before they have had the chance to be transferred to the side valleys. This luminescence band (dashed line in Fig. 3.4) is easily identified from its temporal evolution which just follows the temporal shape of the excitation pulse. The indirect emission (in these experiments involving mainly the X minima, see solid line in Fig. 3.4), however, has typical decay times on the order of 600 ps. The distinction between direct and indirect recombination is thus straightforward [3.64].

The second important conclusion from the temporal development of the luminescence is the assignment of the low-energy bands in Fig. 3.4 (dotted and dashed-dotted lines) to recombination involving the same conduction-band minima. The temporal behavior of the three, partially overlapping bands is found to be identical within the luminescence decay time. The unambiguous identification of these bands was performed in the previous sections: a zero-phonon line resulting from the band mixing via the alloy disorder and two phonon sidebands involving the emission of an GaAs-like or an AlAs-like longitudinal optical (LO) zone-edge phonon [3.65, 66].

Finally, temporally and spectrally resolved luminescence experiments allow one to identify stimulated emission processes from their threshold-like occurrence, their short temporal duration (mostly following the temporal shape of the laser pulse), in combination with their narrow spectral shape and their spectral position at the renormalized gap [3.67, 68]. It is most important that very efficient stimulated recombination of holes with electrons in the side minima at the X and L points occurs in the alloy $Al_xGa_{1-x}As$ with an indirect fundamental gap (Sect. 4.3). We will exploit these stimulated emission processes to discuss the crossing of direct and indirect gaps in Sect. 3.2.3. The

main part of the analysis, especially when a luminescence-line-shape analysis is used, is performed, however, for conditions well below the onset of stimulated emission.

The experimental data for the renormalized band gaps and the carrier densities, which will be compared to the results of the many-particle theories [3.5, 8, 9, 63], are extracted from modelling of the luminescence line shape. The case of indirect-gap $Al_xGa_{1-x}As$ is demonstrated in Fig. 3.4. The modelling of the indirect recombination bands requires the superposition of a zero-phonon line with two phonon sidebands [3.65]. The intensity profile $I(\hbar\omega)$ of the zero-phonon line is given by [3.69]

$$I(\hbar\omega) \propto \hbar\omega \int_0^{\hbar\omega - E_g'} E^{1/2}[\hbar\omega - E - E_g'(n)]^{1/2} f_e(E_e - E_g', n, T) f_h(E_h, n, T)\, dE \ , \tag{3.1}$$

where E_g' denotes the renormalized energy of the fundamental gap, $f_{e,h}(E, n, T)$ are the Fermi functions for electrons and holes, respectively, and the electron and hole energies, E_e and E_h, fulfill $E_e + E_h = \hbar\omega$. The fit parameters are the carrier density n, the renormalized gap E_g' and the carrier temperature T, which can be assumed to be equal for electrons and holes but always deviates from the lattice temperature due to the excess energy acquired during the laser excitation.

The quasi-Fermi energies of 3D electrons and holes $E_{e,h}^F$ are implicitly given by [3.70]

$$n_{e,h} = N_{e,h}^c F_{1/2}(\eta_{e,h}) \ , \tag{3.2}$$

where $\eta_{e,h} = E_{e,h}^F/kT$ are the reduced quasi-Fermi levels, the effective density of states $N_{e,h}^c$ is defined by

$$N_{e,h}^c = 2\left(\frac{2\pi\, m_{e,h}\, kT}{h^2}\right)^{3/2} \tag{3.3}$$

and $F_{1/2}(\eta_{e,h})$ is a Fermi–Dirac integral, k the Boltzmann constant, $h = 2\pi\hbar$, and $m_{e,h}$ the density-of-states effective masses as defined by (1.15, 16). The inversion of (3.2) is done using the approximation of *Aguilera-Navarro* et al. [3.71] which is applicable even for very high carrier densities ($0 \le n/N^c \le 170$)

$$\eta_{e,h} = \ln\left(\frac{n}{N_{e,h}^c}\right) + K_1 \ln\left(K_2 \frac{n}{N_{e,h}^c} + K_3\right) + K_4 \frac{n}{N_{e,h}^c} + K_5 \ , \tag{3.4}$$

with the constants $K_1, \dots K_5$ given in Ref. [3.71]. With the reduced quasi-Fermi levels for a given set of n, T, and E_g', one can now calculate the Fermi functions $f_{e,h}$.

In a multi-valley scenario such as in $Al_xGa_{1-x}As$ close to x_c one has to account for the carrier distribution among several non-equivalent valleys by calculating the total electron density from

$$n_e = n_e^\Gamma + n_e^X + n_e^L \tag{3.5}$$

and assuming a common quasi-Fermi level for all minima, i.e.

$$\eta_e^X = \eta_e^\Gamma - \frac{E_g'^X - E_g'^\Gamma}{kT} \tag{3.6}$$

and

$$\eta_e^L = \eta_e^\Gamma - \frac{E_g'^L - E_g'^\Gamma}{kT} \ . \tag{3.7}$$

The masses for the X and L minima which are used in (3.2, 3) are the combined density-of-states masses for three or four equivalent valleys (Table 5.1). The renormalized gaps $E_g'^\Gamma$, $E_g'^X$, and $E_g'^L$ and the electron densities in the corresponding minima are calculated self-consistently, as outlined in Sect. 3.2.2. We further account for the nonparabolicity of the central minimum by substituting N_{np}^c for N_e^c in (3.2) with [3.70]

$$N_{np}^c = N_e^c \left(1 - \frac{15\,\alpha\, kT}{4\, E_g^\Gamma} \frac{F_{3/2}(\eta_e^\Gamma)}{F_{1/2}(\eta_e^\Gamma)}\right) \ . \tag{3.8}$$

The Fermi–Dirac integrals are approximated according to *Aymerich-Humet* et al. [3.72] and the nonparabolicity coefficient α is given by [3.70]

$$\alpha = -\frac{(1 - m_e/m_0)^2\,(3\,E_g^2 + 4\,E_g\,\Delta_{so} + 2\,\Delta_{so}^2)}{(E_g + \Delta_{so})\,(3\,E_g + 2\,\Delta_{so})} \ . \tag{3.9}$$

The x-dependent spin–orbit splitting Δ_{so} and the direct gaps are taken from Table 5.1.

The quasi-Fermi level for holes is determined from $n_h = n_e$ using the approximation of the valence-band structure close to the Γ point by a single parabolic band with an effective density of states given by (1.15).

The line shape of the phonon sidebands is identical to the zero-phonon line except for being shifted by the energy of the zone-edge GaAs-like or AlAs-like LO phonons and being normalized in height to the experimental spectrum. We do not consider any final-state damping resulting from fast intraband interaction in these line-shape fits. This damping is usually treated in the form of the Landsberg broadening of the actual line shape, which is introduced only phenomenologically [3.73]. Its inclusion in the fit would only slightly change the extracted parameters, especially in the case of relaxed momentum conservation. All material parameters used in these calculations are listed in Table 5.1.

At first sight the fit might appear to be somewhat arbitrary, because all bands are rather broad in the case of a dense EHP. The fit procedure was, however, extensively tested in the case of the electron–hole droplet phase, which is observed in this material system when the temperature of the plasma is below the critical temperature, $T_c = 34\,\text{K}$. In this liquid phase (Sect. 3.5.1) as well as in the excitonic gas (Fig. 2.5) the individual contributions to the overall line shape are clearly separated and the energies of the LO phonons can be

determined accurately [3.65]. The relative intensities of the zero-phonon emission and the side bands in the plasma luminescence (Fig. 3.4) compare well to the ratios found for the excitonic luminescence for the same composition (Fig. 2.5). The investigations are performed here in the EHP phase in order to get detailed information on the BGR in an extended density range. The reason is that the density in the droplet system is insensitive to the excitation conditions and limited to a small density range around $4 \times 10^{18}\,\mathrm{cm}^{-3}$ [3.22]. The theoretical treatment of the BGR is not affected by the actual phase of the dense electron–hole system.

The shape of the direct emission in this indirect-gap case is significantly influenced by the transient state of the electrons in the central valley. The large extension of this band on the high-energy side reflects the high carrier temperature in the electron system of the Γ minimum. Cooling of the carrier distribution by emission of optical phonons is slow in comparison to the intraband thermalization via electron-electron scattering and the interband transfer assisted by optical phonons and alloy disorder. The cooling of the carriers in the side valleys is in comparison much more efficient owing to the fact that a build-up of nonequilibrium phonons is not important in minima with high effective mass and large anisotropy [3.74]. The electrons in the Γ minimum do not have time to thermalize with the carriers which have already scattered into the side valleys. The carrier temperature of the Γ electrons is thus significantly higher than that of the X electrons.

The second consequence of the rapid interband transfer of the electrons is the large difference in the relative carrier densities in the minima at Γ and X point. The electrons are swept out of the central valley, where the majority are generated, into the side valleys where they accumulate. The quasi-Fermi level of the electrons is in any case far below the renormalized Γ minimum. The direct emission thus reflects a rather small carrier density in contrast to the indirect emission.

The extremely fast intraband thermalization of the electrons in the Γ valley enables one to determine the energetic position of the direct gap. This determination, however, is blurred to some extent by the broadening of electron states due to the short lifetime and the previously discussed Landsberg broadening. The broadening is on the order of 3 meV resulting from an intervalley transfer time of about 200 fs (Chap. 4) [3.65, 66]. The final-state damping will mainly produce a tailing of the line shape to the low-energy side of a few meV [3.14]. It is possible now to include the Landsberg broadening into the line-shape analysis. This will give enough fit parameters to reproduce the overall line shape. The analytical form of this broadening, however, is arbitrarily chosen and does not directly compare to the broadening expected from many-body theories [3.75]. The dashed line in Fig. 3.5 indicates the expected lineshape of the direct recombination in a k-conserving model without broadening

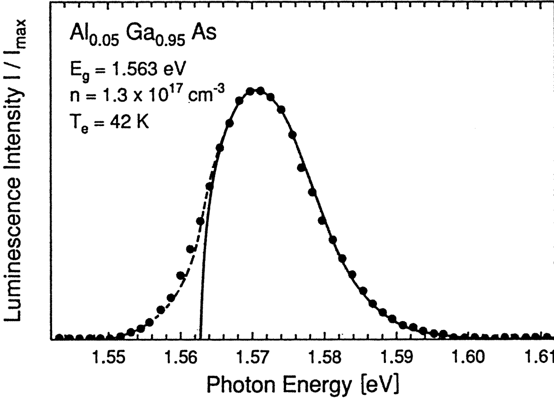

Fig. 3.5. Luminescence signal (dots) of a direct-gap sample taken from Fig. 4 of Ref. [3.14] and line-shape fits with (dashed line) and without (solid line) inclusion of a Landsberg-type broadening [3.11]. The fit parameters for both fits are identical and agree well with the parameters used in Ref. [3.14]

$$I(\hbar\omega) \propto \hbar\omega\,(\hbar\omega - E_{\mathrm{g}}^{\prime\Gamma})^{1/2}\, f_{\mathrm{e}}(E_{\mathrm{e}} - E_{\mathrm{g}}^{\prime\Gamma}, n, T)\, f_{\mathrm{h}}(E_{\mathrm{h}}, n, T) \quad . \tag{3.10}$$

In the case of direct emission in indirect-gap $Al_xGa_{1-x}As$ this line-shape analysis suffices to determine the position of the renormalized direct gap with an uncertainty of at most 10 meV. This uncertainty is in any case much smaller than the effects of reduction in the BGR as will be discussed below. The temperature used for the line-shape fit is in the order of 100–200 K and reflects the transient behavior of the electrons and the nonequilibrium state with the carriers in the side valleys.

The applicability of this simple line-shape analysis can be demonstrated for the case of direct-gap materials, where the carrier distribution and temperature are better defined. A line-shape fit as used by *Capizzi* et al. [3.14], which includes an explicit evaluation of the final-state damping in RPA, is able to reproduce the full line shape. An extensive treatment of the emission shape in RPA is given by *Selloni* et al. [3.76]. This approach eliminates the renormalized gap as a fit parameter and calculates this value self-consistently. This elaborate model gives similar results to Ref. [3.14]. For practical purposes, however, it is only necessary to determine the quantities n, T, and E'_{g}, but not essential to fully reproduce the low-energy tail of the luminescence. This is demonstrated in Fig. 3.5 where we directly compare an analysis with and without a Landsberg-type broadening of a luminescence spectrum taken from Ref. [3.14]. We find that we can extract the necessary fit parameters with negligible deviations from the values obtained in Ref. [3.14] for the same spectrum, when we allow for deviations at the low-energy tail and concentrate on the rest of the spectrum.

3.2.2 The Multi-Valley Model for Band-Gap Renormalization

We will now develop a model to describe the BGR for a semiconductor with various non-equivalent minima in the conduction band. This *multi-valley model* [3.11] answers in particular questions such as how do carriers residing in one minimum interact with the carriers in other minima and do minima which are highly above the quasi-Fermi energy and thus essentially empty still renormalize under high-excitation conditions. In the following we treat the renormalization of the fundamental gap for the condition that the population of higher-energy minima is negligible, and then expand the formalism used here to the multi-valley situation.

The energy of electrons or holes in an electron–hole plasma $E_{\mathrm{e,h}}(\mathbf{k})$ is described by the sum of their respective kinetic energies and the real part of their *single-particle energies* $\Sigma_{\mathrm{e,h}}$ [3.4, 5]

$$E_{\mathrm{e,h}}(\mathbf{k}) = \frac{\hbar^2 k^2}{2m_{\mathrm{e,h}}} + Re\, \Sigma_{\mathrm{e,h}}(\mathbf{k}, E_{\mathrm{e,h}}(\mathbf{k})) \tag{3.11}$$

with $\mathbf{k}$ being the wave vector and $m_{\mathrm{e,h}}$ the effective mass of the electrons or holes. This single-particle energy is given in RPA by the convolution of the single-particle Green's function and the dynamically screened Coulomb interaction typically treated in a single-plasmon-pole approximation. The Green's function incorporates the full characteristics of the band structure. It was shown that the self energy $\Sigma(\mathbf{k}, E(\mathbf{k}))$ is nearly independent of the value and direction of $\mathbf{k}$ and $E(\mathbf{k})$ owing to the local nature of the screened interactions. The consequence is a nearly rigid shift of the band structure in the region of the occupied states within one band extremum and only a small renormalization of the effective masses [3.5]. Note that this rigidity does not apply to the full band structure, i.e., unoccupied states, extrema at different points of the Brillouin zone or different 2D subbands are not shifted rigidly as will be demonstrated below. The rigidity within each band extremum, however, leads to the fact that the band gap and the chemical potential (i.e., the sum of the quasi-Fermi energies $E^{\mathrm{F}}_{\mathrm{e,h}}$) are shifted by the same amount. The BGR ΔE_{g} is thus directly related to the renormalized chemical potential μ

$$\mu = E^{\mathrm{F}}_{\mathrm{e}} + E^{\mathrm{F}}_{\mathrm{h}} + \Sigma_{\mathrm{e}} + \Sigma_{\mathrm{h}} \tag{3.12}$$

and by the contributions of the electron and hole self-energies

$$\Delta E_{\mathrm{g}} = \Sigma_{\mathrm{e}} + \Sigma_{\mathrm{h}} \quad . \tag{3.13}$$

It is more convenient to write the BGR as a function of the excited carrier density n and to combine the self-energy terms which describe the effects of correlation and exchange in the EHP into the *exchange-correlation energy* E_{xc} [3.4–9]. The definition of the chemical potential as a function of density leads to the formula for the BGR of the fundamental gap

$$\Delta E_{\rm g} = E_{\rm xc} + n \frac{\partial E_{\rm xc}}{\partial n} \quad . \tag{3.14}$$

The exchange-correlation energy is typically split into a Coulomb-hole $E_{\rm Ch}$ and a screened-exchange term $E_{\rm sx}$ for further theoretical treatment [3.4, 5]

$$E_{\rm xc} = E_{\rm Ch} + E_{\rm sx} \quad . \tag{3.15}$$

The former term incorporates the correlation effects in the EHP, while the latter describes the results of the Pauli exclusion principle. The screened exchange takes into account that this interaction is reduced by the fact that the Coulomb repulsion prevents the carriers of same charge from approaching each other closely enough for the short-range exchange to be effective.

A quite remarkable finding is that the sum of correlation and exchange energies is nearly independent of band-structure details like the electron–hole mass ratio, the degeneracy, and the anisotropy of band extrema. This was shown by *Vashishta* and *Kalia* who applied a self-consistent mean-field theory to various semiconductor systems [3.8, 9]. The change in one of the contributions to the exchange-correlation energy is always compensated by the other, a tendency which also applies to some extent to the temperature dependence of this energy [3.5]. This property makes it feasible to describe $E_{\rm xc}$ in a *universal formula* applicable to all semiconductors with small polar coupling, once the energy and the carrier density are expressed in reduced units of the excitonic Rydberg state, Ry^* (2.4) and a normalized interparticle distance $r_{\rm s}$, respectively

$$r_{\rm s} = \left(\frac{3}{4\pi n}\right)^{1/3} \frac{1}{a_{\rm B}} \quad . \tag{3.16}$$

This normalized distance is equal to that at which the average volume alotted to each electron–hole pair in the plasma equals the volume of the exciton. Note that the Mott transition from an excitonic gas to an EHP occurs at an $r_{\rm s}$ of 3.4 at 30 K. The universal formula now reads [3.8, 9]

$$E_{\rm xc}(r_{\rm s}) = \frac{a + b r_{\rm s}}{c + d r_{\rm s} + r_{\rm s}^2} Ry^* \tag{3.17}$$

with the material-independent constants $a = -4.8316$, $b = -5.0879$, $c = 0.0152$, and $d = 3.0426$. This simple expression depends on only one parameter, namely the carrier density in reduced units.

The applicability of this formula has been tested for several semiconductor materials, e.g. Si, Ge, and GaAs [3.14, 59]. Only in polar compounds such as II-VI semiconductors does this formula have to be corrected for polaron effects which further reduce the band gap and stabilize the EHP phase [3.20]. We will demonstrate in the following the range of applicability of this approach to the $Al_xGa_{1-x}As$ system and the necessary extensions [3.11]. We will start with the case of indirect-gap $Al_xGa_{1-x}As$, where the population of the minima at

the Γ and L points are negligible. The case of direct-gap $Al_xGa_{1-x}As$ will be discussed later.

The renormalization of the indirect fundamental gap is determined from the luminescence signal of seven different samples. Their x values are between 0.49 and 0.55 to ensure that only the X minima are populated. The carrier densities range between $10^{19}\,cm^{-3}$ and $3 \times 10^{19}\,cm^{-3}$. The BGR is plotted in Fig. 3.6 in reduced units as a function of the normalized interparticle distance. The experimental data are in very good agreement with the universal behavior given in (3.14, 17) (solid line in Fig. 3.6). We want to emphasize again that the theoretical model contains no adjustable parameters. Excellent agreement is also found in samples just above the direct-to-indirect crossover, where the carrier density is between $4 \times 10^{18}\,cm^{-3}$ and $8 \times 10^{18}\,cm^{-3}$, which avoids significant population of the Γ and L minima [3.22]. The VK two-band model thus well describes the BGR of the fundamental gap when higher-energy minima are essentially empty.

The observation of luminescence involving electrons in the central minimum permits one to study the renormalization of the direct gap in indirect $Al_xGa_{1-x}As$. This gap extends between the top of the highly populated valence band and the bottom of the only slightly occupied Γ minimum. Because of the fast transfer of the electrons into the X minima, we can assume the Γ minimum to be essentially empty in comparison to the heavily populated X minima. The gap narrowing of the direct gap is shown in Fig. 3.7 using the direct-gap parameters to determine the reduced units. It is important to note that the narrowing of the direct gap amounts to 25–40 meV, while the fundamental indirect gap is reduced by 60–90 meV as deduced from the same luminescence spectra. The immediate conclusion is that the direct gap in indirect-gap materials renormalizes but by a much smaller amount than the fundamental gap.

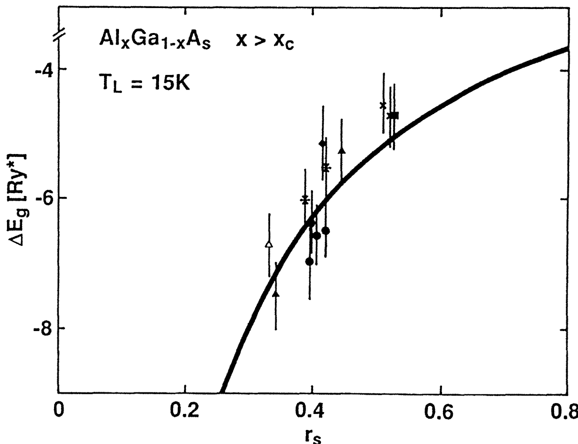

Fig. 3.6. Band-gap renormalization of the fundamental gap in indirect-gap $Al_xGa_{1-x}As$. The different symbols used for the data points stand for results taken in 7 different samples with x-values between 0.49 and 0.55. The solid line represents the universal formula (3.14, 17) [3.11]

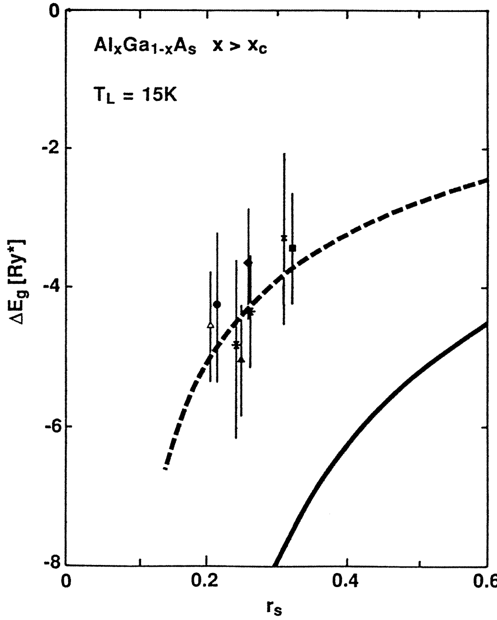

Fig. 3.7. Renormalization of the higher-energy direct gap in indirect-gap $Al_xGa_{1-x}As$ extracted from the same spectra as used for Fig. 3.6. The solid line again stands for the universal formula, while the dashed curve is corrected for the electron-exchange contribution to the BGR according to (3.18–20) [3.11]

The actual amount of renormalization of the direct gap can be calculated from a multi-valley expansion of the simple VK universal formula. The universal formula is again plotted as solid line in Fig. 3.7. This unmodified version of the model overestimates the renormalization by a factor of two, because it assumes all electrons to be in the central valley, which of course is not the case. One expects the few electrons in the Γ minimum to continue to Coulomb interact with the majority of electrons residing in the X minima. The exchange interaction between electrons at different points of the Brillouin zone is expected to be negligible, i.e., the exchange interaction is restricted essentially to electrons within the same valley [3.63]. The contribution of the holes to the narrowing of the direct gap is, however, the same as in the case of the indirect gap. These arguments lead directly to the model for the renormalization of the direct gap. We start from the universal formula (3.14, 17) and simply subtract the exchange interaction between the electrons, which is the only contribution missing, to obtain

$$\Delta E_{\mathrm{g}}^{\Gamma} = E_{\mathrm{xc}} + n\,\frac{\partial E_{\mathrm{xc}}}{\partial n} - \left(E_{\mathrm{x}}^{\mathrm{e}} + n\,\frac{\partial E_{\mathrm{x}}^{\mathrm{e}}}{\partial n}\right) \quad . \tag{3.18}$$

In the calculation of the electron exchange energy $E_{\mathrm{x}}^{\mathrm{e}}$ we use the unscreened interaction, which is given by

$$E_{\mathrm{x}}^{\mathrm{e}} = \frac{-0.916\,\phi(\rho_{\mathrm{e}})}{r_{\mathrm{s}}\,\nu_{\mathrm{e}}^{1/3}} \quad , \tag{3.19}$$

where ν_{e} is the valley degeneracy factor, and ϕ describes the valley anisotropy

as a function of the ratio ρ_e of the transverse and longitudinal effective masses [3.63]

$$\phi(\rho_e) = \rho_e^{1/6} \frac{\sin^{-1}[(1-\rho_e)^{1/2}]}{(1-\rho_e)^{1/2}} \qquad \rho_e < 1 \quad . \tag{3.20}$$

In the case of the Γ minimum both ρ_e and ν_e are unity, which greatly simplifies (3.20).

The justification of this ansatz is deduced from the experimental observation that the BGR is reduced by roughly 50% due purely to the missing electron exchange. This finding demonstrates that the electron correlation effects make only a minor contribution to the renormalization for these very high carrier densities. It is actually expected from theory that the BGR should be essentially determined by the exchange effects in the limit of high densities [3.5]. This behavior has an intuitive explanation: The carriers have no space to be repelled from each other at high carrier densities and r_s has values much smaller than one. The reduction of the exchange interaction by the Coulomb repulsion is thus increasingly compensated. The result of the calculation using the ansatz of (3.18–20) is shown as a dashed line in Fig. 3.7. Again, there is excellent agreement between the experimental data and the model.

We can conclude at this point that this simple approach to the many-particle effects is able to explain the renormalization of both the highly populated lowest, as well as the sparsely populated higher minima in the limit of high total carrier densities [3.11, 12]. The fundamental gap renormalizes according to the two-band VK model. The higher-energy gaps still narrow considerably, because of the strong renormalization of the highly populated valence band. The contribution of the nearly empty conduction-band minimum to the gap reduction is minimal, because the correlation effects are weak and the electron-exchange contribution is negligible. This situation has to be contrasted to the low-density limit: In the case of the ionization of the direct exciton in Ge, the Coulomb screening by electrons in the L minima was found to contribute significantly to the BGR of the direct gap [3.77].

The treatment of the renormalization gets more complex when the higher-energy minima of the conduction band are also significantly populated due to a small energetic separation between the minima or due to high carrier temperature. Here we have to extend the model to include the exchange effects within each conduction-band minimum, for a self-consistent determination of the population and renormalization of each valley [3.11]. The model will be applied to direct-gap $Al_xGa_{1-x}As$ in various valley configurations.

The self-consistent multi-valley model is based on the above demonstrated effect that the electron-exchange contribution to the BGR only results from interaction within the same valley. When the electrons are distributed among several non-equivalent minima, then only the density in each minimum is accounted for in the calculation of E_x^e. We again start the calculation by determining the BGR for the case when all electrons are in the same minimum. This automatically takes care of the contribution of the hole interactions

to the BGR of each gap. We then subtract the full electron-exchange contribution from the BGR according to (3.18–20) and just add the value of $(E_{\mathrm{x}}^{\mathrm{e}} + n_{\mathrm{v}} \frac{\partial E_{\mathrm{x}}^{\mathrm{e}}}{\partial n_{\mathrm{v}}})$ resulting from the actual population n_{v} in each minimum. Here the anisotropy and degeneracy of the X and L minima have to be accounted for. We again assume that the influence of the modifications in the correlation energy are small when the electrons are distributed among various valleys and not situated in one minimum, because the correlation energy is a small contribution at high overall densities anyway.

The population of each conduction-band minimum is given by the Fermi function, the density of states in each valley and the relative energy position of the minima. This relative position, however, is a direct function of the density-induced renormalization of each minimum. The calculation of the renormalization and population of each minimum thus requires a self-consistent treatment. One starts the calculations with fixed carrier densities and temperatures, and literature values for the unrenormalized gaps. The electrons are distributed among the valleys according to the Fermi function. Then one determines the renormalization of each minimum induced by its population. The rearrangement of the relative energy separations between the minima now requires a redistribution of the electrons among the valleys according to the Fermi function and a subsequent redetermination of each renormalization. This procedure is continued until convergence is reached.

We will now describe how to apply this model to the case of direct-gap $Al_xGa_{1-x}As$ [3.16]. Here the self-consistent treatment of population and renormalization has to be included in the analysis of luminescence line shapes. This requirement can be demonstrated by the discussion of some earlier measurements of BGR in this material system. Close to the crossover composition an enhancement of the renormalization of the fundamental gap was reported [3.12, 14]. The carrier density or equivalently the normalized interparticle distance needed for the comparison of the gap shrinkage to the VK universal formula is taken from a line-shape analysis of the direct EHP luminescence. Such a line-shape analysis, however, is not valid when the populations of the higher-energy conduction-band minima at the X and L points are neglected. These populations are not directly accessible in the luminescence experiment, because a radiative recombination of these electrons with holes in the valence band has to proceed via an intermediate state in the Γ valley. The timescale for relaxation within the central valley by intraband scattering is, however, much shorter than the recombination time, which supresses a detectable contribution of indirect recombination to the overall luminescence. This has some important consequences: First, the overall carrier density is larger than the density determined from the line-shape fits, because the direct emission signal is only determined by the difference between the bottom of the Γ minimum and the quasi-Fermi level of the electrons. The carrier distribution in the valence band is only slightly degenerate, if at all, and the difference between

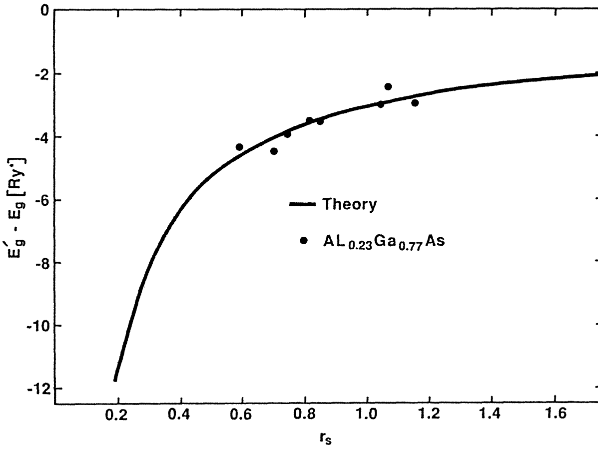

Fig. 3.8. Band-gap renormalization in a direct-gap $Al_xGa_{1-x}As$ sample at $T_L = 15\,K$ for a composition, where the population of side valleys is negligible [3.16]

the top of the valence band and the quasi-Fermi level of the holes does not contribute significantly to the width of the direct luminescence (cf. Fig. 3.3a). The density determined from the fit thus only represents the density in the central valley. The self-consistent calculations show that the overall density, and thus also the hole density, can be higher by a factor of two than the density in the Γ minimum. We will show in the following that this is the reason for the supposed enhancement of the renormalization in $Al_xGa_{1-x}As$ close to the crossover composition.

A line-shape analysis of the direct emission has to include the population of the side valleys and the correct hole density. One incorporates the self-consistent model into the lineshape fits in the following way: The starting parameters density and carrier temperature are determined from a fit to the spectrum. Then one calculates the correct positions and populations of all minima and the valence band with the self-consistent routine. The fit is then repeated using now the calculated band-gap energies rather than the literature values. The newly determined n and T are the input of the next self-consistent calculation. This procedure is repeated until convergence is achieved.

The first test of the multi-valley model is the case of low population in the higher-energy minima. In this scenario the universal formula has to be recovered. We show two examples here: $Al_{0.23}Ga_{0.77}As$, which is far from the crossover composition, and GaAs close to the crossover point as a result of high hydrostatic pressure (Figs. 3.8, 9). In the case of $Al_{0.23}Ga_{0.77}As$, the side valleys at the X and L points are so high in energy that their population at low temperature is negligible in the density range under consideration. In the case of GaAs under high hydrostatic pressure, only the X minima have to be considered. But their population is also negligible at 5 K for pressures well below the crossover pressure ($P_c = 42\,kbar$). The multi-valley model reproduces in both situations the universal formula, whose validity is proven by the excellent agreement with the experimentally determined renormalizations.

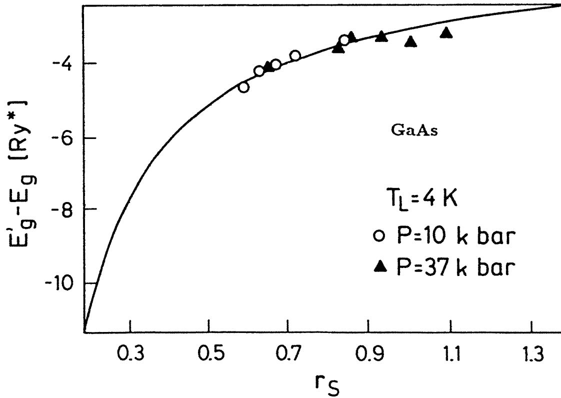

Fig. 3.9. Gap narrowing in GaAs under hydrostatic pressure. Experimental conditions are such that the population of the X valley is insignificant [3.16]

We now apply the multi-valley model to experimental data in $Al_xGa_{1-x}As$ just below the crossover composition as reported by *Capizzi* et al. [3.14]. The renormalization strongly deviates from the simple VK model as is shown in Fig. 3.10. This deviation is observed at high carrier densities for x values exceeding 0.30 and continuously increases towards the crossover composition [3.12, 14]. Note that the original calibration of 0.42 for the sample used in connection with Fig. 3.10 was changed to 0.39 to be consistent with the optical calibration procedure used throughout this text. If one takes the data of Ref. [3.14] and applies the self-consistent model including a line-shape fit to one of the spectra published in [3.14], one finds a population in the side minima comparable to the one in the Γ minimum. Accordingly, the density of holes is about twice as high as the Γ-electron density. We now calculate the renormalization of the fundamental gap taking into account the correct density distribution. The result is depicted in Fig. 3.10, where we use the density in the Γ minimum for the normalization to r_s to enable a direct comparison to *Capizzi's* data. The carrier temperature is chosen to increase slightly with carrier density, as is expected for an EHP. The temperature $T_e = 50\,K$ for the data point at $r_s = 0.83$, which is taken from the fit to the spectrum in Fig. 4 of Ref. [3.14], is equal to the temperature given by *Capizzi* et al. The BGR calculation has to be performed for each temperature separately. The agreement of these calculations with the experimental points is excellent. We want to point out again that the self-consistent model has no adjustable parameters. Only the input values for n and T are chosen so as to fit the luminescence spectra.

This example demonstrates the effect of side-valley populations on the narrowing of the fundamental gap. Using the multi-valley model we were able to solve the question of the enhancement of the BGR in $Al_xGa_{1-x}As$. The same behavior of the direct-gap renormalization is found in $GaAs_xP_{1-x}$ just below the crossover composition. *Fieseler* et al. [3.78] treated the BGR in this multi-valley system in a full RPA theory. The strong BGR of the direct gap could again be explained by the large population in the side valley.

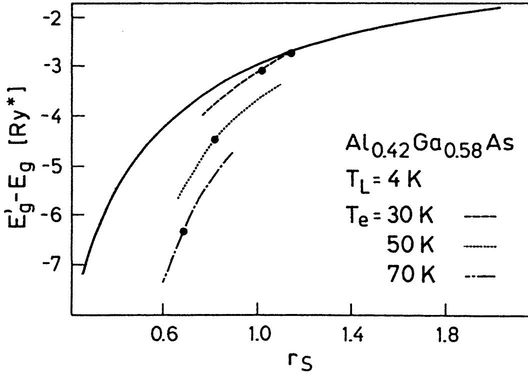

Fig. 3.10. Deviation of the experimental BGR from the universal formula (solid line) in direct-gap $Al_xGa_{1-x}As$ close to x_c. Data points are taken from Ref. [3.14]; the dashed, dotted, and dashed-dotted lines are calculated using the multi-valley BGR model [3.16]

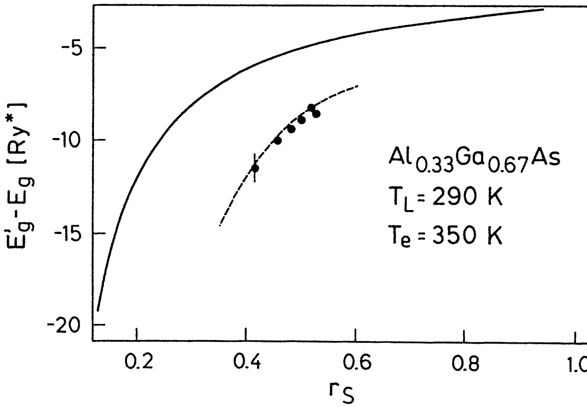

Fig. 3.11. Renormalization of the direct gap in $Al_{0.33}Ga_{0.67}As$ at room temperature. The carrier temperature T_e is taken from fits to the experimental spectra. The dashed line is calculated from the self-consistent multi-valley model [3.16]

Good agreement between experiment and theory was achieved, but with the condition that the relative separation of the Γ and X minima in the unexcited sample was treated as a fit parameter. A recent application of the same model to direct-gap $Al_{0.30}Ga_{0.70}As$ at 2 K [3.79] shows similar trends of the BGR as found in the studies of *Kalt* et al. [3.11]. Another interesting candidate for a test of the multi-valley model would be GaSe, where a simultaneous presence of the direct and indirect EHPs was reported [3.80]. Corresponding calculations, however, have not yet been performed.

The effects of side-valley population get stronger in the case of high carrier temperatures. Here, the high temperature leads to a significant population of the side valleys even for x-values much smaller than x_c. The case of highly excited $Al_{0.33}Ga_{0.77}As$ at room temperature is depicted in Fig. 3.11. The BGR is up to 50% higher than expected for the case when only the population in the central valley is considered (solid line in Fig. 3.11). The multi-valley expansion of the universal formula again gives good agreement with the experimental points using a carrier temperature of 350 K as extracted from line-shape fits.

The applicability of the model to room temperature is not clear a priori, but it appears to be justified in the high-density limit from the following arguments. Modifications of the many-particle interactions at high temperatures result in only minor deviations from the VK formula. The theory applicable to finite temperatures derived in Refs. [3.5, 81] is nearly identical to the VK formula with deviations of less than 2% for a large density range between 5×10^{17} and $2 \times 10^{19}\,\mathrm{cm}^{-3}$ (i.e., r_s between 0.7 and 0.2). The temperature-induced changes of E_c and E_x actually cancel at lower carrier densities resulting in small deviations between $E_{xc}(300\,\mathrm{K})$ and $E_{xc}(0\,\mathrm{K})$. In the high-density limit the energies E_c and E_x individually approach their low temperature behaviors. A comparison to the model of Ref. [3.13], which uses a couple of simplifying approximations, leads to somewhat larger discrepancies. But the deviations from the VK formula are even here only of the order of $1Ry^*$ in the density regime under consideration and, in any case, a factor of 4–5 smaller than the effects due to the side-valley population. The temperature dependence is thus neglected in our model system, which is justified a posteriori by the excellent agreement with the experimental data (Fig. 3.11). Good agreement with calculations using this multi-valley model was also found for the relative gap renormalizations related to the X_6 and X_7 minima in GaAs at 300 K [3.82]. The data were deduced from induced IR absorption spectra after carrier generation by a UV pump pulse.

All these examples show that the BGR in a high-density EHP generated in a semiconductor with multiple non-equivalent valleys is well described by a simple multiple-valley model. This model does not require lengthy many-particle calculations and is easily applicable to various scenarios in highly-excited semiconductors. A recent treatment of the multi-valley situation in the single-plasmon-pole approximation leads to the same results for the renormalization of the fundamental gap [3.83]. The latter calculations are applicable to any temperature. They incorporate the multi-valley scenario by using natural units deduced from a weighted average of the individual valley parameters according to the actual occupation.

In the next section we will give a series of examples of how the differential renormalization of the various gaps influences the optical properties in $Al_xGa_{1-x}As$ close to the crossover composition.

3.2.3 Differential Gap Renormalization in $Al_xGa_{1-x}As$ Close to the Crossover Composition

The first example is the *differential gap renormalization* of the direct and indirect gaps in $Al_{0.42}Ga_{0.58}As$ [3.11]. This material is a direct-gap semiconductor at low optical excitation but has an indirect fundamental gap under high-excitation conditions.

The optical properties at low excitation were already described in Sect. 2.3, where we discussed the simultaneous presence of FE_X and FE_Γ excitons and the interesting minima ordering in this sample. The binding energy of the excitons is different by almost a factor of two, namely 6.8 meV for the FE_Γ and 11.4 meV for the FE_X. Extrapolation from the position of the exciton lines places the direct gap at 2.068 eV and the indirect gap slightly higher at 2.071 eV. The sample is therefore still a direct-gap semiconductor in the picture of the single-particle approximation. Many-particle phenomena (here the indirect excitons), however, dominate the optical properties such as the time-integrated luminescence.

The direct exciton is actually seen as a narrow line only when this excitonic resonance is not degenerate with the indirect-exciton continuum states. Measurements in samples which are clearly indirect due to composition or hydrostatic pressure show the presence of the direct transitions only in a lifetime-broadened short emission during the picosecond excitation pulse. The exciton is very rapidly dissociated due to the fast intervalley scattering of the electron into the X or L minima.

This situation also applies to the case of high-excitation conditions in the $Al_{0.42}Ga_{0.58}As$ sample. Emission from the central valley (now band-to-band recombination) is only seen as short luminescence during the excitation process (Fig. 3.12). The sample becomes an indirect-gap semiconductor during the excitation process. The indirect nature of the fundamental gap after the excitation pulse is evident from the luminescence signal (solid line in Fig. 3.12). The lifetime of this luminescence band is in the order of 1 ns, and thus about a factor of ten larger than the lifetime of the EHP in comparable direct-gap samples. The luminescence can be attributed to the EHP or a liquid phase whose electrons reside in the X minima, depending on the excitation conditions. The properties of these plasma and liquid phases [3.22] are discussed in detail in Sect. 3.5. The renormalized gap in the high-excitation case is determined from the low-energy tail of the luminescence to be about 40 meV below the gap in the unexcited sample in agreement with the prediction from the BGR model.

For further studies of the differential gap renormalization, it is useful to increase the lattice temperature in the $Al_{0.42}Ga_{0.58}As$ sample to 30 K. This procedure has the consequence that the electron–hole system does not condense into a dense liquid phase. One is then able to systematically vary the electron–hole pair density. Further there is some population in the Γ minimum

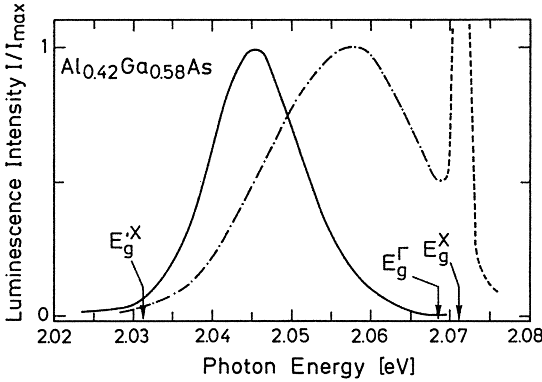

Fig. 3.12. Direct emission (dashed-dotted line) during the excitation process (scattered light from the laser is shown as truncated dashed line) and indirect emission after a delay time of 200 ps (solid line) in $Al_{0.42}Ga_{0.58}As$ at $T_L = 5\,K$. The arrows mark the positions of the renormalized and unrenormalized gaps [3.11]

(about $10^{15}\,cm^{-3}$), which gives a significant contribution to the luminescence signal even at long delay times after the excitation (see high-energy peak or shoulder in spectra of Fig. 3.13). The relatively strong intensity of the direct emission stems from its much higher transition probability compared to the indirect recombination (this difference in transition strength of the order of 100 is also evident from the PLE spectra in Fig. 2.8). The population of the X minima and thus its energy shift is, of course, a function of the excitation level, while the density in the central valley does not change significantly as a result of the differential BGR. A strong decrease in the indirect emission follows, while the intensity of the direct luminescence signal is nearly constant when the excitation level is lowered (Fig. 3.13).

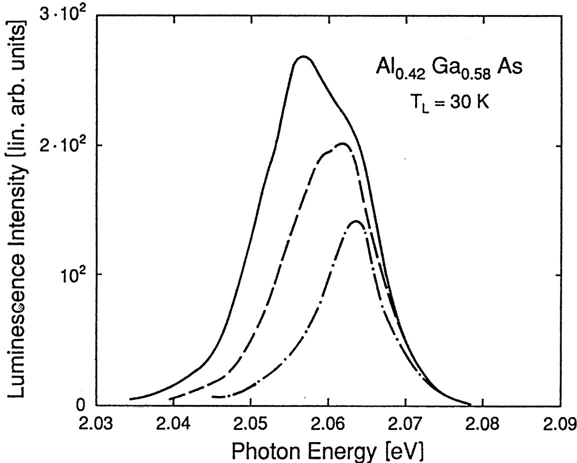

Fig. 3.13. Luminescence at long delay times ($t = 1.3\,ns$) for different excitation levels (solid line: $F = 170\,\mu J/cm^2$; dashed line: $F = 60\,\mu J/cm^2$; dashed-dotted line: $F = 26\,\mu J/cm^2$) [3.11]

Line-shape fits to the emission spectra reveal the carrier densities and the renormalized gaps (Fig. 3.14). The indirect emission is, as usual, treated without momentum conservation, while conservation of momentum is assumed for the direct emission. The energy of the renormalized direct minimum and its population are not adjustable parameters in these fits, but rather calculated self-consistently. The fit parameters are: the energy of the indirect gap, the common carrier temperature and the overall density. The resulting fits to the spectra are not perfect, because again broadening mechanisms are not included, but they are good enough to extract the relative positions of the gaps. The experimentally determined, renormalized gaps are shown in Fig. 3.15 as a function of the overall carrier density. The figure also depicts a self-consistent calculation of the direct and indirect gaps starting from the unrenormalized gap energies as determined from the excitonic luminescence. There is good agreement between the calculation and the experimental points. Both experiment and model demonstrate the transition from a direct-gap semiconductor at low excitation to an indirect-gap material at high carrier densities and the differential renormalization of the gaps. The *excitation-induced direct-to-indirect crossover* occurs at a density of about $10^{16}\,\mathrm{cm}^{-3}$, i.e. close to the Mott density. The nature of the fundamental gap in this semiconductor is thus determined by the excitation level.

A direct consequence of the renormalization-induced direct-to-indirect transition is a shift of the composition of the crossover x_c to slightly lower x values in the case of a highly excited material. This situation is demonstrated in Fig. 3.16, where calculations with the multi-valley model are shown for a fixed carrier density. The actual ordering and position of the individual gaps is determined by the relative distribution of the population among the minima. The crossover composition is 0.408 for the chosen parameters in accordance with the experimental observations. The same effect is also found in samples close to the crossover under hydrostatic pressure. The crossover pressure is

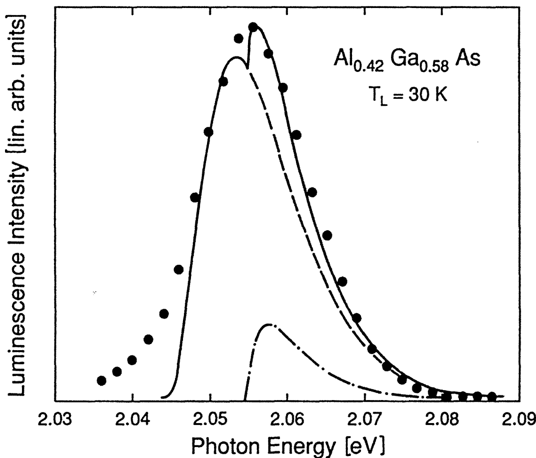

Fig. 3.14. Line-shape fit (solid line) to a luminescence spectrum (dots) in $Al_{0.42}Ga_{0.58}As$ including indirect (dashed line) and direct (dashed-dotted line) emission [3.11]

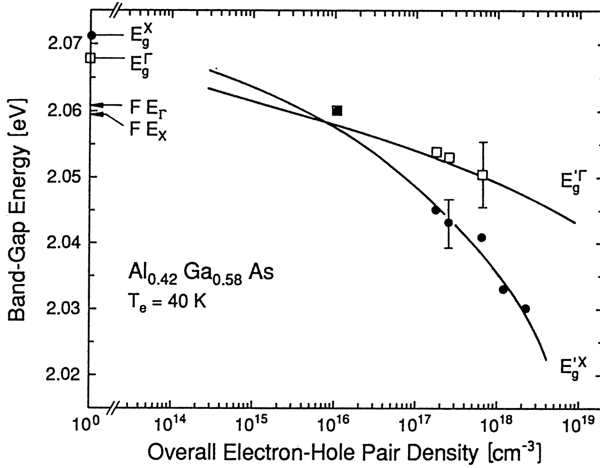

Fig. 3.15. Direct-to-indirect crossover as a function of carrier density. The data points for the direct (squares) and indirect (dots) gaps are extracted from line-shape fits to experimental spectra (Figs. 3.13, 14). The data points at low density are taken from excitonic luminescence spectra. The solid lines are calculated with the multi-valley model for the BGR starting at the position of the unrenormalized gaps [3.11]

reduced in an analogous way in the case of high excitation [3.22]. Differential band-gap renormalization and a reduced crossover pressure at high densities are also found close to the type-I to type-II transition in short-period superlattices [3.84].

A further example of a transition from a direct to an indirect fundamental gap is reflected in the behavior of stimulated emission in $Al_xGa_{1-x}As$ close to the crossover composition. Stimulated emission is possible in this semiconductor alloy for recombination of the electrons in all three valleys of the

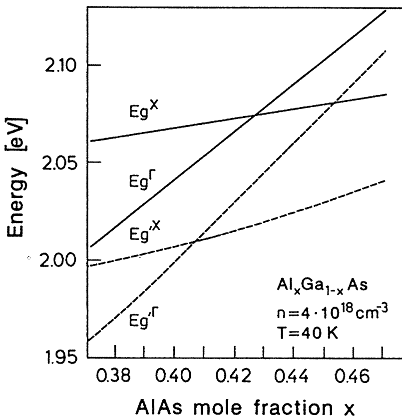

Fig. 3.16. Direct-to-indirect crossover in unexcited (solid lines, compare to Fig. 2.1) and highly excited (dashed lines) $Al_xGa_{1-x}As$. The crossover shifts as a function of density from 0.426 to here 0.408 [3.11]

conduction band. Direct stimulated emission dominates for x values below x_c, while *indirect stimulated transitions* of X-point electrons to the valance band are observed for $x > x_c$ [3.67, 68, 85–88]. The latter process is a zero-phonon recombination induced by the alloy disorder, the transition probability of which is well described by second-order perturbation theory [3.68, 89]. The electron recombines, here, via a virtual intermediate state in the Γ minimum. The energy separation between X and Γ minima thus determines, via an energy denominator, the efficiency of this indirect stimulated emission. The efficiency is, of course, highest when central and side valleys are nearly degenerate. We will discuss these proceses in more detail in Sect. 4.3.

From the temperature dependence of the threshold fluence for optically pumped stimulated emission we are able to demonstrate that $Al_{0.43}Ga_{0.57}As$ changes from an indirect to a direct gap semiconductor as a function of lattice temperature (Sect. 4.3, especially Fig. 4.36) [3.85]. The crossover occurs at about 80 K. The stimulated emission in this sample is thus direct at room temperature, but the side valleys at the X and L points are still close by in energy. With increasing carrier density it is thus possible to switch the stimulated emission for this composition from direct to indirect. The intensity of the stimulated luminescence as a function of excitation fluence (Fig. 3.17) demonstrates this behavior. The intensity rises steeply with excitation level but reaches a saturation level around 8 mJ/cm^2. It is then possible to raise the carrier density in the sample with increasing pump fluence. The relatively large density in the high-mass side valleys finally leads to a crossing of the X minima below the Γ minimum. This can be shown by a calculation of the renormalized band gaps as a function of carrier density (Fig. 3.18). The direct-to-indirect transition is reflected in the stimulated emission by a sudden steep

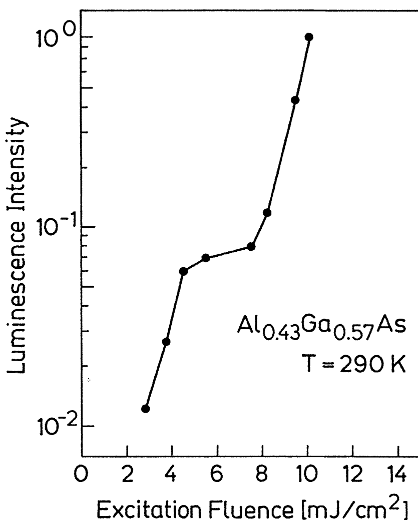

Fig. 3.17. Intensity of stimulated emission as a function of excitation level in $Al_{0.43}Ga_{0.57}As$ at room temperature. The solid line is merely a guide for the eye [3.11]

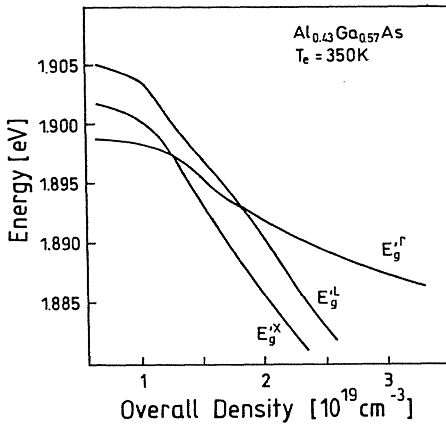

Fig. 3.18. Band-gap energies and minima crossing as a function of the overall carrier density in $Al_{0.43}Ga_{0.57}As$ calculated with the multi-valley model [3.11]

rise in the emission intensity at 11 mJ/cm^2 when the indirect channel becomes dominant. The crossing of the L and Γ minima results in a strong fluctuation of the emission level at higher pump fluences. A similar behavior induced by minima crossing, but without a change in the nature of the fundamental gap, will be discussed in the following.

The stimulated transition in $Al_{0.46}Ga_{0.54}As$ is indirect at all pump levels at room temperature. The origin of the electrons involved, however, can change from the X to the L minima. A calculation of the renormalized band gaps shows that a crossing of the L and Γ minima is expected in the density range around $1 \times 10^{19}\,\mathrm{cm}^{-3}$ as a consequence of the differential renormalization (Fig. 3.19). The L minima are thus close to energetic degeneracy with the central valley. This results in a very large transition probability due to the small energy denominator in the matrix element (4.10). The high population of the L valleys at room temperature then dominates the stimulated emission process in this density range.

This change in the transition channel is demonstrated by the behavior of the stimulated emission. The emission above the threshold is positioned at the low-energy tail of the spontaneous luminescence, i.e., at the indirect X gap

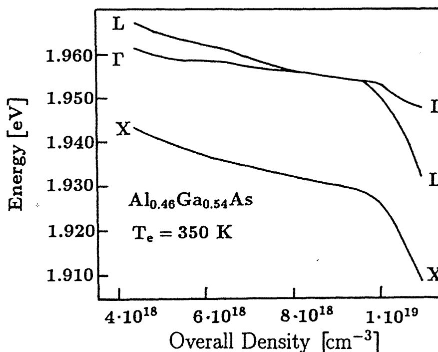

Fig. 3.19. Band-gap energies and minima crossing as a function of the overall carrier density in $Al_{0.46}Ga_{0.54}As$ calculated with the multi-valley model [3.11]

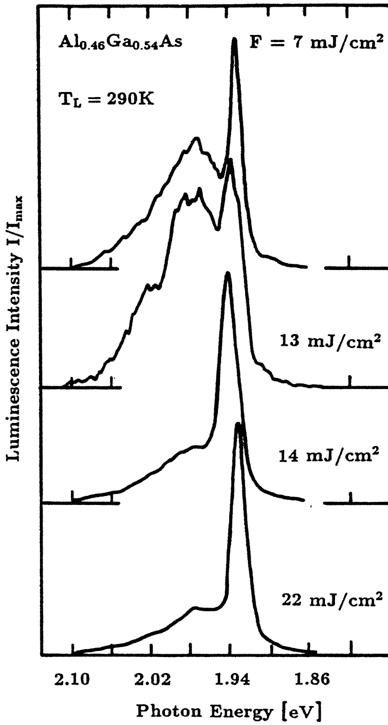

Fig. 3.20. Stimulated and spontaneous emission in $Al_{0.46}Ga_{0.54}As$ at various excitation levels [3.11]

(Fig. 3.20, top curve, $F = 7\,\mathrm{mJ/cm^2}$). The efficiency of the stimulated process drops dramatically when the pump fluence is increased to $13\,\mathrm{mJ/cm^2}$. Simultaneously, additional new emission bands are observed on the high-energy side of both the stimulated and the spontaneous emission. The position of the stimulated emission line jumps to higher photon energies by 25 meV and the intensity rises significantly with a further increase of the pump fluence by only one $1\,\mathrm{mJ/cm^2}$ (Fig. 3.20, middle two curves). This shift in emission energy corresponds exactly to the energy separation between the L and the X minima at the crossing of L and Γ (Fig. 3.19). The behavior of the stimulated emission is thus identified as resulting from the change in the dominant recombination channel from transitions involving the X minima to ones involving the L minima. The dominance of the emission from the L minima is a direct consequence of the close-to-resonance condition of these conduction-band minima, while the X minima are much further away from the intermediate states. With further increase of the excitation density the dominant stimulated emission changes back to the X minima, because the much larger population inversion eventually compensates for the smaller transition probability. At $22\,\mathrm{mJ/cm^2}$ the emission is again related to the lowest indirect gap and the emission at higher photon energies has ceased (Fig. 3.20, bottom curve).

In summary, the band-gap renormalization in semiconductors with multiple inequivalent valleys can be described by a multi-valley expansion of the universal formula of *Vashishta* and *Kalia.* The main modification in this expansion is the explicit treatment of the electron-exchange interaction in each individual minimum. This model is able to describe both the shift of essentially unoccupied conduction-band minima at higher energies, and the renormalization of partially occupied minima in a self-consistent treatment. The model calculations are in excellent agreement with experimental data in both direct- and indirect-gap $Al_xGa_{1-x}As$ for the fundamental and higher-energy band gaps. The differential renormalization of minima with different effective masses, and thus populations, leads to laser-induced crossings of various minima such as the changeover from a direct to an indirect semiconductor in $Al_xGa_{1-x}As$ close to the crossover point. Minima crossings further influence the dominant recombination channel, the efficiency and the emission wavelength of indirect stimulated emission.

3.3 Gap Renormalization in Low-Dimensional Systems

The restriction of carrier mobility due to quantum confinement in one or more directions results in strong modifications of the screening behavior of electrons and holes. We will now detail the consequences of these modifications on the renormalization of both the fundamental and higher subband gaps in highly excited quantum wells (QWs) and quantum-well wires (QWWs).

3.3.1 Subband Renormalization in Quantum Wells

Two main effects influence the renormalization of the fundamental subband gap in QWs: the reduced screening efficiency leads to a lower shift of the gap in units of the excitonic Rydberg than in bulk semiconductors, while the enhanced excitonic binding energy counterbalances this effect such that the absolute shift in meV of the 2D gap is larger than in bulk [3.90]. The carrier densities used in this comparison are expressed in equivalent interparticle distances r_s. The expression for the bulk r_s is found from (3.16) while the two-dimensional r_s is

$$r_s = \frac{1}{\sqrt{\pi n}} \frac{1}{a_1^{2D}} \quad . \tag{3.21}$$

The band-gap renormalization for various GaAs/AlGaAs QWs in comparison to bulk GaAs is shown in Fig. 3.21. The experimental data are extracted from fits to luminescence line shapes. The theoretical 2D renormalization is calculated in the dynamical random-phase approximation using a single plasmon pole while the universal formula (3.14, 17) is plotted for the 3D gap shift.

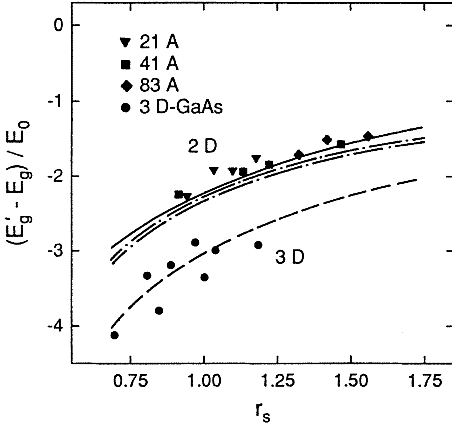

Fig. 3.21. Renormalization of the fundamental (sub-)band gap in two and three dimensions [3.90]

The 2D shift is found to be about one excitonic Rydberg lower at the same r_s than in bulk, while the absolute shift is larger by a factor of 2.5 (compare $\Delta E_g(2D) \approx 40\,\text{meV}$ to $\Delta E_g(3D) \approx 16\,\text{meV}$ for $r_s = 1$). These observations demonstrate the above-mentioned implications of the 2D confinement.

The theoretical dependence of the BGR on 2D pair density was proposed in early calculations of *Schmitt-Rink* et al. [3.91] to be:

$$\Delta E_g^{2D} = -3.1\,(n^{2D}(a_1^{2D})^2)^{1/3}\,E_{\text{bind}}^{2D} \quad . \tag{3.22}$$

This formula is an interpolation of RPA results in the limit of $T = 0\,\text{K}$ and low densities. Similar expressions were found by *Tarucha* et al. from experiments in electrically pumped GaAs/AlGaAs QWs [3.92], by calculations of *Kleinman* and *Miller* for modulation-doped QWs [3.93], and by measurements of the BGR in a one-component plasma in the latter type of samples [3.138]. The relation $\Delta E_g \propto n^{1/3}$ was used in an experimental survey of BGR in several different QW systems, namely GaAs/AlGaAs, GaSb/AlSb and InGaAs/InP, using luminescence spectroscopy in an effort to establish a universal behavior of band-gap renormalization in QWs similar to that in the bulk. These measurements demonstrated a similar behavior of the renormalization in III-V QW systems [3.94]. More careful experiments, however, proved that the universality of (3.22) is not only limited to low temperatures and moderately high densities but also strongly affected by the deviations of realistic QW systems from exact two-dimensionality [3.95]. We will return to this point later.

The determination of band-gap renormalization from a line-shape analysis of luminescence experiments was strongly criticized by several authors [3.24, 96, 97]. In particular, the luminescence spectra in QWs, in contrast to the bulk case, do not show any shift of their maximum with rising density, only broadening on the high and low-energy sides, e.g. [Ref. 3.94, Fig. 1]. This fact was explained as resulting from a compensation of the high-energy shift of the chemical potential by the renomalization of the gap. The BGR is extracted

essentially from a modelling of the low-energy broadening. Alternative explanations were that the plasma-related luminescence is augmented by remnants of the excitonic emission due to the lateral inhomogeneity of a laser-excitation spot [3.97]. It was even claimed that band-gap renormalization saturates at $2E_{\rm bind}^{\rm 2D}$ [3.96]. The latter conclusion was drawn from luminescence studies of highly excited QWs in magnetic fields. Indeed, no shift of the Landau-level related structures in the emission was found above a certain density. On the other hand, no such saturation is found in magneto-luminescence studies of InGaAs/InP QWs [3.98].

These apparent discrepancies were resolved by some additional independent experiments. Density-dependent band-gap renormalization was unambiguously identified in measurements of gain spectra [3.29, 95] and stimulated emission [3.99, 100] in GaAs/AlGaAs QWs. In pump-probe-type measurements of the optical gain related to the electron–hole plasma one determines the chemical potential from the gain-to-absorption crossover independent of the details in the line shape (Fig. 3.22). The position of the chemical potential can be compared to many-body theory once the carrier density is deduced from the width of the gain spectrum. The resulting renormalization and the corresponding calculations in the dynamic plasmon-pole approximation are shown in Fig. 3.23. The comparison to these reliable experiments showed that a pure 2D calculation significantly overestimates the measured renormalization. Effective exciton paramenters (here $E_{\rm bind}^{\rm 2D} = 8.7\,{\rm meV}$ and $a_1^{\rm 2D} = 126$ Å for a 100-Å QW) have to be used to account for the deviations of the screening from strictly two-dimensional behavior in QWs with finite well width. With

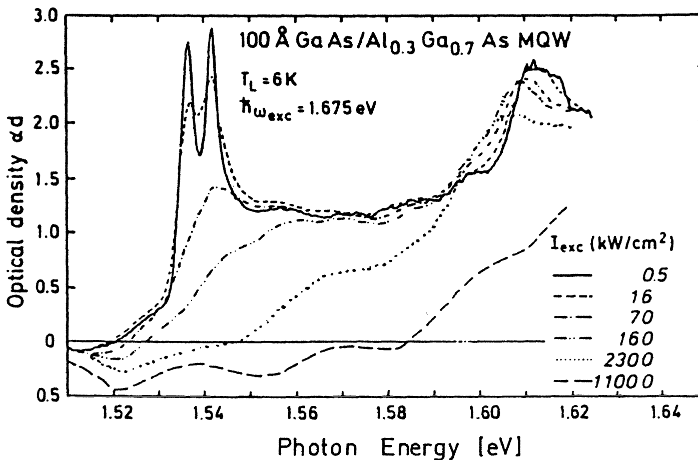

Fig. 3.22. Absorption spectra of a 100-Å GaAs/AlGaAs QW structure under quasistationary excitation (pump intensity $I_{\rm exc}$) at $T_{\rm L} = 6\,{\rm K}$ [3.95]

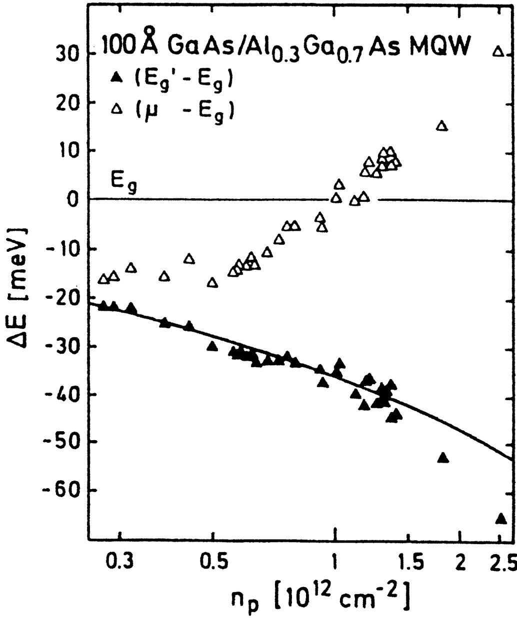

Fig. 3.23. BGR and chemical potential as a function of 2D plasma density. Solid line: theoretical gap shift using effective parameters [3.95]

these effective parameters the BGR can be approximated for a 100-Å QW by the following expression: $\Delta E_{\mathrm{g}}(\mathrm{meV}) \approx 3.1 \times 10^{-3}\,(\mathrm{n_{2D}}\,[\mathrm{cm}^{-2}])^{1/3}$ [3.24].

This density dependence of BGR in QWs was further demonstrated by *Cingolani* et al. [3.99] by the observation of transient band-gap renormalization in a picosecond experiment. The gap shift here is directly determined from the spectral position of a stimulated emission peak in a 106-Å MQW. The stimulated emission perpendicular to the surface in this sample is strongly enhanced by means of a thick $Al_xGa_{1-x}As$ layer between the MQW and the substrate providing optical confinement. The stimulated luminescence (Fig. 3.24) is emitted preferentially at the band edge, where self-absorption losses are reduced, and its spectral position is thus a tag for the energy of the renormalized gap. Accordingly, the stimulated emission peak closely follows the density-dependent shrinkage of the gap. In the first 30 ps, i.e., during the pump pulse, the stimulated emission peak (labeled S in Fig. 3.24) arises at the energy position determined by the initial photo-generated carrier density and shifts to the red with increasing excitation intensity. For longer times, the net BGR decreases following the temporal decrease of the carrier density. As a consequence a pronounced blue-shift of the luminescence is observed over the 150 ps after the excitation pulse.

The transient evolution of the gap shift is displayed in Fig. 3.25 for different initial carrier densities. The BGR reaches its maximum value within the first 30 ps and decreases in time after extinction of the laser pulse. The blue-shift follows a $\Delta E \approx \mathrm{e}^{-t/3\tau}$ decay law consistent with the above $(n(t))^{1/3}$ behavior at all excitation intensities. The deviations at early times for the I_0

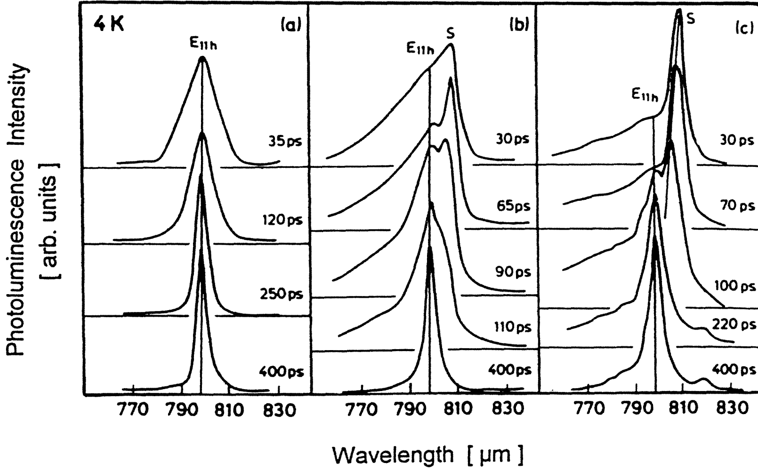

Fig. 3.24. Temporal evolution of luminescence (**a**) below ($I_0/400$) and (**b**), (**c**) above ($I_0/100$, $I_0/40$ with $I_0 = 180\,\mathrm{MW/cm^{-3}}$) the threshold for stimulated emission in a GaAs/AlGaAs MQW [3.99]

curve can be explained by the fact that the S peak merges here with the residual emission from the GaAs substrate. It is important to note that the measured BGR at any given time after the excitation scales with density according to (3.22).

These experiments on the gain and stimulated emission provided additional confirmation of the density-dependent gap shift in semiconductor QWs. The problem of the saturation of the BGR in the magetic field measurements was solved by *Cingolani* et al. [3.100] in the following way. The plasma luminescence in an applied magnetic field was recorded for the above-used sample which has a short carrier lifetime due to the efficient stimulated recombination and compared to results for a similar sample with long lifetime (i.e., without an additional optical confinement layer). For the latter sample the saturation of the BGR in a magnetic field is observed as in Ref. [3.96], whereas the usual density-dependent gap shift is found in the former sample. The strong dependence of the magneto-optical properties on carrier lifetimes indicates that two different phases are formed in the plasma at a high magnetic field: a highly correlated condensed phase in quantum wells with sufficiently long lifetimes and a free electron–hole plasma in heterostructures with short lifetimes. In the former state, the band gap is found to renormalize by an amount equal to twice the excitonic binding energy, independent of the actual photogeneration rate. On the other hand, condensation processes are prevented in the short-lived phase, thus resulting in the expected density BGR. The properties of the condensed electron–hole fluid in the presence of high magnetic fields are

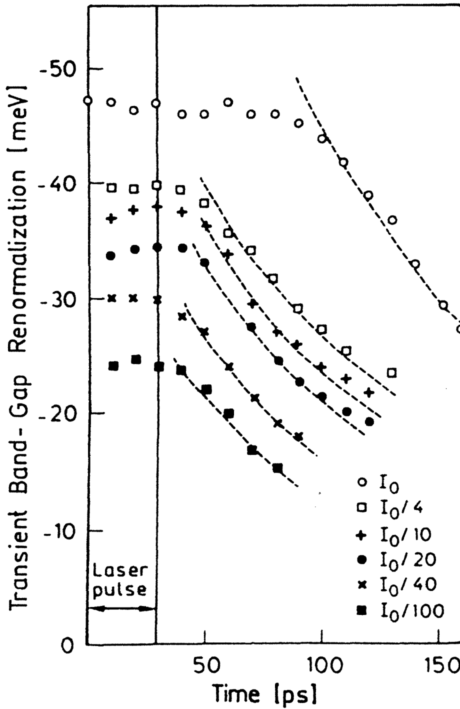

Fig. 3.25. Transient BGR at different excitation intensities and exponential regressions with the $e^{-t/3\tau}$ decay law [3.99]

presently not well understood and require more theoretical and experimental investigations.

The occurrence of density-dependent BGR is meanwhile undisputed and has been subject to a large amount of experimental and theoretical work to detail its properties. The temperature dependence of the gap shift is predicted by RPA theory to be rather small for intermediate densities and to vanish in the high-density regime [3.60, 101]. Indeed, no significant dependence on temperature could be deduced from gain measurements in the relevant density range [3.102]. Calculations within an adiabatic approximation describing the screening by a static plasmon pole, however, predict a much larger temperature sensitivity of the BGR and an approximate coincidence of the entire ΔE_g versus r_s curves for 3D and 2D in ideal, reduced units at room temperature [3.13].

We have already mentioned the influence of the well width on the actual amount of the gap shift. This effect was found in several studies in both GaAs/AlGaAs [3.29, 95, 103] and InGaAs/InP QWs [3.61]. The transition from 2D to 3D screening behavior occurs for well widths of at most 200 Å, as was demonstrated by *Lach* et al. [3.104] in luminescence studies on etched mesa-type structures, in order to achieve homogeneous excitation conditions. The way to account for this well-width dependence in the theoretical models is to use effective excitonic parameters as already discussed

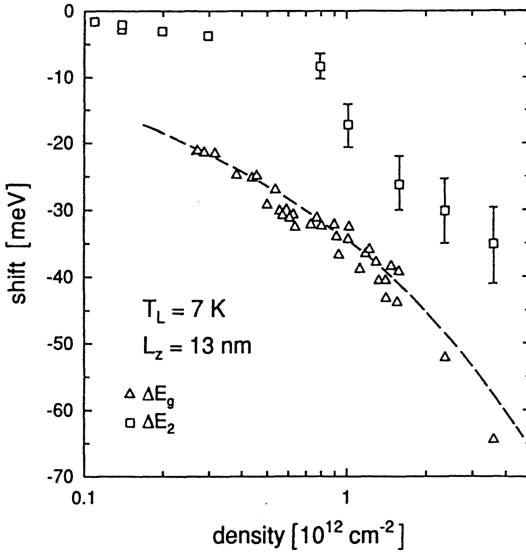

Fig. 3.26. Shift of the fundamental subband gap ΔE_g and the $n_z = 2$ gap ΔE_2 in a 130-Å GaAs/AlGaAs QW [3.29]

above [3.95, 101]. *Das Sarma* et al. [3.105, 106] proposed a universality of the BGR in QWs when the exciton Bohr radius and the well width are expressed in effective dimensionless parameters. Even an approximate (to within 20%) one-parameter universality similar to the 3D case is expected. One limitation of this approach, however, is that in contrast to many bulk materials (like Si or GaAs) even moderate densities can lead to a sizeable population of higher subbands in QW systems with well width of 10 nm and more. The resulting modifications of the gap shift, and thus the unavoidable deviations from universality, will be discussed in the following.

Up to now, we have not considered in our discussion any deviations of the gap shift from rigidity. It is typically assumed that both the band gap and the chemical potential renormalize by the same amount with increasing density. Even a rigid shift of the whole subband structure, i.e., also of unoccupied bands, has been proposed in early calculations of the many-body interactions

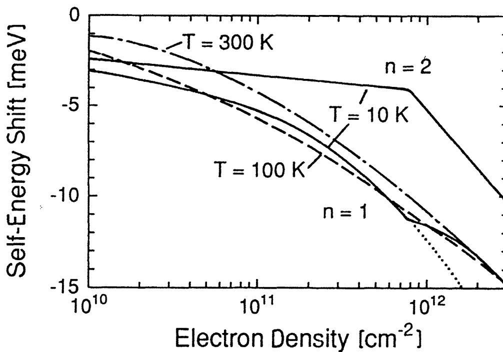

Fig. 3.27. Calculated self-energy shift of the first and second sublevel in an n-doped 200-Å GaAs/AlGaAs Qw [3.60]

in QWs [3.93]. But recent experimental and theoretical work clearly shows that the band-structure modifications are far from being rigid. A representative result is shown in Fig. 3.26 for renormalization of the $n_z = 1$ and $n_z = 2$ subbands in a 130 Å GaAs/AlGaAs QW. The lowest subband gap shift, as discussed above, is well described by calculations using effective parameters. The $n_z = 2$ subband gap, however, displays only a minor shift to the red of some 10% as long as the corresponding conduction-subband minimum is not populated. This direct result of the small Coulomb screening between different sublevels in 2D systems is also evident from time-resolved transmission measurements (Fig. 3.2), from the gain spectra under steady state conditions in Fig. 3.22, and also from experiments on modulation-doped QWs (see next section). The renormalization of the higher subbands suddenly increases once the population in the subbands is no longer negligible at high overall densities. Similar results have been deduced by *Levenson* et al. [3.107] from absorption measurements, by *Lach* et al. [3.108] from room-temperature luminescence studies in the GaAs/AlGaAs system, and by *Kulakovskii* et al. [3.61] from luminescence studies on InGaAs/InP QWs.

The observed behavior can be understood qualitatively in the following way: The correlation between the electrons in the lowest subband and those in higher subbands is quite small due to the small overlap of the corresponding wave functions, which have a maximum in the center of the well for $n_z = 1$, but two extrema close to the interfaces for $n_z = 2$. The exchange interaction between orthogonal wave functions vanishes and is only important for carriers within the same subband. This situation is thus rather similar to the multi-valley scenario in $Al_xGa_{1-x}As$ as was discussed in the previous section. The main difference, besides the reduced strength of screening in low dimensions, is that optical transitions in QWs are only symmetry allowed between electron and hole subbands with same index n_z. The first (considerably occupied) hole subband thus only affects the lowest energy transition and does not influence any higher ones. These qualitative features, however, are only reproduced in some of the theoretical models of the BGR in QWs. Figure 3.27 shows a calculation in the random-phase approximation at finite temperatures including the intersubband screening and the finite well width [3.60]. Note that the renormalization is considerably smaller than for the experimental results of Fig. 3.26, because the calculation treats an n-doped QW and thus a one-component plasma. We will return to the screening in such one-component plasmas later. The calculations demonstrate the effect of occupation on the second electronic subband as found in the experiments. Calculations using the local density approximation, however, significantly overestimate the gap shift for unoccupied bands (see [3.108, 109] and discussion in [3.60]). Much stronger intersubband exchange effects are proposed by *Bongiovanni* et al. [3.62]. The latter results can only be understood if one interprets the strong oscillator strength related to the higher subband gaps in terms of a correla-

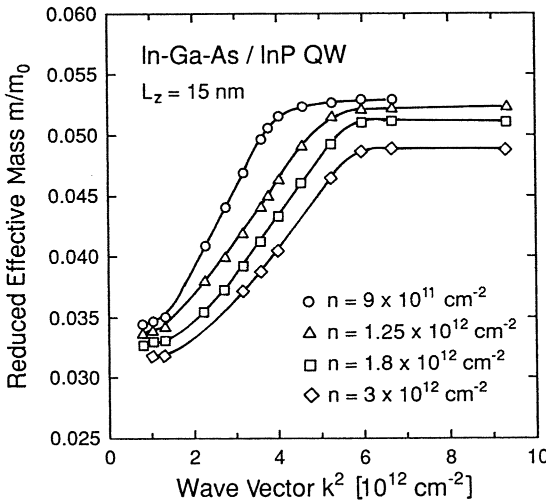

Fig. 3.28. Dependence of the reduced carrier effective mass in a InGaAs/InP QW on the wave vector squared for different plasma densities [3.98]

tion enhancement rather than an exciton as proposed by *Bauer* et al. [3.109]. These questions still require further elucidation.

A further phenomenon, the description of which is not yet consistent, is the occurrence of an effective-mass renormalization, i.e., the non-rigid shift of the states within one subband. A reduction of the effective mass of up to 25%, depending on the k-vector, was deduced in InGaAs/InP QWs and in strained InGaAs QWs from the Landau-level spacing in magnetoluminescence by *Butov* et al. (Fig. 3.28) [3.98, 110]. This reduction is explained qualitatively in terms of an increasing hh-lh subband splitting as a result of differential renormalization. The difference in subband shift is due to the comparatively small population of the lh subband, similar to the case just discussed of higher electron subbands. The increasing splitting then results in a reduction of the mixing between lh and hh subbands and thus a reduction of the heavy-hole mass. On the other hand, a reduction of the effective electron mass resulting from redistributions of the density of states at the subband edge due to electron–phonon interaction is predicted by the calculations of *Jalabert* and *Das Sarma* [3.106].

We can summarize here by stating that BGR in QWs is qualitatively well understood when accounting for all relevant subband gaps. The quantitative agreement between experiment and theory for the case of the higher subbands still has to be improved. Some further details such as the mass renormalization still have to be treated explicitly.

3.3.2 Band-Gap Narrowing in Quantum Wires

The properties of the electron–hole plasma and the BGR in quantum-well wires (QWW) are not well studied yet. Recent results on BGR in a QWW array extracted from time-resolved luminescence data (Figs. 3.29, 30) are shown in Fig. 3.31 [3.34]. The QWW array was fabricated by holographic lithography and plasma etching from a GaAs/AlGaAs multiple quantum-well structure resulting in QWWs of about 60 nm lateral width [3.33]. High optical excitation was achieved by picosecond pulses (25 ps FWHM) from a frequency doubled, amplified, actively and passively modelocked Nd:YAG laser. The temporal evolution of the luminescence spectra at a 5 K lattice temperature was analysed by a combination of a spectrometer and a streak camera.

The spectra (Figs. 3.29, 30) are typical for band-filling luminescence in low-dimensional structures. Broadening of the spectra on both the low- and the high-energy side at short delay times (i.e., high pair densities) reflects the BGR and the hot carrier distribution. Comparison of the spectral features to subband calculations show that up to five occupied wire subbands can be distinguished (Fig. 3.29) [3.33]. The luminescence spectra are analysed using a line-shape model which includes momentum conservation, a one-dimensional joint density of states, summation over several subbands, the selection rule

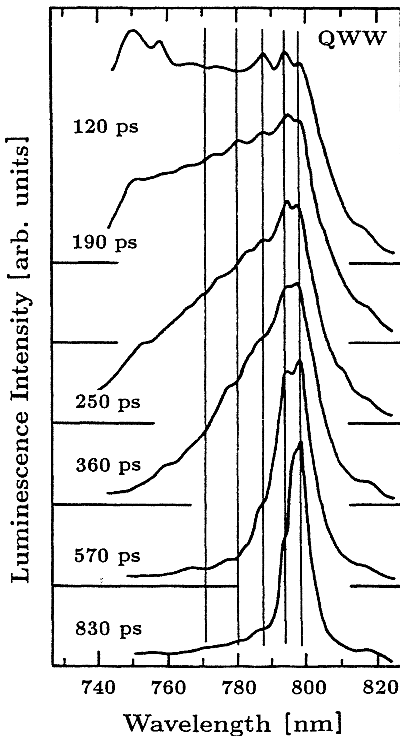

Fig. 3.29. Band-filling luminescence in a QWW array [3.33]

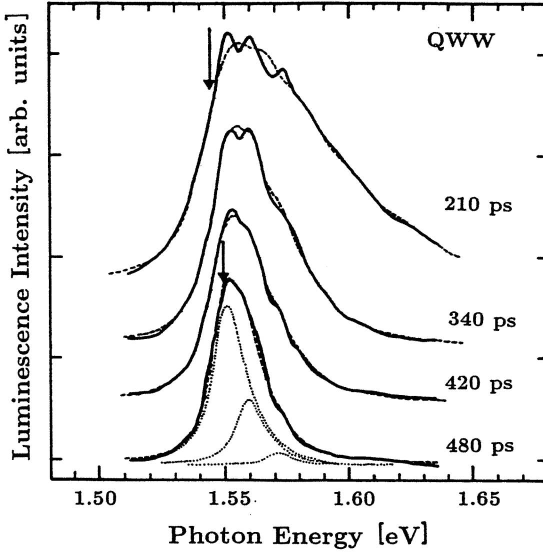

Fig. 3.30. Temporal evolution of the band-filling luminescence in 60-nm quantum-well wires after excitation with 25-ps pulses at 2.33 eV with a fluence of $F = 12.5\,\mathrm{mJ/cm^2}$. The dashed lines reflect line-shape fits including several wire subbands as indicated by the dotted lines in the lowest spectrum. The arrows mark the position of the renormalized gap [3.34]

$\Delta n_y = 0$, and broadening of all transitions by a Lorentzian to account for final state damping (for more details see [3.34]). The fits are excellent for spectra at long delay time but less satisfactory at short times, i.e., highest densities (Fig. 3.30). One problem here is the unknown relative renormalization of the subbands. A rigid shift was assumed for simplicity and only the BGR of the lowest subband transition was extracted as a fuction of the overall pair density. Arrows in Fig. 3.30 indicate the position of the renormalized gap for two of the spectra.

The BGR with respect to the unshifted gap at $E_g = 1.566\,\mathrm{eV}$ is plotted in Fig. 3.31 in comparison to calculations from Ref. [3.150]. The BGR shows a clear density dependence with values between 25 and 12 meV in the observed density range. The latter value corresponds to the excitonic Rydberg state in this QWW system indicating that the Mott transition occurs close to the related density. The theory shows a similar trend but the absolute values are sligthly smaller for the appropriate wire width. This discrepancy could be partly due to neglect of the hole contributions to the BGR in the theory. Calculations in Refs. [3.31, 151] predict a larger BGR than found in the experiments, but these calculations were performed for a harmonic wire potential of much narrower width and for the extreme 1D quantum limit, respectively,

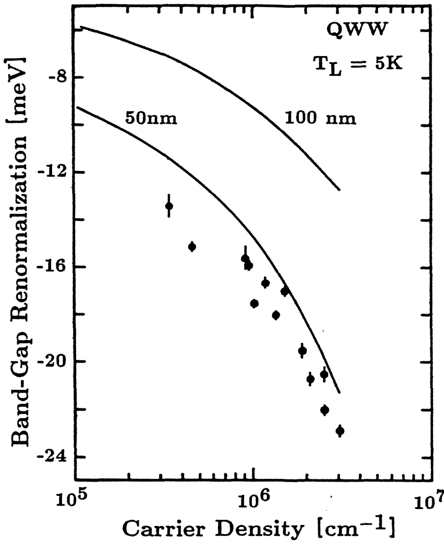

Fig. 3.31. Density dependence of the renormalization of the lowest subband gap in the QWWs. Dots: experimental data extracted from the line-shape fits [3.34]; solid lines: theoretical renormalization for different wire diameters from Ref. [3.150]

and cannot be compared directly to the experiments. None of the available theoretical works [3.31, 150, 151] include the population of several subbands as is the case in the experiments.

It is desirable for the future to have a treatment of multi-subband effects in the theory and also experiments on QWWs with larger subband spacings to exclude or limit such effects. The latter task might not be easy because it requires QWWs with small diameters, where localization (e.g., at interface fluctuations) could inhibit screening effects.

3.4 Screening in One-Component Plasmas

The previous sections have dealt with the consequences of screening in electron–hole plasmas in 3D, 2D, and 1D semiconductor systems. We will now detail the optical properties and many-body effects related to *one-component plasmas*, i.e., plasmas consisting predominantly of either electrons or holes. Such situations are achieved by heavy doping of the semiconductor material with donors or acceptors, respectively, beyond the metallic limit.

Raising the doping level in bulk semiconductors merges the donor- (or acceptor-)related electron (hole) levels close to the band-edge to form impurity bands which eventually overlap with the free-carrier bands. In such a way, a plasma of free electrons (holes) moving against a background of fixed, oppositely charged defect ions is prepared. According to the metallic properties of this plasma, the transition is called a *metal–insulator transition* or a *Mott transition* [3.111]. Such a one-component plasma shows many-body effects similar to those discussed above. Band-gap renormalization due to ex-

change and correlation effects is now, however, only related to one charge species and intrinsically present even without optical excitation [3.112–114]. Optical studies of the many-body phenomena involve the generation of additional electron–hole pairs. The situation in n-type material is typically chosen such that the number of electrons is more-or-less unchanged due to the optical excitation, while the number of holes is determined by the excitation level. The holes then display some correlation effects, while the exchange effects are negligible unless very high excitation levels are reached. Corresponding properties for the opposite charges are of course found in p-type semiconductors.

Additional large contributions to the screening and renormalization effects arise from the interactions of the free carriers with the impurities. In n-type semiconductors these are the electron–ionized-donor interaction as well as the correlation between holes and bound dopant electrons or ionized donors. In particular, the free-carrier–ion interaction results in significant deviations from a rigid shift of the band gap (Fig. 3.32) which holds approximately in the two-component plasma [3.113, 115]. The corresponding effects are again found in p-type materials, but with two important differences: First, due to their larger effective mass, screening by holes is less efficient which makes the gap shift smaller for the case of p-doping than for the same level of n-doping. Second, the non-rigid shift of the valencebands implies that the heavy- and light-hole bands shift by the same amount only for $k \approx 0$, which requires a self-consistent treatment of the population and the stretching of the valence bands as a function of hole density [3.114].

It is currently still under discussion whether momentum conservation in optical transitions in doped semiconductors is relaxed or not, and whether band tailing only occurs due to lifetime broadening or also due to localized tail states [3.113, 115]. The presence of the impurities thus rather complicates the interpretation of optical experiments. For further review of the optical properties and many-body effects in doped semiconductors we refer to Ref. [3.112].

A more clear-cut situation arises when the free carriers are spatially separated from the dopant ions. Such a separation is achievable by *modulation doping*, where the dopant atoms are deposited in a small region (e.g., the center) of the barrier layers of a heterostructure or a quantum-well structure as is demonstrated in Fig. 3.33 for the case of an n-type *modulation-doped quantum well* (MDQW) structure. The excess electrons of the donors transfer to the initially empty states of the lowest quantized level in the well in order to achieve a spatially constant Fermi level throughout the structure. The electrons are thus separated from the ionized donors with important impact on the properties of the electronic system: extremely high carrier mobilities are achieved because impurity scattering is now absent and the carriers form a real one-component plasma without much perturbing influence from the fixed opposite charges [3.116]. The separation of the carriers from the

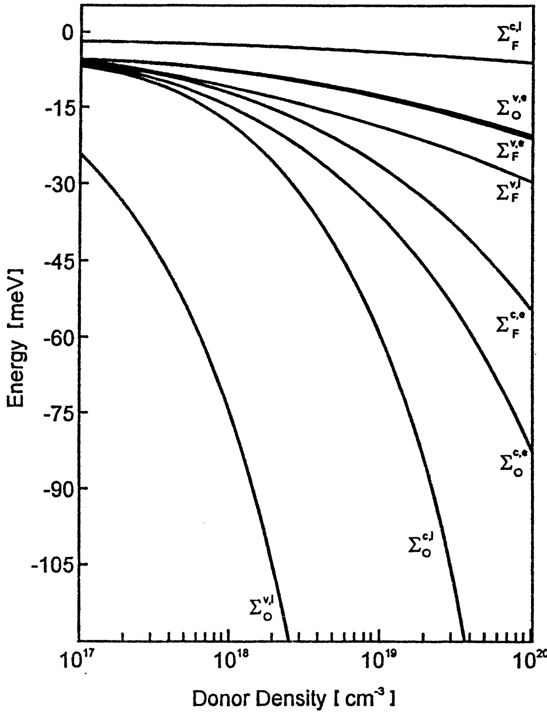

Fig. 3.32. Self-energy shifts for electrons Σ^c and holes Σ^v in states with zero momentum (subscript 0) and Fermi momentum (subscript F) individually split into their electron–electron (superscript e) and electron–ion (superscript i) parts as a function of donor density [3.113]

dopant ions, however, leads to internal electric fields resulting in a bending of the band structure. Self-consistent calculations of the charge-carrier densities and the field effects show that the effects on the quantized levels and the free-carrier distribution in the wells is small in symmetric MDQWs (Fig. 3.33) [3.117]. Strong band bending, on the other hand, occurs in asymmetric structures [3.118] and in center-doped structures [3.119] which we will discuss below.

The many-body properties of 2D one-component plasmas are reflected in their optical spectra. In particular, the singularity of the optical spectra at the Fermi edge is much more pronounced in 2D structures than in bulk, where this effect is less significant. The *Fermi-edge singularity* (FES) or *Mahan exciton* arises in n-type modulation-doped quantum wells from the correlation between a photo-excited hole and the sea of electrons in the wells. The re-

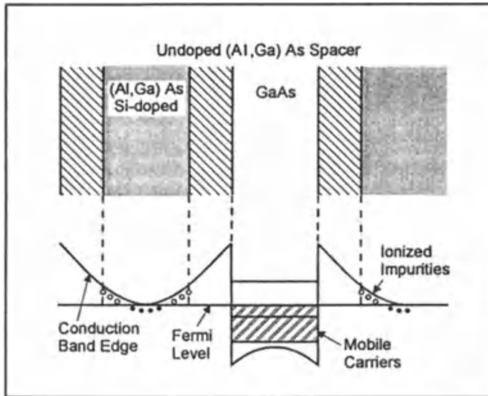

Fig. 3.33. Schematic representation of the energy levels together with the carrier and dopant distributions in modulation-doped quantum wells

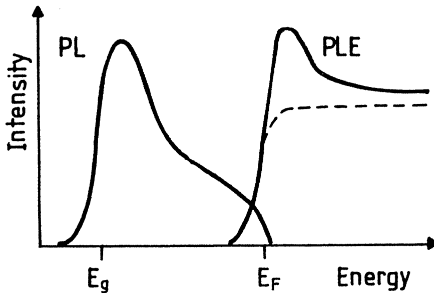

Fig. 3.34. Schematic representation of optical spectra in MDQWs. Solid line: luminescence; dotted: absorption; dashed: absorption without enhancement

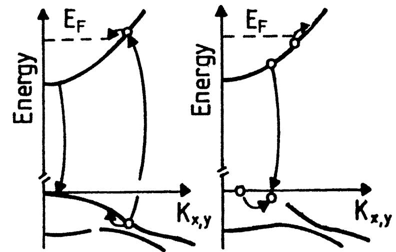

Fig. 3.35. Carrier dispersion, optical transitions, and relaxation mechanisms in MDQWs

arrangements in the Fermi sea in order to screen the Coulomb interaction between the hole and the electrons lead to a strong enhancement of the oscillator strength for optical transitions of electrons close to the Fermi level (Fig. 3.34). These electrons are the only ones that are able to scatter (and thus contribute to the screening).

The carrier dispersion, optical transitions, and possible relaxation mechanisms in MDQWs are illustrated in Fig. 3.35. The left part of the figure shows the generation of an electron–hole pair by optical excitation. Due to the negligible momentum of the absorbed photon, the hole is created in a state with large quasi-momentum **k**. The electron relaxes to states close to the Fermi energy while the hole relaxes towards the Γ point. Subsequent electron–hole recombination mainly occurs close to the band-gap energy. The right part of Fig. 3.35 shows a *shake-up process* of the Fermi sea: a hole is transferred to a state at larger quasi-momentum, while an electron is scattered across the Fermi level. The hole then later recombines with a different electron.

The enhancement at the Fermi level was first described by *Mahan* for the case of X-ray spectra in metals, where the excitation of bound electrons by X-ray quanta leaves a core hole state which correlates with the electron Fermi sea [3.1]. A similar type of multiple electron–hole scattering was invoked to explain the spectral shape of optical gain related to degenerate electron–hole plasmas in bulk semiconductors [3.4]. The enhancement in the latter case, however, is rather minor and never shows up as a distinct feature [3.120]. Much stronger are the enhancement effects in 2D systems where the correlation is far more efficient as a result of the rather weak screening. The first calculations proposing such strong enhancements for optical spectra of electron–hole plasmas in quantum well structures were done on the basis of the theory by *Mahan* [3.2]. Although these calculations are only of qualitative nature and the proposed enhancements are far from reality, one can deduce some characteristic features which can be used to identify the FES in optical experiments (Figs. 3.36, 37). The enhancement at the Fermi edge is most sensitive to temperature and carrier density. Raising the temperature washes out the sharp edge at the Fermi level, while increasing the carrier density reduces the correlation. Both effects lead to a vanishing of the singularity. Similar results for the $n_z = 1$ and higher transitions are proposed from calculations in the local-density function formalism [3.109, 137].

Because optical transitions are predominantly direct [3.121], a sufficient number of the involved holes have to have k vectors in the range of the Fermi wave vector, k_{F}, of the electrons (Fig. 3.34). Consequently, the holes have to be localized to achieve such large quasi-momentum $\mathbf{k}$ in emission processes. The FES in 2D semiconductor structures was first identified in a luminescence experiment on InGaAs/InP n-type MDQWs by *Skolnick* et al. [3.3] and theoretically modelled by *Rorison* [3.122]. The emission spectra (Fig. 3.38) display a strong enhancement peak which vanishes with increasing temperature. In these QW structures, the holes are sufficiently localized at fluctuations of

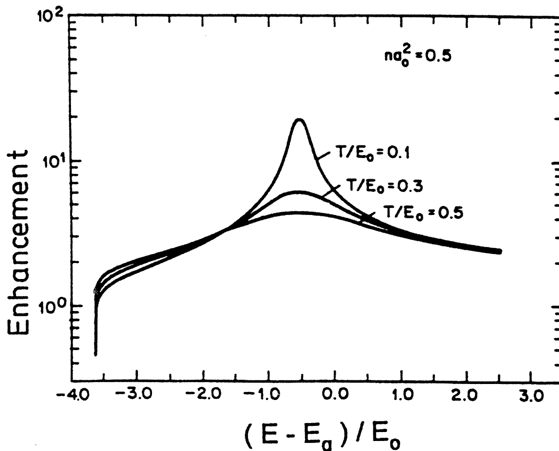

Fig. 3.36. Theoretical excitonic-enhancement spectra in QW structures as a function of lattice temperature in reduced units (electron density would be $5 \times 10^{11}\,\mathrm{cm}^{-2}$ for a 100 Å QW) [3.2]

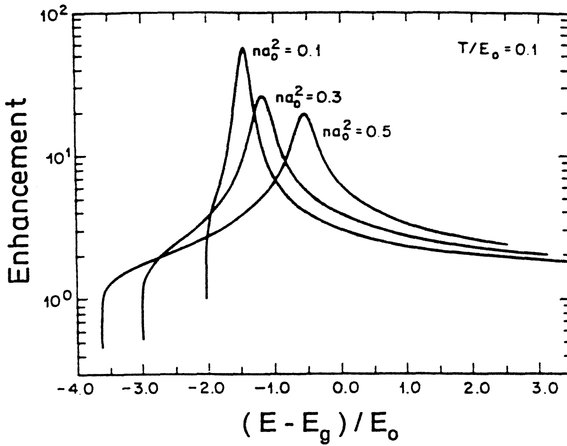

Fig. 3.37. Theoretical excitonic-enhancement spectra in QW structures as a function of pair density in reduced units (temperature would be 10 K for a 100 Å QW) [3.2]

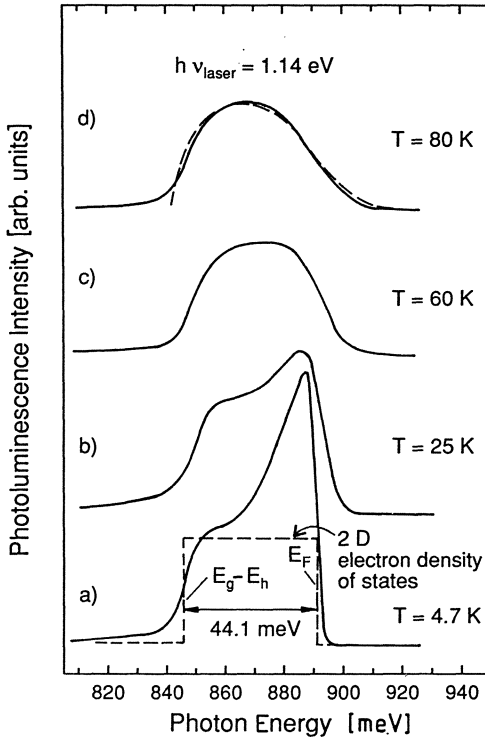

Fig. 3.38. Temperature dependence of luminescence spectra in a InGaAs/InP MDQW with $n = 9.1 \times 10^{11}\,\mathrm{cm}^{-2}$. The dashed line in curve (d) is a lineshape fit without enhancement [3.3]

the lattice potential related to alloy disorder and interface roughness. Similar effects are observed in GaAs/AlGaAs heterostructures, when the holes (or the electrons in p-type doped samples [3.123]) are localized at the interfaces [3.124]. It was later pointed out by *Zhang* et al., that the localization of the hole has to lead to a positively charged center in order for the correlation effect to be observed [3.125]. Consequently, a FES is not present in the emission

spectra of Si MOSFETs or such MD GaAs/AlGaAs heterostructures, where the holes become localized at ionized acceptors resulting in neutral centers. The enhancement is also not observable in samples with a lack of sufficient localization of the holes, e.g., GaAs/AlGaAs undoped QWs or MDQWs with good structural quality.

Localization does not play a role in absorption processes (Fig. 3.35), because the holes are generated in the optical transition at wave vectors larger than the Fermi wave vector of the electrons. The FES is thus an intrinsic property of absorption processes and can be observed in transmission or photoluminescence excitation (PLE) spectroscopy. The enhancement leads to a peak in the spectra at $(1 + m_e/m_h)E_F$ which again disappears with rising temperature [3.117, 121, 124, 126, 127].

PLE spectra taken on a 9-nm GaAs/AlGaAs MQW, with the central 9 nm of each 35-nm thick barrier being Si-doped to a level of $n = 1.2 \times 10^{12}\,\mathrm{cm}^{-2}$, are shown in Fig. 3.39 [3.127]. The detection wavelength can be chosen close to the maximum of the luminescence signal (1.549 eV) due to a large Stokes shift of the latter with respect to the absorption edge. The PLE spectrum is independent of the detection wavelength for heavily doped MDQWs. Two steps related to the transitions to the $n_z = 1$ (at 1.6 eV) and $n_z = 2$ subband (at 1.7 eV) in the conduction band are observed. Strong excitonic enhancement of the absorption is found in both steps. The temperature dependence of the spectra, however, shows that the character of the enhancement mechanisms is different. The peak at the $n_z = 2$ step broadens only slightly with increasing temperature, as is typical for a band-edge exciton resonance [3.152]. In contrast, the $n_z = 1$ peak vanishes almost completely for increasing temperature. This behavior resembles the theoretically expected characteristics of the Fermi-edge singularity as described above.

It is possible to extract the enhancement factor by comparison of these experimental results to a simple model spectrum without correlation enhancement, which is given by $D_0(E)[1 - f_e(E)]$ where $D_0(E)$ is a step function starting at the bandgap energy E_g and $f_e(E)$ is the Fermi function of the electron gas. The temperature used in the Fermi function is adjusted to fit the slope of the experimental spectra at the Fermi level. The height of the plateau in the spectrum at 80 K is taken as the reference level for the step function for the following reason: The temperature dependence in Fig. 3.39 shows that the level of the first plateau decreases strongly when raising the temperature from 5 K to 20 K. This decrease, however, levels off around 60 K and disappears for further increase of T. This effect is much less pronounced in MDQW with lower doping and not found in undoped MQWS. In the latter case, i.e., in the limit of band-edge excitons, the relative height of the $n_z = 1$ and $n_z = 2$ steps is constant in this temperature regime. The relative decrease of the $n_z = 1$ plateau in the MDQW, when the PLE spectrum is normalized to the region above the $n_z = 2$ exciton, results from the reduction of the correlation at the Fermi edge. The remaining enhancement in the spectrum at

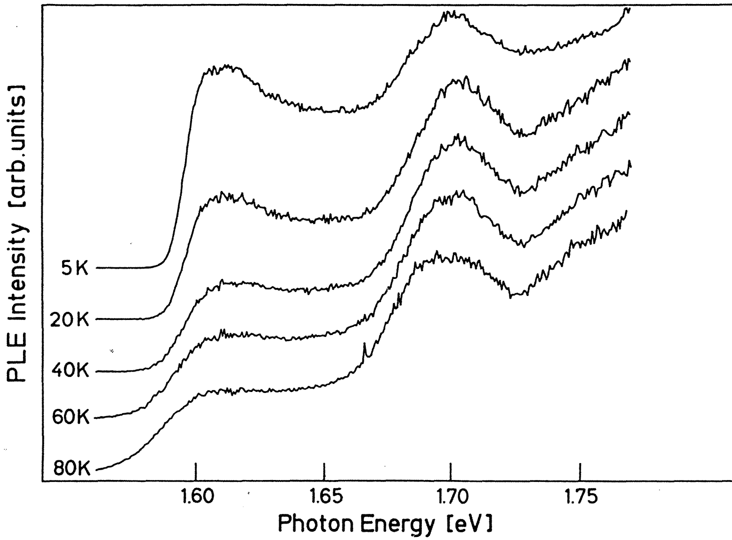

Fig. 3.39. Low-excitation PLE spectra in a heavily doped GaAs/AlGaAs MDQW as a function of lattice temperature. The curves are normalized to equal height above 1.72 eV [3.127]

$T = 80\,\mathrm{K}$ is negligible, which makes this spectrum suitable as a reference. The extracted enhancement factor is displayed in Fig. 3.40. A maximum enhancement factor of 2.4 is found at low temperature. The strong dependence of the enhancement on T, not only at its peak but also at the plateau, is evident.

At this point, a critical remark concerning some experiments and their comparison to the theoretical description of the FES is necessary. The complete disappearance of the FES peak is only observed at very high doping level. In n- and p-type samples with densities of $6 \times 10^{11}\,\mathrm{cm}^{-2}$ or less a significant enhancement remains up to room temperature. Due to the smooth

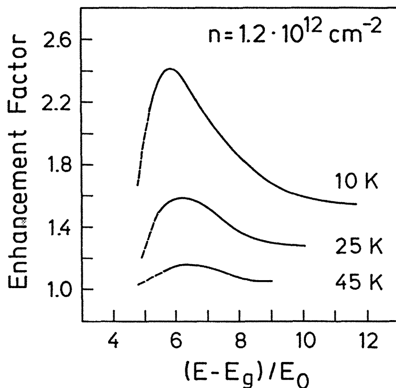

Fig. 3.40. Enhancement factor for low excitation density. The listed effective temperatures are extracted from the model (see text). An excitonic binding energy of $E_0 = 10\,\mathrm{meV}$ is assumed [3.127]

transition between the two extrema of the screening process [3.128], significant contributions with the character of the band-edge exciton are present in the spectra for MDQW with lower doping. This is also evident in [Ref. 3.117, Fig. 5]. Direct comparison of these experiments to calculations in the limit of the FES are therefore questionable.

Furthermore, experimental values of the enhancement factor are considerably smaller and the widths of the enhancement curves broader than expected from many-body calculations in the strict 2D limit as shown in Figs. 3.36, 37. A number of reasons for these discrepancies are dicussed in the literature, including various broadening mechanisms and the use of unrealistic QW parameters in the calculations. Some fundamentally different theoretical models are also proposed. We will summarize this discussion in the following.

The introduction of broadening parameters smoothes out the logarithmic singularity at the Fermi level. Such broadening is arbitrary and is introduced without physical justification in some calculations, just to manage the numerical integration [3.2, 117]. There are, on the other hand, several geniune broadening mechanisms in realistic QW structures. Most obvious is the inhomogeneous broadening and localization of the hole as a result of alloy disorder or interface fluctuations in the structures in which the FES is observed in emission. These effects were explicitly accounted for in the modelling of the luminescence spectra in InGaAs/InP MDQWs by a qualitative inhomogeneous broadening of the order of 5 meV as well as a finite localization radius r_{h} of 30 Å of the holes (Fig. 3.41) [3.3, 122]. The theoretical fit to the spectra, with relaxation of momentum conservation, reproduces the experimental results with some remaining discrepancies in the width of the enhancement peak.

A most efficient reduction of the enhancement factor results from the deviation from the strict 2D limit of the electron–hole Coulomb interaction. When one allows for the spread of the carrier wave function in the direction of the quantization, which was done in Ref. [3.129] by introducing a structural factor in the Coulomb potential, the discrepancy in the enhancement values is greatly reduced. But, still the agreement with the experiment (see Fig. 3.42, where the data of *Livescu* et al. [3.117] are used for comparison) is not yet satisfactory.

A calculated absorption spectrum in the so-called screened ladder approximation, which describes the multiple electron–hole scattering, is compared to an experimental PLE spectrum in Fig. 3.43. The theory treats k-conserving transitions between the $n_z = 1$ hh as well as lh subbands and the Fermi sea, includes potential form factors in the Coulomb attraction and in the screening, and uses a Gaussian broadening factor of 6 meV to describe homogeneous and inhomogeneous broadening. The calculations yield enhancement factors of the correct order of magnitude, but the enhancement at the lh transition appears to be overestimated. Possible reasons for the discrepancies are the simplified valence-band structure, neglecting crossing diagrams (i.e., shake-up

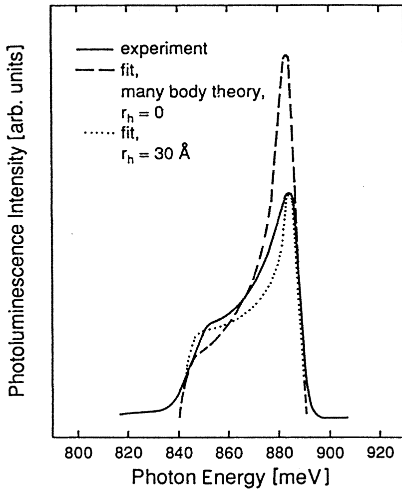

Fig. 3.41. Fit to the low temperature spectrum of Fig. 3.38 using different values for the localization radius r_h of the holes [3.3, 122]

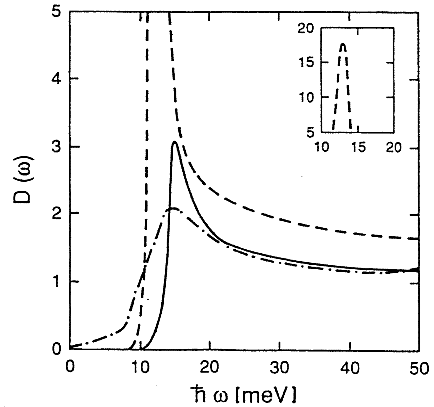

Fig. 3.42. Theoretical absorption spectra in the ideal 2D limit (dashed) and using realistic QW parameters (solid). An experimental spectrum from Ref. [3.117] (dashed-dotted) is shown for comparison [3.129]

processes in the Fermi sea) and possible influences of the relaxation mechanisms involved in the PLE measurements.

Evidence for the importance of homogeneous broadening and final-state damping on the FES is given by the following experiments. The enhancement at the Fermi edge in PLE spectra of GaAs/AlGaAs MDQWs can be suppressed completely when the density of photo-excited carriers is increased (Fig. 3.44) [3.127]. The absorption enhancement is already strongly affected for excitation densities which are two orders of magnitude less than the density of the electron gas (see spectrum for $9I_0$ in Fig. 3.44). In comparison to the lowest excitation (I_0), the number of electrons has not changed significantly so that effects related to increasing phase-space filling (cf. Fig. 3.37) are not significant. On the other hand, the number of holes has increased by almost one order of magnitude. The strong reduction of the enhancement is thus caused by a comparatively low density of photo-excited holes and can only be explained by the increasing damping related to hole–hole scattering.

Further broadening mechanisms are related to the ultra-fast relaxation of the electrons generated at some excess energy above the Fermi energy in the absorption process. Damping due to carrier–carrier scattering was shown to have a minimum right at the Fermi energy, but to rapidly increase for energies

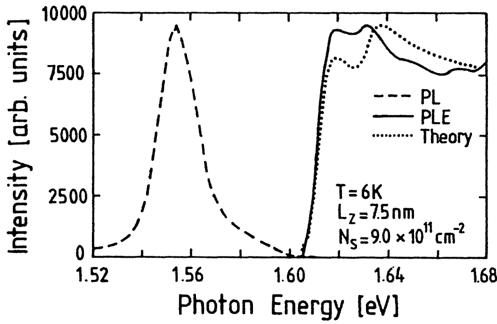

Fig. 3.43. Photoluminescence (PL) and PLE spectra of an n-type MD single QW at low temperature. Fermi-edge enhancement is observed at both $n_z = 1$ hh and lh transitions in PLE but absent in the PL spectrum. The theoretical absorption spectrum is shown for comparison [3.130]

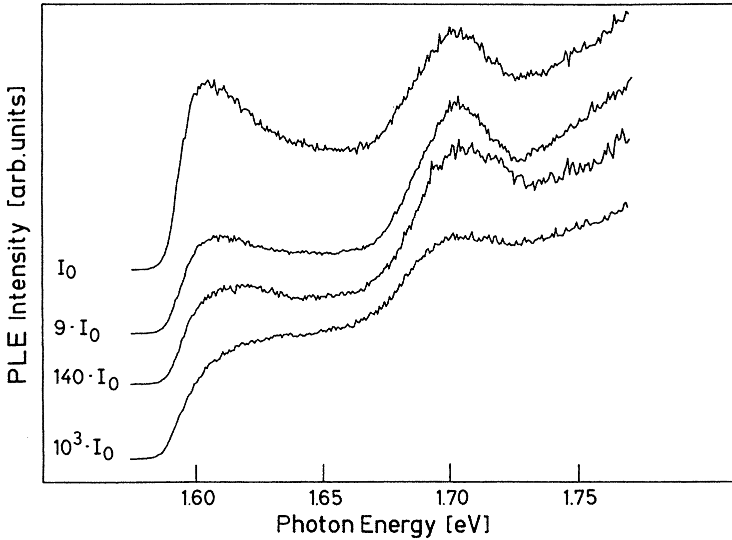

Fig. 3.44. PLE signal in a GaAs/AlGaAs MDQW with $n = 1.2 \times 10^{12}\,\mathrm{cm}^{-2}$ at various excitation levels ($10^3 I_0$ corresponds to a density of photo-excited carriers of $1.4 \times 10^{12}\,\mathrm{cm}^{-2}$). The curves are normalized, except for $10^3 I_0$ [3.127]

above E_F [3.75]. At low temperatures this interaction with the electron gas should occur on the timescale of some 100 fs and thus lead to a significant state broadening. This damping increases with rising temperature due to the increasing scattering possibilities within the electron gas. Thermalization of excess photo-excited carriers was found to be extremely fast (< 10 fs) in n-MDQW at room temperature [3.46].

The observed importance of damping might explain the failure to resolve the FES in the luminescence of undoped MQWS where the holes are not localized. These experiments are typically performed under conditions where the hole distribution is not yet degenerate. The carrier densities, however, are large enough for significant broadening of the hole states at k-vectors corresponding to the k-vector at the electron Fermi level. The effect of the FES is then, as shown above, suppressed.

Possible alternative mechanisms causing broadening of the singularity are based on the finite mass of the hole. The influence of the finite mass was qualitatively described in Ref. [3.128] and recently calculated explicitly in Ref. [3.131]. The finite valence-band dispersion causes the recoil of the hole and the thermal distribution of the hole states. Both effects reduce the strength of the FES, especially for emission spectra, because the thermal distribution of the holes is not operative in the absorption process.

Thus far, we have only described the effects within the picture of a rigid Fermi sea. A comprehensive interpretation of the spectral features found in 2D one-component plasmas is further complicated by dynamical effects within the plasma. Such effects are, for example, the shake-up of the Fermi sea and Auger-like indirect transitions. These dynamic processes result from the sudden appearance (or disappearance) of the hole in the electron Fermi sea. A possible reaction of the electron system is that the hole is scattered, simultaneously creating a pair excitation or a plasmon in the conduction band. Another electron recombines later with the scattered hole. A consequence of this dynamic response of the electron sea is the enhancement of the mixing between hh and lh valence bands [3.132, 134]. Further, dynamic processes lead to charge- and spin-density excitations counterbalancing the polarization of the suddenly created hole. The polarization of the hole then disappears faster than the polarization of the Fermi sea leading to polarization anomalies in the optical spectra [3.135]. Moreover, Auger-like indirect optical transitions may become possible, washing out the FES and leading to a low-energy tailing of the optical spectra [3.128, 135].

Concerning the theoretical description, it is extremely difficult to treat both consequences of the Coulomb interaction, namely the modifications of the electron and hole energies (self-energy effects) and the correlations between electrons and holes (vertex corrections) simultaneously in a quantitative way. Theoretical work is thus often qualitative or calculates only one of the two effects, band-gap renormalization or optical line shape [3.2, 128]. An attempt to include band-gap renormalization, screening, shake-up processes, and the finite hole mass in the description of the continuous transition from excitons to a Fermi-edge singularity as a function of electron density was recently presented by *Hawrylak* [3.136]. This work appears to reproduce the results for the case of localized holes in emission, but predicts two distinct peaks in absorption spectra related to the FES and to a single electron–hole pair in the environment of the Fermi sea. This feature is not observed in the

experimental spectra. Moreover, the FES is predicted to be absent in absorption spectra of GaAs MDQWs, in striking contrast to the above discussed experimental findings.

We will turn now to the influence of the presence of a Fermi sea of electrons on the optical properties at higher subband transitions. We have already stressed the weakness of intersubband screening in connection with the properties of an electron–hole plasma (previous section). Similar effects are found in the case of a one-component plasma in MDQWs, as is obvious in Figs. 3.39, 44. The excitonic enhancement at the second subband transition displays a dependence on temperature and carrier density as expected for a band-edge exciton. The dependence of the enhancements at both subband transitions on the density in the Fermi sea is shown in Fig. 3.45. The peak at the $n_z = 2$ step is remarkably little influenced by the increasing electron density. The enhancement at the fundamental edge, on the other hand, shows a significant reduction of the enhancement with increasing density. The feature at this step develops from a double structure related to the hh and lh subbands to a broad single peak reflecting the increasing mixing of the hh and lh valence bands for the increasing hole k-vectors involved in the absorption. It is interesting to note that the temperature sensitivity of the enhancement displays the previously discussed behavior of a transition from the pure FES to excitons strongly dressed with excitations in the Fermi sea [3.128, 135].

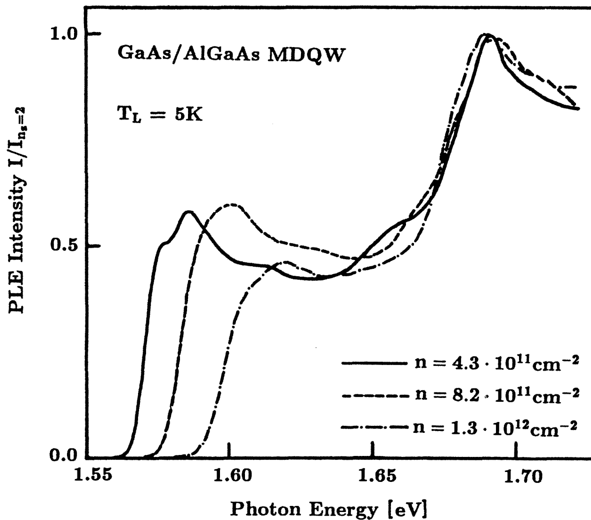

Fig. 3.45. PLE spectra of an n-type MDQWs at low temperature for three different electron densities. Strong modifications of the Fermi-edge enhancement are observed at the lowest subband transition while the exciton peak at the second subband is nearly unchanged

The enhancement disappears completely at 60 K for the highest electron density, while a significant enhancement persists up to temperatures higher than 130 K for the lowest density, reflecting the remnants of the character of the band-edge exciton.

Another class of heterostructures that are well suited for the study of effects at higher subband edges are asymmetric or single-side modulation-doped QWs. The asymmetric doping profile leads to strong band-bending effects as shown in Fig. 3.46. The holes are, to some extent, spatially separated from the electrons, which reduces the luminescence efficiency of the E_{11} transition. A most interesting effect is the possibility to extrinsically control the carrier density in the electron sea by photo-excitation or by application of an electric field, e.g., in a field-effect transistor arrangement. In such a way, the continuous transition from excitonic properties to spectral features related to the electron plasma can be studied, reflecting the above described reormalization and screening effects for the first and second electronic subband [3.138, 139].

The resonance of the electron Fermi energy with the second electron subband in asymmetric MDQWs leads to some interesting screening and enhancement phenomena. The description of these effects is much more complex than for symmetrical MDQWs. The reasons are mainly the spatial separation of the $n_z = 1$ electrons and holes, which affects their Coulomb interaction, and the density-dependent band bending, which again influences the charge separation. The latter effect is decribed in the calculations of the E_{21} exciton binding energy in the presence of the $n_z = 1$ electron sea in Ref. [3.140]. The binding energy is first continuously lowered by screening with increas-

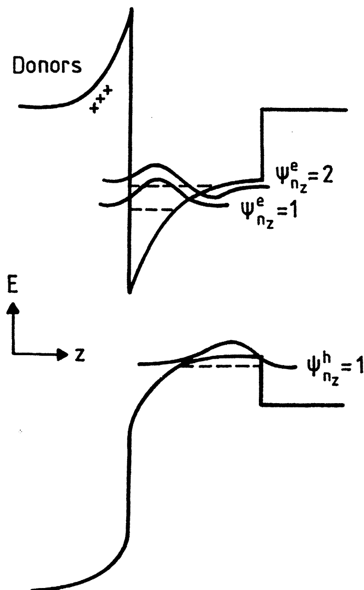

Fig. 3.46. Schematic diagram of doping profile, the band energies, and the electron and hole wave functions in asymmetrical n-type MDQWs

ing $n_z = 1$ electron density. This behavior, however, displays a turning point when the increasing band bending separates the $n_z = 1$ electrons and the E_{21} exciton such that the effect of screening on the binding energy is reversed.

A strong enhancement of the oscillator strength for transitions involving electrons at the Fermi energy is found experimentally, in accord with theoretical predictions when E_F is just below resonance with the E_{21} exciton [3.141, 143]. The reason is as follows: the $n_z = 1$ electrons at the Fermi level have only weak correlation effects with photo-excited $n_z = 1$ holes relaxed to the top of the hole subband owing to the small spatial overlap of their wave functions (Fig. 3.46) and the large k-vector difference. When the electrons are able to interact with the $n_z = 2$ electron states via multiple Coulomb scattering, the overlap increases drastically and the electrons now have $k \approx 0$. The result is a peak in the luminescence spectra below the E_{21} exciton which strongly increases when E_F approaches the $n_z = 2$ electron level (Fig. 3.47). This feature is only observed in a very narrow density range where E_F is not too far below and not above the $n_z = 2$ states. This correlation enhancement peak displays the typical sensitivity to temperature increase as is shown in Fig. 3.48 [3.141]. These features are qualitatively described by theories treating the dynamic response (shake-up processes) of the Fermi sea [3.142, 143]. When the electron Fermi level lies well within the $n_z = 2$ electron subband, a FES is observed in photoluminescence excitation spectra at the E_{21} transition (Fig. 3.49) [3.144]. The temperature dependence of the E_{21} peak as well as the higher energy exciton peak now display the expected different behavior. On the other hand, typical FES behavior is not found when the $n_z = 2$ subband is only slightly populated. *Skolnick* et al. [3.144] conclude from this finding that the correlation of the $n_z = 2$ electrons with the holes is not significantly influenced by the presence of the $n_z = 1$ electrons. For even higher population of the second subband, the Fermi-edge singularity is again observed in luminescence due to relaxed momentum conservation resulting

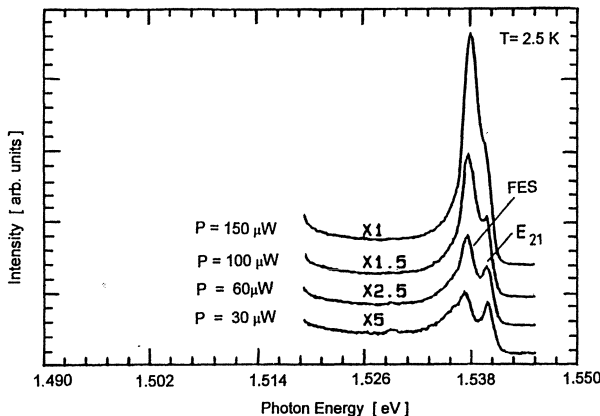

Fig. 3.47. Photoluminescence spectra from an asymmetrical n-type MDQW in the region of the $n_z = 2$ electron to $n_z = 1$ heavy-hole transition showing the FES and its dependence on optical excitation level, as well as the E_{21} exciton [3.141]

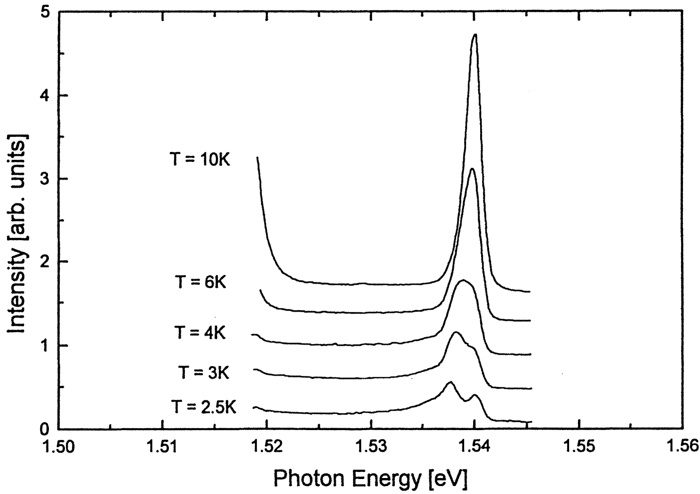

Fig. 3.48. Temperature dependence of the PL spectrum showing the quenching of the FES emission and the buildup of the E_{21} exciton from thermal excitation of electrons into the $n_z = 2$ subband [3.141]

from a weak hole localization at the hetero-interface opposite the electron gas region [3.145].

We finally want to address in this section the properties of center-doped (also called *anti-modulation doped*) quantum wells. The dopant atoms in these structures are situated in the central region of the quantum well, sometimes in the form of δ doping [3.119, 123, 146]. This type of doping introduces a strong groove-like distortion of the potential in the well center which can even introduce new quantized levels for the electrons (or holes). Additional strong band bending is observed when the excess carriers become spatially separated from the dopant ions, for example, by transfer to unsaturated states at the sample surface. The optical properties in the latter case are governed by capture of the photo-generated excitons by the ionized impurities on a 100-ps timescale [3.119].

Center-doped QWs undergo a transition to metallic behavior with increasing doping density similar to MDQWs [3.147]. This Mott transition occurs in n-type center-doped QWs at an electron sheet density of $10^{12}\,\text{cm}^{-2}$ which is significantly higher than in the MDQW case (here $n = 4 \times 10^{11}\,\text{cm}^{-2}$). The reasons are the presence of an additional density of states related to the donors and a further reduction of screening due to localization of the excitons resulting from the impurity-induced potential fluctuations. A breakdown of momentum conservation for optical transitions is observed in photoluminescence from center-doped QWs in the degenerate limit, in contrast to the MDQW case.

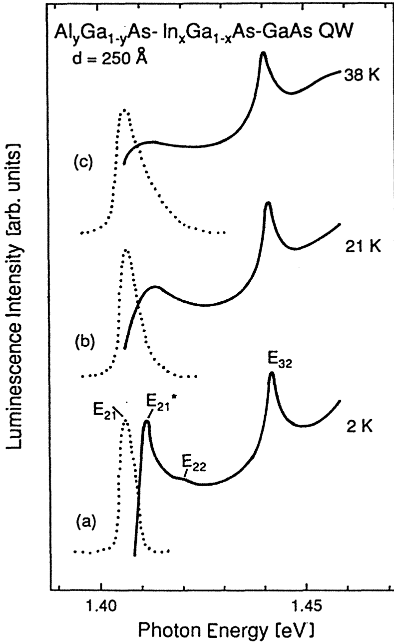

Fig. 3.49. Temperature dependence of PL (dotted) and PLE (solid line) spectra in an InGaAs asymmetrical n-type MDQW. The presence of $1 \times 10^{11}\,\mathrm{cm}^{-2}$ electrons in the $n_z = 2$ electron subband gives rise to a FES-type behavior at the E_{21} PLE peak [3.144]

The behavior of the center-doped structures can also be contrasted to that of doped bulk material. The exciton in bulk GaAs is already screened at a donor-doping level of a few $10^{16}\,\mathrm{cm}^{-3}$ far below the metallic limit of about $5 \times 10^{17}\,\mathrm{cm}^{-3}$ [3.148]. The optical transitions in center-doped structures are excitonic right up to the metallic limit and, in the case of higher subband transitions, even far above the Mott transition [3.147]. This result of reduced screening in the low-dimensional case is here related to both the increased exciton binding energy and the stronger binding to the impurity in comparison to the bulk values. The enhancement of the donor binding energy by a factor of 2 in the QW is also responsible for the 2–3 times higher equivalent doping concentration necessary to reach the metallic limit. The higher binding energy means that the donor band created at higher doping levels is broader in the 2D case and sustains more donor electrons until the distribution merges with the conduction band.

Correlation effects are observed in the optical spectra of center-doped QWs [3.123, 149]. The description of these effects, however, turns out to be far more complicated than in MDQWs due to the presence of the fixed array of charges related to the ionized impurities. In the following we will qualitatively discuss the role of dynamic interactions between free electrons (intrinsic and photo-excited), photo-excited holes, and fixed positively charged ionized donors in the case of an n-type center-doped QW. The role of the fixed charges is especially important in such samples due to a reduction of the degenerate

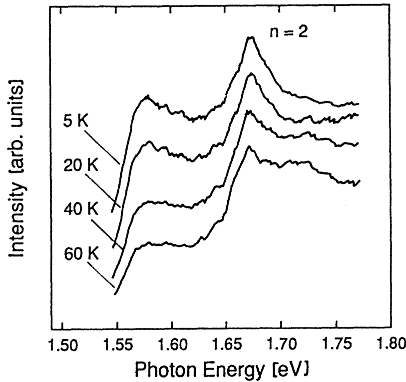

Fig. 3.50. Photoluminescence excitation spectra from an n-type center-doped QW showing a correlation enhancement and its typical dependence on temperature [3.149]

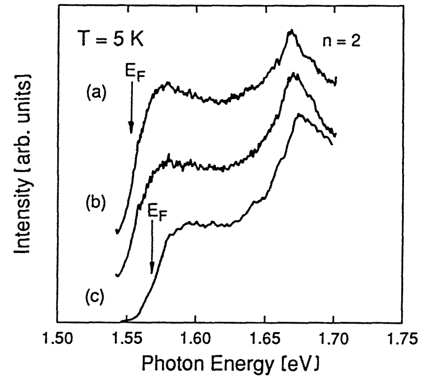

Fig. 3.51. Photoluminescence excitation spectra from an n-type center-doped QW as a function of excitation level of the exciting laser: (a) low excitation, (b) high excitation, and (c) with additional excitation at 2.41 eV [3.149]

electron density via transfer to states at the sample surface leaving an excess of positive charges in the well.

Photoluminescence excitation spectra taken at the low-energy side of the broad luminescence band display features very similar to those of the one-component plasma in MDQWs [3.149]: an excitonic peak is found at the $n_z = 2$ transition while an enhancement similar to the FES dominates the $n_z = 1$ transition. This enhancement is gradually quenched as a function of both temperature (Fig. 3.50) and density of carriers (Fig. 3.51) in the well. The density can be altered via the intensity of the excitation laser or via additional deposition of electrons in the well by a second excitation source at high photon energies. The latter process creates electron–hole pairs; the holes have enough excess energy to move to the surface or to the substrate while the electrons are collected in the well. These additional electrons effectively neutralize a portion of the ionized donors.

The findings described above indicate that correlation effects are present in the center-doped sample. The picture of correlation between the Fermi sea of electrons and the photo-excited hole, however, cannot alone explain the experimental results. The enhancement is only observed for a detection wavelength at the low-energy tail of the luminescence, i.e., when probing the recombination of largely localized holes with electrons. This localization process is reflected in picosecond time-resolved luminescence studies as a continuous red shift of the luminescence band resulting from a hopping relaxation

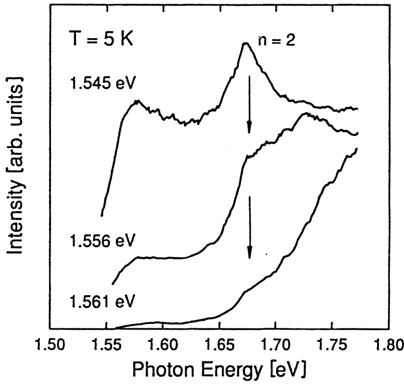

Fig. 3.52. PLE spectra of an n-type center-doped QW for different detection wavelengths [3.149]

of the holes. This localization process, on the other hand, is strongly dependent on the band bending in the well. The latter is efficiently reduced when further electrons, which compensate the excess positive charge, are deposited via pair generation with high photon energy. Probing the luminescence in the PLE experiment on the high-energy side of the luminescence band means probing the recombination of free carriers. Free holes are mainly created for the case of flat-band conditions. The PLE spectrum (Fig. 3.52) changes accordingly: reduction of the band-bending is only achieved for excitation at high photon energies.

These experiments demonstrate that the description of center-doped QWs is rather complex. Further experimental and theoretical work is required to achieve a detailed understanding of the interconnected processes of screening, band bending, localization and radiative transitions.

To summarize this section, one can state that one-component plasmas represent a most interesting system for studying many-body effects in optical experiments. In particular, the correlation of a whole Fermi sea of one carrier type with a single carrier of opposite charge shows up as a pronounced effect. The most elegant way to obtain such one-component plasmas without disturbing the background of fixed charges is the system of modulation-doped heterostructures.

3.5 Electron–Hole Droplet Formation

The condensation of an electron–hole system below a critical temperature, T_c, into a liquid state in equilibrium with an excitonic gas is well established in the indirect-gap semiconductors Si and Ge [3.6, 18]. Growth of *electron–hole droplets* up to macroscopic size is observed as a consequence of extremely long carrier lifetimes in these materials [3.153]. In contrast, carrier lifetimes are too short to allow an equilibrium phase separation in direct-gap semiconductors such as GaAs or CdS [3.154, 155]. Here, experimental results are

consistently described by a nonequilibrium dynamics of small electron–hole clusters [3.154].

In this context the semiconductor alloy $Al_xGa_{1-x}As$ with an indirect fundamental gap represents an intermediate situation. This material provides a large density of states for optically excited electrons [3.166] just as in Si. The transition probability for indirect electron–hole recombination in $Al_xGa_{1-x}As$ close to the crossover point, however, is greatly enhanced with respect to Si or Ge. These indirect transitions proceed via virtual states at the Γ point, which are nearly resonant with the initial states at the X point (Sects. 2.3 and 4.1.2) [3.67]. This results in a lifetime of electron–hole pairs in the nanosecond regime [3.64], which is more comparable to the situation in GaAs. But droplet condensation still occurs in indirect-gap $Al_xGa_{1-x}As$. The nucleation dynamics, however, is two orders of magnitude faster than in Si as a consequence of disorder-induced potential fluctuations [3.22].

The stability of the electron–hole-liquid phase in low-dimensional semiconductor structures has been proposed, for example, for the case of GaAs quantum wells with large well width [3.156], type-II GaAs superlattices [3.157], or Ge/Ge_xSi_{1-x} quantum wells [3.156]. Although a low-dimensional liquid should be more stable than a three-dimensional one [3.158], the only conclusive experimental evidence for the existence of such a liquid phase has been given up to now by *Kalt* et al. [3.11] for the case of a type-II QWW SL (see also Sect. 2.5). The separation of the electrons and holes in this system in different wires and the indirect nature of the recombination in k-space result in a sufficiently long pair lifetime, while the enhanced surface area and thus the considerable amount of disorder accelerate the droplet growth.

The properties of the electron–hole system can be illustrated by a schematic picture of its phase diagram (Fig. 3.53). The excitonic gas exists at low pair densities and undergoes a Mott transition to the plasma phase with increasing density. At temperatures below a critical temperature, T_c, the excitonic gas and the liquid plasma phase represent the low and high density limits, respectively. A coexistence region is found for intermediate densities. Here, the gas and liquid phases separate such that electron–hole droplets are

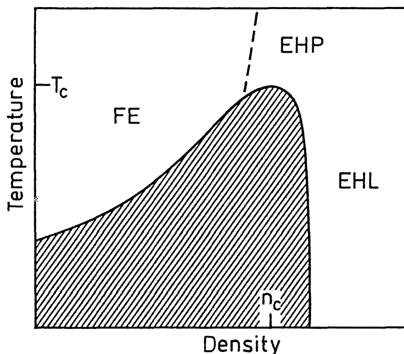

Fig. 3.53. Schematic phase diagram of the electron–hole system in a highly excited semiconductor. FX: free-exciton gas; EHP: plasma phase; EHL: liquid phase; slanted area: coexistence region

surrounded by the gas of excitons (and a minor contribution of free carriers stemming from ionized excitons at finite temperatures).

Accordingly, the presence of a liquid phase in a highly excited semiconductor can be demonstrated in a photoluminescence experiment by verification of some of the following five characteristic criteria: (1) High-density droplets exist simultaneously with a surrounding low-density excitonic gas. The excitonic emission line under these high excitation conditions is unshifted with respect to the low excitation case [3.156]. (2) The detection of a luminescence band extending between the renormalized band gap E'_g and the chemical potential μ of the electron–hole system. This emission line has to be situated entirely below the exciton energy reflecting the stability or binding energy of the liquid phase with respect to the excitonic gas [3.156]. (3) For a constant carrier temperature, the pair density within the electron–hole droplets (EHDs) should be independent of the laser power within a certain excitation range [3.156]. (4) An increase of the density in the EHDs with decreasing temperature is expected from the theoretical phase diagram below a critical temperature T_c [3.6, 3.18]. (5) A homogeneous electron–hole-plasma (EHP) phase, which shows the opposite density versus temperature behavior, should be observed at temperatures above T_c [3.6, 18]. We will demonstrate in the following that these criteria are fulfilled for both $Al_xGa_{1-x}As$ and the QWW SL, providing evidence for the formation of EHDs in these indirect-gap substances close to their crossover points.

3.5.1 Picosecond Electron–Hole Droplet Formation in Indirect-Gap $Al_xGa_{1-x}As$

Droplet formation in $Al_xGa_{1-x}As$ is verified by photoluminescence studies on a picosecond timescale [3.22]. The samples are excited by pulses (5 ps FWHM) from a tunable, synchronously pumped dye laser using Rhodamine 6G as the gain medium. The luminescence signal is spectrally and temporally resolved by a combination of a 0.32-m spectrometer and a streak camera with a two-dimensional readout. The temporal resolution of the system is limited by trigger jitter to about 10 ps.

A variety of $Al_xGa_{1-x}As$ samples close to the crossover from a direct-gap to an indirect-gap semiconductor either due to their composition or due to hydrostatic pressure are compared to GaAs, which has an indirect-gap when subjected to high pressure. The latter sample is a thin GaAs layer (0.6 μm thick) grown between two 7 μm thick $Al_{.30}Ga_{.70}As$ barrier layers. The GaAs substrate was completely removed to eliminate the luminescence from the substrate. The sample is an indirect-gap semiconductor for hydrostatic pressures in excess of 42 kbar [3.167]. This choice of sample provides the possibility to simulate the same constellation of Γ and X minima in the

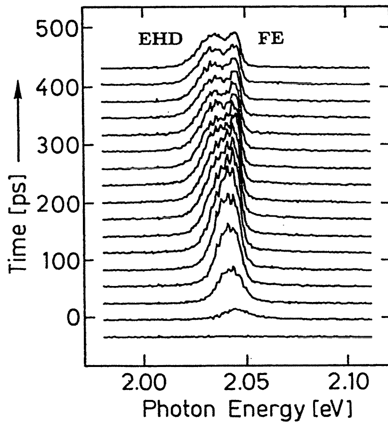

Fig. 3.54. Temporal development of the luminescence signal in $Al_{.38}Ga_{.62}As$ at a hydrostatic pressure of $P = 6.9$ kbar and for excitation with $2.2\,\mu J/cm^2$ [3.22]

conduction band at different levels of alloy disorder in order to demonstrate the importance of disorder in the nucleation process.

The temporal evolution of the luminescence spectra reflects the dynamic phase separation into the excitonic gas and droplet phases on a picosecond timescale. The luminescence splits progressively into two lines (Fig. 3.54). The narrow line at higher photon energies coincides with the free exciton at the indirect gap observed in time-averaged luminescence at very low excitation; cf. citerium (1). The broad line at lower photon energies shows some red shift with time, but is nearly constant in line shape for times longer than 200 ps. This emission stems from the recombination in the condensed electron–hole droplets. The red shift results from surface effects accompanying droplet growth as will be discussed below.

First, unambiguous evidence of droplet condensation is given by the construction of part of the phase diagram using experimental plasma parameters extracted from line-shape analysis of the time-resolved luminescence spectra at long delay times. A fit to the droplet line is performed analogously to the case of plasma emission discussed in Sect. 3.2.1. The exciton line shape is modelled, again neglecting homogeneous and inhomogeneous broadening, by [3.18]:

$$I(\hbar\omega) \propto (\hbar\omega - E_{FE})^{1/2} \exp\left(-\frac{\hbar\omega - E_{FE}}{k_B T}\right) . \tag{3.23}$$

Only zero-phonon recombination is taken into account. Phonon side bands only play a role for larger separations of Γ and X minima, i.e., for higher pressures or x values, respectively [3.159]. The fit parameters are the renormalized indirect band gap E'_g, the pair density n, the energy of the free exciton E_{FE}, and the common temperature T for the excitons and the plasma.

A typical result of this procedure is shown in Fig. 3.55 (see also Fig. 4.15 for a fit including side bands). The experimental line shape is well reproduced by the model. Some minor mismatch remains at the low energy sides of the

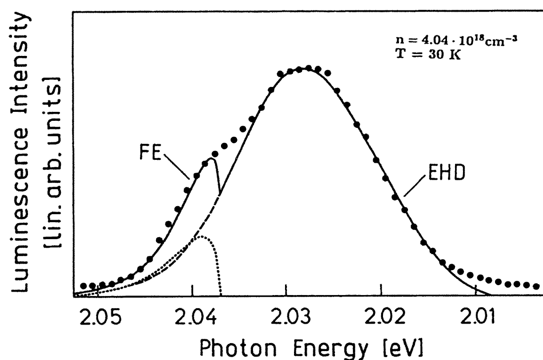

Fig. 3.55. Fit (solid line) to a photoluminescence spectrum (dots) at a time delay of 360 ps after excitation with $16\,\mu J/cm^2$. Dashed line: electron–hole droplet; dotted line: free exciton. The fit parameters are $n = 4 \times 10^{18}\,cm^{-3}$ and $T = 30\,K$ [3.22]

exciton and plasma line shape. Resonant excitation of the exciton at low fluence shows that part of the tail in the exciton line results from localized excitons (Sect. 2.3). Additional contributions might stem from recombination accompanied by inelastic scattering. No broadening due to final-state damping accompanied by plasmon excitation [3.6, 18] is included in the plasma line shape. But in the case of indirect recombination, these mechanisms are expected to change the fit parameters only slightly.

We find from the line-shape fits that the plasma parameters for long delay times do not directly depend on the excitation density in the range between 1 and $16\,\mu J/cm^2$ thus fulfilling criterium (3). The only consequence of the increased excitation level is that the carrier temperature is slightly higher. The carrier density for $t > 200$ ps is always in the range of $3\text{–}4 \times 10^{18}\,cm^{-3}$ although the excitation fluence is varied by a factor of 16. The dependence of the carrier density on the carrier temperature for these conditions is shown in Fig. 3.56 (crosses). The n-T diagram shows exactly the signature of an electron–hole liquid phase diagram (cf. Fig. 3.53), i.e., the density decreases with rising temperature [criterium (4)]. This is definite evidence for the condensation into electron–hole droplets.

A first experimental phase diagram is given by simply connecting the experimental points (dashed line in Fig. 3.56). It is clear that more data, especially for stationary excitation conditions, are necessary to complete this diagram. It is possible, however, to get reasonable estimates of the liquid parameters. The critical temperature T_c is estimated to be 34 K, the critical density n_c and the ground-state density n_0 are about $2 \times 10^{18}\,cm^{-3}$ and $4.5 \times 10^{18}\,cm^{-3}$, respectively. The binding energy of the liquid E_{bind}, which is determined by the difference between the chemical potential of the liquid at

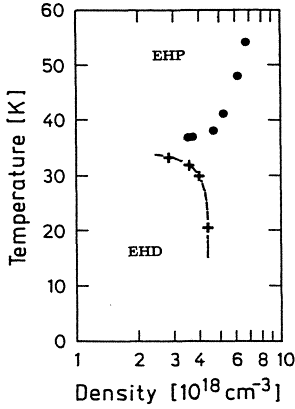

Fig. 3.56. Temperature–density diagram for $Al_{.38}Ga_{.62}As$ ($P = 6.9$ kbar). Dashed line: proposed phase diagram (see text) [3.22]

$T = 0$ K and the energy of the free exciton, is found to be 6(±2) meV. These liquid parameters are similar to those found for Si [3.6].

The plasma density and temperature for the case of excitation with a maximum fluence of $F_{\text{max}} = 64\,\mu\text{J/cm}^2$ is represented by the dots in Fig. 3.56. The carrier temperature stays above T_c here for times up to 500 ps. The carrier density increases with temperature for this excitation level. We will discuss the properties of the electron–hole plasma above the critical parameters in more detail below.

First, we want to describe a model to estimate the theoretically expected parameters of the electron–hole liquid. Only the band-structure and exciton parameters of the material under investigation are required in this model. The many-body effects are treated by a simple approximation.

We first determine the equilibrium density n_0 and the binding energy E_{bind} of the liquid phase. We start with a calculation of the ground-state energy E_G at $T = 0$ K from [3.6]:

$$E_G = \bar{E}_{\text{kin}} + E_{\text{xc}} \,. \tag{3.24}$$

The average kinetic energy $\bar{E}_{\text{kin}}$ is determined for a given carrier density n by the Fermi energies $E_F^{e,h}$ of electrons and holes:

$$\bar{E}_{\text{kin}}(n) = \frac{3}{5}[E_F^e(n) + E_F^h(n)] \,. \tag{3.25}$$

We use the band parameters (Table 5.1) of $Al_{.45}Ga_{.55}As$ for the calculation of the density-of-states masses needed in (3.25). The exchange-correlation energy E_{xc}, which describes the self-energy corrections due to many-body effects in the electron–hole system, is approximated in units of the excitonic Rydberg state, Ry^*, by the universal formula (3.14, 17). The minimum of the ground-state energy as a function of r_s defines the ground-state density n_0 and the liquid binding energy E_{bind}.

The critical parameters of the liquid phase are determined from a calculation of a set of isotherms of the chemical potential μ as a function of pair density n:

$$\mu(n,T) = E'_{\mathrm{g}}(n) + E^{\mathrm{e}}_{\mathrm{F}}(n,T) + E^{\mathrm{h}}_{\mathrm{F}}(n,T) \ . \qquad (3.26)$$

We again use E_{xc} from the universal formula (3.14, 17) to calculate the renormalized bandgap E'_{g} in (3.26):

$$E'_{\mathrm{g}} = E_{\mathrm{g}} + \Delta E_{\mathrm{g}} = E_{\mathrm{g}} + n\frac{\partial}{\partial n}E_{\mathrm{xc}} + E_{\mathrm{xc}} \ . \qquad (3.27)$$

It was shown in Sect. 3.2 that this method is valid in indirect-gap $Al_xGa_{1-x}As$. The critical temperature T_{c} is then given by the isotherm of the chemical potential μ, the derivative of which is zero at the turning point. Finally, the critical density n_{c} is calculated from the scaling law $n_{\mathrm{c}}/n_0 = 0.34$ [3.160].

The experimental and calculated parameters are summarized in Table 3.1. The data are in reasonable agreement, although we used a rather crude approximation for the many-body effects. This agreement strongly supports the interpretation of the experimental data in terms of a fast droplet formation.

Now we want to focus on the dynamics of the droplet formation and the phase separation. The experimental phase diagram of indirect-gap $Al_xGa_{1-x}As$ close to the crossover point is found to be very similar to that of Si. This is expected considering the similarity of the exciton parameters in the two materials. The formation of electron–hole droplets in Si was measured to occur on a time scale of 50 ns [3.161]. The nucleation dynamics in $Al_xGa_{1-x}As$ is obviously much faster, illustrating some distinct differences between an elemental and an alloy semiconductor.

The onset of the droplet luminescence (Fig. 3.57) in $Al_xGa_{1-x}As$ depends on the excitation fluence and the density of initially excited carriers. The onset time is faster for excitation at F_{med}, which corresponds to an initial carrier density n_{in} of $5 \times 10^{17}\,\mathrm{cm}^{-3}$, than for F_{low} ($n_{\mathrm{in}} = 7 \times 10^{16}\,\mathrm{cm}^{-3}$). The initial densities are estimated from the absorption coefficient. The luminescence decay, however, is exactly equal for both excitation densities. This demonstrates that stable droplets have formed within about 150 ps.

The rather fast dynamics of the droplet formation indicates that the condensation in indirect-gap $Al_xGa_{1-x}As$ occurs from the plasma phase, in contrast to Si where free excitons are formed first. The free excitons in Si first cluster into multi-exciton complexes and eventually form droplet embryos which

Table 3.1. Electron–hole liquid parameters in $Al_xGa_{1-x}As$

	n_0 [cm^{-3}]	E_{bind} [meV]	n_{c} [cm^{-3}]	T_{c} [K]
Theory	3×10^{18}	9.6	1×10^{18}	25
Experiment	4.5×10^{18}	6(±2)	2×10^{18}	34(±2)

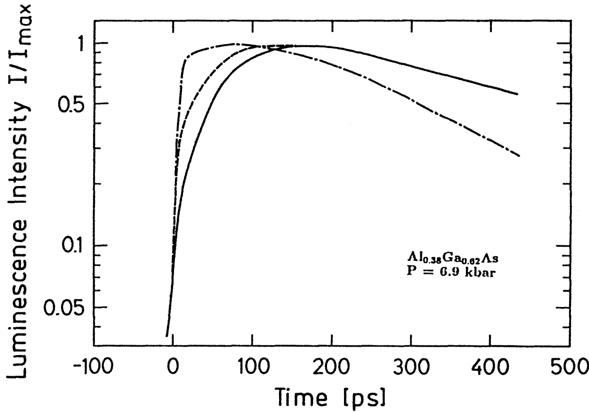

Fig. 3.57. Time dependence of the spectrally integrated electron–hole luminescence for various excitation levels. Solid line: F_{low}; dashed line: F_{med}; dashed-dotted line: $F_{\max}$ [3.22]

grow to macroscopic size [3.153]. No multi-exciton lines, only free-exciton and bimolecular recombination in the liquid, are observed in $\mathrm{Al}_x\mathrm{Ga}_{1-x}\mathrm{As}$.

Many tiny droplets thus appear to nucleate in the alloy semiconductor. An equilibrium with the simultaneously forming excitonic gas phase can only be reached once the droplets have grown big enough, i.e., when the droplet surface is large enough for an efficient exchange of excitons through it. Consequently, the droplets are not necessarily in equilibrium with the exciton gas surrounding them. Equilibrium implies a common temperature for excitons and droplets, i.e., a fit to the overall luminescence line shape is possible with a common temperature as described above. This is not the case, however, for low excitation levels and short delay times after the excitation pulse. Here, it is only possible to fit the line shape of the two entities separately. The temperature of the exciton gas is always found to be lower than the temperature of the liquid. A common temperature for both subsystems is reached at about 200 ps for F_{med} and 360 ps for F_{low}. No equilibrium is reached, however, for even lower excitation at 1 $\mu\mathrm{J/cm}^2$ within 1 ns. The attainment of equilibrium phase separation depends, as expected, on the initially excited carrier density, i.e., on the size of the droplets.

A large number of tiny droplets implies, of course, that a huge number of condensation seeds is available. These condensation seeds are inherently provided in $\mathrm{Al}_x\mathrm{Ga}_{1-x}\mathrm{As}$ by the random potential fluctuations due to alloy disorder [3.89, 162]. We prove this point by studying the nucleation dynamics in different samples. We find that the dynamics of droplet formation is even faster in samples with slightly higher disorder (e.g., about 120 ps in $\mathrm{Al}_{.42}\mathrm{Ga}_{.58}\mathrm{As}$). No droplet formation at all, however, is observed in GaAs which is indirect due to application of hydrostatic pressure. In the latter case the pair luminescence for all excitation levels is consistent with an electron–hole plasma phase, i.e., the density increases with temperature. No disorder is present in this sample of course. The velocity of nucleation thus scales with the amount of alloy disorder in the material, which immediately explains the differences between Si and $\mathrm{Al}_x\mathrm{Ga}_{1-x}\mathrm{As}$.

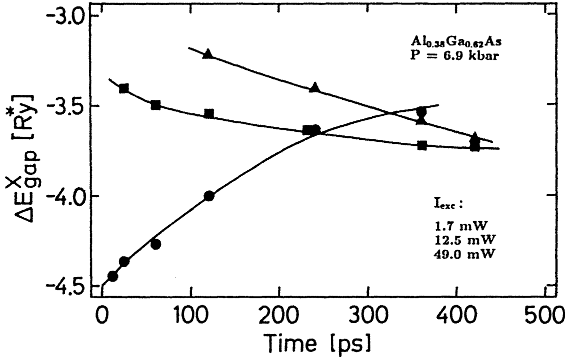

Fig. 3.58. Temporal development of the renormalization $\Delta E^X_{\rm gap}$ of the indirect gap in units of the excitonic Rydberg state (11 meV) for various excitation levels. Triangles: $F_{\rm low}$; squares: $F_{\rm med}$; dots: $F_{\rm max}$. The solid lines are merely to guide the eye [3.22]

The band-gap renormalization for the case of a fog of small droplets is most interesting. The dynamics of the band-gap renormalization $\Delta E^X_{\rm gap}$ for the electron–hole system below and above the critical parameters is illustrated in Fig. 3.58. We observe a renormalization increasing with time in the case of condensation to electron–hole droplets ($F_{\rm low}$ and $F_{\rm med}$). Two processes can contribute to the band-gap narrowing: first, the carrier density in the droplets increases as a result of carrier cooling by emission of acoustic phonons. Second, the average surface energy per carrier decreases when the droplets grow in size [3.154].

We want to illustrate the magnitude of both effects for the example of medium excitation. The pair density in the droplets for $t = 120\,$ps and $t = 360\,$ps is 3.86×10^{18} and $4.04 \times 10^{18}\,{\rm cm}^{-3}$, respectively. The theoretical renormalizations are calculated according to (3.14, 17) to be 43 meV and 44 meV. The experimental values (39 ± 2 and $42\pm2\,$meV), which are extracted from the line-shape fits, are only slightly smaller than those theoretically predicted and show the same tendency to increase.

The contribution of the surface energy to the renormalization is calculated from [3.154]:

$$\Delta E_{\rm g} = \frac{2}{3}\, 4\pi\, R_N^2\, \frac{\sigma}{N}\ . \tag{3.28}$$

Here, N is the number of electron–hole pairs in the droplets, σ is the surface tension, and R_N is the radius of the droplets given by:

$$R_N = \left(\frac{3}{4\pi}\frac{N}{n_0}\right)^{1/3}\ . \tag{3.29}$$

To our knowledge, no many-body calculation is available for the value of the surface tension in $Al_xGa_{1-x}As$. We thus assume $\sigma = 10^{-2}\,{\rm erg/cm^2}$, which cor-

responds to the magnitude of the surface tension in Si [3.153]. This assumption is reasonable, because optical masses and the static dielectric constant are very similar in both materials. The resulting contribution to the renormalization is only significant for rather small droplets, e.g., $\Delta E_g = 2\,\text{meV}$ for $N = 6$ and $\Delta E_g = 1\,\text{meV}$ for $N = 50$. The droplet dynamics, which was discussed in the previous section, indicates that small droplets are dominant in the materials under consideration.

We conclude from these calculations that both the increasing density and reduction of surface energy are of the correct magnitude and can contribute to the experimentally observed temporal shift of the band gap (Fig. 3.58). The method of luminescence line-shape analysis, however, is limited to an accuracy of about ± 2 meV for the determination of the experimental band gap. Therefore, we are not able to explicitly separate the two contributions.

The temporal development of the band-gap renormalization for the case of high excitation level shows a completely different behavior to that just discussed: the band gap increases with time. The experimental values of the renormalized band gap are in excellent agreement with (3.14, 17), as is demonstrated in Fig. 3.59. We will discuss some properties of this electron–hole plasma phase above the critical parameters in the following.

We have already demonstrated that the properties of the electron–hole system for excitation with $F_{\max}$ correspond to the expected behavior of a plasma phase above the critical parameters. The signatures of this phase are in many respects different from the liquid. Both temperature and density decrease with time (dots in Fig. 3.56) causing a shift of the band gap to higher energies (Figs. 3.58, 59).

The determination of the chemical potential of the plasma shows that the plasma phase in indirect-gap $Al_xGa_{1-x}As$ is still bound with respect to the free exciton. The binding energy of the plasma increases with time (Fig. 3.60) and approaches the binding energy determined for the liquid phase (6 meV). Consequently, this plasma phase is self-confined, i.e., it does not expand. A phase transition to a liquid state is not possible, however, because the carrier

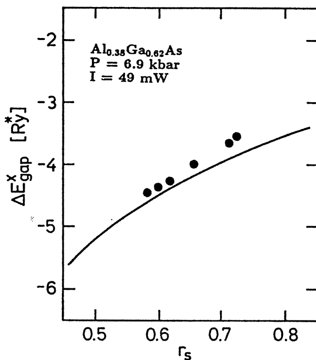

Fig. 3.59. Band-gap renormalization for excitation with $F_{\max}$. The dots are the experimental values determined from fits to spectra at various delay times after excitation (cf. dots in Fig. 3.58). The solid line is the theoretical band-gap narrowing according to (3.14, 17) [3.22]

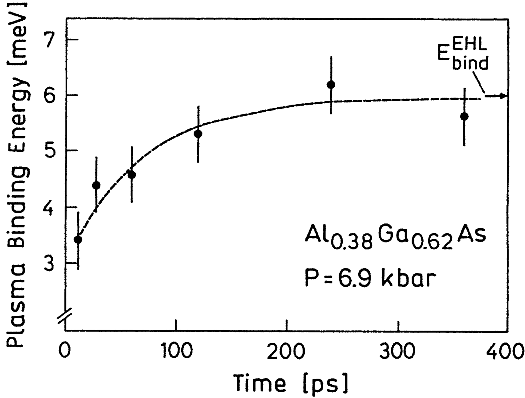

Fig. 3.60. Binding energy of the plasma phase for excitation with F_{max} as a function of time. The dashed line is a guide for the eye [3.22]

temperature does not drop below the critical temperature within the rather short lifetime of the electron–hole pairs.

The fact that the plasma state is self-confined is supported by comparison to our theoretical model. The band-gap renormalization of an expanding electron–hole plasma is found to deviate significantly from the theoretical behavior (3.14, 17), unless the line-shape analysis is corrected for the drift velocity of the carriers [3.59]. Theory and experiment in the case of high excitation in our samples, however, are in excellent agreement without any correction, confirming that no plasma expansion occurs. The tendency of the plasma to a self-confinement is further proven by a comparison of the plasma density with the initially excited carrier density. The latter is estimated from the excitation fluence and the absorption coefficient to be $2 \times 10^{18}\text{cm}^{-3}$. The density in the plasma (Fig. 3.56) is about a factor of three higher. Similar arguments for a confinement of the plasma above T_c were also given by *Cohen* et al. [3.86]. However, they were not able to determine the critical parameters of the plasma.

A definite distinction between the two phases of the electron–hole system in indirect-gap $Al_xGa_{1-x}As$, i.e., between liquid and self-confined plasma, is only possible from their density-versus-temperature characteristics. The density in the incompressible liquid phase varies only little in time, if at all, and decreases with rising temperature. The density in the confined plasma increases with temperature. Its temporal evolution, however, strongly depends on experimental conditions such as the initially excited pair density. For sufficiently long carrier lifetimes, as can be reached in samples with barrier layers, the plasma density does not vary significantly in time, because the self-confinement counterbalances the carrier losses by recombination. It was shown in Refs. [3.12, 15] that the band-gap renormalization is well described by theory even for carrier densities in excess of $10^{19}\,\text{cm}^{-3}$. This is consistent with a negligible expansion of the plasma even for extremely high carrier densities. However, the plasma is far above the critical parameters for liquid formation as a result of extremely high excitation fluences. These conditions

prevailed in the experiments of *Cohen* et al. [3.86], *Bimberg* et al. [3.163] and *Kalt* et al. [3.64]. Their observations are consistent with the properties of a self-confined plasma phase.

The occurrence of this self-confinement on a picosecond timescale is actually rather surprising. Negative diffusion constants resulting from temperature gradients were proposed by the nonequilibrium thermodiffusion model [3.164]. Diffusion, however, is not expected to be significant on a picosecond timescale. It thus seems that the properties of the plasma phase in $Al_xGa_{1-x}As$ cannot be explained in the framework of the theories developed for Si and Ge. At this point one can only speculate about the reason for these differences. The nucleation of droplets in Si occurs on a scale which is longer than the time constants for diffusion. This is in contrast to the results in $Al_xGa_{1-x}As$. Here, the nucleation dynamics, and thus also a possible buildup of local density fluctuations in the plasma phase, is extremely fast, presumably as a result of the alloy disorder. It is clear that much more theoretical and experimental work is necessary to achieve a comprehensive understanding of these nonequilibrium phenomena.

In summary, the electron–hole system in indirect-gap $Al_xGa_{1-x}As$ undergoes a phase transition to a liquid state on a timescale of few hundred picoseconds. The velocity of this phase transition scales with the amount of alloy disorder in the material and is orders of magnitude faster than in elemental indirect-gap semiconductors. Whether thermal equilibrium of the electron–hole droplets with the surrounding gas of free excitons is achieved depends on the density of initially excited carriers. An experimental phase diagram is constructed and the critical parameters and the groundstate density of the liquid phase are estimated. The many-body effects in the plasma, especially band-gap renormalization, can be described consistently by a theoretical model based on the universal formula. The electron–hole plasma above the critical parameters is still bound with respect to the free exciton and is thus self-confined. Previous experimental observations in indirect-gap $Al_xGa_{1-x}As$ published by other authors can be explained consistently when this self-confinement is taken into account.

3.5.2 Quantum-Confined Electron–Hole Droplets

The criteria for the formation of EHDs involving quantum-confined carriers were recently demonstrated by *Kalt* et al. [3.11] in a laser-excited type-II short-period (SP) superlattice (SL) of GaAs/AlAs quantum-well wires (QWWs). These experiments represent the first substantial evidence for the long-sought phase transition of the electron–hole system into a liquid in a low-dimensional system. The formation of droplets appears to be supported by the special structure of the sample, which results in a one-dimensional anisotropy

of the carrier mobilities, a separation of the electrons and holes into different wires and an enlarged interface compared to usual SPSLs [3.168].

The structure of the sample is described in detail in Sect. 2.5 (Fig. 2.24). The photoluminescence experiments are performed using a synchronously pumped DCM dye laser emitting pulses of about 5 ps full width at half maximum. The excitation wavelength (650 nm) corresponded to the absorption maximum related to the direct band-to-band transition in the GaAs wire. The transfer of the electrons into the subsidiary X minima in the AlAs wires is expected to occur on a sub-picosecond timescale [3.170]. The detection system consisted of a 0.32-m spectrometer and a synchroscan streak camera with resolutions of 1 meV and 15 ps, respectively. The lifetime of the QWW SL luminescence was considerably longer than the time between successive excitation pulses (12.5 ns) so that spectra had to be recorded temporally integrated. No significant changes between the luminescence signal just before and immediately following the picosecond laser excitation were detected, indicating that conditions close to steady state were achieved.

Emission resulting from bimolecular recombination of the electron–hole pairs in the liquid phase is detected as a zero-phonon luminescence band below the exciton line. The dependence of both exciton and droplet luminescence on excitation intensity and lattice temperature (T_L) is illustrated in Figs. 3.61, 62. Low-excitation spectra (I_0 in Fig. 3.61) display only the recombination of the type-II indirect heavy-hole excitons: a zero-phonon line (X_{hh}) due to the mix-

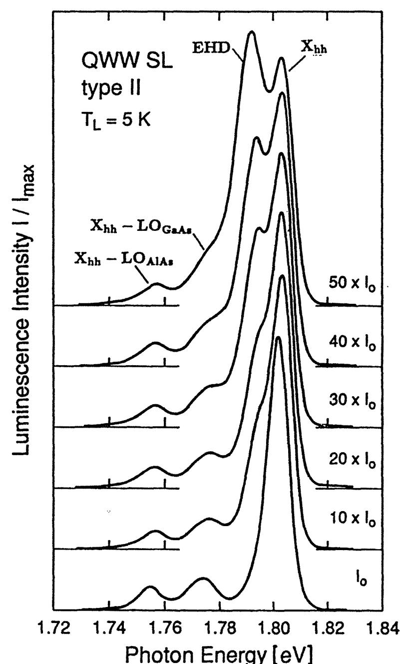

Fig. 3.61. Luminescnce signal due to excitonic (X_{hh}) and electron–hole droplet (EHD) recombination as a function of laser intensity ($I_0 = 19\,\mathrm{kW/cm^2}$ per pulse) [3.11]

ing of the X-point electron wave functions in the AlAs wires with the wave functions at the Γ point of the GaAs induced by the structural periodicity and potential fluctuations related to interface disorder. Additionally, indirect exciton recombination assisted by the emission of GaAs-like ($X_{\mathrm{hh}}-\mathrm{LO}_{\mathrm{GaAs}}$) and AlAs-like ($X_{\mathrm{hh}}-\mathrm{LO}_{\mathrm{AlAs}}$) zone-edge longitudinal optical phonons are detected. With rising excitation power a new luminescence line develops as a shoulder on the low-energy side of the X_{hh} line and shifts increasingly to the red until a stable position is reached at $50 \times I_0$. No further shift occurs for higher excitation levels (cf. $200 \times I_0$ in Fig. 3.62). The exciton lines remain at the same energy position as in the low excitation case. The exciton emission disappears completely as the lattice temperature is raised while the EHD line develops into a structureless broad band (Fig. 3.62).

In order to verify the criteria (1)–(5) for liquid formation described above we extract the electron–hole-pair density n and temperature T from a line-shape analysis of the EHD emission for various excitation conditions. Two different procedures are employed to isolate the EHD emission from the overall spectrum: first, we subtract the exciton line taken at low excitation from the high-excitation spectra (Fig. 3.63). The second way is to determine the temperature of the electron–hole plasma from the high-energy tail of the exciton line and then to model the peak and the low-energy parts of the the EHD line only (Fig. 3.64). The assumption of a common temperature for the exciton and liquid phases is appropriate considering the quasi-steady-state behavior of the luminescence signal. Both procedures give the same results within the tolerance ranges of the fits when the EHD and X_{hh} zero-phonon line

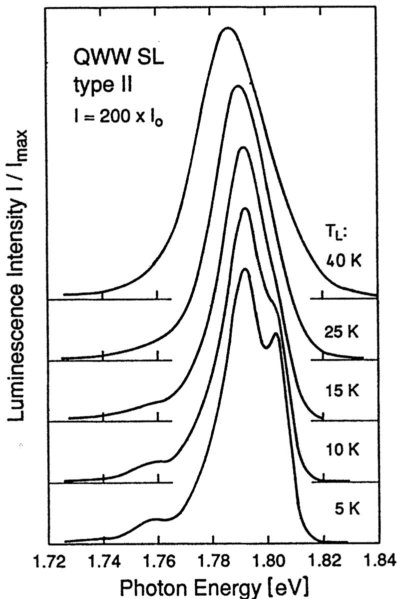

Fig. 3.62. Luminescence signal due to excitonic and electron–hole droplet recombination at fixed excitation level for various lattice temperatures [3.11]

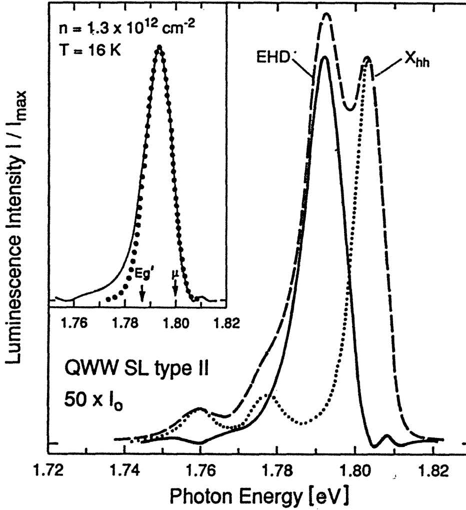

Fig. 3.63. Line-shape fit (dots) to to a EHD spectrum (solid line, see inset) after subtraction of the exciton emission at low excitation (dotted line) from the overall spectrum (dashed line) [3.11]

are well separated, as is the case for all spectra except the lowest excitation levels in Fig. 3.61.

In the line-shape model, we assume a two-dimensional density-of-states (DOS) for electrons and holes ($D_{\mathrm{e,h}}$), which is justified due to a significant lateral coupling of the wires. Potential fluctuations at the interfaces are taken into account by replacing the standard heavyside function by [3.29]:

$$D_{\mathrm{e,h}}(E_{\mathrm{e,h}}) = \frac{m_{\mathrm{e,h}}}{\pi\hbar^2}\left[1+\exp\left(\frac{-E_{\mathrm{e,h}}}{\Gamma_{\mathrm{e,h}}}\right)\right]^{-1} . \qquad (3.30)$$

The effective DOS masses $m_{\mathrm{e,h}}$ are chosen to be $m_{\mathrm{e}} = 0.8m_0$, which is the bulk DOS mass of the AlAs X minima, and $m_{\mathrm{h}} = 0.34m_0$, which is the heavy-hole mass of GaAs quantum wells confirmed by transport measurements in such QWW SLs. The broadening parameters $\Gamma_{\mathrm{e,h}}$ are fit parameters which were chosen to be equal and were in the range of 1.8 ± 0.3 meV.

The luminescence line shape as a function of photon energy $I(\hbar\omega)$ is calculated assuming relaxation of the quasi-momentum conservation from:

$$I(\hbar\omega) \propto \hbar\omega \int_{-\infty}^{+\infty} D_{\mathrm{e}}(E_{\mathrm{e}})D_{\mathrm{h}}(E_{\mathrm{h}})f_{\mathrm{e}}(E_{\mathrm{e}})f_{\mathrm{h}}(E_{\mathrm{h}})\,dE \qquad (3.31)$$

where the electron and hole energies fulfill $E_{\mathrm{e}} + E_{\mathrm{h}} = \hbar\omega$ and $f_{\mathrm{e,h}}$ are the respective Fermi functions. The fit parameters are the renormalized gap E'_{g}, the pair density n and the EHD temperature or the exciton temperature, respectively. We did not include in the fit a Landsberg-type broadening which has only minor influence on the line shape in the absence of momentum conservation.

An example of a line-shape fit with the first model is given in the inset of Fig. 3.63. The theoretical line shape excellently reproduces the EHD

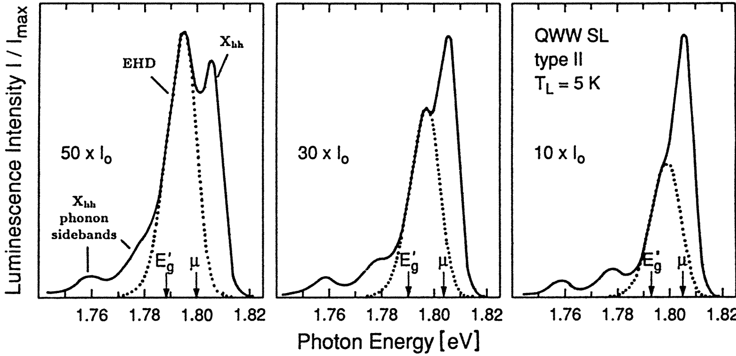

Fig. 3.64. Line-shape fits (dots) with the second model to three EHD spectra taken from Fig. 3.61 demonstrating the rigid shift of the EHD line as a function of excitation level. The fit parameters n, T, and $\Gamma_{\mathrm{e,h}}$ (see text) are identical for all spectra [3.11]

emission. The fit parameters for this example are: $n = 1.3(\pm 0.1) \times 10^{12}\,\mathrm{cm}^{-2}$, $T = 16(\pm 1)\,\mathrm{K}$, $E_{\mathrm{g}}' = 1.7885(\pm 0.0002)\,\mathrm{eV}$ and $\Gamma_{\mathrm{e}} = \Gamma_{\mathrm{h}} = 2.1(\pm 0.1)\,\mathrm{meV}$. The chemical potential μ is calculated to be 11.5 meV above the gap energy.

It is most important that the EHD lines taken between $30I_0$ and $200I_0$ from Figs. 3.61, 62 can be modelled with the second procedure with exactly the same fit parameters except for a normalization factor for the relative height of the EHD line and a rigid shift to higher photon energies. Even the spectra at lower excitation levels are consistently explained by the same line shape (Fig. 3.64) although the fits are not unambiguous in these cases. Systematic variations of the fit parameters, however, show that the low-energy slope of the spectra is very sensitive to changes in the carrier density. Possible significant changes in the EHD parameters would show up in deviations from the model spectrum, which are not observed. We are thus able to conclude that the droplet parameters n and T are independent of the excitation intensity for variations of I by at least a factor of 5, and probably even by a factor of 20, hence verifying criterium (3) for the identification of droplets. The red shift of the luminescence line by 4.5 meV with rising laser intensity is thus here not a density-related renormalization effect but attributable to the droplet size. The tension σ at the surface of the droplets results in a reduction $\Delta\phi$ of the energy per electron–hole pair (and thus the binding energy of the liquid with respect to the exciton line) given in a 2D system by the radius of the drops r and the number of electron–hole pairs per drop N: $\Delta\phi \propto 2\pi r\sigma/N \propto 2\sigma/nr$. Increasing the laser intensity leads to a larger number of electron–hole pairs, which can nucleate to droplets thus increasing the average size of the drops and diminishing the reduction in binding energy of the drops by the surface effects. The result is a red shift of the whole emission band with increasing

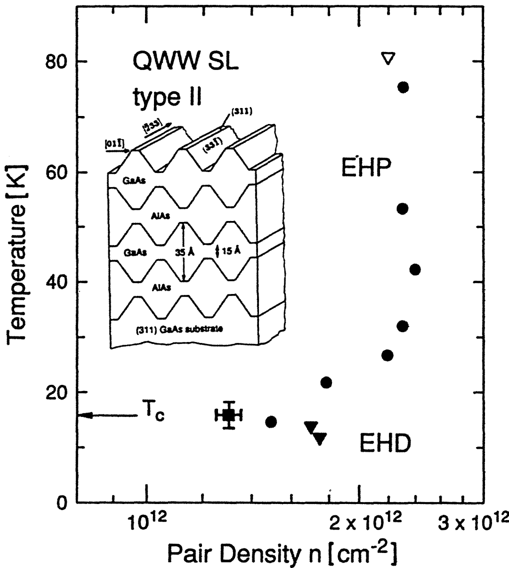

Fig. 3.65. Diagram of temperature versus pair density demonstrating the formation of EHD and EHP phases. The arrow marks the critical temperature T_c. The different symbols represent measurements with different excitation spot sizes. The square represents the data taken from fits (Fig. 3.64) to the five EHD spectra in Fig. 3.61 [3.11]

droplet size. Such surface effects are well established in bulk materials like Si, Ge, and indirect-gap $Al_xGa_{1-x}As$ (see also the discussion in Sect. 3.5.1) [3.22, 154].

The binding energy of the EHD is derived from the above described behavior related to the surface effects. At the threshold intensity for droplet formation ($10 \times I_0$) we find the chemical potential energetically coincident with the peak of the FE line, indicating that this is the highest possible chemical potential for the liquid phase to remain bound with respect to the exciton. The energy of the free exciton is thus situated close to the center of the X_{hh} peak as is often found in multiple-quantum wells where the excitons are partially localized at interface fluctuations [3.165]. The EHD binding energy is then determined to be 4.5 meV from the fit to the $50 I_0$ spectrum where the surface effects are negligible. The observed behavior is in accord with the stability requirement for droplet formation [criterium (2)].

We focus now on the temperature-versus-density characteristics (Fig. 3.65) in this electron–hole system. Slightly higher densities are achieved in the electron–hole droplets when the laser is focussed to smaller spot sizes (minimum 20 μm) than used for the spectra in Figs. 3.61, 62 (130 μm). For such conditions the pathlength which excitons have to migrate to be incorporated

into a drop is greatly reduced by the higher excited density. We find from the analysis of the EHD and X_{hh} line shapes that the temperature of the electron–hole pairs and excitons is reduced, in this case, by as much as 4 K. This tendency to lower temperatures for increasing density in the drops represents the behavior expected from the theoretical phase diagram of electron–hole liquids and thus verifies criterium (4). The critical temperature for the phase transition to a liquid is found from Fig. 3.65 to be $T_c = 16$ K.

For temperatures above T_c, which are achieved by elevating the lattice temperature (Fig. 3.61), we find at first a pronounced increase of the carrier density and then saturation at around $2.3 \times 10^{12}\,\mathrm{cm}^{-2}$. This tendency is the opposite to that found for the EHDs and identifies the presence of an electron–hole plasma according to criterium (5). The saturation effect of the plasma density is not well understood yet, but not unexpected: the electron–hole plasma in disordered materials displays a self-confinment as already discussed for the case of $Al_xGa_{1-x}As$ in the previous section.

We have already mentioned several times the similarities of the EHDs observed here to those found in the bulk semiconductor $Al_xGa_{1-x}As$ with $x \geq 0.43$. It is evident, however, that the droplets in the QWW SL are not a 3D phenomenon. The macroscopic composition of the QWW SL is determined from X-ray diffraction to be $x = 0.483$ [3.168]. The luminescence of the corresponding alloy [3.171] would be shifted by 240 meV to the blue with respect to the actual emission photon energy (Figs. 3.61, 62, 55). The observed luminescence is thus clearly identified as resulting from electrons and holes quantum-confined in the AlAs and GaAs wires.

After having definitely identified the low-dimensional EHD phase, we now discuss some of its properties as related to a given sample structure. It is interesting to note that a condensation into droplets is not found in a reference type-II SPSL grown in the same charge but on a (100) substrate. Some speculations about the presence of a liquid phase in similar SPSL structures of Ref. [3.169] were based on the temporal development of the luminescence decay time. But no conclusive proof [e.g. by verification of any of the criteria (1)–(5)] could be given. The main difference between the QWW SL and the latter system is the additional confinement in the wires, which leads to a 1D anisotropy of the carrier diffusion and to an enhancement of the exciton binding energy with respect to the purely 2D SPSL. Further, the interface area is enlarged by the corrugation introducing additional fluctuations in the QWW SL, which can accelerate the nucleation dynamics by providing a multitude of condensation seeds. This is similar to the effect of alloy disorder found in $Al_xGa_{1-x}As$ (Sect. 3.4.1) [3.22]. The size-related reduction of the liquid binding energy directly demonstrates that a multitude of small droplets is formed in the QWW SL. The condensation of the drops in areas with maximum interface disorder is evidenced by the fact that only zero-phonon recombination is observed for the EHD line.

The influence of screening between adjacent (311) layers of AlAs (or GaAs, respectively) appears to be unimportant for the stabilization of the droplet phase. An upper limit for this interaction can be estimated from the 3D Thomas–Fermi screening length [3.4], which describes the spatial decay of the Coulomb interaction. The calculated value of $l_{\mathrm{TF}} \approx 60\,\mathrm{Å}$ would be comparable to the SL period of 45 Å. But the the limited mobility of the carriers along the wires implies a low-dimensional screening behavior. Moreover, a residual coupling of adjacent wells should have the same effect in the conventional type-II superlattices, where EHD formation is not observed.

In conclusion, strong evidence for the formation of quantum-confined electron–hole droplets is found in a type-II QWW SL. The stability of the droplet phase seems to be related to the additional fluctuations introduced by the corrugation at the interfaces, similar to the case of bulk alloy semiconductors.

3.6 Optical Nonlinearities at the Direct Gap of Indirect-Gap Semiconductors

The optical generation of dense electron–hole systems in semiconductors dramatically affects the optical properties of the excited material. In the previous sections we discussed the implications of many-particle interactions on the band structure as well as the filling of states with increasing excitation level. Such a simultaneous shift and removal of oscillators coupling to the electromagnetic field results in significant modifications of the optical absorption and the refractive index as long as the generated electron–hole pairs are present. The optical properties of the semiconductor are thus a function of the intensity of the optical excitation. Such optical nonlinearities are most interesting for applications in electro-optical devices such as optical switches for communication technology.

Great efforts have been made in recent decades to understand and apply optical nonlinearities in semiconductor materials. Recent reviews of these efforts are given, for example, in Refs. [3.7, 172]. Most of the work was related to the nonlinearities close to the direct fundamental gap of the materials under investigation. It is far beyond the scope of this book to review these activities. We prefer to focus on one special kind of optical nonlinearity namely the interesting phenomena occurring in indirect-gap and type-II semiconductors at the higher-energy direct absorption edge.

The nonlinear effects in these materials rely on the influence of an electron–hole plasma, associated with the $\Gamma - X$ gap, on the oscillator strength at the Γ–Γ absorption edge, and on the fast transfer of electrons from the central to the side valleys. The first example of this is indirect-gap $\mathrm{Al}_x\mathrm{Ga}_{1-x}\mathrm{As}$ [3.64, 173]. The transmission with and without additional picosecond excitation in the region of the direct gap of a sample with $x = 0.52$ is displayed in

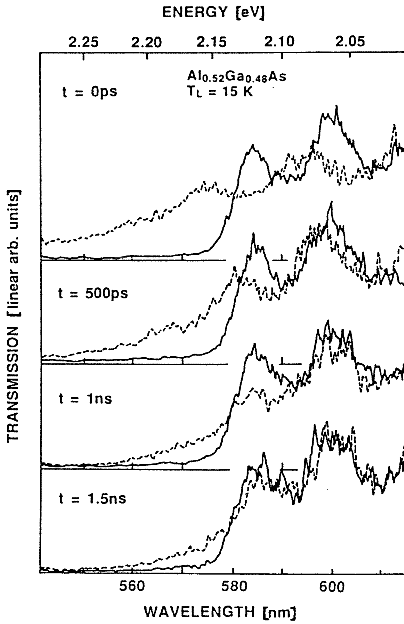

Fig. 3.66. Transmission of $Al_{0.52}Ga_{0.48}As$ in the vicinity of the direct absorption edge without excitation (solid line) and with excitation of an EHP by a 40-ps pulse of $F = 11\,\mathrm{mJ/cm^2}$ at 532 nm (dashed line) for different delay times t [3.64]

Fig. 3.66 as a function of delay time after excitation. The absorption for the case without excitation is governed by the direct absorption edge, while the indirect absorption at lower photon energies is negligible in such few-μm thick samples. A sharp exitonic resonance at the absorption edge is missing due to disorder-induced inhomogeneous and lifetime-induced homogeneous broadening of this transition. The latter effect results from the fast Γ–X transfer of the electron bound to the hole in the direct exciton. We will return to the implications of this mechanism in the discussuion of the type-II QWs below. The modulation of the transmission below the direct gap in the spectra of Fig. 3.66 is caused by Fabry–Perot interferences within the sample layer. The excitation of an electron–hole plasma (here in the density range of $10^{19}\,\mathrm{cm^{-3}}$) strongly modifies the transmission: one finds a persistent bleaching of the absorption to the Γ conduction band, an induced absorption below the the direct gap and a significant blue shift of the Fabry–Perot fringes.

The absorption bleaching results from a strong band filling in the valence band at these carrier densities. The Γ minimum of the conduction band, on the other hand, is essentially empty on this time scale due to the fast Γ–X transfer of the electrons. Further contributions to the bleaching stem from the screening of the excitonic continuum related to the direct gap by the generated electron–hole plasma. Thus, the bleaching of the absorption at the direct gap is caused by an electron–hole plasma related to the indirect gap. Although this material is an intrinsic semiconductor, the blocking of the transitions from the valence to the conduction band is caused by only one type of excited carrier, i.e., the holes. Thus the indirect-gap $Al_xGa_{1-x}As$ has more similarities with

Ge [3.77] than with GaAs. The duration of the bleaching is consistent with the plasma lifetime determined from simultaneous photoluminescence studies.

The Γ minimum in this sample is renormalized mainly via the hole exchange and correlation effects as was discussed in Sect. 3.2.2. This renormalization results in an induced absorption below the direct absorption edge which decreases as a function of carrier density, but is still visible for delay times up to 1 ns. The shift of the absorption edge of the order of 40 meV is consistent with the multi-valley model for the band-gap renormalization. This effect is further confirmed by experiments where the plasma is excited using a laser energy below the direct absorption edge. The strength of the absorption bleaching decreases monotonically when the laser photon energy is tuned below the direct gap. Significant bleaching is still found, however, for excitation at 2100 eV, i.e., 40 meV below the absorption edge. The carrier densities required for such a bleaching can only be reached when the direct absoption edge shifts below the laser photon energy during the excitation process due to band-gap renormalization.

The blue shift of the Fabry–Perot fringes can finally be used to calculate the strong plasma-induced changes of the refractive index. These changes reach values up to $\delta n = -9.9 \times 10^{-2}$ just below the direct gap at $t = 0$ ps. This negative change (or blue shift) demonstrates that band filling of the valence band and screening dominate the induced index changes rather than the gap renormalization.

Optical nonlinearities of the same order of magnitude are also found in this material at room temperature [3.173]. A transient transmission spectrum taken well after the excitation pulse is shown in Fig. 3.67 for near resonant excitation and $T = 300$ K. Again, strong induced bleaching, changes of the refractive index and some induced absorption are observed. Thus, indirect-gap $Al_xGa_{1-x}As$ is a prominent candidate for achieving optical switching by various types of optical bistabilities in the visible. It should be possible to

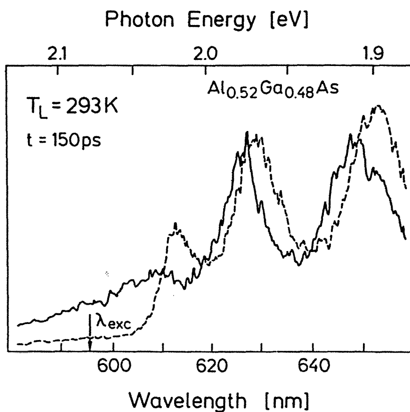

Fig. 3.67. Transmission of $Al_{0.52}Ga_{0.48}As$ without excitation (dashed line) and with near-resonant excitation at λ_{exc} (solid line) of $F = 18\,mJ/cm^2$ at room temperature ($t = 150$ ps) [3.173]

vary the wavelength of operation of such a device over a large spectral range by varying the AlAs mole content between 0.43 and 1.0.

A similar scenario, but using a type-II $Al_xGa_{1-x}As/AlAs$ MQW was studied and actually applied as an ultrafast saturable absorber by *Feldmann* et al. [3.174, 175]. They investigated the differential transmission (DT) at the direct-gap exciton in these structures in a pump-probe-beam experiment. The resulting DT signal, i.e., the difference in the probe-beam transmission with and without additional pump beam, is displayed in Fig. 3.68 as a function of delay between probe and pump. An initial bleaching of the transmission is followed by a rapid recovery of this bleaching to a residual long-lived value. The level of the residual bleaching depends on the spectral position of the probe beam with respect to the excitonic resonance (inset in Fig. 3.68) and can even turn into an induced absorption on the low-energy tail of the exciton.

This rather fast transient behavior of the optical nonlinearity is explained in terms of an initial phase-space filling during the pump pulse which leads to the observed bleaching. The electrons excited at the direct gap of the $Al_xGa_{1-x}As$ layer subsequently transfer to the X-point minima in the AlAs barrier layers with a time constant of 20 ps at low temperature and of 2 ps at 300 K. The transferred electrons are then lost for the state filling and excitonic enhancement at the direct gap, resulting in a reduction of the bleaching. The transition to induced absorption requires an additional red shift or broadening at the direct absorption edge which is attributed to the collision broadening of the excitonic resonance resulting from exciton–heavy hole collisions.

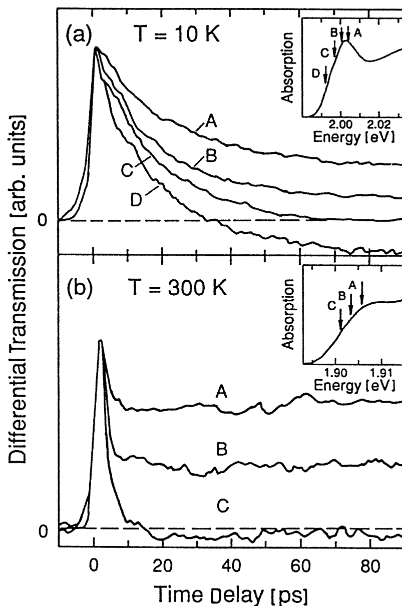

Fig. 3.68. Normalized differential transmission versus time delay between pump and probe in a type-II AlGaAs/AlAs MQW at (**a**) 10 K and (**b**) 300 K. The respective linear absorption spectra at the band gap are shown as insets. The arrows labelled A-D indicate the laser photon energies [3.174]

The above described induced bleaching and its fast recovery at room temperature was used for passive mode locking of a synchronously pumped dye laser [3.175]. The type-II MQW served as a saturable absorber for laser wavelengths in the tail of the absorption edge (position C in Fig. 3.68b). *Feldmann* et al. demonstrated that due to the fast dynamics of the nonlinearity, type-II structures are well suited for applications as nonlinear optical devices with high repetition rates.

Strong optical nonlinearities in type-II QWs involving the correlation of single electrons in the first direct subband and a hole plasma in the first hh subband in the limit of the Fermi-edge singularity were recently reported by *Olbright* et al. [3.176] and theoretically modelled by *Binder* et al. [3.177]. The nonlinearity is observed as a pronounced blue shift of the absorption peak at the direct hh-exciton transition (Fig. 3.69) after the excitation of a high density ($n \approx 10^{12}\,\mathrm{cm}^{-2}$) one-component hole plasma in the well. The simultaneously generated electrons transfer rapidly to the barrier layers and do not significantly influence the optical properties at the direct absorption edge under the quasi-steady state conditions achieved for ns-laser excitation. Measurements with fs temporal resolution demonstrate that the nonlinearity first develops as a bleaching of the hh-exciton absorption on a sub-picosecond time scale with a subsequent blue shift of the remaining absorption peak to a steady-state value of $\approx 15\,\mathrm{meV}$ within 100 ps.

Calculations using a many-body theory similar to the plasma theory of bulk semiconductors reveal that the observed blue shift of the absorption results from the transition to the Mahan exciton at the Fermi edge (Fig. 3.70). The renormalized band gap is situated below the hh-exciton resonance for the relevant carrier densities. In contrast to type-I structures, gain at the direct gap is not possible in this highly excited type-II QW because the Γ conduction band is empty. The lh exciton experiences only a minor shift due to the screening by the hh plasma. The delayed onset of the blue shift of the resonance is related to the cooling of the hole plasma on a 100-ps time scale as can be shown by temperature-dependent calculations. The initial absorption bleaching is simply a result of the hole phase-space filling [3.176, 177].

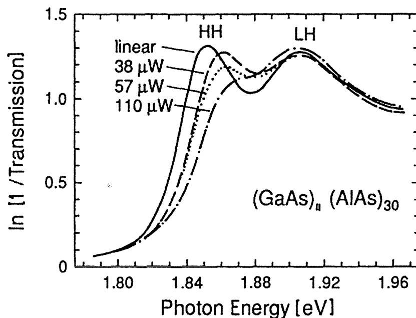

Fig. 3.69. Excitation-intensity-dependent absorption spectra of a (11/30) GaAs/AlAs type-II QW at $T = 15\,\mathrm{K}$ under quasi-steady state excitation [3.176]

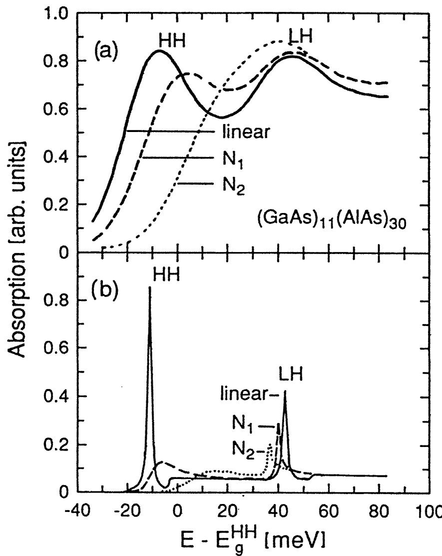

Fig. 3.70. (**a**) Calculated absorption spectra including inhomogeneous broadening ($N_0 = 0.3a_B^{-2}$). (**b**) Corresponding spectra without inhomogeneous broadening revealing the presence of the FES [3.176]

The above-described examples demonstrate strong optical nonlinearities at the direct gap of indirect-gap or type-II semiconductors. *Band-gap engineering* by variation of material composition or structure allows one to tune the nonlinearities over a large spectral range. The indirect character of the samples leads to a fast dynamics of the observed effects which makes them very interesting for applications in fast opto-electronic devices.

4. Intervalley Coupling

In the preceding sections, we discussed the optical properties of III-V semiconductors with the focus on the impact of multi-valley scenarios on excitonic properties and many-body interactions such as screening. We have assumed for the most part that dynamic processes leading to a distribution of the present carriers among the band extrema are fast with respect to the phenomena discussed. We will detail in the following how to extract quantitative information on the actual mechanisms and efficiencies of *intervalley coupling* from optical spectroscopy of excitons and plasmas.

There are two principal ways in which intervalley coupling acts upon carriers in semiconductors. The first is the *transfer* of electrons or holes between real states in the band structure which results in a limited lifetime of the particular carrier in the initial state. This lifetime can be measured directly with time-resolved techniques in the pico- and femtosecond regime or extracted from the homogeneous (i.e., lifetime-induced) broadening of optical transitions. It is an important prerequisite for any theoretical treatment of such experiments that, despite the rather strong mixing of the wave functions in different valleys by phonons or potential fluctuations, one can still apply the usual band-structure concepts. The intervalley coupling can be treated in the *weak scattering limit*, i.e., as a small perturbation, and the wave vector $\mathbf{k}$ is still a good quantum number. The theoretical background based on Fermi's golden rule will be outlined in Sect. 4.1.1.

The second way to find the impact of intervalley coupling is in the form of *indirect optical transitions*, i.e., transitions which proceed via virtual intermediate states and whose initial and final states are situated close to different high-symmetry points of the Brillouin zone. This situation can be well treated in second-order perturbation theory as will be described in Sect. 4.1.2. Following these theoretical considerations we are able to interpret optical spectra and deduce the coupling strengths related to phonon-assisted (Sect. 4.2.1) and disorder-induced (Sect. 4.2.2) processes. We will continue with a discussion of intervalley transfer in type-II heterostructures, which involves transitions in both real and momentum space (Sect. 4.2.3). Finally, we will focus on an application of the efficient disorder-induced intervalley coupling close to direct-to-indirect crossover, namely, indirect stimulated emission (Sect. 4.3).

4.1 Theoretical Considerations

4.1.1 Transfer Between Real Band States and Scattering Potentials

Intervalley transfer of electrons between conduction-band minima at different points in the Brillouin zone is one of the most important relaxation processes of hot carriers in semiconductors. Such intervalley scattering processes can be extremely efficient, occurring on pico- and subpicosecond timescales [4.1]. The understanding of these fundamental mechanisms is thus essential for the design of semiconductor devices, as we pointed out in Chap. 1. We will limit our discussion here to the scattering processes of electrons between different valleys of the conduction band and refer to Ref. [4.2] for a review of intervalence-band transitions of holes, to Refs. [4.3–5] for intersubband transitions in quantum wells and to Ref. [4.6] for transfer processes which involve tunnelling through a potential barrier.

In a transfer process between valleys at different high-symmetry points of bulk material, an electron has to undergo a drastic change of quasi-momentum $\mathbf{k}$. This large quasi-momentum $\mathbf{k}$ has to be provided by scattering from fluctuations in the lattice potential affecting the plane-wave part of the electron wave function. The scattering rate or inverse scattering time τ^{-1} of such a processes is given by *Fermi's golden rule* as the sum over all final conduction band states ψ_c^f: [4.7]

$$\frac{1}{\tau} = \frac{2\pi}{\hbar} \sum_f |\langle \psi_c^f | \mathcal{H}_{\text{scat}} | \psi_c^i \rangle|^2 \delta[E^f - E^i] \tag{4.1}$$

with ψ_c^i being the initial state and $\mathcal{H}_{\text{scat}}$ is the scattering Hamiltonian. The energy conservation implicitly given in the delta function has to be corrected by the energy a second quasi-particle gains or loses if the scattering process is not elastic. The applicability of the law of quasi-momentum conservation depends on the character of the potential fluctuation: If the fluctuation is strictly periodic, as is the case for vibrational modes of the lattice, the conservation law applies. For the case of random fluctuations such as in alloy semiconductors, on the other hand, the translational invariance is violated, thus relaxing the conservation law.

The relevant length scales of the periodic or random fluctuations involved in intervalley scattering are evident from a Fourier expansion of the scattering Hamiltonian in real space [4.7]:

$$\mathcal{H}_{\text{scat}}(\mathbf{r}) = \sum_{\mathbf{k}} A(\mathbf{k}) e^{i\mathbf{k}\cdot\mathbf{r}} \ . \tag{4.2}$$

Inserting this expression for the scattering Hamiltonian into (4.1) shows that the Fourier coefficients $A(\mathbf{k})$ have to be significant for large quasi-momentum

k, if the initial and final state are at different high-symmetry points of the Brillouin zone. Such scattering Hamiltonians are given in the case of zone-edge phonons or other periodic or random fluctuations occurring on a length scale comparable to the lattice constant.

We now want to be more specific about the relevant potential fluctuations which induce intervalley coupling in GaAs and its related compounds, alloys, and heterostructures. We will concentrate only on the scattering processes within the lowest conduction band, i.e., transfer between the central Γ minimum at (0,0,0), the L minima at (1,1,1) and the X minima at (1,0,0) and equivalent points in this class of materials. The mechanisms which have to be considered are *deformation-potential scattering, alloy-disorder scattering interface-disorder scattering*, and the so-called *interface mixing.*

Phonon-assisted transfer processes are inelastic, i.e., they include the absorption or the emission of a phonon and, thus, a change in energy. Including further the conservation of momentum and accounting for the density of states $\varrho(E_f)$ in the energy interval around the final energy E_f leads to the following modification of Fermi's golden rule [4.8, 9, 11]:

$$\frac{1}{\tau} = \frac{2\pi}{\hbar} |\langle\psi_c^f(\mathbf{k}\pm\mathbf{q}), N_q^l \mp 1|\mathcal{H}_{\mathrm{phonon}}^{if}|\psi_c^i(\mathbf{k}), N_q^l\rangle|^2 \; \varrho(E_f) \; \times \\ \times \; \delta[E_f(\mathbf{k}\pm\mathbf{q}) \pm \hbar\Omega^l(\mathbf{q}) - E_i(\mathbf{k})] \tag{4.3}$$

for scattering involving a phonon of branch l, energy $\hbar\Omega$ and wave vector $\mathbf{q}$ between the initial electronic state with wave function $\psi_c^i(\mathbf{k})$ and the final state $\psi_c^f(\mathbf{k}\pm\mathbf{q})$. The indices i, f are chosen from (Γ, X, L) with $i \neq f$. The phonon occupation number N_q^l is given by Bose–Einstein statistics:

$$N_q^l = [\exp(\hbar\Omega^l(\mathbf{q})/k_B T) - 1]^{-1} \tag{4.4}$$

and increases or decreases by one for emission or absorption of a phonon, respectively.

The electron–phonon interaction Hamiltonian $\mathcal{H}^{if}$ is given for intervalley processes by deformation-potential scattering. In principal, an electron interacts also with the long-range polarizations related to polar-optical phonons (Fröhlich interaction) or to piezo-electric fields. Both interactions, however, vanish for large phonon wave vectors and are unimportant for intervalley transfer. A well-known approximation for the intervalley deformation potential (IDP) scattering rate is *Conwell's* formula [4.8]:

$$\frac{1}{\tau} = \frac{D_{if}^2 \, m_f^{3/2}}{\sqrt{2}\,\pi\,\hbar^2\,\rho\,\hbar\Omega^l} \, (\Delta_{if} \mp \hbar\Omega^l)^{1/2} \; (N_q^l + \tfrac{1}{2} \mp \tfrac{1}{2}) \; . \tag{4.5}$$

Here, the scattering matrix element is replaced by the IDP D_{if} in its usual definition and the phonon occupation. The density of final states for the scattering is given in the approximation of an average parabolic band by the

density-of-states mass of the final valley m_f and the square-root dependence in energy (here Δ_{if} is the energy difference between the initial and final states). Additionally, one finds for the (IDP) coupling strict selection rules, provided the scattering occurs between states at the high-symmetry points. In the case of $Ga_xAl_{1-x}As$, IDP scattering between Γ_6 and X_6 minima is allowed for LO phonons only, while $\Gamma_6 - L_6$ tansfer is mediated by LA and LO phonons [4.10, 11].

The Conwell formula, however, does not describe the typical intervalley-scattering experiments where, for example, electrons are injected with high excess energies into the central valley or where electrons populate states with high energies (and thus large quasi-momentum $\mathbf{k}$) at a temperature of 300 K or more [4.11]. In such cases, the scattering is not between states close to the high-symmetry points. Consequently, scattering with additional phonon modes such as transverse modes becomes allowed and one has to account for the wave-vector dependence of the IDPs, as was pointed out by *Zollner* et al. [4.11]. They demonstrated that this dependence is significant and that intervalley scattering can be extremely anisotropic for scattering from one point in $\mathbf{k}$-space to points within the same star close to a different high-symmetry point. The appropriate way to treat such experiments and the temperature dependence of the intervalley-scattering time is to calculate the phonon spectral function for all possible modes by integrating over the whole Brillouin zone and then to integrate over all phonon energies after multiplication with the Bose–Einstein factor. A review of the theory based on the rigid-pseudo-ion model is given in Ref. [4.11]. One can conclude that an interpretation of experiments on the intervalley transfer between real states requires careful and extensive modelling.

The second important intervalley coupling mechanism in intrinsic bulk semiconductors is the elastic scattering at random fluctuations induced by alloy disorder, as found, for example, in ternary compounds like $Al_xGa_{1-x}As$. The substitution of one kind of atom in the lattice by a second kind (e.g. Ga by Al) results in a violation of the translational invariance of the lattice on a microscopic scale. Again, these fluctuations are treated in the weak scattering limit, i.e., as small perturbations [4.12, 13].

Scattering involving alloy disorder is typically ignored in both experimental and theoretical publications on intervalley transfer. Only the case of intraband alloy scattering [4.14–23] is extensively treated. But disorder-induced intervalley coupling was recently shown experimentally by *Kalt* et al. [4.24] and then theoretically by *Grein* et al. [4.13] and *Güncer* et al. [4.25] to result in efficient intervalley scattering.

The largest problem in the theoretical description of the disorder-induced transfer is the definition of a scattering potential. Several proposals have been made in the context of carrier mobility in alloy semiconductors, e.g., giving the potential as the difference between the band gaps of the alloy constituents (GaAs and AlAs in the model substance $Al_xGa_{1-x}As$) [4.14]. This ansatz

directly leads to questions such as: What is the meaning of a band structure at the position of a single ion, and which gaps have to be considered when one constituent is a direct-gap and the other one an indirect-gap semiconductor? Other approaches are the use of the electron affinity differences, the differences in electronegativity, or an effective-charge model [4.15, 17, 18, 21]. A second problem is the description of the relative disorder, i.e., whether or not any clustering occurs in the distribution of the constituents [4.26].

The experimental proof of any of these concepts by transport measurements is difficult because alloy scattering tends to give only a minor to moderate contribution to the limitation of the carrier mobility [4.18–20, 22, 23]. Further, the intravalley scattering is made possible by a variety of processes such as deformation-potential, piezo-electric and polar optical scattering at phonon modes, as well as ionized-impurity scattering. The mobility in alloys with a direct-to-indirect crossover is also strongly affected by the intervalley transfer. A direct access to the contribution of the disorder-related scattering is thus not possible in mobility measurements.

An intuitive and instructive picture of the scattering at potential fluctuations was given by *Oosaka* et al. [4.26]. Here, the alloy is modelled by tiny clusters of AlAs or GaAs, which cause random positive or negative fluctuations in the crystal potential (Fig. 4.1). The overlap of atomic potentials within such a cluster leads to smoother fluctuations in the lattice potential than in the models mentioned above. The cluster potentials can be modeled as spheres which have radii of r_i and which occur with probability $W_i^{\pm}$ given by Poisson distribution functions:

$$W_i^{\pm} = \lambda_{\pm}^{i-1}\,\mathrm{e}^{-\lambda_{\pm}}/(i-1)! \qquad (i = 1, 2, 3, \ldots), \tag{4.6}$$

where i is the number of atoms in a cluster with radius r_i and $\lambda_{\pm} + 1$ is the expectation value for the number of Ga and Al atoms, respectively, in a cluster. The number of clusters $n_i^{\pm}$ containing i atoms can then be estimated from:

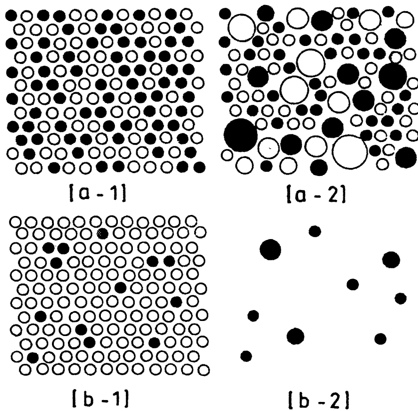

Fig. 4.1. Distribution of Ga (open circles) and Al (solid dots) atoms in $Al_xGa_{1-x}As$ with $x \approx 0.5$ (a-1) and x close to 0.0 (b-1). The corresponding spatial distributions of spherical potential clusters for the same x values are given in (b-1) and (b-2). Here, black and white dots are negative and positive potential clusters, respectively [4.26]

$$n_i^+ = W_i^+ N(1-x)/(\lambda_+ + 1) \quad \text{and} \quad n_i^- = W_i^- Nx/(\lambda_- + 1) \,, \tag{4.7}$$

where x is the AlAs mole fraction and N the total concentration of Ga and Al atoms.

A direct estimate of the scattering efficiency from this model is again difficult because the expectation values $\lambda_\pm$ or the average cluster size for a given x value have not been determined theoretically. Mobility data for several ternaries suggest that they lie between 2 and 10 in the crossover region. These numbers lead to two important conclusions: first, the concentration of clusters with i of about 2, which are required for effective intervalley coupling by the disorder, can be estimated from the above expressions to be at least $10^{17}\,\mathrm{cm}^{-3}$. This concentration is sufficient for the disorder scattering to compete effectively with the IDP scattering. Further, it is evident that due to the rather small cluster sizes one gets large Fourier coefficients, $A(\mathbf{k})$, mainly for large $\mathbf{k}$, i.e., the disorder scattering has more importance for intervalley than for intravalley processes consistent with the experimental findings [4.27].

The transfer time for the proposed disorder-assisted intervalley transfer should follow an expression similar to that derived for the intravalley process, but taking into account the appropriate density of final states [4.24]:

$$\frac{1}{\tau} = \frac{(a(x))^3\, x(1-x)\, (V_{if}^{\mathrm{alloy}})^2\, m_f^{3/2}}{2\sqrt{2}\,\pi\,\hbar^4} (\varDelta_{if})^{1/2} \;. \tag{4.8}$$

The disorder is included here in the disorder potential V_{if}^{alloy} and the relative disorder factor $x(1-x)$.

A full calculation of the k-dependence of the disorder potential was performed recently by *Güncer* and *Ferry* [4.25]. They treat the disorder as a perturbation to the Hamiltonian $H_{\mathrm{VC}} = xH_A + (1-x)H_B$ in the *virtual-crystal* (VC) *approximation* for alloys of the form $A_xB_{1-x}C$. The VC approximation describes the Hamiltonian of the alloy as an average of the Hamiltonians H_A and H_B of the binary constituents. A random component is added to account for the scattering from the disorder. The alloy Hamiltonian then reads: $H_{\mathrm{alloy}} = H_{\mathrm{VC}} + \Sigma_n V_n$, where V_n denotes the difference between the average VC potential at the lattice site n and the actual atomic potential, which depends on whether the site is occupied by an A or an B atom.

Again, the fact that the exact distribution of the cations is unknown requires a configuration averaging of the alloy Hamiltonian which can be done within the frame of the *coherent potential approximation* (CPA). Here, the random potential is replaced by a coherent potential, such that the average scattering on an atomic site vanishes. The result of these calculations of *Güncer* and *Ferry* is the CPA self-energy in the Brillouin zone. The real part of the self-energy gives the energy corrections to the band structure of the virtual crystal, while the imaginary part gives the state broadening due to the disorder scattering. The quantitative results will be discussed below.

We will now turn to the $\Gamma - X$ transfer of electrons in type-II superlattices or quantum wells, which includes a real-space charge transfer of the electron from the (Al)GaAs to the AlAs layers besides the scattering in momentum space [4.28–31]. The scattering processes have the following origins in these structured materials: (1) phonon-assisted transfer, (2) mixing of Γ and X_z wave functions resulting from the superperiodicity in superlattice structures [4.32, 34] and (3) mixing of Γ and $X_{x,y}$ wave functions via interfacial roughness [4.35, 38]. The first process is similar to that discussed for bulk but with possible additional contributions from interface-phonon modes. The other two processes arise from the layer structure in such type-II materials.

The periodic part of the electron Bloch functions are subject to the artifical periodicity in the growth (z) direction in the case of a superlattice. This restriction of the translational symmetry of the superlattice results in the lifting of the degeneracy of the $X_{\rm z}$ and $X_{\rm x,y}$ minima. The confinement energy of these states is determined by the longitudinal or by the transverse mass, respectively, which differ significantly [4.38–40]. As a further consequence of the superperiodicity, one finds a zone folding of the electron dispersion into a mini-Brillouin zone between $-\pi/d$ and π/d where d is the superlattice constant, i.e., the sum of the thicknesses of one (Al)GaAs and one AlAs layer [4.36, 39, 41, 42]. This zone folding is illustrated for a simplified band structure in Fig. 4.2. The mini-Brillouin zone will continuously grow towards the bulk BZ for decreasing superlattice period. The consequence of the folding is that the original $X_{\rm z}$ wave functions transfer to Γ-type wave functions resulting in pseudo-direct transitions between the valence and the $X_{\rm z}$ minimum. The $X_{\rm x,y}$ states, on the other hand, fold into states with M symmetry, i.e., with wave vectors in the layer plane, which can couple to the Γ valence band via the disorder at the interface or the phonons. This concept of zone folding seems to be appropriate for $n = m \leq 6$ [4.36].

Results of group-theoretical considerations imply that the zone folding can occur only for certain combinations of n and m, which are the numbers of monolayers in the well and barrier materials. The mixing is only present for wave functions of equal parity and the parity of the $X_{\rm z}$ wave functions is different for odd or even m. The example of the Γ and $X_{\rm z}$ wave functions in the type-II SL $(Al_{0.28}Ga_{0.72}As)_{28}/(AlAs)_m$ with $m = 7$ or 8 (Fig. 4.3) demonstrates the resulting mixing [4.39]. The mixing is present here for $m = 7$,

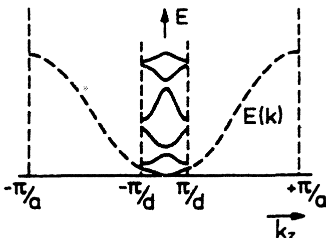

Fig. 4.2. Brillouin-zone folding in a superlattice with periodicity d

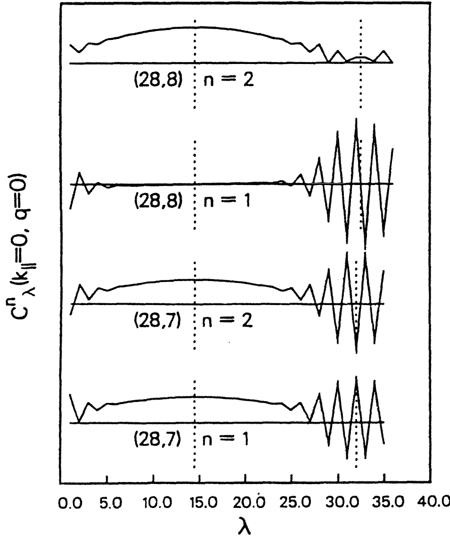

Fig. 4.3. Coordinate space envelope wave functions in a type-II $Al_{0.28}Ga_{0.72}As/AlAs$ superlattice demonstrating the different degree of mixing of the $n_z = 1$ and $n_z = 2$ states for even ($m = 8$) and odd ($m = 7$) number of monolayers (λ) of AlAs [4.39]

while it is absent for $m = 8$. However, experimental studies in such SLs show that the strict selection rules are not upheld in realistic structures due to the presence of fluctuations in the layer thickness of the order of one monolayer.

A coupling of the AlAs $X_{x,y}$ minima to the (Al)GaAs Γ minimum requires a quasi-momentum $\mathbf{k}$ component of the scattering potential perpendicular to the z direction. This component can be provided by the potential fluctuations related to interface roughness, i.e., by the fluctuations in the confinement energies of the carriers. This roughness has to occur on a length scale comparable to the lattice constant for efficient $\Gamma - X_{x,y}$ coupling similar to the disorder scattering in bulk. The relative importance of the $\Gamma - X_z$ and the $\Gamma - X_{x,y}$ coupling mechanisms will be outlined in the dicussions of optical spectroscopy below.

For all three $\Gamma - X$ coupling processes in type-II SLs the initial and final states are spatially separated. This results in a major influence of the spatial overlap of the corresponding wave functions on the transfer times. It can be shown for the scattering matrix elements, cf. (4.2), that [4.30]

$$\langle\psi_c^X|\mathcal{H}_{\Gamma X}|\psi_c^\Gamma\rangle \propto \langle\psi_c^X|\sum_{\mathbf{k}} A(\mathbf{k})e^{i\mathbf{k}\cdot\mathbf{r}}|\psi_c^\Gamma\rangle \propto A(\mathbf{k_0})\langle\psi_c^X|\psi_c^\Gamma\rangle \qquad (4.9)$$

i.e., the scattering matrix element is only nonvanishing for expansion coefficients $A(\mathbf{k})$ of wave vector ($\mathbf{k}_0$) close to the zone edge. The transition rate is then proportional to the overlap integral of the initial and final wave functions which have their maximum amplitudes in different slabs [4.30, 39].

4.1.2 Transitions Involving Virtual Intermediate States

The second possibility for observing intervalley coupling between the central and the side valleys is related to *indirect optical transitions* involving, for example, electrons in the X or L valleys and holes in the Γ valence bands. The initial and final states of the electrons here have strongly different wave vectors which cannot be achieved by the emission or absorption of the photon. An additional scattering process has to contribute – namely, one of the above-described intervalley processes. The fluctuations in the lattice potential induced by the vibration modes, the disorder, or the superperiodicity can be regarded as small perturbations because the experimental observables like the exciton Bohr radius or the carrier mean free path are larger than the length scale of the fluctuations. This justifies a treatment of the indirect transitions in second-order perturbation theory [4.12].

The indirect transitions (here recombination) can be visualized as processes involving two subsequent steps. An example is given by the indirect recombination in $Al_xGa_{1-x}As$ as demonstrated in Fig. 4.4. Other transfer scenarios, such as recombination in type-II heterostructures follow similar lines. First, the electron is scattered from its initial state ψ_c^X in the side valley to a virtual state at the Γ point. This intermediate state is described by a wave function ψ_v^Γ close to the Γ minimum of the conduction band, but it is taken at the wrong energy. This energy either equals the energy of the initial state in elastic scattering processes or is lowered, by one phonon energy, for inelastic IDP scattering. This intermediate state can be occupied by the electron only virtually, i.e., only for a time given by the uncertainty relation for energy and time $\Delta E \Delta t \gtrsim \hbar$. In the second step, the electron recombines with a hole in the valence band with wave function ψ_v^Γ under emission of a photon. The transition probability for indirect recombination of electrons in the X minima with holes in the Γ valence band is then given by [4.24]:

$$|\mathrm{M}_{\Gamma \mathrm{X}}|^2 = \left| \frac{\langle \psi_v^\Gamma | \mathcal{H}_{\mathrm{dipole}} | \psi_c^\Gamma \rangle \langle \psi_c^\Gamma | \mathcal{H}_{\Gamma \mathrm{X}} | \psi_c^\mathrm{X} \rangle}{\Delta_{\Gamma \mathrm{X}}} \right|^2 . \tag{4.10}$$

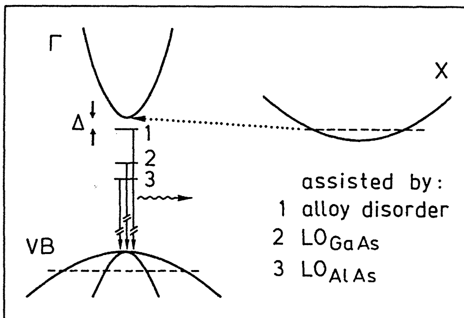

Fig. 4.4. Schematic representation of indirect recombination in $Al_xGa_{1-x}As$ above the crossover point

The detuning between the initial state and the virtual intermediate state (i.e., essentially the energy separation between the Γ and X minima $\Delta_{\Gamma X}$) enters in the energy denominator for elastic scattering from the disorder. In the case of phonon emission or absorption one has to replace the denominator by $\Delta_{\Gamma X} \mp \hbar\Omega_{\text{phonon}}$. For the case of recombination in type-II SLs the spatial overlap of the initial and final wave functions will enter into the scattering matrix element [4.30]. Thus, the transition strength depends on the intervalley coupling strength and varies quadratically with the inverse of the gap-energy difference. We will show in the next section how to deduce the coupling strength from indirect-emission experiments when the gap difference can be tuned systematically, e.g., by application of hydrostatic pressure. The main advantage of such studies is that simultaneously occurring coupling mechanisms can be separated, because they result in isolated emission lines. Finally, a small gap-energy difference in combination with an efficient intervalley scattering process can lead to stimulated recombination at an indirect gap as will be demonstrated in Sect. 4.3 for the case of alloy coupling in indirect-gap $Al_xGa_{1-x}As$.

4.2 Optical Spectroscopy of Intervalley Coupling

4.2.1 Timescales of Carrier Dynamics in Semiconductors

We will describe here how the coupling between different conduction bands can be extracted from optical experiments. The experimental techniques include both time-resolved spectroscopy with modern pico- and femtosecond lasers as well as continuous-wave experiments. We will also compare the results of direct scattering between real states and transitions involving virtual intermediate states, as introduced above.

Intervalley scattering in GaAs and related compounds has recently been investigated by a large variety of experimental methods. In particular, the development of pico- and femtosecond lasers and measurement techniques has triggered numerous experiments. The main intent of these investigations is to understand the fast relaxation processes of hot carriers in semiconductors. Ultrafast lasers have made it possible to directly probe this relaxation, whereas experiments with continuous-wave excitation give only indirect access to these mechanisms, e.g., via the homogeneous broadening of optical transitions. We will show, however, using the example of the phonon-assisted intervalley transfer of electrons that only the combination of both experimental approaches gives useful information on the ultrafast dynamics.

The dynamics of optically generated carriers in a semiconductor can be divided into three major classes of effects: (1) *dephasing*, (2) *thermalization and relaxation*, and (3) *recombination*. The first class (dephasing) encompasses all processes which lead to a loss of the coherence of the optical excitation in

the semiconductor with the driving light field. Dephasing mechanisms are elastic and inelastic scattering processes of the carriers with other carriers, phonons, impurities, or disorder. The timescale of these dephasing processes strongly depends on the actual experimental conditions as well as on sample properties. It can be as short as few femtoseconds as for the dephasing by electron–electron scattering in highly excited GaAs [4.43], or as long as several hundreds of picoseconds to a few nanoseconds for localized excitons in mixed crystals [4.44, 45]. For reviews on such dephasing studies and the wealth of interesting physics related to the regime where the excited polarizations are still in phase, e.g., the optical Stark effect, coherent oscillations and quantum beats, and photon echos, the reader is referred to Refs. [4.46–53].

The second class of dynamic processes includes all mechanisms which lead to the redistribution of the optically generated carriers in the density of states towards a thermal quasi-equilibrium. These are the establishment of a thermal distribution (Fermi–Dirac or Boltzmann), the relaxation to the minima (in the case of the holes to the maxima) of the band structure, the loss of excess energy with respect to these extrema (i.e., carrier cooling), or the heating of carriers [4.55] resonantly excited at $k \approx 0$ to a distribution in equilibrium with the lattice. These processes cover the same time scale as the dephasing processes and are also strongly sensitive to the special experimental conditions like carrier densities or lattice temperature (e.g. [4.56] and Refs. therein).

The third type of process, namely recombination, leads back to the equilibrium in the solid which was perturbed by the optical excitation. Typical recombination times are a few hundred picoseconds to several nanoseconds for direct, and up to milliseconds for indirect recombination.

Intervalley scattering can contribute to all three classes of carrier dynamics. It can be a source of fast dephasing, it leads to efficient relaxation and cooling of the carriers, and is essential for indirect recombination. Studies of the carrier dynamics will thus give useful information on the intervalley transfer. The drawback of most experimental methods, however, is that several relaxation mechanisms occur simultaneously with similar timescales. This is the case, for example, in studies with femtosecond-laser excitation. These experiments are usually carried out with an excitation energy of 2 eV which corresponds to the photon energy of a colliding-pulse mode-locked dye laser. In GaAs this excitation couples states in the heavy-hole, light-hole, and split-off valence bands to the conduction bands. Due to the combined large spectral width of these pulses (up to 100 meV for the shortest pulses of 6 fs), one monitors the relaxation of an enormous spectral distribution of carriers (Fig. 4.5).

In this light, we summarize in the following the experiments on intervalley transfer starting with deformation potential scattering. Most of the ultrafast experiments have to be understood in the sense of giving useful information about the actual relaxation times of the carriers when injected

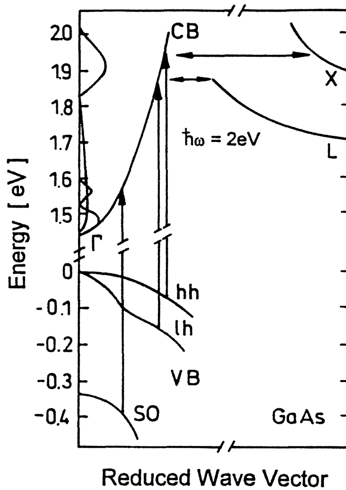

Fig. 4.5. Schematic picture of the band structure in GaAs indicating the optically allowed transitions for 2-eV photons and possible intervalley scattering channels

with high excess energies. This information is essential for the developement of modern ultrafast semiconductor devices. The individual processes however are difficult to isolate and the relaxation times extracted typically describe a combination of different processes such as transfer involving several, different phonon modes. The isolation of various contributions is often better achieved in (quasi-) cw experiments such as an absorption or recombination experiments where the band structure is tuned by the application of hydrostatic pressure. These experiments give much more reliable numbers for the individual intervalley scattering potentials. However, they do not reflect experimental conditions present in actual devices such as lasers, Gunn oscillators, or hot-electron-transfer devices.

4.2.2 Deformation-Potential Scattering

One of the first optical experiments using picosecond laser techniques to study intervalley transfer was the *Raman spectroscopy of non-equilibrium LO phonons* by *Collins* and *Yu* [4.57, 58]. The non-equilibrium or *hot* phonons are created after the injection of electrons into the conduction band with some excess energy. The electrons relax towards the bottom of the band in a phonon cascade emitting LO phonons with a time constant of 165 fs each [4.59]. The lifetime of these phonons (7 ps [4.60]) is considerably longer than the emission time of the electrons so that a nonequilibrium distribution of phonons is established. This effect is mainly responsible for the reduced carrier cooling rates in highly excited semiconductors due to possible reabsorption of the phonons [4.46]. If one monitors the population of these nonequilibrium phonons as a function of electron excess energy, it is expected that one will find a drop once the electrons are able to scatter to one of the side valleys

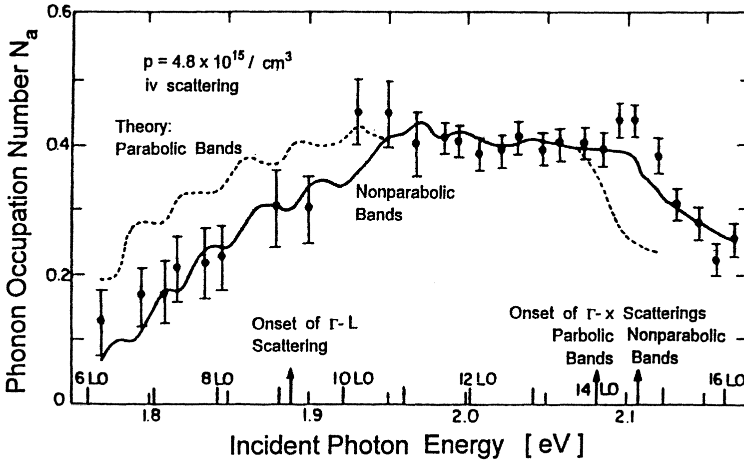

Fig. 4.6. Comparison between experimental nonequilibrium phonon occupation number (solid circles) and theoretical results based on either a parabolic-band model (dashed curves) or a nonparabolic-band model [4.58]

in the band structure and are thus lost for the intravalley relaxation. Such a drop was indeed found for the onset of Γ–X scattering but not for Γ–L scattering in GaAs (Fig. 4.6) [4.57, 58]. The data were modelled using non-parabolic conduction bands and with the *intervalley deformation potentials* $D_{\Gamma X} = 11$ eV/Å, $D_{\Gamma L} \leq 1.5$ eV/Å and $D_{XL} = 2.75$ eV/Å. A possible explanation for the missing effect at the onset of the Γ–L transfer is the rather fast return time of the electrons to the central valley of about 2 ps [4.11, 61], whereas the X electrons return to the Γ valley mainly by a detour via the L valleys [4.11].

In experiments using a similar technique but with subpicosecond laser pulses, *Kim* and *Yu* demonstrated that the intervalley scattering to the L valleys plays an important role in the cooling of the electrons [4.62, 63]. The cooling is significantly faster when the transfer is possible and the temperature of the hot phonons actually overshoots the temperature of the electrons. The deformation potential of $D_{\Gamma L} = 7$ eV/Å extracted from the analysis can be explained from comparison to the theory of *Zollner* et al. [4.11] as resulting from scattering involving LA, LO, and TA phonons.

We will turn now to pump-probe experiments employing femtosecond laser pulses. In these experiments one excites nonequilibrium carrier distributions and probes the initial ultrafast relaxation mechanisms. We are not able to give a complete review of these studies and want to limit our discussion to some key experiments reflecting the influence of intervalley scattering on the ultrafast dynamics.

The so-called *equal-pulse optical correlation technique* was applied by *Tang* and coworkers to test the ultrafast carrier relaxation in GaAs, AlGaAs and GaAs quantum wells [4.64–67]. Two 35-fs laser pulses, which are orthogonally polarized, collinearly propagating, and equal in energy (1.98 eV), are here used to test the saturation of absorption in the region of the optically coupled states. The detected transmission as a function of delay between the pulses reflects the removal of carriers from their initial states after the excitation. The most prominent process leading to a very fast decay of the incoherent component of the signal is attributed to intervalley scattering of the carriers in combination with carrier–carrier scattering for high carrier densities. In bulk GaAs for example, a three-component decay is found with a fast time constant of 34 fs, an intermediate time constant of 160 fs and a slow component of 1600 fs. Ensemble Monte Carlo simulations [4.68] of these results yield an effective deformation potential of $D_{\Gamma L} = 9\,\mathrm{eV/Å}$ at room temperature from the fast component and identify the intermediate decay to result from intravalley scattering with polar optical phonons. The slow component is attributed to band filling of the states in the optically coupled region and consequent cooling of these carriers.

Noncollinear pump-probe measurements but with the same excitation laser (CPM dye laser) were performed by *Lin* et al. on $Al_xGa_{1-x}As$ [4.69, 70]. They find only two decay components of 30 to 13 fs and 1500 fs in GaAs. The slow decay is attributed to the cooling of the carriers after thermalization consistent with the interpretation of *Tang* et al. A comparison of the fast relaxation to studies of *spectral hole burning* leads *Lin* et al. to the conclusion that carrier–carrier scattering is the most important intravalley scattering process in contrast to the interpretation of *Tang* et al. (see also [4.71]). The importance of these two relaxation mechanisms was afterwards long disputed in the literature (e.g. [4.72]). The principal difference in the relaxation dynamics is that with phonon scattering being the dominant mechanism the electrons would sustain a nonthermal distribution and even show cascades in their distribution at multiples of the optical-phonon energy on time scales of several hundreds of femtoseconds. Recent time-resolved luminescence or pump-probe measurements, however, clearly demonstrate that such a cascading does not occur even at rather low carrier densities [4.73, 74]. The thermalization due to carrier–carrier scattering thus appears to be the most efficient process.

Lin et al. further investigated the relaxation dynamics as a function of AlAs mole fraction of their samples. They found a significant reduction of the initial fast time constant with increasing x-value and modifications of the slow component. The experimental results are summarized in Fig. 4.7. The initial decay slows down to 330 fs for $x = 0.40$. There are three main resons for these observations. First, the direct gap increases with x value which reduces the excess energy of the electrons in the optically coupled states. Further, the contribution of electrons excited from the split-off valence band disappears. This diminishes the number of cool carriers close to the bottom of

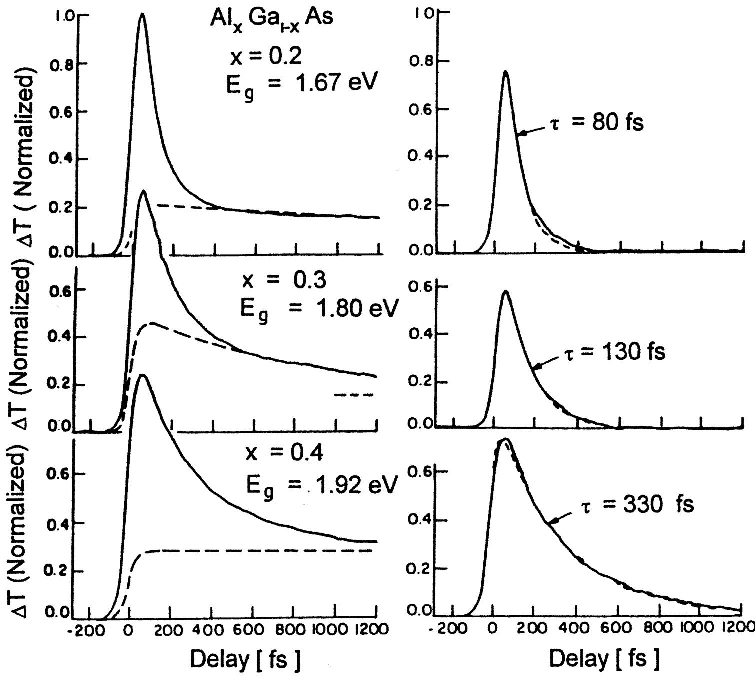

Fig. 4.7. Absorption saturation responses for $Al_xGa_{1-x}As$ with $x = 0.2$, 0.3, 0.4. The traces on the left are experimentally measured data. The traces on the right show the initial rapid transient and are obtained by subtracting the longer response components. Dashed lines indicate the theoretical fits [4.70]

the band which affects both the thermalization by carrier–carrier scattering as well as the cooling (slow time component). Finally, scattering to the X valley gets more and more unlikely and finally impossible with increasing x value. These mechanisms qualitatively explain the observed features. A fast initial relaxation time of 33 fs attributed to Γ–X scattering in GaAs at room temperature was later also determined by *Becker* et al. who applied pulses of 6 fs duration in pump-probe measurements. These experiments delete the requirement to deconvolute decay times shorter than the laser pulse width as in the previously described studies. The drawback of the short pulse duration is the even larger spectral band width and thus carrier spread.

An alternative approach to the determination of intervalley deformation potentials is the investigation of the L to Γ scattering. Carriers excited in the central valley with sufficient excess energy to transfer to the L (or X) valleys will eventually return to the central valley. This mechanism was, for example, pointed out by *Nuss* et al. in a subpicosecond *electro-optic sampling* experiment probing the hot-electron mobility in GaAs [4.75]. A carrier mobility of less than 500 cm^2/Vs was measured immediately after injection indicating

the transfer of the electrons to the low-mobility L minima. The mobility then rose with a time constant between 1.8 and 3.2 ps to a value of 4200 cm^2/Vs reflecting the return of the electrons to the central valley.

Further insight in this phenomenon was gained by the *subpicosecond luminescence experiments* by *Shah* et al. [4.1, 61, 76]. The temporal resolution of luminescence experiments is significantly increased with respect to the streak-camera detection by the use of an up-conversion scheme where the luminescence signal is mixed with the subpicosecond pump pulse [4.77]. Figure 4.8. shows the rise of the luminescence signal close to the band edge as well as the spectrally integrated luminescence in GaAs and InP recorded with this detection method. The excitation wavelength is such that the carriers in GaAs are able to transfer to the L valleys while this process is inhibited in InP. The difference in luminescence rise time is attributed to the this transfer and the subsequent return of the electrons to the central valley. The determination of the actual L–Γ transfer time and potential requires a modelling with ensemble Monte Carlo calculations of the rather complicated scenario. The luminescence dynamics is well reproduced using a $D_{\Gamma L} = 6.5\,\mathrm{eV/Å}$ or a L–Γ return time of 2.5 ps. This rather slow time constant in comparison to the inverse process is simply a consequence of the much smaller effective mass or density of final states in the central valley.

Similar results were found when GaAs luminescence data were compared for excitation with photon energies above and below the onset of transfer to the L minima [4.76]. A time constant of 8 ps is found in the diffracted signal from a *transient grating* in a thin layer of GaAs. This fast decay is attributed to the return of the electrons from the L to the Γ valley [4.78].

These data can be compared to the calculations of *Zollner* et al. (Fig. 4.9) [4.11]. They find a return time of 2.2 ps in good agreement with the result of *Shah* et al. [4.61], but the scattering mechanism involves LA, LO, and TA phonons. An experimentally determined deformation potential can thus only be understood in terms of an effective potential describing the overall scattering process. The scattering time increases by a factor of three between room temperature and low lattice temperatures. This temperature dependence is due to the phonon occupation, where as the deformation potential is temperature independent [4.11, 79]. Also plotted are the scattering times for the

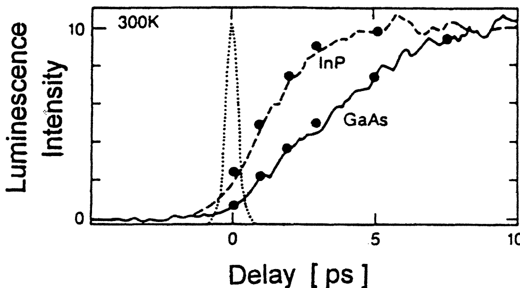

Fig. 4.8. Rise of the near band-gap and integrated luminescence (dots) in GaAs and InP [4.1]

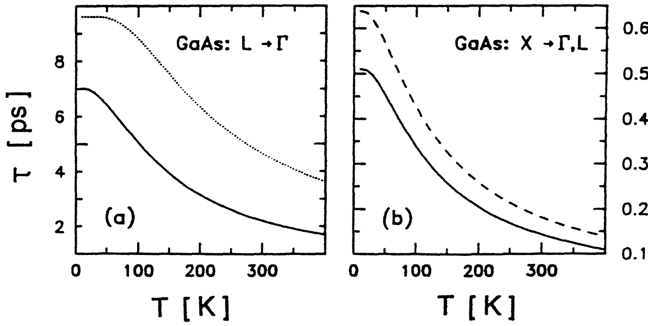

Fig. 4.9. Calculated return times of electrons from the L and X valleys as a function of temperature (solid line). Dotted: TA phonons neglected; dashed: scattering from X to L only [4.11]

return from the X valley. The calculations show that the scattering from the X valley will lead mainly to the L valley as a result of the larger deformation potential. The return to the central valley will thus proceed mainly via the L valley and a intravalley relaxation in these minima as an intermediate step.

We will now turn to spectroscopic methods using cw excitation to probe the intervalley transfer times. A rather elegant method to test these transfer mechanisms in the regime of low carrier densities (i.e., carrier–carrier scattering can be neglected) is the *recombination of non-equilibrium electrons with neutral acceptors* (e,A^0) [4.80–87]. *Mirlin* et al. [4.80, 84] first applied this spectroscopy to determine intervalley scattering times from the depolarization of the luminescence in a magnetic field. They deduced scattering times of 250 fs and 30 fs for Γ–L and Γ–X scattering corresponding to $D_{\Gamma L} = 8\,\mathrm{eV/Å}$ and $D_{\Gamma X} = 15\,\mathrm{eV/Å}$, respectively. It is likely, however, that the carrier scattering processes are modified by the presence of the magnetic field.

The hot (e,A^0) emission displays three series of oscillations on its high-energy side as is illustrated in Fig. 4.10 [4.81]. The optically generated carrier densities in these experiments are so low ($\leq 3 \times 10^{15}$ cm^{-3}) that the previously discussed cascading relaxation of the electrons via the emission of optical phonons is observed. The emission spectra reflect this process in the oscillations which are energetically separated by the LO-phonon energy. Two of the series stem from electrons that are excited from the heavy-hole and light-hole valence bands; these shift with the energy of the exciting laser. The third series is fixed in energy (re-entrant series) and results from the cascading of electrons which have returned to the central valley from the bottom of the L minima. The phonon emission can actually be used as a built-in clock, because the phonon emission time is well known. The intensity of the observed luminescence bands is then given by the relative scattering rate for alternative processes, such as intervalley transfer, in comparison to the LO-

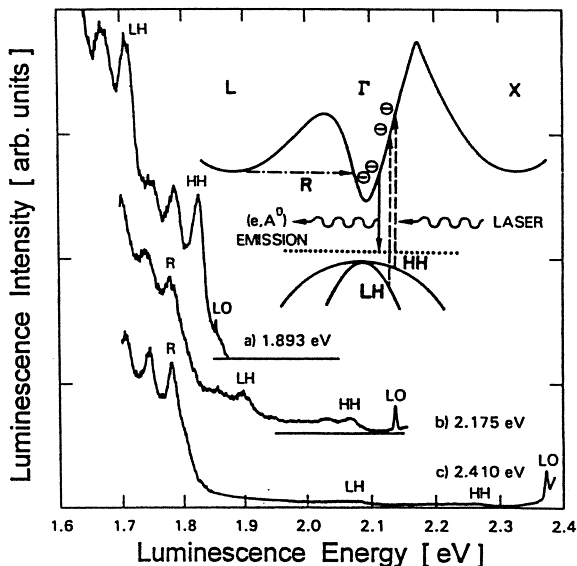

Fig. 4.10. Hot (e,A^0) luminescence spectra at $T = 25\,\mathrm{K}$ for GaAs:Mg for different excitation energies. The origins of the oscillations are illustrated in the inset (LH: light-hole, HH: heavy-hole, R: re-entrant series, LO: Raman peaks) [4.81]

phonon emission rate. The transfer times deduced by *Ulbrich* et al. [4.81] are $\tau_{\Gamma L} = 540\,\mathrm{fs}$ for electrons with 480 meV excess energy and $\tau_{\Gamma X} = 180\,\mathrm{fs}$ for 580 meV excess energy. *Fasol* et al. [4.83, 86, 87] analysed the broadening of the first hot (e,A^0) peak and determined Γ–L scattering times of 150–200 fs and $D_{\Gamma L} = 9.4\,\mathrm{eV/Å}$.

A comparison of the above described cw experiments probing femtosecond time scales to theory was made by *Zollner* et al. (Fig. 4.11) [4.88]. The calculations which include the emission of all possible phonon modes are in

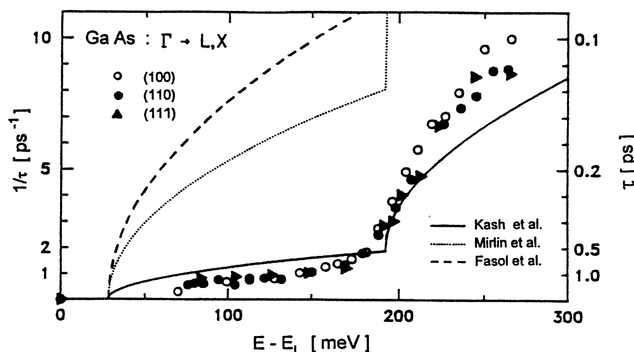

Fig. 4.11. Calculated lifetimes of electrons in the Γ valley with wave vectors along different directions (symbols) as a function of electron energy [4.88]. The solid, dotted and dashed lines give fits with Conwell's formula to experimental data of Refs. [4.81, 84, 87]

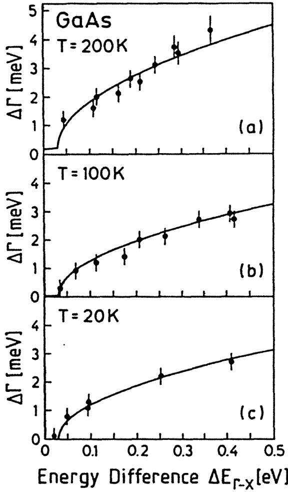

Fig. 4.12. Broadening of the direct exciton absorption line in GaAs for pressure above the crossover point as a function of energy separation between the central and side valleys. Solid lines are fits using *Conwell's* formula [4.89]

reasonable agreement with the modelling of the data by *Ulbrich* et al. using *Conwell's* formula [4.81]. Large deviations are found in comparison to calculated curves when using the deformation potentials measured by *Mirlin* et al. [4.80, 84] and Fasol et al. [4.87]. The reasons for these discrepancies are the possible modifications of the scattering mechanisms in a magetic field in the first case and the influence of alternative mechanisms like the phonon dispersion and other scattering processes on the line broadening in the second case. The discrepancies become even greater at room temperature due to the increasing importance of the transverse phonons.

Finally, we would like to address some experiments which deduce the intervalley deformation potential from the *broadening of excitonic absorption or emission lines* when tuning the separation of the Γ and X minima by application of hydrostatic pressure. *Goñi* et al. [4.89] studied the width of the exciton absorption line at low temperatures for pressures exceeding the crossover pressure. The linewidth increases as a result of the increasing transfer rate for the electron to the side valleys as a function of $\Delta E_{\Gamma X}$ or pressure, respectively (cf. Sect. 2.2). The results for three different temperatures are displayed in Fig. 4.12. The data are modelled with *Conwell's* formula giving a deformation potential $D_{\Gamma X} = 4.8\,\mathrm{eV/Å}$ independent of temperature. Due to the relatively small momentum $\mathbf{k}$ of the final states in the X minima close to the crossover pressure, the influence of transverse phonons is still limited and Conwell's formula might be a reasonable approach. The calculated value of *Zollner* et al. [4.11], however, is still smaller ($D_{\Gamma X} = 2.9\,\mathrm{eV/Å}$).

A relatively high value of $D_{\Gamma X} = 10.7\,\mathrm{eV/Å}$ was deduced by *Satpathy* et al. from the resonance broadening of the direct excitonic emission for pressures above the crossover point [4.90]. The possible reason for the disagreement of this result with the values discussed above is the following: The rather short

transfer times of the electron to the side valley inhibit the formation of a bound exciton state. The observed luminescence (see also Sects. 2.3 and 4.2.3) probably stems from free electron–hole pairs and the observed width reflects the high carrier temperature rather than the lifetime broadening.

We can summarize this section with the following remarks. The intervalley transfer assisted by phonons is reasonably well understood when keeping in mind that the selection rules for the allowed phonon modes are relaxed for scattering between states away from the high-symmetry points. The interpretation of experimental data has to reflect this fact by considering the coupling by all possible phonon modes. Further, the intervalley transfer rates are very sensitive to the lattice temperature as a result of the phonon occupation and the changing relative importance of different phonon modes. When these facts are taken into account, most experimental results can be explained consistently. The main difference between time-resolved and cw experiments is that the time-resolved data typically reflect the relaxation of a spectrally broad ensemble of carriers via several competing scattering mechanisms, while the direct determination of deformation potentials requires a careful preparation of the experimental scenario which is often easier in cw experiments.

4.2.3 Alloy-Disorder-Induced Intervalley Coupling

Alloy-disorder-induced intervalley coupling is a very efficient mechanism in ternary and quaternary semiconductors as was demonstrated by *Kalt* et al. [4.24]. Its importance in indirect optical transitions is reflected in a variety of properties. A strong absorption tail was found in indirect-gap $Al_xGa_{1-x}As$ below the direct gap [4.91], which, from comparison to calculations in the coherent-potential approximation, was attributed in the main to disorder-induced mixing of the X and Γ valleys [4.92]. Strong zero-phonon recombination is characteristic for excitonic or free electron–hole pair luminescence in indirect-gap alloys [4.12, 93, 94], and even indirect stimulated emission was observed (Sect. 4.3) [4.95–98]. On the other hand, not much attention has been paid to this mechanism in the literature in connection with transfer between real band states. No reference to this mechanism was made, for example, in transport studies [4.20, 22, 99] or recent time-resolved measurements [4.69, 70, 100] of the intervalley transfer in alloys. We have already mentioned the large deficiency in the theoretical treatment of disorder-induced *inter*valley coupling, while *intra*valley scattering [4.14–23] has been examined in detail.

We describe in the following a method to determine the effective coupling potential $V_{\Gamma X}^{\text{alloy}}$ between the Γ and X minima induced by alloy disorder in $Al_xGa_{1-x}As$ [4.24]. This disorder-induced potential is extracted from a comparison between phonon-assisted and disorder-assisted indirect recombination

of electron–hole pairs as a function of Γ–X separation. Picosecond excitation and detection techniques are applied to excite high carrier concentrations and to identify unambiguously disorder- and phonon-related recombination mechanisms. Systematic tuning of the band structure by application of hydrostatic pressure allows one to modulate the relative strength of the contributing transfer processes without changing the disorder in the sample or the sample quality. The fact that zero-phonon recombination stems from alloy disorder is deduced from direct comparison with GaAs under hydrostatic pressure.

Investigations of the carrier dynamics were performed in $Al_{0.38}Ga_{0.62}As$ and GaAs which were placed in a diamond-anvil cell with He or Xe as pressure medium [4.101]. The whole cell is part of a He cryostat where lattice temperatures of 5 K are achieved. The pressure cell is warmed up to room temperature each time the pressure is changed to ensure hydrostatic conditions at low temperatures. The crossover pressures, P_c, for the direct and indirect gaps are $P_c = 6.9$ kbar for $x = 0.38$ and $P_c = 40$ kbar for GaAs under high excitation conditions. The crossover pressures are slightly lower than expected for the unexcited samples. This is a result of the differential renormalization of the direct and indirect gaps as was extensively discussed in Sect. 3.2.3 [4.102–104].

The samples were grown by liquid-phase epitaxy on GaAs substrates. The epitaxial layer of the $x = 0.38$ sample has a thickness of 2 μm. The substrate is polished to a thickness of about 40 μm so that the sample is suitable for being placed in the diamond-anvil cell. The GaAs layer is 0.6 μm thick and grown between two 7-μm thick $Al_{0.30}Ga_{0.70}As$ barrier layers. The substrate is completely removed and the sample is used as a free standing double heterostructure. This sample preparation is necessary to eliminate the otherwise dominant luminescence from the substrate. The results are compared to studies on samples which are indirect-gap semiconductors due to their alloy composition. In particular, an epitaxial layer of $Al_{0.42}Ga_{0.68}As$ is used, which is identified from its optical properties to be very close to the crossover point. This sample is also an indirect-gap semiconductor under high excitation (cf. Sect. 3.2.3).

All $Al_xGa_{1-x}As$ layers under investigation are of excellent quality showing both free and donor-bound exciton luminescence lines at very low excitation. The linewidth of the free exciton in the indirect-gap alloys as well as in the direct sample above the crossover pressure is 2–3 meV. Localization occurs only within the low-energy tail of the luminescence line as can be shown by resonant excitation. The bound-exciton line has a width of 6–7 meV as is typical [4.105] for random alloys. More details about the exciton dynamics at the crossover are given in Sect. 2.3.

An electron–hole plasma is generated optically by excitation of the samples with a pulsed (5 ps FWHM), tunable Rhodamine 6G laser which is synchronously pumped by an Ar-ion laser. The luminescence resulting from the bimolecular recombination of the electron–hole pairs is spectrally and tempo-

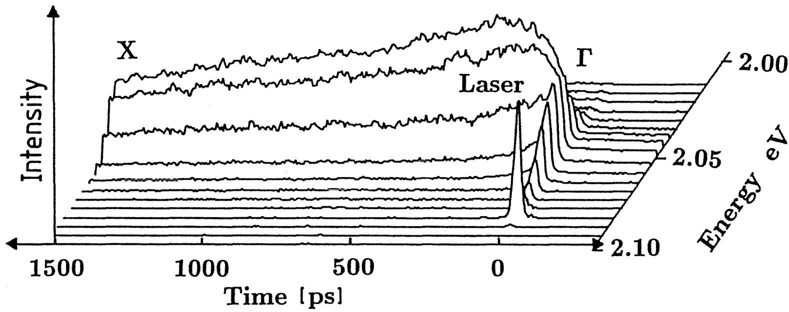

Fig. 4.13. Temporal evolution of the direct (Γ) and indirect (X) luminescence in $Al_{0.42}Ga_{0.58}As$ [4.24]

rally dispersed by a combination of a 0.32-m spectrometer and a synchroscan streak camera. The temporal resolution of this system is about 10 ps. The direct-to-indirect crossover is easily identified with this setup from the dynamics of the luminescence signal.

Figure 4.13 shows an example of the luminescence in $Al_xGa_{1-x}As$ which is just above the crossover point. A long-lived indirect recombination, labeled X, is observed. The direct recombination, labeled Γ, is spectrally broad and disappears within the temporal resolution of the detection system. The separation between the initial Γ and final X states in this sample and under these excitation conditions are smaller than the LO phonon energies (cf. Sect. 2.3). Nevertheless, the rapid disappearence of the direct recombination indicates a fast transfer of electrons from the Γ to the X point which can only be explained by disorder-induced coupling. We will first discuss, however, the features of the long-lived indirect recombination, since it provides quantitative information about the relative efficiency of phonon- and disorder-assisted intervalley scattering processes.

The dynamics of the indirect emission process is greatly influenced by the formation of electron–hole droplets on a timescale of less than 200 ps [4.106]. This accumulation process results in the initial rise of the indirect recombination signal as seen in Fig. 4.13. The experimental proof for the droplet formation in indirect-gap $Al_xGa_{1-x}As$, the phase diagram of the electron–hole system, and the dynamics of the phase separation are described in detail in Sect. 3.5.1. Indirect recombination and droplet formation are observed at this pressure as in the samples with an x-value above the crossover composition.

The excitation conditions were carefully chosen for these experiments such that an electron–hole liquid is formed in all cases. This procedure ensures that the carrier density is fixed for all measurements (even when independent of the excitation level, as is characteristic for a liquid phase). Further, the luminescence stems from defined areas (i.e., inside the droplets), so that both the

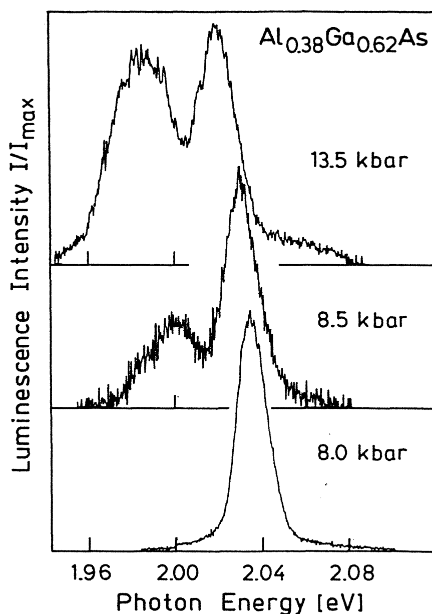

Fig. 4.14. Indirect recombination from electron–hole droplets in $Al_{0.38}Ga_{0.62}As$ for various pressures above the crossover point [4.24]

phonon- and disorder-assisted luminescence originate from the same regions in the sample.

The line shape of the indirect emission strongly depends on the applied hydrostatic pressure as depicted in Fig. 4.14. We find only a single emission line resulting from zero-phonon recombination at 8.0 kbar, i.e., just above the crossover pressure. Additional luminescence at lower photon energies is observed at higher pressures. This broad band is actually a superposition of two phonon side bands, as is evident from the line-shape analysis using the model of Sect. 3.2.1 (Fig. 4.15). We find a growing importance of this phonon-assisted recombination for increasing pressure. Note that the spectra in Fig. 4.14 are normalized to the maximum of the zero-phonon line. The absolute intensities of all emission lines decrease with pressure.

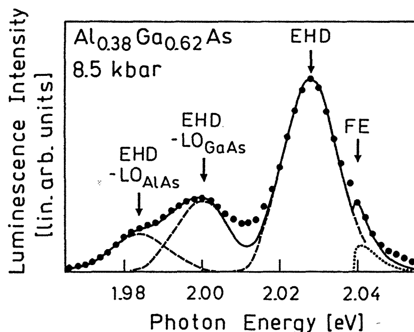

Fig. 4.15. Line-shape analysis of the luminescence (large dots) at 8.5 kbar. Solid line: overall line shape; dashed lines: zero-phonon and phonon-assisted luminescence from the droplets; dotted line: indirect-exciton line [4.24]

A line-shape analysis was performed for the experimental spectra in order to get the relative intensities. The zero-phonon line consists of the electron–hole droplet band (labeled EHD in Fig. 4.15) plus some luminescence from the excitonic gas surrounding the droplets. Both lines are modeled with the usual expressions for indirect recombination processes (more details are given in Sects. 3.2.1 and 3.5.1). The fit parameters used in Fig. 4.15 are the renormalized indirect gap $E'^{X}_{\text{gap}} = 2.011\,\text{eV}$, the carrier density $n = 3.4 \times 10^{18}\,\text{cm}^{-3}$, the carrier temperature $T = 32\,\text{K}$ and the energy of the indirect-gap free exciton FE (2.039 eV). The EHD and FE line shapes are modelled with the same temperature T. The parameters are consistent with the phase diagram of the electron–hole liquid in $\text{Al}_{0.38}\text{Ga}_{0.62}\text{As}$, which is an indirect-gap semiconductor under appropriate hydrostatic pressure [4.106]. The side bands are replicas of the EHD emission and simply shifted by the energy of the GaAs-like and AlAs-like zone-edge LO phonons, respectively. The relative height was treated as a single additional adjustable parameter. It is important to mention that the relative intensities of the droplet bands stay constant for several hundred picoseconds. The side bands of the exciton line give only minor contributions to the overall line shape and are neglected here. The fit procedure excellently reproduces the overall experimental luminescence signal.

The possible indirect recombination processes in indirect-gap $\text{Al}_x\text{Ga}_{1-x}\text{As}$ were already discussed in Sect. 4.1.2 (Fig. 4.4). For a quantitative analysis of the relative scattering efficiencies we apply (4.10) with some simplifications concerning the experimental conditions. Due to a slight band filling in the X valley of typically 6–8 meV, one actually would have to sum over all occupied states in the X minima using the corresponding wave functions ψ_c^X and detunings Δ. Here, we rather take average entities related to the the electron Fermi energy $E^{\text{e}}_{\text{Fermi}}$, where the density of occupied states is highest (Figs. 4.4, 16). This approximation is used in the case of the zero-phonon as well as the phonon-assisted recombination, and should thus not significantly influence the interpretation of the relative luminescence intensities. The operator $\mathcal{H}_{\Gamma X}$ in (4.10) is the intervalley coupling via the deformation potential in the case of the phonon-assisted recombination [4.11, 79] or the coupling via disorder, respectively. Only scattering involving LO phonons has to be taken into account here. For symmetry reasons, LO phonon processes are the only ones allowed for scattering between the Γ and X points [4.10]. These symmetry restrictions, however, can be relaxed to some extent by the presence of disorder [4.107]. Additionally, phonon branches other than the LO become increasingly important when states away from the highest symmetry points are involved [4.11]. The X states in our experiment, however, are still rather close to the X point. The luminescence line shape under both high excitation (Fig. 4.15) and low excitation conditions (Sect. 2.3) show that only the two LO phonon modes efficiently contribute to the indirect recombination. The dipole operator $\mathcal{H}_{\text{dipole}}$ is assumed to be identical for all transitions, because it couples the same states in the conduction and valence bands for each case,

and the energy difference between the various emitted photons is small with respect to their absolute photon energies.

The transition probability is thus sensitive to the energy difference $\Delta_{\Gamma X}$ (or $\Delta_{\Gamma X} + \hbar\Omega_{LO}$) and the intervalley coupling strength $|\langle\psi_c^\Gamma|\mathcal{H}_{\Gamma X}|\psi_c^X\rangle|^2$. By application of hydrostatic pressure to an $Al_xGa_{1-x}As$ sample it is possible to systematically tune the former quantity, while the latter one is kept essentially fixed. Pressure-induced distortions of the X-point wave functions are expected to be small in the applied pressure range. The same dependence of the transition probability on the detuning Δ is found in the case of indirect stimulated emission in $Al_xGa_{1-x}As$ (Sect. 4.3) [4.97]. This stimulated process occurs for the zero-phonon component of the luminescence. A quadratic increase of the threshold for the stimulated emission with Δ is found here, as expected from (4.10).

The pressure dependence of the luminescence in Fig. 4.14 is easily intelligible from (4.10) and the schematic depiction of the indirect recombination processes in Fig. 4.4. The detuning $\Delta_{\Gamma X}$ for the zero-phonon process is much smaller than the detuning $(\Delta_{\Gamma X} + \hbar\Omega_{LO})$ for the phonon side bands given a small separation between the Γ and X minima (i.e., just above the crossover) (Fig. 4.4). The transition probability is thus much larger for the former process. With increasing pressure, and thus increasing Γ–X separation, the difference between the detunings becomes increasingly unimportant relative to their absolute values. For the limit of infinite pressure the ratio $I_{\text{phonon}}/I_{\text{alloy}}$ is determined only by the relative coupling strengths $|\langle\psi_c^\Gamma|\mathcal{H}_{\Gamma X}^{\text{alloy}}|\psi_c^X\rangle|^2$ and $|\langle\psi_c^\Gamma|\mathcal{H}_{\Gamma X}^{\text{phonon}}|\psi_c^X\rangle|^2$. From the comparable intensities of the zero-phonon line and the phonon side bands at high pressures (Fig. 4.14) one can directly conclude that the intervalley coupling via LO phonons and via disorder have to be of the same order of magnitude.

The ratio of the transition probabilities is given by:

$$\frac{I_{\text{phonon}}}{I_{\text{alloy}}} = C\frac{\Delta_{\Gamma X}^2}{(\Delta_{\Gamma X} + \hbar\Omega_{LO})^2} , \tag{4.11}$$

with a relative coupling strength C:

$$C = \left|\frac{\langle\psi_c^\Gamma|\mathcal{H}_{\Gamma X}^{\text{phonon}}|\psi_c^X\rangle}{\langle\psi_c^\Gamma|\mathcal{H}_{\Gamma X}^{\text{alloy}}|\psi_c^X\rangle}\right|^2 . \tag{4.12}$$

The only unknown quantity in (4.11) is the transition probability for the alloy-disorder-assisted transfer. The experimental determination of this quantity (or of C) follows directly from the pressure dependence of the relative intensities of the phonon replicas and the zero-phonon line.

The relative emission intensities are plotted in Fig. 4.16 as a function of the detuning Δ. The ratio $I_{\text{phonon}}/I_{\text{alloy}}$ rises from roughly zero to about unity for increasing pressure. The solid and the dashed lines in Fig. 4.16 are calculated from (4.11) using values of $C = 1.75$ (GaAs-like) and 2.0 (AlAs-like). These calculated curves give good agreement with the experimental

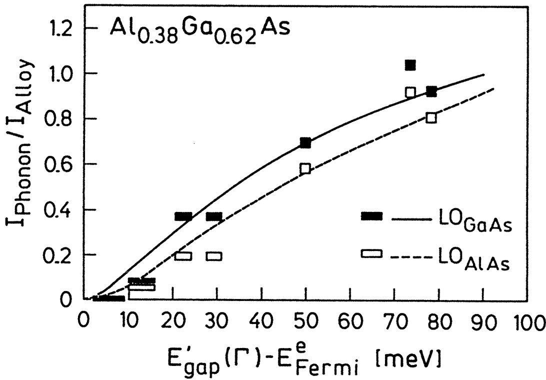

Fig. 4.16. Ratio of phonon-assisted recombination I_{phonon} with respect to zero-phonon emission I_{alloy} as a function of the detuning $\Delta = E'_{\mathrm{g}}(\Gamma) - E^{\mathrm{e}}_{\mathrm{Fermi}}$ [4.24]

points. Some deviations close to the crossover point ($\Delta \approx 0$) are probably due to the relatively large uncertainty in the determination of Δ in this range. The AlAs-like LO phonon side band is found to be weaker than the GaAs-like one in the range of pressures used in our experiment. It turns out, however, that this is actually a result of the larger detuning ($\Delta + \hbar\Omega_{\mathrm{LO}}$) for the former with respect to the latter due to the larger phonon energy. The calculated curves in Fig. 4.16 cross for higher pressures, i.e., the AlAs-like replica is strongest in the limit of high pressures. This pressure range, however, is not accessible to our experiment.

The determination of C from Fig. 4.16 yields two important results. First, the intervalley coupling induced by the alloy disorder is about half as strong as the coupling via the deformation potential related to each of the possible LO phonon modes. The latter was found to be very efficient ($D = 4.8\,\mathrm{eV/Å}$) for GaAs [4.89], and is not expected to change dramatically with x-value. We conclude that alloy-disorder-assisted intervalley coupling also has to be taken into account as fairly strong transfer mechanism, in particular for recombination close to the crossover point and for Γ–X scattering of electrons with low excess energy as will be described below.

The second important result is a determination of the relative strength of the phonon-assisted processes, which strongly depends on the AlAs-mole fraction. We find a relative strength of the AlAs-like phonon coupling $C_{\mathrm{AlAs}}/(C_{\mathrm{AlAs}} + C_{\mathrm{GaAs}}) = 0.53$, i.e., the AlAs-phonon processes, even in $\mathrm{Al_{0.38}Ga_{0.62}As}$ where the x-value is still considerably smaller than 0.50, are slightly stronger than the GaAs-phonon ones. This result compares well to the value of 0.56 which was determined for this x-value in the case of intravalley Fröhlich scattering [4.108]. The larger interaction between electrons and the AlAs-like LO phonons is a consequence of the higher polarizability (or longitudinal–transverse splitting) of these phonon modes with respect to the GaAs-like ones [4.108–110].

We will now use the relative probabilities for disorder- and phonon-assisted intervalley transfer to estimate the scattering times for Γ–X transfer

of electrons and, finally, the disorder-related intervalley potential $V_{\Gamma X}^{\mathrm{alloy}}$. We start these calculations from the experimental value [4.89] of the intervalley deformation potential in GaAs of 4.8 eV/Å, which is in good agreement with the theory of *Zollner* et al. [4.11]. The experimental value was determined from the line broadenings of the excitonic absorption in GaAs under hydrostatic pressure. Here, of course, only GaAs-like LO phonons contribute to the intervalley coupling.

It is a reasonable assumption that the overall intervalley coupling involving LO phonons stays about constant when increasing the AlAs mole fraction to the value of $x = 0.38$ used in our experiments. The coupling is then distributed roughly equally among the two contributing phonon modes, i.e., the GaAs-like and the AlAs-like LO phonons. This sum rule was found, for example, for the case of the intravalley Fröhlich interaction in $\mathrm{Al}_x\mathrm{Ga}_{1-x}\mathrm{As}$ [4.108]. As a consequence, the alloy-disorder-induced Γ–X scattering times should be about four times longer than the times found in GaAs.

Quantitative estimates can be obtained from the expressions for the intervalley transfer rates as described above (Sect. 4.1.1). In the case of low temperature (5 K), when only phonon emission is possible and the occupation of the optical phonons is negligible, the transfer rate for deformation potential scattering (4.5) reduces to:

$$\frac{1}{\tau} = \frac{D_{\Gamma X}^2\, m_X^{3/2}}{\sqrt{2}\,\pi\,\hbar^2\,\rho\,\hbar\Omega_{\mathrm{LO}}}\,(\Delta_{\Gamma X} - \hbar\Omega_{\mathrm{LO}})^{1/2}\,. \tag{4.13}$$

The mass m_X is here the combined mass for three equivalent ellipsoids and ρ is the material density. The Γ–X scattering time for electrons in the Γ minimum with an excess energy $(\Delta_{\Gamma X} - \hbar\Omega_{\mathrm{LO}})$ of 100 meV is calculated from (4.13) to be 250 fs. We can conclude from the above-mentioned sum rule that the scattering times for the intervalley transfer involving GaAs-like and AlAs-like LO phonons have to be 500 fs each. The intervalley deformation potentials for $\mathrm{Al}_{0.38}\mathrm{Ga}_{0.62}\mathrm{As}$ are then: $D_{\Gamma X}^{\mathrm{GaAs}}(x = 0.38) \approx D_{\Gamma X}^{\mathrm{AlAs}}(x = 0.38) \approx D_{\Gamma X}(x = 0)/\sqrt{2} = 3.4\,\mathrm{eV/Å}$.

The intervalley scattering times for the alloy-disorder-related transfer are hence of the order of 1 ps. We use the expression for the intervalley scattering rate given in Sect. 4.1.2 (4.8). With a lattice constant $a(x = 0.38) = 5.66 \times 10^{-8}$ cm and $x(1 - x) = 0.236$ one finds:

$$\frac{1}{\tau} = 2.55 \times 10^{14}\,\mathrm{s}^{-1}\,\mathrm{eV}^{-5/2}\,(V_{\Gamma X}^{\mathrm{alloy}})^2\,(\Delta_{\Gamma X})^{1/2}\,. \tag{4.14}$$

Inserting the estimated scattering time of 1 ps for $\Delta_{\Gamma X} = 100$ meV we find $V_{\Gamma X}^{\mathrm{alloy}} = 110$ meV.

The relative coupling strengths were determined here for an AlAs mole fraction of $x = 0.38$. It is straightforward to estimate the effect of the disorder for higher x-values using the simple ansatz $1/\tau \propto x(1 - x)$ (4.8), because the

x-dependence of the effective mass m_X is negligible. The Γ–X transfer rate will be about 6% higher for $x = 0.50$ than for the sample under investigation. The changes in the range of medium alloy compositions are thus expected to be rather minor.

Our experimental value for the alloy scattering potential $V_{\Gamma X}^{\text{alloy}}$ is in reasonable agreement with the theoretical result of *Güncer* and *Ferry* [4.25]. Their calculations of the wave-vector-dependent scattering potential give a value of about 78 meV for the Γ–X coupling. They also show that the scattering potential between the L and Γ minima is only about one half of the X–Γ value.

A value of about 200 meV for the intervalley disorder potential was determined by *Sturge* et al. [4.93] from the decay dynamics of localized indirect excitons. In these experiments the random nature of the lattice-potential fluctuations was observed to result in a nonexponential decay of localized excitons. The localization in areas of different composition leads to a distribution of recombination rates as a consequence of the microscopically random degree of Γ–X mixing. The resulting decay of the localized excitons is nonexponential in agreement with the theory of *Klein* et al. [4.111]. Free excitons or carriers, on the other hand, average over the compositional variations and recombine with an exponential decay law, as is also observed in our studies.

The value used by *Grein* et al. [4.13] in a theoretical modelling of alloy-disorder-induced intervalley scattering was 510 meV, taken from the difference in electron antibonding. This value appears to be much too high and the calculated scattering times are far from being realistic. The calculated x-dependence of alloy scattering of Ref. [4.13] was compared to ellipsometry and Raman data of line broadening at the E_0 gap. Such direct comparison is only useful for line broadening in the excitonic absorption in GaAs under hydrostatic pressure as analysed by *Goñi* et al. [4.89]. This type of comparison, however, is questionable in the case of the ternary compounds. First, the exciton line here is inhomogeneously broadened [4.105, 112]. Second, it is evident that a definite separation of the alloy-disorder-assisted processes from the phonon-asssisted ones is only achievable when the latter are not possible. This situation occurs only in a narrow spectral region close to the crossover point. Here, however, the intervalley scattering of excitons into both bound states of the indirect exciton and continuum states is possible, which makes the analysis of such an experiment impossible. Evidence for disorder-assisted transfer for such near-resonant conditions, but at high excitation levels, where the exciton resonances are screened, will be given below.

All other available values for alloy-disorder scattering are deduced from intravalley transfer. The unknown distribution of the potential clusters sizes in $Ga_xAl_{1-x}As$, as introduced in the model of *Oosaka* [4.26], and thus the values of the Fourier coefficients, make a direct comparison to the intervalley results difficult. The extracted potentials are always effective values, which are valid for completely different wave-vector ranges. Still, the intravalley poten-

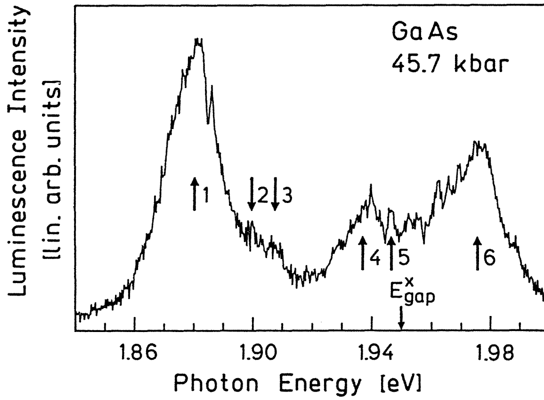

Fig. 4.17. Luminescence in GaAs above the crossover pressure for excitation with $150\,\mu J/cm^2$. The attribution of the arrows 1–6 is described in the text [4.24]

tials are of similar magnitude as the intervalley ones: 120 meV and 300 meV as calculated by *Ferry* [4.17] and *Saxena* [4.20], respectively, from the electronegativity difference. A value of 145 meV was deduced by *Rode* and *Fedders* [4.21] from a fit to data taken by *Chandra* and *Eastman* [4.18], using an effective charge model rather than potential wells.

Measurements in GaAs under hydrostatic pressure confirm that the zero-phonon processes in $Al_xGa_{1-x}As$ indeed result from alloy disorder. Only one indirect-emission band (labeled 1 in Fig. 4.17) is observed for pressures above the crossover point. No droplet formation is found within the luminescence decay time [4.106]. The low-energy tail of the electron–hole plasma line is considerably shifted with respect to the indirect band gap in the unexcited sample (Fig. 4.17). This shift is consistent with a band-gap renormalization of about 50 meV, as expected for carrier densities of $3 \times 10^{18}\,cm^{-3}$ [4.102–104], plus the shift by the energy of the emitted GaAs LO phonon of about 32 meV.

The additional structures on the high-energy tail of this luminescence band (2) and (3) can be attributed to recombination of free excitons and excitons bound to neutral donors [4.113]. The energy shift of these lines with respect to E^X_{gap} corresponds well to the phonon energy (32 meV) plus the binding energy of 11 meV for the indirect exciton. The donor-bound exciton is further shifted by its binding energy of 10 meV. This excitonic luminescence apparently originates from areas in the sample which are less strongly excited. These luminescence bands are sustained for a long time after the picosecond excitation and also dominate the emission at low excitation levels. The same emission bands and binding energies are found in indirect-gap $Al_xGa_{1-x}As$, where, however, additional zero-phonon lines and the AlAs-like phonon sideband are observed (cf. Sect. 2.3).

The luminescence at photon energies above 1.93 eV originates from the $Al_{0.30}Ga_{0.70}As$ barriers which are also indirect-gap materials at such pressures. These barriers are excited by indirect absorption into the X minima assisted

by the intervalley transfer processes discussed above. The direct gap in the barriers is larger than the photon energy of the laser, which makes direct absorption impossible. The indirect absorption is strong enough to lead to a sizable population in the X minima. This excitation, however, is somewhat inhomogeneous in depth and the luminescence features are thus not very well resolved. Especially, bound-exciton luminescence from less excited regions perturbs the emission line shape. The arrows (4)–(6) in Fig. 4.17 indicate the expected energetic positions of the sidebands (4),(5) and the zero-phonon line (6) of the plasma emission. A detailed analysis of this luminescence is not useful due to the inhomogeneous excitation, but its origin as indirect emission from the barriers is unambiguous. Direct emission from the Γ minimum in the GaAs occurs in the same spectral region, but disapears right after the laser pulse due to fast phonon-assisted intervalley scattering (cf. the discussion below). The barrier luminescence, however, has a decay time in the nanosecond range. Direct and indirect luminescence can further be identified from their shift with pressure, which exactly corresponds to the shift expected from the pressure coefficients [4.114, 115].

These measurements on GaAs show that zero-phonon emission is negligible here. The processes described above are thus indeed related to the alloy disorder, which is the only difference between the samples.

We finally address the direct recombination observed in indirect-gap semiconductors. A spectrally broad but temporally short luminescence from the Γ minimum is observed during the excitation (Figs. 4.13, 18, 19) for all indirect-gap materials [4.94, 116]. The identification of this emission line is easily made from both its pressure dependence, which shows a shift of about 10 meV/kbar characteristic of the direct gap [4.115], and its temporal behavior (Fig. 4.19).

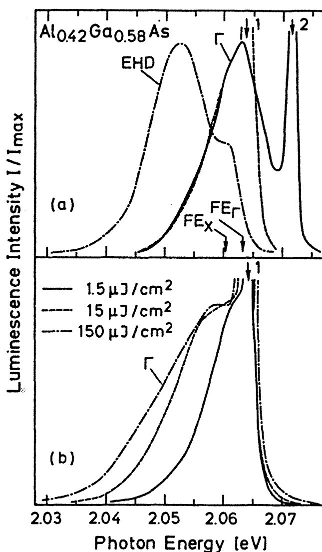

Fig. 4.18. Direct luminescence (Γ) in indirect-gap $Al_xGa_{1-x}As$ for excitation at different photon energies (**a**) and with different excitation levels (**b**). The dashed-dotted line in (**a**) is the indirect luminescence taken 200 ps after the excitation [4.24]

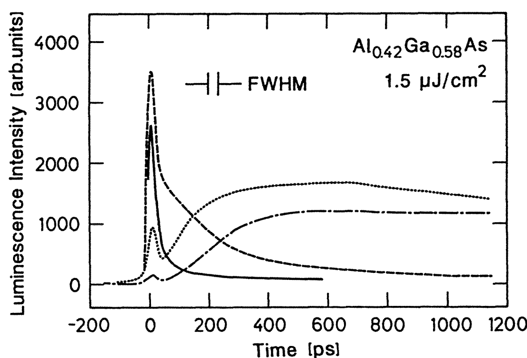

Fig. 4.19. Temporal development of the luminescence depicted in Fig. 4.18a for excitation at 2.072 eV (arrow 2) at various photon energies (solid: 2.066 eV, dashed: 2.062 eV, dotted: 2.050 eV, dashed-dotted: 2.045 eV) [4.24]

For high excitation levels this luminescence band extends to photon energies well below the energy of the renormalized indirect gap (Figs. 4.13, 18b, 19). We attribute this tailing mainly to a lifetime broadening of the electron states in the central valley resulting from fast scattering of these carriers.

The Γ-luminescence signal follows the temporal shape of the picosecond excitation pulse. This is demonstrated in Fig. 4.19, which shows the temporal development of the luminescence for excitation conditions as in Fig. 4.18a with the laser being at position (2). A fast luminescence component with the same FWHM as the laser pulse (indicated in Fig. 4.19) is visible for photon energies as low as 2.045 eV, which shows the strong tailing of this signal to low energies. Luminescence only from the Γ minimum is detected at 2.066 eV (solid line). This short direct emission is followed by indirect emission at photon energies of 2.062–2.045 eV. Within the first 200 ps a phase separation into an exciton gas and electron–hole droplets occurs, reflected by the decreasing signal at 2.062 eV and the rising signal in the range of the droplet band (dotted and dashed-dotted lines). The dynamics of this process is desribed in detail in Sect. 3.5.1.

Additional strong indications of an efficient alloy-disorder-related transfer of electrons from the Γ to the X minima are deduced from near-resonant-excitation studies in samples just at the crossover point. The configuration of the conduction band minima is chosen by a suitable x-value or pressure in such a way that the sample is an indirect-gap semiconductor under high-excitation conditions. The relative separation of the renormalized band gaps, however, is smaller than the energy of the LO phonons in this ternary materials. Phonon-assisted transfer between the Γ and X point in this material system is only allowed with the assistance of LO phonons [4.10]. The band-gap energies are determined from the luminescence signals during and after the picosecond excitation (Fig. 4.18).

The separation between the Γ and X minima of the conduction band in multi-valley semiconductors is determined by the number of carriers populating each minimum. The carriers are initially deposited predominatly in the central minimum by direct absorption during the excitation. The lumi-

nescence is detected only close to the band edge independent of the excess energy of the laser, i.e., only electrons which had the chance to relax within the central valley are detected. This observation is a clear indication of a fast intravalley scattering. When carrier scattering into the side valley is possible, particularly in the case when it is faster than the duration of the laser pulse, the latter minimum will strongly renormalize as a result of the large effective mass, and the corresponding high population of this minimum with respect to the Γ minimum. The different populations, and thus different contributions of the electron-exchange interaction to the renormalization of each valley, lead to a differential band-gap shrinkage [4.102–104]. The minima at the Γ and X point in $Al_{0.38}Ga_{0.62}As$ at 6.9 kbar are separated from near alignment in the unexcited case by up to about 40 meV for the highest achievable carrier densities ($n = 6 \times 10^{18}\,cm^{-3}$ for the self-confined plasma phase) [4.106]. The observed renormalizations are in good agreement with the model of Sect. 3.2.3. The differential renormalization of the valleys thus gives us a means of tuning their relative separation via the excitation level. The tunability of the excitation laser additionally provides the possibility of adjusting the excess energy of the electrons excited in the Γ minimum.

The Γ luminescence recorded at $t = 0$ ps as a function of excess energy and intensity of the laser is shown in Figs. 4.18(a) and (b), respectively. The low-energy tail of the direct luminescence does not depend on the excess energy of the laser for low excitation levels [Fig. 4.18(a)]. Only the high-energy part of the spectra differs for excitation at position 1 and 2. This reflects the higher carrier temperature in the latter case. The dashed-dotted line in Fig. 4.18(a) shows the indirect emission at a time of 200 ps after the excitation. We select this rather large delay because the phase separation into the liquid and excitonic phases has then occurred. The luminescence shows clearly the structure of a droplet band (EHD) and the free-exciton emission (FE_X) originating from the low-density excitonic gas surrounding the droplets. This line shape makes it easy to identify the position of the indirect exciton. The spectrum observed immediately after the laser pulse has ceased is actually not much different. Only indirect luminescence is additionally detected at a 15 ps delay. The spectrum is shifted by about 5 meV to higher energies and the excitonic structure has not evolved yet.

The excitation at position 1 in Fig. 4.18(a) is resonant with the free exciton at the Γ point, the energy of which is known from the low excitation luminescence. The energy is thus even lower than the continuum states related to the X minima (i.e., the indirect gap in the unexcited sample). The renormalization of the gap resulting from the excited carrier density dynamically rearranges the ordering of the minima during the laser pulse and the band gaps shift below the photon energy of the laser. But, even when all electrons have transferred to the side valleys at the end of the laser pulse, the excitation energy is still less than one LO-phonon energy above the renormalized X minima around 2.04 eV. Nonetheless, the Γ luminescence rapidly

disappears and only the indirect luminescence is detected after the excitation, which indicates an efficient Γ–X transfer of the electrons in a scenario where phonon-assisted scattering is not possible.

The low-energy tail of the direct luminescence broadens with increasing excitation fluence [Fig. 4.18(b)]. The central valley becomes populated during the excitation process right up to the laser energy. The red shift of the luminescence band reflects the increasing renormalization with rising population of the Γ minimum. Again, in all cases only the indirect emission is observed after the excitation, although phonon-assisted scattering is still not possible.

There are good arguments that electron–electron scattering and even coherent excitation of electron pairs at opposite k vectors should not contribute significantly to the zero-phonon processes. Electron–electron scattering should also be detectable for the reversed scattering process (i.e., indirect recombination). The measurements in GaAs (see above), however, show that this is not the case. Only phonon-assisted processes are significant in this case. Coherent scattering can be excluded by the fact that the direct luminescence is detected close to the band gap. The electrons thus rapidly relax within the central valley and lose their coherence. This leaves only the disorder-assisted scattering which was already shown to be efficient.

The line shape of the direct band-to-band luminescence in indirect gap $Al_xGa_{1-x}As$ is unfortunately not well suited for a quantitative analysis of the intervalley coupling strength via the alloy-disorder potential. The high-energy tail of the luminescence band is determined by temperature and band-filling effects, as discussed above. The low-energy tail shows a significant broadening with respect to the square-root dependence expected for direct recombination. This broadening, however, is a superpositon of several contributions such as lifetime broadening due to inter- and intravalley scattering and final state damping (Landsberg broadening [4.117]). The relative positions of the Γ and X minima shift continuously during the scattering process as a result of the band-gap renormalization. An unambiguous quantitative analysis of the direct luminescence line shape in indirect-gap $Al_xGa_{1-x}As$ seems to be impossible and was not attempted. Lower limits of the transfer times can only be estimated from the broadening of the low energy tail of the direct luminescence with respect to the square-root shape. This gives limits on the order of few hundred fs [4.118].

We can summarize at this point by saying that alloy-disorder in ternary compounds like $Al_xGa_{1-x}As$ leads to a very efficient coupling of the central valley of the conduction band to the sidebands. We determine the strength of the Γ–X coupling via alloy disorder to be about 25% of the coupling via the deformation potential, which involves two LO-phonon modes. The transfer assisted by AlAs-like LO phonons is found to be slightly stronger than for scattering employing GaAs-like LO phonons in $Al_{0.38}Ga_{0.62}As$. The indirect zero-phonon recombination is dominant just above the crossover compositon or pressure, while reference measurements in GaAs under hydrostatic

pressure show that here sigificant indirect recombination is only possible via emission of GaAs-like LO phonons. This confirms that the zero-phonon processes in the ternary compounds stem from alloy disorder. The efficiency of disorder-assisted intervalley scattering is further demonstrated by the properties of direct recombination in indirect-gap $Al_xGa_{1-x}As$. This luminescence disappears right after the picosecond excitation even when phonon-assisted scattering is not possible.

4.2.4 Real-Space Transfer in Type-II Heterostructures

Information on the *real-space transfer* of electrons in type-II heterostructures can be gained from time-resolved differential-transmission spectroscopy. Here one probes the change of transmission after generation of electron–hole pairs with respect to the unexcited case in the region of the direct exciton resonances in the GaAs or $Al_xGa_{1-x}As$ slabs as a function of time. The excitonic absorption is bleached after the excitation due to screening and phase-space filling, as was discussed in Sect. 3.1. In contrast to the temporal behavior in type-I heterostructures, one finds a fast initial decay of this bleaching in type-II structures, which was attributed by *Feldmann* et al. [4.28] and *Saeta* et al. [4.29] to the fast transfer of the electrons to the AlAs slabs.

Examples of these experimental observations are displayed in Figs. 4.20, 21. Besides the bleaching of the lh and hh exciton absorption, a bleaching of the transition involving the split-off valence band is found, which can only result from the electrons in the Γ minimum because no holes are excited in this band for excitation at 2.0 eV. The temporal evolution of the differential transmission shows a fast partial recovery for all three transitions due to the carrier

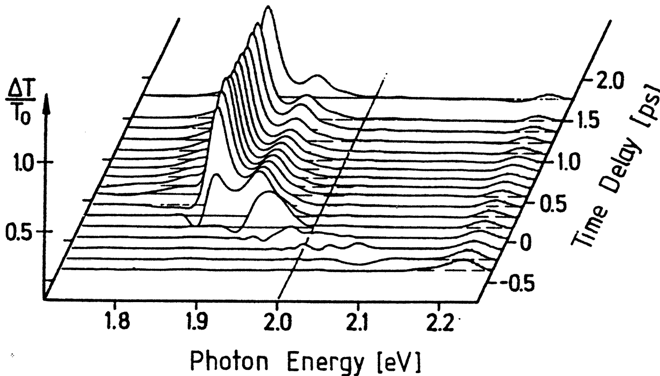

Fig. 4.20. Energy- and time-resolved differential transmission spectra in a $(GaAs)_{11}/(AlAs)_{24}$ SPSL at $T = 10\,K$. The varying onset of the signal as a function of photon energy is a result of the chirp in the probe pulse [4.30]

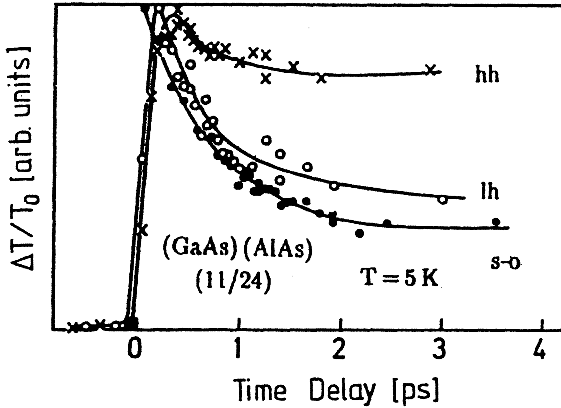

Fig. 4.21. Temporal evolution of the differential transmission signal at the hh, lh, and split-off transitions in the $(GaAs)_{11}/(AlAs)_{24}$ SPSL [4.30]

transfer (Fig. 4.21). The remaining signal for longer delay times is related to the filling of the hole states (only in the case of the hh and lh transitions) and to screening by the now spatially separated electron–hole pairs.

A systematic study of the Γ–X transfer times as a function of layer thicknesses in GaAs/AlAs SPSLs and $Al_xGa_{1-x}As/AlAs$ QWs revealed that these times depend strongly on the spatial overlap of the initial and final state wave functions [4.28, 30]. In particular, the transfer was sensitive to the thickness of the (Al)GaAs layers but not to the thickness of the AlAs. The transfer time is plotted as a function of the calculated overlap for the envelope wave functions S_{X_z} in Fig. 4.22. This plot, which is based on the assumption that the scattering is elastic and proceeds to the X_z states only, demonstrates the expected dependence on the overlap. The fit to the data is actually much better than for the case where the overlap to all final X-point states is calculated. These results indicate that the mixing via the superperiodicity is the main coupling mechanism in GaAs/AlAs SPSLs.

The role of the phonon-assisted scattering can be deduced from the temperature dependence of the scattering rate. Such a dependence is found for $Al_xGa_{1-x}As/AlAs$ type-II quantum wells. These structures can be designed with larger well width because of the larger direct gap than in GaAs. The scattering time shows an increasingly strong rise from room temperature to low temperatures for larger well width reflecting the greater importance of the phonons. No such temperature dependence is found in the GaAs/AlAs SLs with thicknesses below 12 monolayers. The elastic coupling via the mixing potentials dominates in these ultrathin structures [4.30].

The latter finding is supported by the pressure-dependent experiments of *Nunnenkamp* et al. [4.31]. Here, a transition from type-I to type-II band alignment is achieved by application of hydrostatic pressure to a $(GaAs)_{15}/(AlAs)_5$ SPSL. This transition is reflected in the differential transmission transients at the direct transition (Fig. 4.23). The transient at low pressure shows the typical type-I behavior: a fast rise of the bleaching due to screening

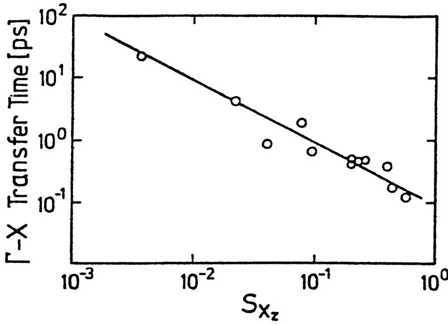

Fig. 4.22. Experimentally determined Γ–X transfer times versus calculated overlap S_{X_z}. The solid line reflects the expected theoretical behavior (Sect. 4.1) [4.30]

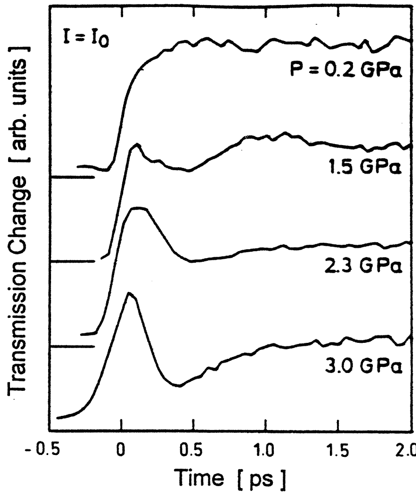

Fig. 4.23. Differential transmission transients for the type-I transition of a $(GaAs)_{15}/(AlAs)_5$ SPSL at various pressures [4.31]

by the excited carriers and phase-space filling followed by a long decay of the signal over several hundred picoseconds due to radiative and nonradiative recombination. The signal at higher pressures displays the fast rise and the subsequent transfer-induced rapid decay followed by some slow rise due to the cooling of the holes. The long-living signal is then caused by the hole phase-space filling and screening due to the carriers present in the whole structure.

The analysis of these experiments (Fig. 4.24) leads to following conclusions [4.31]: The transfer from the GaAs Γ to the AlAs X valleys occurs after a fast relaxation of the electrons within the Γ minimum. Due to the formation of minibands in the structure, the decay time decreases with the separation of the Γ and X valleys (i.e., with pressure) according to $\tau \propto \Delta_{\Gamma X}^{-1/2}$ in a manner which is similar to the behavior in bulk material (solid line in Fig. 4.24). The crossover pressure is shifted to a lower pressure $P_{c_{dyn}}$ for high excitation levels as a result of the differential gap renormalization (see discussion in Sect. 3.2.3). A further depletion of the electron population in the central valley of the GaAs layers is found when the pressure exceeds the Γ–X crossover

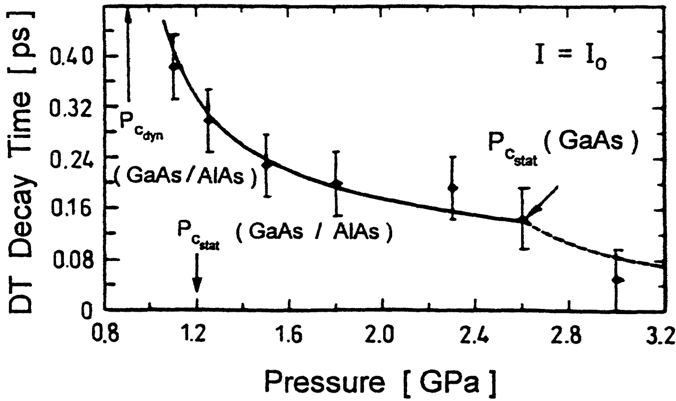

Fig. 4.24. Differential transmission decay times for the type-I transition of a $(GaAs)_{15}/(AlAs)_5$ SPSL as a function of pressure [4.31]

pressure in this layer. Consequently, a drop in the decay time is observed (dashed line in Fig. 4.24). And finally, a comparison of the experimental data to *Conwell's* formula for the emission and absorption of phonons reveals that these mechanisms are not important in this sample in agreement with the above-discussed findings of *Feldmann* et al. [4.30].

Again, such time-resolved experiments give valuable information on the realistic timescales for intervalley scattering as are needed for the modelling of the behavior of modern semiconductor devices. For a more detailed separation of the different contributions to the transfer we turn now to cw optical spectroscopy. In the following, we want to identify the various phonon modes involved, to distinguish between mixing via the superiodicity and the interface disorder, respectively, and to deduce some quantitative information on the intervalley coupling strength.

An identification of the phonon modes involved is possible from the experiments of *Zrenner* et al. using a GaAs/AlAs heterostructure (i.e., a single period of a SL) sandwiched between $Al_{0.5}Ga_{0.5}As$ barriers [4.119]. Application of an electric field across this structure results in a strong Stark shift of spatially indirect transitions, while spatially direct transitions are much less affected. For a suitable design of the layer thicknesses (25 Å GaAs, 28 Å AlAs) the sample can easily be tuned between type-I and type-II behavior. Steady-state luminescence spectra reflecting this transition are displayed in Fig. 4.25. The strong Stark shift of the type-II luminescence is evident. The rather broad type-I luminescence is partially hidden. The crossover occurs around zero bias voltage which is confirmed by the behavior of the luminescence decay time.

The intensity of the type-II luminescence shows some nonmonotonic dependence on bias voltage which is further illustrated in Fig. 4.26. The signal

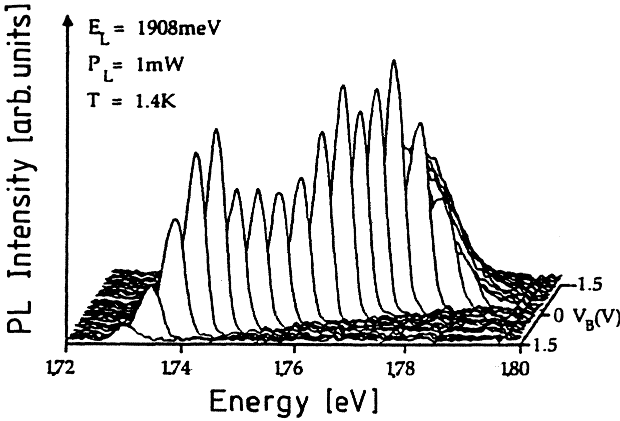

Fig. 4.25. Steady state PL spectra for a GaAs/AlAs QW structure as a function of bias voltage [4.119]

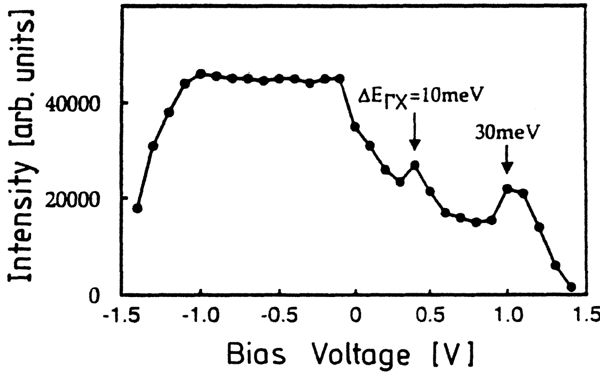

Fig. 4.26. Luminescence intensity in the GaAs/AlAs QW around the crossover as a function of bias voltage [4.119]

for voltages beyond the crossover decreases due to the increasing Γ–X separation. Two step-like features are observed, however, on top of this decrease. The voltages where these features appear correspond to Γ–X separations of 10 meV and 30 meV, respectively. At these energies the real-space transfer from the Γ to the X minima increases as a result of the threshold for additional transfer channels, which are identified to be assisted by the GaAs TA and LO phonons. The separation of these processes from elastic-scattering contributions is possible here, because the mixing due to superperiodicity is absent (or weak) and the transfer is mainly related to the much weaker interface disorder.

A comparison of the cw luminescence in a similar sample to calculations of the zone-edge phonon energies identifies the AlAs LO, TO, and LA phonon modes which contribute to the emission. These data, in combination with the just described nonmonotonic behavior of the intensity as a function of bias voltage, indicate that the GaAs phonon modes are responsible for the real-space transfer, while the AlAs phonons are involved in the indirect emission processes [4.119].

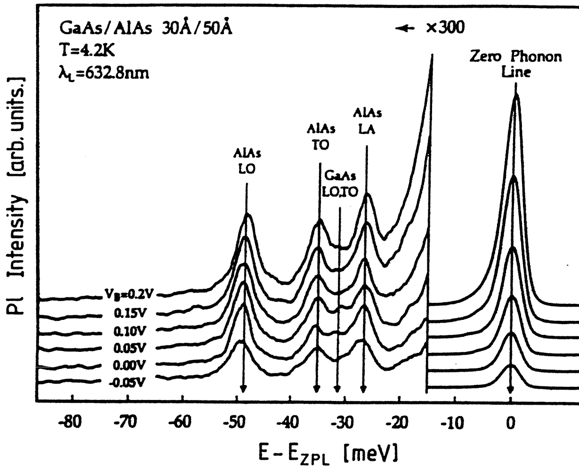

Fig. 4.27. Identification of phonon side bands from steady-state PL spectra of a GaAs/AlAs QW structure [4.119]

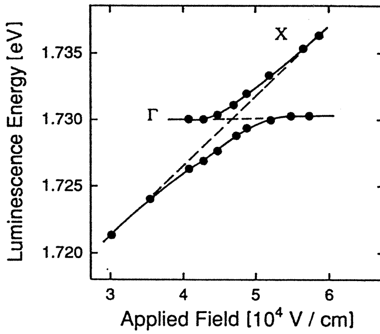

Fig. 4.28. Energies of the direct and indirect transitions in a 35 Å GaAs / 80 Å AlAs SL. A pronounced anticrossing is evident in the crossover region [4.120]

Spectroscopy of the zero-phonon emission in type-II SLs yields information on the elastic intervalley-coupling processes and their relative efficiency. These emission processes result from the mixing of the X-point wave functions in the AlAs layers to Γ-point states. This mixing was experimentally verified by *Meynadier* et al. in their experiments on the type-I to type-II crossover as a function of applied axial field [4.120]. At moderately high electric fields they find a pronounced anticrossing of the type-I and type-II emission (Fig. 4.28). This anticrossing is a result of the saturation of the quantum-confined Stark effect and a remaining blue shift of the type-II transition due to the voltage drop across the structure. The splitting of the transitions in the anticrossing region directly reflects the presence of the mixing according to perturbation theory. The mixing potential entering into the intervalley-coupling matrix element is determined to be of the order of 1 meV.

One of the important results of luminescence measurements is that the different contributions to the intervalley coupling can be isolated. This holds for the separation of phonon-assisted and elastic coupling, and also for the separation of the different interface mixing processes. The shift of the type-II

transition in the experiment just described is consistent with the large mass of the X minima aligned parallel to the growth (z) direction [4.120]. The observed mixing is thus a result of the superperiodicity of the structure.

The degeneracy of the X_z and $X_{x,y}$ minima is lifted in the type-II structures due both to different confinement energies and to the energy shift induced by strain. The actual ordering of the minima, however, was long debated because the confinement effect can be overcompensated by a shift due to interfacial strain (e.g. [4.37] and references therein). A clear identification of the nature of the lowest conduction-band minimum is essential for investigations of the various mixing potentials. The ordering of the minima in symmetric $(GaAs)_n/(AlAs)_n$ SLs can be summarized from the experiments of *van Kesteren* et al. [4.37] and *Ge* et al. [4.40] as follows: The $X_{x,y}$ minima are lowest for $n < 4$ while the X_z minima are lowest for $n \geq 4$. Only recombinations involving the lowest minima contribute to the luminescence signal at low excitation levels. Thus, the relative strength of the emission lines gives direct information on the coupling strength related to the individual mechanisms.

A typical result of luminescence experiments is that a strong zero-phonon emission is observed from the X_z minima while this line is weak compared to the phonon side bands for the $X_{x,y}$ related emission [4.36–38, 40]. These findings are illustrated in Fig. 4.29, which compares the emission in very thin SLs and in $Al_{0.5}Ga_{0.5}As$. It is obvious that the Γ–X coupling via the superiodicity is far more efficient than either the inelastic coupling via the phonons or the coupling resulting from the interfacial disorder. This finding is supported by the pressure-dependent luminescence measurements of *Skolnick* et al. (Fig. 4.30) [4.121]. The relative intensity of the lowest phonon side band compared to the zero-phonon line is plotted here as a funtion of pressure

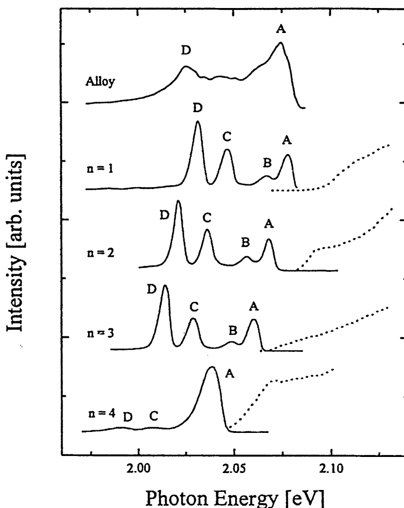

Fig. 4.29. PL (full line) and PLE (dots) spectra of $(GaAs)_n/(AlAs)_n$ SPSLs with $n = 1, 2, 3$, and 4, and of $Al_{0.5}Ga_{0.5}As$ at $T = 2.2\,K$. A: zero-phonon line; B: defect-related line; C and D: phonon side bands [4.40]

(or Γ–X separation). This dependence can be modelled by perturbation theory similar to the procedure described in Sect. 4.2.2. This indicates that the phonon-assisted and the zero-phonon processes proceed via the same intermediate states at the Γ point. The ratio of the emission intensities saturates at a value of about 1.5% underlining the strong elastic coupling which is due here to the superperiodicity.

The following important results complete the present knowledge on the properties of the zero-phonon processes. The strength of Γ–X_z mixing depends on the superlattice period: it decreases with increasing n but the product $n \times V_{\mathrm{mix}}$ has a constant value of about 40 meV for SL periods up to 88 Å [4.120]. Further, the theoretically predicted dependence of the Γ–X_z mixing on the (even or odd) number of the AlAs monolayers is not observed. This can be explained by the fact that fluctuations of the order of one monolayer occur at the interfaces relaxing the selection rule for the zone-folding process. Consistently, one finds a nonexponential temporal decay of the X_z-related zero-phonon emission [4.40]. Such a behavior is expected in the presence of disorder, as was already discussed for the case of alloy disorder (Sect. 4.2.2). Here, the interface fluctuations lead to a random distribution of layer thicknesses and thus to a random fluctuation of the Γ–X_z coupling strength. A similar nonexponential decay is found for the zero-phonon emission related to the Γ–$X_{x,y}$ mixing by the interface disorder [4.122].

We close this discussion with a qualitative comparison of the elastic coupling processes in thin SPSLs and $Al_xGa_{1-x}As$ alloys, i.e., between the scattering related to regularly ordered and random distributions of the atoms in samples with macroscopically equal composition. The zero-phonon line (ZPL) in the thin SLs is weaker than the phonon-assisted emission while in the alloy the ZPL dominates (Sect. 4.2.2 and Fig. 4.29). The coupling via the interface disorder is thus less efficient than that via alloy disorder. The direct comparison of the zone-folding process of the X_z minima to the disorder coupling

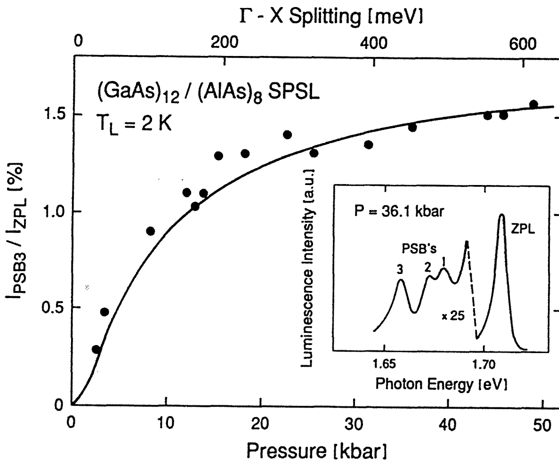

Fig. 4.30. Intensity ratio of the third phonon side band (PSB3) and the zero-phonon line (ZPL) (inset) as a function of pressure and of Γ–X splitting, respectively [4.121]

is more difficult. The zero-phonon line in the SPSL is much stronger than the side bands (Figs. 4.29, 30). But this can partially be a result of a possible reduced coupling to the phonon modes of the X_z minima. This recombination requires a phonon with a k-vector perpendicular to the layer. Time-resolved measurements (of a broad ensemble of carriers) reveal zero-phonon intervalley scattering times of as low as 120 fs . This time is already measured on a sample with SL layer thicknesses of $n = 8$ monolayers, where the electrons are injected with relatively small excess energy compared to the X minima. The scattering time is expected to be significantly smaller for thinner SLs. The transfer time for alloy-disorder scattering in bulk $Al_xGa_{1-x}As$ is found to be little less than 1 ps for similar excess energies of the electrons. These considerations indicate that the Γ–X coupling due to the periodic arrangement of the atoms in the SL is significantly stronger than the coupling due to the random distribution in the alloy.

4.3 Indirect Stimulated Emission

Double-heterostructure lasers with a direct band-gap ternary alloy such as $Al_xGa_{1-x}As$, $In_xGa_{1-x}P$, or $GaAs_xP_{1-x}$ as the active layer material show a rapid decrease of efficiency and a strong rise in lasing threshold as a function of mole fraction x or photon energy of the stimulated emission, respectively (Fig. 4.31). All these substances approach a direct-to-indirect crossover in the intermediate x-value regions. Consequently, an increasing number of electrons will transfer to the side valleys as a result of the efficient intervalley coupling via zone-edge phonons and alloy disorder. The applicability of such alloys for

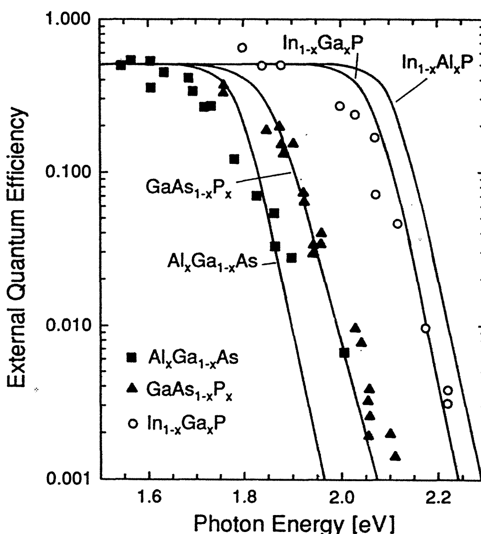

Fig. 4.31. Quantum efficiency of direct recombination in alloy semiconductors [4.125]

achieving visible stimulated emission is thus rather limited [4.123–126]. This deficiency can be overcome by using indirect-gap alloy semiconductors close to the crossover composition.

Stimulated emission is not usually observed in indirect-gap semiconductors. A weak stimulated emission is only found in the recombination of isoelectronic traps in some indirect-gap materials (N in $GaAs_{1-x}P_x$ or $In_{1-x}Ga_xP$ [4.127, 128]) due to the extension of the trapped-electron wave function across the whole Brilloiun zone. For the case of band–band recombination, the gain in materials like Si or Ge is too low to overcome the losses from free-carrier absorption by reason of the relatively low transition probability for indirect recombination [4.129]. This situation is completely different in indirect-gap $Al_xGa_{1-x}As$ just above the crossover composition. Here, the vast majority of electrons can be found in the lowest conduction-band minimum, e.g., the X minima in $Al_xGa_{1-x}As$. The strong intervalley coupling of these minima to the Γ minimum via alloy disorder in combination with the close-to-resonant alignment of the different valleys leads to a indirect transition probability which is large enough to achieve stimulated emission [4.95, 96] and optically pumped lasing [4.130]. This emission range extends well into the orange spectral region at room temperature and is thus a promising alternative approach to achieving visible semiconductor lasers.

Spectra of the spontaneous emission just below, and the stimulated emission above the threshold for the case of optical pumping with an intense picosecond laser pulse at 532 nm are shown in Figs. 4.32, 33 at low and room temperatures. The spontaneous emission typically consists of a zero-phonon and two phonon side bands as was described in Sect. 3.2.1. The narrow emission lines are identified to result from stimulated indirect electron–hole recom-

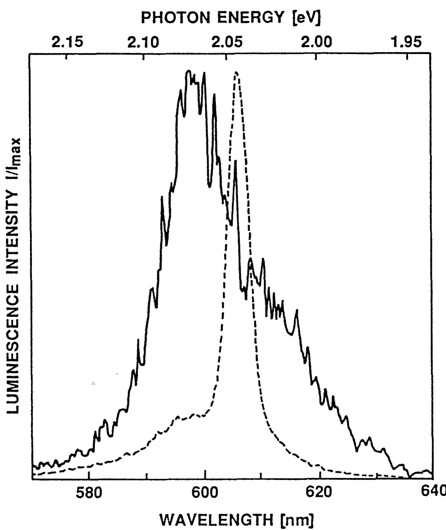

Fig. 4.32. Spontaneous and stimulated indirect recombination at $T = 15\,K$. The spectra are taken for $F = 5.4\,mJ/cm^2$, $t = 150\,ps$ and for $F = 12\,mJ/cm^2$ and $t = 0\,ps$ [4.96]

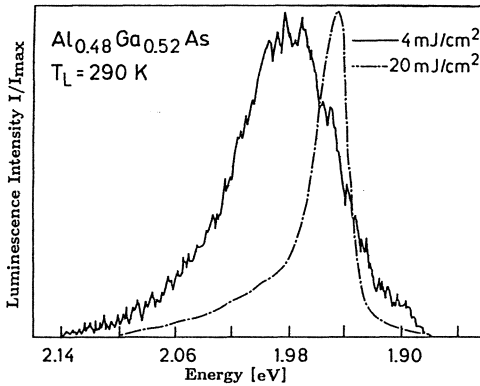

Fig. 4.33. Spontaneous and stimulated indirect recombination at $T = 290\,\mathrm{K}$ at $t = 0\,\mathrm{ps}$. The threshold for stimulated emission is at $F = 8\,\mathrm{mJ/cm^2}$ [4.97]

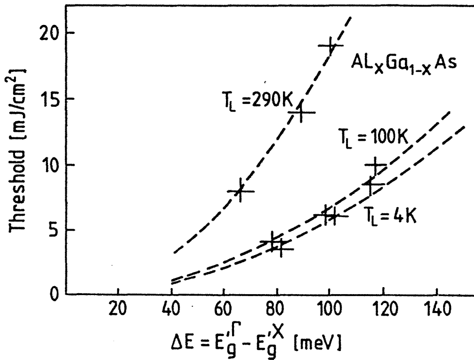

Fig. 4.34. Threshold for indirect stimulated emission as a function of energetic separation between the renormalized central and side valleys at different temperatures. The lines are quadratic fits to the data [4.97]

bination from their threshold-like occurrence, from their spectral position at the fundamental gap where re-absorption losses are minimal, from their temporal evolution essentially following the picosecond pump-laser pulse, and from the observation of optical gain for stripe-type optical excitation. The stimulated emission occurs at wavelengths as short as 623 nm at room temperature and 607 nm at liquid-He temperature.

The stimulated-emission intensity in samples with different alloy composition is well explained by second-order perturbation theory (cf. Sect. 4.1), i.e., the threshold for stimulated emission increases quadratically with increasing Γ–X separation as expected from (4.10). The threshold fluence as a function of separation between the renormalized gaps is shown in Fig. 4.34 [4.97].

Gain measurements using the variable-stripe-length method on crossover-near $Al_xGa_{1-x}As$ at low temperatures were performed by *Sarfaty* et al. [4.95]. The comparison of the spectral region of gain and excitation spectra demonstrate the transition from direct to indirect stimulated recombination by the increasing shift between emission and absorption (Fig. 4.35). The highest gain is found in a sample right at the crossover composition. This sample is an indirect-gap semiconductor at high excitation levels as a result of the differential gap renormalization. The strong increase in gain up to $1000\,\mathrm{cm}^{-1}$

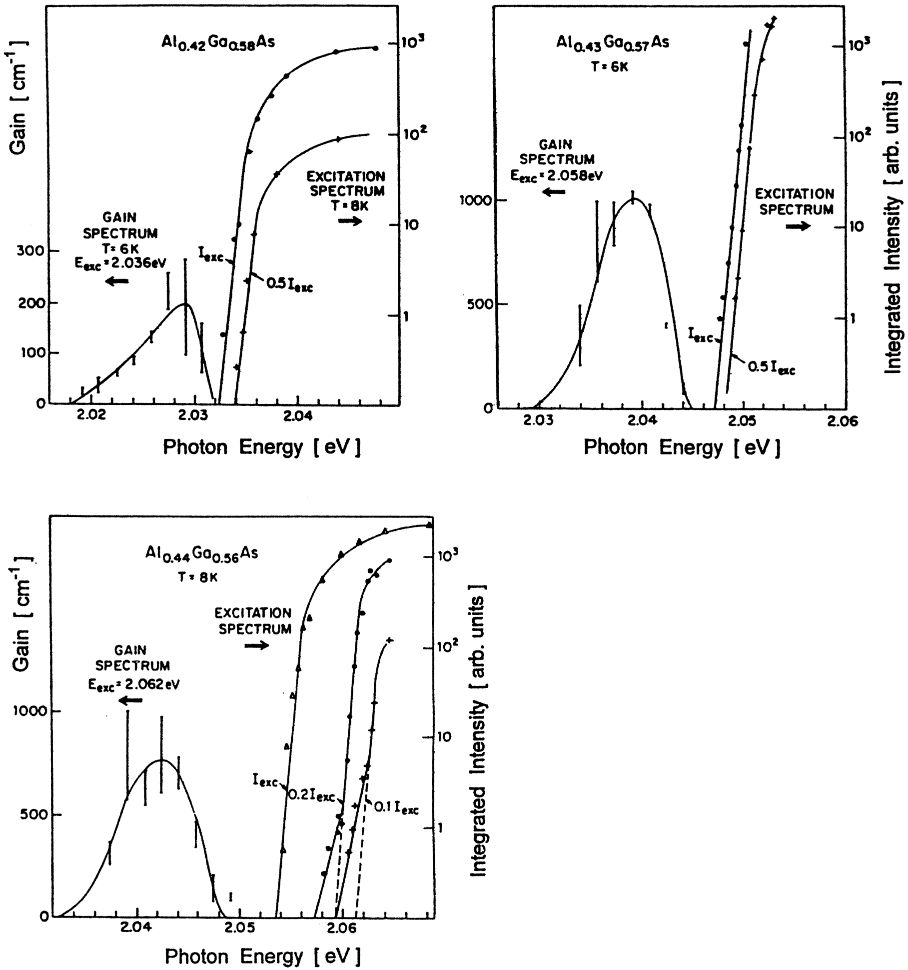

Fig. 4.35. Gain and excitation spectra in $Al_xGa_{1-x}As$ samples close to the crossover composition. The solid gain curves are fits using a model with relaxation of momentum conservation [4.95]

results from the strong difference in effective mass between the direct and indirect minima. Also, in direct-gap samples just below the crossover the population of the side valleys is even larger than the number of carriers in the central valleys. These carriers cannot directly contribute to the direct stimulated emission. In the indirect-gap case, on the other hand, all these carriers contribute to the lasing process. The gain decreases for samples with higher x-values as is expected due to the increasing Γ–X separation.

The temperature dependence of the threshold fluence F_{th} for stimulated emission (Fig. 4.36) reveals some dramatic differences between direct and indi-

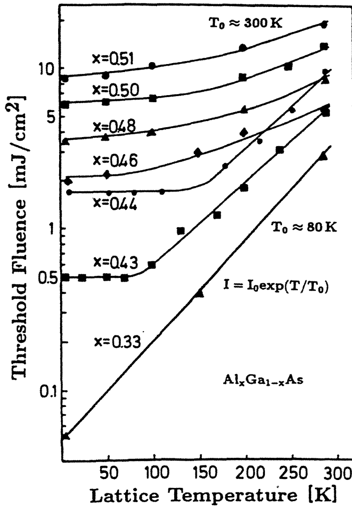

Fig. 4.36. Threshold for stimulated emission as a function of lattice temperature in $Al_xGa_{1-x}As$ close to the crossover composition. A temperature-induced indirect-to-direct crossover occurs in the samples with $x = 0.43$ and $x = 0.44$ [4.98]

rect recombination [4.98]. This dependence is described in direct-gap semiconductors by a heuristic exponential law $F_{th} = F_0 \exp(T/T_0)$ with T_0 being a fit parameter, which directly reflects the sensitivity of the laser process to lattice temperature T [4.124]. We demonstrate this law in Fig. 4.36 for $Al_{0.33}Ga_{0.76}As$ with a T_0 of 80 K. Optimized bulk GaAs double-heterostructure lasers have a T_0 parameter of 165 K. In indirect-gap $Al_xGa_{1-x}As$ with $x \geq 0.46$ we find a remarkably high value of $T_0 \approx 300$ K. Such high values of T_0 are otherwise only found in quantum-well lasers. The threshold rises only by a factor of 2 between liquid He and room temperatures in indirect-gap $Al_xGa_{1-x}As$ samples, while the increase amounts to nearly 2 orders of magnitude for direct-gap samples. As a result, the room temperature threshold in $Al_{0.46}Ga_{54}As$ is of the same order of magnitude as in the standard laser material $Al_{0.33}Ga_{0.67}As$. The extremely flat temperature dependence in combination with the visible emission wavelength makes indirect-gap $Al_xGa_{1-x}As$ a most interesting material for laser applications.

Samples in the direct vicinity of the crossover composition ($x = 0.43$ and $x = 0.44$ in Fig. 4.36) display a temperature-induced transition from indirect to direct stimulated emission. This change comes about due to different Varshni coefficients for the temperature variations of the direct and indirect gaps [4.98]. The crossover composition varies correspondingly from $x_c \approx 0.43$ at 5 K to $x_c \approx 0.45$ at room temperature. The resulting change in dominant stimulated recombination channel at intermediate T for samples in this composition range is evident from the different slopes of the temperature dependence of the threshold in Fig. 4.36 [4.98].

Of great importance is the influence of the differential gap renormalization on the stimulated emission processes [4.103, 131]. This influence was already discussed in detail in Sect. 3.2.3. We find that the direct stimulated emission

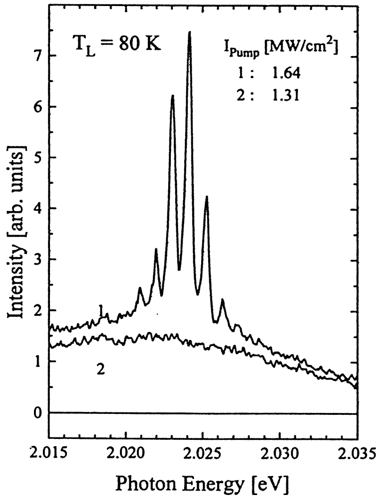

Fig. 4.37. Onset of lasing emission in a 100 μm cleaved resonator of indirect-gap $Al_{0.48}Ga_{0.52}As$

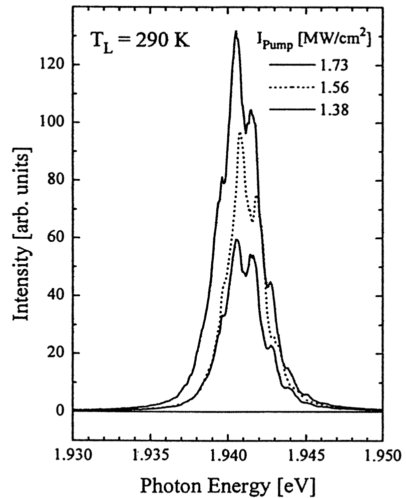

Fig. 4.38. Emission from a 100 μm cleaved resonator of indirect-gap $Al_{0.46}Ga_{0.54}As$ at room temperature. The center wavelength is 638 nm

in $Al_{0.43}Ga_{0.57}As$ (Fig. 4.36) turns into an indirect stimulated process with increasing pump intensity. The change results from an excitation induced direct–indirect transition as described in Sect. 3.2.3. This experimental finding is supported by self-consistent calculations in our multi-valley renormalization model (Figs. 3.19, 20).

A switching from indirect stimulated emission involving the X minima to one involving the higher energy L minima is observed in $Al_{0.46}Ga_{0.54}As$. Here, a crossing of the Γ and L minima, which are both above the X minima, occurs giving a comparatively large transition probability according to (4.10) for the L-related recombination. The emission switches back to the original channel when the increasing degeneracy at the X–Γ gap overcompensates for the smaller transition probability. The experimentally observed shifts of the emission wavelength and the corresponding model calculations are shown in Figs. 3.22 and 3.21, respectively.

Recently, optically pumped semiconductor lasers with an indirect band gap were demonstrated by *Westphäling* et al. based on indirect stimulated emission in $Al_xGa_{1-x}As$ [4.130]. Samples cleaved to resonators of 100–200 μm width showed intense lasing emission with distinct intensity modulation due to resonator feedback. First results are shown in Figs. 4.37, 38.

We can summarize that indirect stimulated emission assisted by alloy disorder is a promising alternative approach to the realization of visible laser diodes. In particular, the above-described concepts should apply to all ternary or quaternary compounds which show a direct to indirect crossover. Laser emission in the green spectral region should be achievable in indirect-gap $In_{1-y}(Ga_xAl_{1-x})_yP$ which can be grown lattice-matched to GaAs substrates, provided good-quality material can be grown. However, it is important to find mechanisms to further reduce the threshold of the indirect stimulated process for this process to be competitive the recently achieved visible laser emission in II-VI compounds [4.132, 133] or in quaternary alloys [4.134]. This threshold reduction might be achieved by exploiting the strong Γ–X coupling in type-II superlattices.

5. Summary and Outlook

In this book we have described the optical properties of semiconductors with a multi-valley band structure. GaAs, $Al_xGa_{1-x}As$ and related heterostructures are well suited as model systems for such semiconductors, because the band-gap energies and the constellation of various conduction-band minima can be tuned over a wide range. The character of the fundamental gap can even be changed from direct to indirect, both in reciprocal and in real space. This flexibility of the band structure allows one to systematically study the impact of a multi-valley scenario on the carrier dynamics as well as the modifications of the band structure due to the presence of carriers that are distributed among several valleys. This information is essential for the design of modern ultrafast electronic and optical devices.

The optical properties of semiconductors at low excitation levels are governed by excitonic effects. Optical transitions involving free or bound excitons reveal the energy as well as the character of the related band gap. Thus, spectroscopy of excitons is an efficient tool to monitor the transition of a direct-gap semiconductor to an indirect-gap one, which is achieved, for example, in $Al_xGa_{1-x}As$ as a function of mole-fraction x or applied hydrostatic pressure or in GaAs/AlAs short-period superlattices as a function of layer thickness. A most interesting situation occurs in $Al_xGa_{1-x}As$ right at this crossover point, where the dynamic interaction of excitons related to the direct and the indirect gap can be studied. The interaction reflects the efficient coupling of the electron states at different points of the Brillouin zone by alloy disorder.

For high carrier densities, as achieved by strong optical pumping or by heavy doping, the optical properties are significantly modified by many-body effects. Most important is the screening of the Coulomb interaction which leads to a renormalization of the carrier self-energy and to the break-up of the excitons into a plasma of free electrons and holes. The efficiency of the screening is significantly weaker for the boson-like excitons than for free carriers and is further reduced by the resticted mobility of the carriers in low-dimensional structures. The optical properties in the latter systems are more strongly affected by Pauli-blocking of states in phase space than by screening.

An important consequence of screening is the shrinkage of the band gap as a function of carrier density, which shifts the energies of optical transi-

tions. But not only the fundamental gap renormalizes due to the exchange and correlation effects in the dense electron–hole plasma: The higher-energy gaps are also affected, although the exchange interaction between valleys at different points of the Brillouin zone can be neglected. The result is a differential shrinkage of gaps related to highly populated and to only slightly populated conduction-band minima. Even a carrier-density-induced change-over from a direct-gap to an indirect-gap semiconductor can be demonstrated in $Al_xGa_{1-x}As$. The renormalization effects are well explained by a multi-valley model which treats self-consistently the shift and population of each valley and accounts especially for the corresponding exchange effects.

A similar differential behavior is found for the subband shifts in semiconductor quantum wells. The renormalization effects here are weaker than in bulk material when compared in reduced units of the Rydberg energies. The comparison of a large variety of optical experiments and theory demonstrates that quantum well systems have to be described as quasi-two dimensional systems due to the influence of the finite thickness of the wells.

A many-body analog to the exciton, called the Fermi-edge singularity, is found in low-dimensional one-component plasmas. The rearrangement of a degenerate electron gas in order to screen the positive charge related to an optically created hole leads to a strong enhancement of the optical oscillator strength close to the Fermi energy. Again, significant differences are observed between the optical properties at the lowest and the higher-energy subband gaps in the presence of the Fermi sea. The lowest gap is influenced by band filling and the singularity just mentioned, while an excitonic character is found for the optical transitions at the unpopulated gaps. A resonant enhancement of the Fermi-edge singularity is observed when the Fermi level approaches the next highest sublevel with increasing electron density.

Below a critical temperature the electron–hole plasma in indirect-gap $Al_xGa_{1-x}As$ relaxes into a fog of small incompressible droplets surrounded by a low-density exciton gas. This phase separation occurs in this alloy semiconductor on a 200-ps timescale which is much faster than in Si or Ge. The accelerated dynamics of the nucleation as well as some unusual properties such as a self-confinement of the homogeneous plasma phase are induced by the presence of disorder. Fluctuations of the lattice potential also appear to be essential for the stabilization of a liquid phase in low-dimensional systems. The first stable quantum-confined electron–hole droplets are found in a type-II quantum-well wire superlattice, which is directly grown on a high-index (311) GaAs surface.

Strong optical nonlinearities due to band filling and screening are observed at the direct band gap of indirect-gap or type-II materials. A very fast dynamics of the nonlinearities results from the transfer of the electrons on a pico- or subpicosecond timescale to subsidiary valleys in real and/or reciprocal space. The wide tunability of the spectral position of the nonlinearities by

band-gap engineering in combination with the ultrafast response gives these effects great potential for application in optical switching devices.

Optical spectroscopy of excitons and electron–hole plasmas by both time-resolved and steady-state methods is applied to deduce quantitative information on the coupling between valleys at nonequivalent points of the Brillouin zone. This coupling is observed as fast carrier transfer between real band states as well as mixing of wave functions which is essential for indirect optical transitions. The important coupling mechanisms are deformation-potential scattering and alloy-disorder-induced transfer in bulk materials and, additionally, mixing of wave functions by zone-folding or by interface disorder in type-II heterostructures. All of these processes rely on the fact that periodic or random fluctuations of the lattice potential on a length scale comparable to the lattice constant induce efficient long wave-vector scattering of the electrons. Typical transfer times for electrons lie in the range of 100 fs as is deduced, for example, from femtosecond time-resolved experiments, from the homogeneous broadening of optical transitions or from hot electron–acceptor recombination. The comparison of such experiments and of the extracted scattering potentials requires careful consideration of all transfer mechanisms allowed by selection rules, their temperature dependence, and the density of final states given by the energetic distribution of the injected carriers.

A direct consequence of the efficient intervalley coupling via alloy disorder in combination with a near resonant alignment of the central and side valleys is the observation of stimulated emission at the indirect gap of $Al_xGa_{1-x}As$ above the crossover point. Its emission wavelength in the orange spectral region, the insensitivity of the threshold to lattice temperature variations, and the still reasonable threshold values make this process most interesting for application in visible wavelength laser diodes.

The investigations reviewed here into the impact of multi-valley scenarios on the optical properties of III-V semiconductors have contributed significantly to the understanding of the physical limitations of ultrafast electronic and light-emitting devices. They have also introduced some interesting new effects such as ultrafast optical nonlinearities and a new approach to visible wavelength laser emission. Furthermore, multi-valley scenarios are most valuable for investigations into the basic properties of excitons or electron–hole plasmas and well suited to test experimentally the related many-body theories.

The future will bring significant improvements in the quality of one- and zero-dimensional semiconductor systems and, hopefully, with it the expected possibilities of band-gap engineering, the enhancement of nonlinear optical effects, and the further lowering of laser thresholds. It will surely also trigger a wealth of new results increasing our understanding of the physics of low-dimensional systems.

In relation to optical devices such as light-emitting diodes, semiconductor lasers or optical modulators there will be a strong competition between the

III-V compounds and the II-VI semiconductors, which have experienced a strong revival since the recent demonstration of a blue-green laser diode. Future developments towards expanding the laser wavelengths across the whole visible spectral region will focus on the growth of III-V quaternary alloys and ZnSe-related heterostructures, which can both be integrated on GaAs chips due to a close lattice match. Potential candidates for lasers in the ultraviolet are also nitrides. Blue and green LEDs have been demonstrated using these compounds. It will be interesting to see whether this competition finally turns out in favor of the III-V alloys due to their well developed technology, in favor of the II-VI compounds, which also display large optical nonlinearities and piezo-electric effects, but suffer from large densities of defects, or even in favor of the nitrides, although these are difficult to handle technologically.

Table 5.1. Material parameters of $Al_xGa_{1-x}As$

Parameter	Composition dependence		Reference
E_g^Γ (300 K)	(1.424 + 1.247x) eV if $0 \leq x \leq 0.45$		[5.1]
	$(1.424 + 1.247x + 1.147(x - 0.45)^2)$ eV if $0.45 \leq x \leq 1$		[5.1]
E_g^L (300 K)	$(1.708 + 0.642x)$ eV		[5.1]
E_g^X (300 K)	$(1.900 + 0.125x + 0.143x^2)$ eV		[5.1]
E_g^Γ, E_g^L, E_g^X (5 K)	according to Fig. 2.2		[5.2]
Δ_{so}	$(0.34 - 0.065x)$ eV		[5.3]
m_e^Γ	$(0.067 + 0.083x)\ m_0$		[5.1]
m_e^L	$(0.55 + 0.12x)\ m_0$		[5.1]
m_e^X	$(0.85 - 0.07x)\ m_0$		[5.1]
m_l^X	$(1.9 - 0.34x)\ m_0$		[5.4, 5]
m_t^X	$0.19\ m_0$		[5.4, 6]
m_l^L	$1.9\ m_0$		[5.4, 7]
m_t^L	$(0.076 + 0.02x)\ m_0$		[5.4, 7]
m_{hh}	$(0.51 + 0.25x)\ m_0$		[5.4]
m_{lh}	$(0.082 + 0.068x)\ m_0$		[5.3]
ϵ_s	$12.6 - 2.5x$		[5.4]
$Ry^*(\Gamma)$	6.5 meV ($x = 0.38$)	7.5 meV ($x = 0.52$)	
$Ry^*(X)$	11.0 meV ($x = 0.38$)	12.1 meV ($x = 0.52$)	
$Ry^*(L)$	7.0 meV ($x = 0.38$)	7.5 meV ($x = 0.52$)	
$E_{LO}^{GaAs}(001)$	29 meV ($x = 0.42$)	30 meV ($x = 0.52$)	
$E_{LO}^{AlAs}(001)$	45 meV ($x = 0.42$)	47 meV ($x = 0.52$)	

References

Chapter 1

1.1 O. Madelung: *Grundlagen der Halbleiterphysik* (Springer, Berlin, Heidelberg 1970)
1.2 O. Madelung: *Festkörpertheorie I-III* (Springer, Berlin, Heidelberg 1972)
1.3 J.M. Ziman: *Principles of the Theory of Solids* (Cambridge Univ. Press, London 1972)
1.4 E.O. Kane: J. Phys. Chem. Solids **1**, 82 (1956)
1.5 Landoldt-Börnstein: New Series, Group III, Vol.17a (Springer, Berlin, Heidelberg 1982)
1.6 J.S. Blakemore: J. Appl. Phys. **53**, R123 (1982)
1.7 R.S. Knox, A. Gold: *Symmetry in the Solid State* (Benjamin, New York 1964)
1.8 G.F. Koster, J.O. Dimmock, R.G. Wheeler, H. Statz: *Properties of the Thirty-Two Point Groups* (MIT Press, Cambridge 1963)
1.9 S.M. Sze: *Physics of Semiconductor Devices* (Wiley, New York 1981)
1.10 H.C. Casey, M.B.Panish: *Heterostructure Lasers*, Pts.A and B (Academic, New York 1978)
1.11 H. Kressel, J.K. Butler: *Semiconductor Lasers and Heterojunction LED's* (Academic, New York 1977)
1.12 See, e.g., Proc. Int'l Conf. on hot carriers in semiconductors published biannually in Solid-State Electronics
1.13 E.M. Conwell, M.O. Vassell: Phys. Rev. **166**, 797 (1968)
1.14 M. Heilblum, M.V. Fischetti: In *Physics of Quantum Electron Devices*, ed. by F. Capasso, Springer Ser. Electron. Photon., Vol.26 (Springer, Berlin, Heidelberg 1990)
1.15 I.B. Gunn: IBM J. Res. Develop. **8**, 141 (1964)
1.16 A historical background to hot-electron physics has been given by C. Hilsum: Solid-State Electron. **21**, 5 (1978)
1.17 E. Schöll: *Adv. Solid-State Physics* **26**, 309 (Vieweg, Braunschweig 1986)
1.18 M. Asche: *Adv. Solid-State Physics* **31**, 279 (Vieweg, Braunschweig 1991)
1.19 A.K. Saxena: J. Appl. Phys. **2**, 5643 (1981)
1.20 D.J. Wolford, W.Y. Hsu, J.D. Dow, B.G. Streetman: J. Lumin. **18/19**, 863 (1978)
1.21 D.J. Wolford, J.A. Bradley: Solid State Commun. **53**, 1069 (1985)
1.22 J. Nishizawa, M. Koike, C.C. Jin: J. Appl. Phys. **54**, 2807 (1983)
1.23 P.F. Barbara, W.H. Knox, G.A. Mourou, A.H. Zewail (eds.): *Ultrafast Phenomena IX*, Springer Chem. Phys., Vol.60 (Springer, Berlin, Heidelberg 1994);

proceedings of the earlier conferences were published in the Springer Series in Chemical Physics, Vols.55(VIII), 53(VII), 48(VI), 46(V), 38(IV), 23(III), 14(II), 4(I)
1.24 E.O. Göbel: *Adv. Solid-State Physics* **30**, 269 (Vieweg, Braunschweig 1990)
1.25 H. Haug, S. Schmitt-Rink: Prog. Quantum Electron. **9**, 3 (1984)
1.26 R. Zimmermann: *Many-Particle Theory of Highly Excited Semiconductors* (Teubner, Leipzig 1988)
1.27 T.M. Rice: *Solid State Physics* **32**, 1 (Academic, New York 1977)
1.28 H. Kalt: *Adv. Solid-State Physics* **32**, 145 (Vieweg, Braunschweig 1992)
1.29 H. Kalt, M. Rinker: Phys. Rev. B **45**, 1139 (1992)
1.30 K. Bohnert, H. Kalt, A.L. Smirl, D.P. Norwood, T.F. Boggess, I.J. D'Haenens: Phys. Rev. Lett. **60**, 37 (1988)
1.31 E.O. Göbel, K. Ploog: Prog. Quant. Electron. **14**, 289 (1990)
1.32 H. Kalt, A.L. Smirl, T.F. Boggess: J. Appl. Phys. **65**, 294 (1989)
1.33 M. Rinker, H. Kalt, K. Köhler: Appl. Phys. Lett. **57**, 584 (1990)
1.34 M. Rinker, H. Kalt, Y.-C. Lu, E. Bauser, P. Ganser, K. Köhler: Appl. Phys. Lett. **59**, 1102 (1991)

Chapter 2

2.1 C. Klingshirn, H. Haug: Phys. Rep. **70**, 315 (1981)
2.2 *Excitons*, ed. by E.I. Rasba, M.D. Sturge (North Holland, Amsterdam 1982)
K. Cho (ed.): *Excitons*, Topics Curr. Phys., Vol.14 (Springer, Berlin, Heidelberg 1979)
2.3 *Optical Nonlinearities and Instabilities in Semiconductors*, ed. by H. Haug (Academic, New York 1988)
F.-J. Niedernostheide (ed.): *Nonlinear Dynamics and Pattern Formation in Semiconductors and Devices*, Springer Proc. Phys., Vol.79 (Springer, Berlin, Heidelberg 1995)
2.4 J.O. Dimmock: in Semiconductors and Semimetals Vol.3, (Academic, New York 1967) p.259
2.5 P.J.Dean, D.C.Herbert: In *Excitons*, ed. by K.Cho, Topics Curr. Phys., Vol.4 (Springer, Berlin, Heidelberg 1979) p.55
2.6 P.J. Dean: In *Collective Excitations in Solids*, ed. by B. DiBartolo, J. Danko (Plenum, New York 1983) p.247
2.7 J.R. Haynes: Phys. Rev. Lett. **4**, 361 (1968)
2.8 S. Zollner, S. Gopalan, M. Garriga, J. Humicek, L. Viña, M. Cardona: Appl. Phys. Lett. **57**, 2838 (1990)
2.9 D.J. Wolford, W.Y. Hsu, J.D. Dow, B.G. Streetman: J. Lumin. **18/19**, 863 (1978)
2.10 H.C. Casey, M.B. Panish: *Heterostructure Lasers*, Pts.A and B (Academic, New York 1978)
2.11 Y.P. Varshni: Physica **34**, 149 (1967)
2.12 G. Oelgart, R. Schwabe, M. Heider, B. Jacobs: Semicond. Sci. Technol. **24**, 68 (1987)
2.13 C. Bosio, J.L. Staehli, M. Guzzi, G. Burri, R.A. Logan: Phys. Rev. B **38**, 3263 (1988)

2.14 T.F. Kuech, D.J. Wolford, R. Potemski, J.A. Bradley, K.H. Kelleher, D. Yan, J. Paul Farrell, P.M.S. Lesser, F.H. Pollak: Appl. Phys. Lett. **51**, 505 (1987)
2.15 D. Huang, G. Ji, U.K. Reddy, H. Morkoc, F. Xiong, T.A. Tombrello: J. Appl. Phys. **63**, 5447 (1988)
2.16 B. Lambert, J. Caulet, A. Regreny, M. Baudet, B. Deveaud, A. Chomette: Semicond. Sci. Technol. **2**, 491 (1987)
2.17 H. Kalt, K. Reimann, W.W. Rühle, M. Rinker, E. Bauser: Phys. Rev. B **42**, 7058 (1990)
2.18 P.J. Pearah, W.T. Masselink, J. Klem, T. Henderson, H. Morkoc, C.W. Litton, D.C. Reynolds: Phys. Rev. B **32**, 3857 (1985)
2.19 D.J. Wolford, J.A. Bradley: Solid State Commun. **53**, 1069 (1985)
2.20 S. Adachi: J. Appl. Phys. **58**, R1 (1985)
2.21 R.A. Faulkner: Phys. Rev. **173**, 991 (1968)
2.22 A.N. Pikhtin: Fiz. Tekh. Poluprov. **11**, 425 (1977) [Sov. Phys. – Semicond. **11**, 245 (1977)
2.23 R.J. Nelson: In [Ref.2.2, p.319]
2.24 M.D. Sturge, E. Cohen, R.A. Logan: Phys. Rev. B **27**, 2362 (1983)
2.25 H. Mariette, D.J. Wolford, J.A. Bradley: Phys. Rev. B **33**, 8373 (1986)
2.26 C. Trallero-Giner, V.I. Gavrilenko, M. Cardona: Phys. Rev. B **40**, 1238 (1989)
2.27 D.D. Sell, P. Lawaetz: Phys. Rev. Lett. **26**, 311 (1971)
2.28 A.R. Goni, A. Cantarero, K. Syassen, M. Cardona: Phys. Rev. B **41**, 10111 (1990)
2.29 H. Kalt, M. Rinker: Phys. Rev. B **45**, 1139 (1992)
2.30 M. Chandrasekhar, U. Venkateswaran, H.R. Chandrasekhar, B.A. Vojak, F.A. Cambers, J.M. Meese: In *Proc.18th Int'l Conf. on the Physics of Semiconductors*, ed. by O.Engström (World Scientific, Singapore 1986) p.943
2.31 E. Cohen, M.D. Sturge: Phys. Rev. B *25*, 3828 (1982)
2.32 J.A. Kash, A. Ron, E. Cohen: Phys. Rev. B **28**, 6147 (1983)
2.33 H. Kalt, J. Collet, Le Si Dang, J. Cibert, K. Saminadayar, S. Tatarenko: In *Proc. 20th Int'l Conf. on the Physics of Semiconductors*, ed. by E.M. Anastassakis, J.D. Joannoupulos (World Scientific, Singapore 1990) p.1174
2.34 J. Collet, H. Kalt, Le Si Dang, J. Cibert, K. Saminadayar, S. Tatarenko: Phys. Rev. B **43**, 6843 (1991)
2.35 M.V. Klein, M.D. Sturge, E. Cohen: Phys. Rev. B **25**, 4331 (1982)
2.36 B. Monemar, H. Kalt, C.I. Harris, P. Bergmann, P.O. Holtz, M. Sundaram, J.L. Merz, A.C. Gossard, K. Köhler, T. Schweizer: Supperlattices and Microstructures **9**, 281 (1991)
2.37 B. Monemar, P.O. Holtz, P. Bergmann, C.I. Harris, H. Kalt, M. Sundaram, J.L. Merz, A.C. Gossard: Surf. Sci. **263**, 556 (1992)
2.38 J.P. Bergmann, P.O. Holtz, B. Monemar, M. Sundaram, J.L. Merz, A.C. Gossard: Phys. Rev. B **43**, 4765 (1991)
2.39 E.O. Göbel, K. Ploog: Prog. Quant. Electr. **14**, 289 (1990)
2.40 J.L. Birman, M. Lax, R. Loudon: Phys. Rev. **145**, 620 (1966)
2.41 A.C. Gossard: In *Thin Films: Preparation and Properties*, ed. by K.N. Tu, R. Rosenberg (Academic, New York 1983)
2.42 A. Forchel, H. Leier, B.E. Maille, R. Germann: *Adv. Solid-State Phys.* **28**, 99 (Vieweg, Braunschweig 1988)
2.43 U. Merkt: *Adv. Solid-State Phys.* **30**, 77 (Vieweg, Braunschweig 1990)

2.44 D. Heitmann, T. Demel, P. Grambow, K. Ploog: *Adv. Solid-State Phys.* **29**, 285 (Vieweg, Braunschweig 1989)
2.45 R. C.Miller, D.A. Kleinman, A.C. Gossard: Phys. Rev. B **29**, 7085 (1984)
2.46 R. Dingle, W. Wiegmann, C.H. Henry: Phys. Rev. Lett. **33**, 827 (1974)
2.47 G. Bastard, J.A. Brum, R. Ferreira: *Solid State Physics* **44**, 229 (Academic, New York 1991)
2.48 M. Shinada, S. Sugano: J. Phys. Soc. Jpn. **21**, 1936 (1966)
2.49 U. Jorda, U. Rössler: Superlattices and Microstructures **8**, 481 (1990)
2.50 S. Schmitt-Rink, D.S. Chemla, D.A.B. Miller: Adv. Phys. **38**, 89 (1989)
2.51 B.I. Greene, K.K. Bajaj, D.E. Phelps: Phys. Rev. B **29**, 1807 (1984)
2.52 T. Ishibashi, S. Tarucha, H. Okamoto: AIP Conf. Proc. **63**, 587 (1981)
2.53 D.S. Chemla, D.A.B. Miller: J. Opt. Soc. Am. B **2**, 1155 (1985)
2.54 P. Dawson, K.J. Moore, G. Duggan, K.T. Ralph, C.T.B. Foxon: Phys. Rev. B **34**, 6007 (1986)
2.55 J. Cibert, P.M. Petroff, G.J. Dolan, S.J. Pearton, A.C. Gossard, J.H. English: Appl. Phys. Lett. **49**, 1275 (1986)
2.56 M.A. Reed, J.N. Randall, R.J. Aggarwal, R.J. Matyi, T.M. Moore, A.E. Wetsel: Phys. Rev. Lett. **60**, 535 (1988)
2.57 A. Lorke, J.P. Kotthaus, K. Ploog: Phys. Rev. Lett. **64**, 2559 (1990)
2.58 D. Gershoni, J.S. Weiner, S.N.G. Chu, G.A. Baraff, J.M. Vandenberg, L.N. Pfeiffer, K. West, R.A. Logan, T. Tabun-Ek: Phys. Rev. Lett. **65**, 1631 (1990)
2.59 M. Tsuchiya, J.M. Gaines, R.H. Yan, R.J. Simes, P.O. Holtz, L.A. Coldren, P.M. Petroff: Phys. Rev. Lett. **62**, 466 (1989)
2.60 R. Nötzel, N.N. Ledentsov, L. Däweritz, M. Hohenstein, K. Ploog: Phys. Rev. Lett. **67**, 3812 (1991); and Phys. Rev. B **45**, 3507 (1992)
2.61 A.L. Efros, A.L. Efros: Sov. Phys. – Semicond. **16**, 772 (1982)
2.62 V. Esch, B. Fluegel, G. Khitrova, H.M. Gibbs, Xu Jiajin, K. Kang, S.W. Koch, L.C. Liu, S.H. Risbud, N. Peyghambarian: Phys. Rev. B **42**, 7450 (1990)
2.63 M.G. Bawendi, W.L. Wilson, L. Rothberg, P.J. Carroll, T. M. Jedju, M.L. Steigerwald, L.E. Brus: Phys. Rev. Lett. **65**, 1623 (1990)
2.64 W.S.O. Rodden, C.M. Sotomayor Torres, C.N. Ironside, D. Cotter, H.P. Girdlestone: Superlattices and Microstructures **9**, 421 (1991)
2.65 A.I. Ekimov: Physica Scripta **39**, 217 (1991)
2.66 U. Woggon, S. Gaponenko, W. Langbein, A. Uhrig, C. Klingshirn: Phys. Rev. B **47**, 3684 (1993)
2.67 N. Peyghambarian, B. Fluegel, D. Hulin, A. Migus, M. Joffre, A. Antonetti, S.W. Koch, M. Lindberg: IEEE J. QE-**25**, 2516 (1989)
2.68 M. Kohl, D. Heitmann, W.W. Rühle, P. Grambow, K. Ploog: Phys. Rev. B **41**, 1233 (1990)
2.69 R. Cingolani, H. Lage, L. Tapfer, H. Kalt, D. Heitmann, K. Ploog: Phys. Rev. Lett. **67**, 891 (1991)
2.70 L. Banyai, I. Galbraith, C. Ell, H. Haug: Phys. Rev. B **36**, 6099 (1987)
L. Banyai, I. Galbraith, H. Haug: Phys. Rev. B **38**, 3931 (1988)
2.71 T. Takagahara: Phys. Rev. B **36**, 9293 (1987)
2.72 A.I. Ekimov, I.A. Kudryavtsev, M.G. Ivanov, Al.L. Efros: J. Lumin. **46**, 83 (1990)
2.73 A. Bugayev, H. Kalt, J. Kuhl, M. Rinker: Appl. Phys. A **53**, 75 (1991)
2.74 B.A. Wilson: IEEE J.QE-**24**, 1763 (1988)

2.75 P. Dawson, B.A. Wilson, C.W. Tu, R.C. Miller: Appl. Phys. Lett. **48**, 541 (1986)
2.76 E. Finkman, M.D. Sturge, M.C. Tamargo: Appl. Phys. Lett. **49**, 1299 (1986)
2.77 W. Ge, M.D. Sturge, W.D. Schmidt, L.N. Pfeiffer, K.W. West: Appl. Phys. Lett. **57**, 55 (1990)
2.78 R. Cingolani, K. Ploog, L. Baldassarre, M. Ferrara, M. Lugara, C. Moro: Appl. Phys. A **50**, 189 (1990)
2.79 B.A. Wilson, C.E. Bonner, R.C. Spitzer, R. Fischer, P. Dawson, K.J. Moore, C.T. Foxon, G.W. 't Hooft: Phys. Rev. B **40** 1825 (1989)
2.80 A. Zrenner: *Adv. Solid-State Phys.* **32**, 61 (Vieweg, Braunschweig 1992)
2.81 G. Peter, E. Göbel, W.W. Rühle, J. Nagle, K. Ploog: Superlattices and Microstructures **5**, 197 (1989)
2.82 J. Feldmann, R. Sattmann, E.O. Göbel, J. Kuhl, J. Hebling, K. Ploog, R. Muralidharan, P. Dawson, C.T. Foxon: Phys. Rev. Lett. **62**, 1892 (1989)
2.83 X.D. Zhang, K.K. Bajaj: Phys. Rev. B **44**, 10913 (1991)
2.84 R. Zimmermann, D. Bimberg: Phys. Rev. B **47**, 15789 (1993)
2.85 H. Kalt, R. Nötzel, K. Ploog, H. Giessen: Solid State Commun. **83**, 285 (1992); Phys. Status Solidi (b) **173**, 389 (1992)
2.86 M.-H. Meynadier, R.E. Nahory, J.M. Worlock, M.C. Tamargo, J.L. de Miguel, M.D. Sturge: Phys. Rev. Lett. **60**, 1338 (1988)
2.87 J. Nunnenkamp, K. Reimann, J. Kuhl, K. Ploog: Phys. Rev. B **44**, 8129 (1991)
2.88 M.G.W. Alexander, M. Nido, K. Reimann, W.W. Rühle, K.Köhler: Appl. Phys. Lett. **55**, 2517 (1989)
2.89 K. Reimann, M. Holtz, K. Syassen, J. Nunnenkamp, J. Kuhl, R. Nötzel, A.J. Shields, K. Ploog: High Press. Res. **9**, 83 (1992)
2.90 J.E. Golub, P.F. Liao, D.J. Eilenberger, J.P. Harbison, L.T. Florez, Y. Prior: Appl. Phys. Lett. **53**, 2584 (1988)
2.91 J.E. Golub, P.F. Liao, D.J. Eilenberger, J.P. Harbison, L.T. Florez: Solid State Commun. **72**, 735 (1989)
2.92 A. Forchel, U. Cebulla, G. Tränkle, E. Lach, T.L. Reinecke, H. Kroemer, S. Subbanna, G. Griffiths: Phys. Rev. Lett. **57**, 3217 (1986)
2.93 U. Venkateswaran, M. Chandrasekhar, H.R. Chandrasekhar, B.A. Vojak, F.A. Chamber, J.M. Meese: Superlattices and Microstructures **3**, 217 (1987)

Chapter 3

3.1 G.D. Mahan: Phys. Rev. **153**, 882 (1967)
3.2 S. Schmitt-Rink, C. Ell, H. Haug: Phys. Rev. B **33**, 1183 (1986)
3.3 M.S. Skolnick, J.M. Rorison, K.J. Nash, D.J. Mowbray, P.R. Tapster, S.J. Bass, A.D. Pitt: Phys. Rev. Lett. **58**, 2130 (1987)
3.4 H. Haug, S. Schmitt-Rink: Prog. Quantum Electron. **9**, 3 (1984)
3.5 R. Zimmermann: *Many-Particle Theory of Highly Excited Semiconductors* (Teubner, Leipzig 1988)
3.6 T.M. Rice: *Solid State Physics* **32**, 1 (Academic, New York 1977)
3.7 *Optical Nonlinearities and Instabilities in Semiconductors*, ed. by H. Haug (Academic, New York 1988)
3.8 P. Vashishta, R.K. Kalia: Phys. Rev. B **25**, 6492 (1982)

3.9 P. Vashishta, R.K. Kalia, K.S. Singwi: In *Electron-Hole Droplets in Semiconductors*, ed. by C.D. Jeffries, L.V. Keldysh (North Holland, Amsterdam 1983) p. 1
3.10 H. Kalt: *Adv. Solid-State Phys.* **32**, 145 (Vieweg, Braunschweig 1992)
3.11 H. Kalt, M. Rinker: Phys. Rev. B **45**, 1139 (1992)
3.12 K. Bohnert, H. Kalt, A.L. Smirl, D.P. Norwood, T.F. Boggess, I.J. D'Haenens: Phys. Rev. Lett. **60**, 37 (1988)
3.13 H. Haug, S.W. Koch: Phys. Rev. A **39**, 1887 (1989)
3.14 M. Capizzi, S. Modesti, A. Frova, J.L. Staehli, M. Guzzi, R.A. Logan: Phys. Rev. B **29**, 2028 (1984)
3.15 H. Kalt, K. Bohnert, A.L. Smirl, T.F. Boggess: In *Proc. 19th Int'l Conf. on the Physics of Semiconductors*, ed. by W. Zawadski (Polish Academy of Science, Warsaw 1988) p. 1377
3.16 M. Rinker, H. Kalt, K. Reimann, Y.-C. Lu, E. Bauser: Phys. Rev. B **42**, 7274 (1990)
3.17 H. Kalt, K. Reimann, M. Rinker, W.W. Rühle, E. Bauser: In *Proc. 20th Int'l Conf. on the Physics of Semiconductors*, ed. by E.M. Anastassakis, J.D. Joannoupulos (World Scientific, Singapore 1990) p. 2498
3.18 J.C. Hensel, T.G. Phillips, G.A. Thomas: *Solid State Physics* **32**, 88 (Academic, New York 1977)
3.19 G.W. Fehrenbach, W. Schäfer, J. Treusch, R.G. Ulbrich: Phys. Rev. Lett. **49**, 1281 (1982)
3.20 M. Rösler, R. Zimmermann: Phys. Status Solidi (b) **83**, 85 (1977)
3.21 D.W. Snoke, J.P. Wolfe, A. Mysyrowicz: Phys. Rev. B **41**, 11171 (1990)
3.22 H. Kalt, K. Reimann, W.W. Rühle, M. Rinker, E. Bauser: Phys. Rev. B **42**, 7058 (1990)
3.23 S. Schmitt-Rink, D.S. Chemla, D.A.B. Miller: Phys. Rev. B **32**, 6601 (1985)
3.24 S. Schmitt-Rink, D.S. Chemla, D.A.B. Miller: Adv. Phys. **38**, 89 (1989)
3.25 H. Haug, S. Schmitt-Rink: J. Opt. Soc. Am. B **2**, 1135 (1985)
3.26 W.H. Knox, C. Hirlimann, D.A.B. Miller, J. Shah, D.S. Chemla, C.V. Shank: Phys. Rev. Lett. **56**, 1191 (1986)
3.27 W.H. Knox, R.L. Fork, M.C. Downer, D.A.B. Miller, D.S. Chemla, C.V. Shank, A.C. Gossard, W. Wiegmann: Phys. Rev. Lett. **54**, 1306 (1985)
3.28 N. Peyghambarian, H.M. Gibbs, J.L. Jewell, A. Antonetti, A. Migus, D. Hulin, A. Mysyrowicz: Phys. Rev. Lett. **53**, 2433 (1984)
3.29 K.H. Schlaad, Ch. Weber, J. Cunningham, C.V. Hoof, G. Borghs, G. Weimann, W. Schlapp, H. Nickel, C. Klingshirn: Phys. Rev. B **43**, 4268 (1991)
3.30 J. Kuhl, A. Honold, L. Schultheis, C.W. Tu: *Adv. Solid-State Phys.* **29**, 157 (Vieweg, Braunschweig 1989)
3.31 S. Benner, H. Haug: Europhys. Lett. **16**, 579 (1991)
3.32 B. Yu-K. Hu, S. Das Sarma: Phys. Rev. Lett. **68**, 1750 (1992)
3.33 R. Cingolani, H. Lage, L. Tapfer, H. Kalt, D. Heitmann, K. Ploog: Phys. Rev. Lett. **67**, 891 (1991)
3.34 R. Cingolali, R. Rinaldi, M. Ferrara, G.C. La Rocca, H. Lage, D. Heitmann, K. Ploog, H. Kalt: Phys. Rev. B **48**, 14331 (1993)
3.35 H. Kalt, J. Lumin. **60/61**, 262 (1994)
3.36 C.V. Shank, R.L. Fork, R.F. Leheny, J. Shah: Phys. Rev. Lett. **42**, 112 (1979)
3.37 J.L. Oudar, D. Hulin, A. Migus, A. Antonetti, F. Alexandre: Phys. Rev. Lett. **55**, 2074 (1985)

3.38 J. Shah, T.C. Damen, B. Deveaud, D. Block: Appl. Phys. Lett. **50**, 1307 (1987)
3.39 T. Elsässer, J. Shah, L. Rota, P. Lugli: Phys. Rev. Lett. **66**, 1757 (1991)
3.40 D.N. Mirlin, I.Ya. Karlik, L.P. Nikitin, I.I. Reshina, V.F. Sapega: Solid State Commun. **37**, 757 (1981)
3.41 R.G. Ulbrich, J.A. Kash, J.C. Tsang: Phys. Rev. Lett. **62**, 949 (1989)
3.42 D.W. Snoke, W.W. Rühle, Y.-C. Lu, E. Bauser: Phys. Rev. Lett. **68**, 990 (1992); Phys. Rev. B **45**, 10979 (1992)
3.43 P. Luglia, D.K. Ferry: Phys. Rev. Lett. **56**, 1295 (1986)
3.44 S.M. Goodnick, P. Lugli: Appl. Phys. Lett. **51**, 584 (1987)
3.45 S.M. Goodnick, P. Lugli: Phys. Rev. B **37**, 2578 (1988)
3.46 W.H. Knox, D.S. Chemla, G. Livescu, J.E. Cunningham, J.E. Henry: Phys. Rev. Lett. **61**, 1290 (1988)
3.47 J. Collet, J.L. Oudar, T. Ammand: Phys. Rev. B **34**, 5443 (1986)
3.48 J. Nunnenkamp, J.H. Collet, J. Klebniczki, J. Kuhl, K. Ploog: Phys. Rev. B **43**, 11047 (1991)
3.49 T. Gong, P.M. Fauchet, J.F. Young, P.J. Kelly: Phys. Rev. B **44**, 6542 (1991)
3.50 P.C. Becker, H.L. Fragnito, C.H. Brito Cruz, J. Shah, R.L. Fork, J.E. Cunningham, J.E. Henry, C.V. Shank: Appl. Phys. Lett. **53**, 2089 (1988)
3.51 J.-Y. Bigot, M.T. Portella, R.W. Schoenlein, J.E. Cunningham, C.V. Shank: Phys. Rev. Lett. **67**, 636 (1991)
3.52 Y. Masumoto, B. Fluegel, K. Meissner, S.W. Koch, R. Binder, A. Paul, N. Peyghambarian: J. Crystal Growth **117**, 732 (1992)
3.53 A.M. Kriman, M.J. Kann, D.K. Ferry, R. Joshi: Phys. Rev. Lett. **65**, 1619 (1990)
3.54 A. Mysyrowicz, D. Hulin, A. Antonetti, A. Migus, W.T. Masselink, H. Morkoc: Phys. Rev. Lett. **56**, 2748 (1986)
3.55 A. von Lehmen, J.E. Zucker, J.P. Heritage, D.S. Chemla, A.C. Gossard: Appl. Phys. Lett. **48**, 1479 (1986)
3.56 M. Joffre, D. Hulin, A. Antonetti: J. Physique C **5**, 537 (1987)
3.57 D. Hulin, A. Mysyrowicz, A. Antonetti, A. Migus, W.T. Masselink, H.Morkoc, H.M. Gibbs, N. Peyghambarian: Appl. Phys. Lett. **49**, 749 (1986)
3.58 Proc. Int'l Conf. on Optical Nonlinearity an Bistability of Semiconductors: Phys. Status Solidi (b) **150** (1989)
3.59 A. Forchel, H. Schweitzer, G. Mahler: Phys. Rev. Lett. **51**, 501 (1983)
3.60 R. Zimmermann, E.H. Böttcher, N. Kirstaedter, D. Bimberg: Superlattices and Microstructures **7**, 433 (1990)
3.61 V.D. Kulakovskii, E. Lach, A. Forchel, D. Grützmacher: Phys. Rev. B **40**, 8087 (1989)
3.62 G. Bongiovanni, J.L. Staehli, A. Bosacchi, S. Franchi: Superlattices and Microstructures **9**, 479 (1991)
3.63 W.F. Brinkman, T.M. Rice: Phys. Rev. B **7**, 1508 (1973)
3.64 H. Kalt, K. Bohnert, D.P. Norwood, T.F. Boggess, A.L. Smirl, I.J. D'Haenens: J. Appl. Phys. **62**, 4187 (1987)
3.65 H. Kalt, W.W. Rühle, K. Reimann, M. Rinker, E. Bauser: Phys. Rev. B **43**, 12364 (1991)
3.66 H. Kalt, W.W. Rühle, K. Reimann: Solid State Electron. **32**, 1819 (1989)
3.67 H. Kalt, A.L. Smirl, T.F. Boggess: J. Appl. Phys. **65**, 294 (1989)
3.68 M. Rinker, H. Kalt, K. Köhler: Appl. Phys. Lett. **57**, 584 (1990)
3.69 G. Lasher, F. Stern: Phys. Rev. **133**, A553 (1964)

3.70 J.S. Blakemore: J. Appl. Phys. **53**, R123 (1982)
3.71 V.C. Aguilera-Navarro, G.A. Estevez, A. Kostecki: J. Appl. Phys. **63**, 2848 (1988)
3.72 X. Aymerich-Humet, F. Serra-Mestres, J. Millan: Solid State Electron. **24**, 981 (1981)
3.73 R.W. Martin, H.L. Störmer: Solid State Commun. **22**, 523 (1977)
3.74 W.W. Rühle, K. Leo, E. Bauser: Phys. Rev. B **40**, 1756 (1989)
3.75 H. Haug, D.B. Tran Thoai: Phys. Status Solidi (b) **98**, 581 (1980)
3.76 A. Selloni, S. Modesti, M. Capizzi: Phys. Rev. B **30**, 821 (1984)
3.77 H. Schweitzer, A. Forchel, A. Hangleiter, S. Schmitt-Rink, J.P. Löwenau, H. Haug: Phys. Rev. Lett. **51**, 698 (1983)
3.78 H. Fieseler, R. Schwabe, J.L. Staehli: Phys. Status Solidi (b) **159**, 411 (1990)
3.79 H. Fieseler, R. Schwabe, K. Unger, J.L. Staehli: In *Proc. 20th Int'l Conf. on the Physics of Semiconductors*, ed. by E.M. Anastassakis, J.D. Joannoupulos (World Scientific, Singapore 1990) p. 1093
3.80 R. Cingolani, M. Ferrara, M. Lugara: Phys. Rev. B **36**, 9589 (1987)
3.81 M. Rösler, R. Zimmermann, W. Richert: Phys. Status Solidi (b) **121**, 609 (1984)
3.82 M.A. Cavicchia, R.R. Alfano: Phys. Rev. B **48**, 5696 (1993)
3.83 P.P. Paskov: Europhys. Lett. **20**, 143 (1992)
3.84 J. Nunnenkamp, K. Reimann, J. Kuhl, K. Ploog: Phys. Rev. B **44**, 8129 (1991)
3.85 M. Rinker, H. Kalt, Y.-C. Lu, E. Bauser, P. Ganser, K. Köhler: Appl. Phys. Lett. **59**, 1102 (1991)
3.86 E. Cohen, M.D. Sturge, M.A. Olmstead, R.A. Logan: Phys. Rev. B **22**, 771 (1980)
3.87 R. Sarfaty, A. Ron, E. Cohen, R.A. Logan: J. Appl. Phys. **59**, 780 (1986)
3.88 M. Rinker, H. Kalt, Y.-C. Lu, E. Bauser, K. Köhler, P. Ganser: Appl. Phys. A **53**, 198 (1991)
3.89 A.N. Pikhtin: Fiz. Tekh. Poluprov. **11**, 425 (1977) [Sov. Phys. – Semicond. **11**, 245 (1977)]
3.90 G. Tränkle, H. Leier, A. Forchel, H. Haug, C. Ell, G. Weimann: Phys. Rev. Lett. **58**, 419 (1987)
3.91 S. Schmitt-Rink, C. Ell, S.W. Koch, H.E. Schmidt, H. Haug: Solid State Commun. **52**, 123 (1984)
3.92 S. Tarucha, H. Kobayashi, Y. Hoikoshi, H. Okamoto: Jpn. J. Appl.Phys. **23**, 874 (1984)
3.93 D.A Kleinman, R.C. Miller: Phys. Rev. B **32**, 2266 (1985)
3.94 G. Traenkle, E. Lach, A. Forchel, F. Scholz, C. Ell, H. Haug, G. Weimann, G. Griffiths, H. Kroemer, S. Subbanna: Phys. Rev B **36**, 6712 (1987)
3.95 C. Weber, C. KLingshirn, D.S. Chemla, D.A.B. Miller, J.E.Cunningham, C. Ell: Phys. Rev. B **38**, 12748 (1988)
3.96 M. Potemski, J.C. Maan, K. Ploog, G. Weimann: Surf. Sci. **229**, 380 (1990)
3.97 R. Cingolani, K. Ploog, A. Cingolani, C. Moro, M. Ferrara: Phys. Rev. B **42**, 2893 (1990)
3.98 L.V. Butov, V.D. Kulakovskii, E. Lach, A. Forchel, D. Grützmacher: Phys. Rev. B **44**, 10680 (1991)
3.99 R. Cingolani, H. Kalt, K. Ploog: Phys. Rev. B **44**, 7655 (1990)
3.100 R. Cingolani, G.C. La Rocca, H. Kalt, K. Ploog, M. Potemski, J.C. Maan: Phys. Rev. B **43**, 9662 (1991)
3.101 S. Schmitt-Rink, C. Ell: J. Lumin. **30**, 585 (1985)

3.102 C. Klingshirn, Ch. Weber, D.S. Chemla, D.A.P. Miller, J.E. Cunningham, C. Ell, H. Haug: NATO ASI series B **194**, 353 (1989)
3.103 G. Bongiovanni, J.L. Staehli, D. Martin: Phys. Status Solidi (b) **150**, 685 (1988)
3.104 E. Lach, G. Lehr, A. Forchel, K. Ploog, G. Weimann: Surf. Sci. **228**, 168 (1990)
3.105 S. Das Sarma, R. Jalabert, S.R. Eric Yang: Phys. Rev. B **41**, 8288 (1990)
3.106 R. Jalabert, S. Das Sarma: Surf. Sci. **229**, 405 (1990)
3.107 J.A. Levenson, I. Abram, R. Raj, G. Dolique, J.L. Oudar, F. Alexandre: Phys. Rev B **38**, 13443 (1988)
3.108 E. Lach, A. Forchel, D.A. Broido, T.L. Reinecke, G. Weimann, W. Schlapp: Phys. Rev. B **42**, 5395 (1990)
3.109 G.E.W. Bauer: Proc. 19th Int'l Conf. on the Physics of Semiconductors, ed. by W. Zawadski (Polish Academy of Science, Warsaw 1988) p.1545
3.110 L.V. Butov, V.D. Kulakovskii, T.G. Andersson: Phys. Rev.B **44**, 1692 (1991)
3.111 N.F. Mott: *Metal-Insulator Transitions* (Taylor and Francis, London 1974)
3.112 R.A. Abram, G.J. Rees, B.L.H. Wilson: Adv. Phys. **27**, 799 (1978)
3.113 Bo E. Sernelius: Phys. Rev. B **33**, 8582 (1986)
3.114 Bo E. Sernelius: Phys. Rev. B **34**, 5610 (1986)
3.115 H. Yao, A. Compaan: Appl. Phys. Lett. **57**, 147 (1990)
3.116 R. Dingle, H.L. Störmer, A.C. Gossard, W. Wiegmann: Appl. Phys. Lett. 33, 665 (1978)
3.117 G. Livescu, D.A.B. Miller, D.S. Chemla, M. Ramaswamy, T.Y. Chang, N. Sauer, A.C. Gossard, J.H. English: IEEE J.QE-**24**, 1677 (1988)
3.118 C. Delalande: Physica Scripta **19**, 129 (1987)
3.119 C.I. Harris, B. Monemar, G. Brunthaler, H. Kalt, K. Köhler: Phys. Rev. B **45**, 4227 (1992)
3.120 K. Bohnert, M. Anselment, G. Kobbe, C. Klingshirn, H. Haug, S.W. Koch, S.Schmitt-Rink, F.F. Abraham: Z. Physik B **42**, 1 (1981)
3.121 R. Cingolani, W. Stolz, K. Ploog: Phys. Rev. B **40**, 2950 (1989)
3.122 J. Rorison: J. Phys. C **20**, L311 (1987)
3.123 J. Wagner, A. Ruiz, K. Ploog: Phys. Rev. B **43**, 12134 (1991)
3.124 J.S. Lee, Y. Iwasa, N. Miura: Semicond. Sci. Technol. **2**, 657 (1987)
3.125 Y.H. Zhang, N.N. Ledentsov, K. Ploog: Phys. Rev. B **44**, 1399 (1991)
3.126 A. Pinczuk, J. Shah, R.C. Miller, A.C. Gossard, W. Wiegmann: Solid State Commun. **50**, 735 (1984)
3.127 H. Kalt, K. Leo, R. Cingolani, K. Ploog: Phys. Rev. B **40**, 12017 (1989)
3.128 A.E. Ruckenstein, S. Schmitt-Rink: Phys. Rev. B **35**, 7551 (1987)
3.129 J.-W. Wu: Phys. Rev. B **39**, 7992 (1989)
3.130 S. Haacke, R. Zimmermann, D. Bimberg, H. Kalt, D.E. Mars, J.N. Miller: Phys. Rev. B **45**, 1736 (1992)
3.131 T. Uenoyama, L.J. Sham: Phys. Rev. Lett. **65**, 1048 (1990)
3.132 R. Sooryakumar, D.S. Chemla, A. Pinczuk, A. Gossard, W. Wiegmann, L.J. Sham: Solid State Commun. **54**, 859 (1985)
3.133 Y.-C. Chang, G.D. Sanders: Phys. Rev. B **32**, 5521 (1985)
3.134 R. Sooryakumar, A. Pinczuk, A. Gossard, D.S. Chemla, L.J. Sham: Phys. Rev. Lett. **58**, 1150 (1987)
3.135 A.E. Ruckenstein, S. Schmitt-Rink, R.C. Miller: Phys. Rev. Lett. **56**, 504 (1986)

3.136 P. Hawrylak: Phys. Rev. B **44**, 3821 (1991)
3.137 G.E.W. Bauer: Surf. Sci. **229**, 374 (1990)
3.138 C. Delalande, G. Bastard, J. Orgosani, J.A. Brum, H.W. Liu, M. Voos, G. Weimann, W. Schlapp: Phys. Rev. Lett. **59**, 2690 (1987)
3.139 I. Bar Josph, J.M. Kuo, C. Klingshirn, G. Livescu, T.Y. Chang, D.A.B. Miller, D.S. Chemla: Phys. Rev. Lett. **59**, 1357 (1987)
3.140 A.B. Henriques: Phys. Rev. B **44**, 3340 (1991)
3.141 W. Chen, M. Fritze, A.V. Nurmikko, M. Hong, L.L. Chang: Phys. Rev. B **43**, 14738 (1991)
3.142 P. Hawrylak: Phys. Rev. B **44**, 6262 (1991)
3.143 J.F. Müller, A. Ruckenstein, S. Schmitt-Rink: Mod. Phys. Lett. **5**, 135 (1991)
3.144 M.S. Skolnick, D.M. Wittaker, P.E. Simmonds, T.A. Fisher, M.K. Saker, J.M. Rorison, R.S. Smith, P.B. Kirby, C.R.H. White: Phys. Rev. B **43**, 7354 (1991)
3.145 Y.H. Zhang, D.-S. Jiang, R. Cingolani, K. Ploog: Appl. Phys. Lett. **56**, 2195 (1990)
3.146 A.M. Vasil'ev, P.S. Kop'ev, M.Yu. Nadtochil, V.M. Ustinov: Sov. Phys. – Semicond. **23**, 1320 (1989)
3.147 C.I. Harris, B. Monemar, H. Kalt, K.Köhler: Phys. Rev. B **48**, 4687 (1993)
3.148 E. Hanamura: J. Phys. Soc. Jpn. **28**, 120 (1970)
3.149 C.I. Harris, H. Kalt, B. Monemar, K.Köhler: Surf. Sci. **262**, 462 (1992)
3.150 B. Y.-K. Hu, S. Das Sarma: Phys. Rev. Lett. **68** (1992) 1750
3.151 B. Y.-K. Hu: Phys. Rev. B **47**, 1687 (1993)
3.152 D.S. Chemla, D.A.B. Miller: J. Opt. Soc. Am. B **2**, 1155 (1985)
3.153 R.M. Westervelt: In *Electron-Hole Droplets in Semicoductors*, ed. by C.D. Jeffries, L.V. Keldysh (North-Holland, Amsterdam 1983) p.187 and references therein
3.154 H. Haug, F.F. Abraham: Phys. Rev. B **23**, 2960 (1981)
3.155 K. Bohnert, M. Anselment, G. Kobbe, C. Klingshirn, H. Haug, S.W. Koch, S. Schmitt-Rink, F.F. Abraham: Z. Physik B **42**, 1 (1981)
3.156 D.A. Kleinman: Phys. Rev. B **33**, 2540 (1986)
3.157 P. Hawrylak: Phys. Rev. B **39**, 6264 (1989)
3.158 Y. Kuramoto, H. Kamimura: J. Phys. Soc. Jpn. **37**, 716 (1974)
3.159 H. Kalt, K. Reimann, W.W. Rühle, K. Syassen, E. Bauser: Quantum Electronics and Laser Science Technical Digest Series **12**, 51 (Optical Society of America, Washington, DC 1989)
3.160 A. Forchel, B. Lawich, J. Wagner, W. Schmid, T.L. Reinecke: Phys. Rev. B **25**, 2730 (1982)
3.161 J. Collet, J. Barreau, M. Brousseau, H. Maaref: Phys. Status Solidi (b) **80**, 461 (1977)
3.162 F. Oosaka, T. Sugano, Y. Okabe, Y. Okada: Jpn. J. Appl. Phys. **15**, 2371 (1976)
3.163 D. Bimberg, W. Bludau, R. Linnebach, E. Bauser: Solid State Commun.37, 987 (1981)
3.164 G. Mahler, G. Maier, A. Forchel, B. Laurich, H. Sanwald, W. Schmid: Phys. Rev. Lett. **47**, 1855 (1981)
3.165 J. Hegarty, L. Goldner, M.D. Sturge: Phys. Rev. B **30**, 7346 (1984)
3.166 H.C. Casey, M.B. Panish: *Heterostructure Lasers* Pts.A and B (Academic, New York 1978)
3.167 D.J. Wolford, J.A. Bradley: Solid State Commun. **53**, 1069 (1985)

3.168 R. Nötzel, N.N. Ledentsov, L. Däweritz, M. Hohenstein, K. Ploog: Phys. Rev. Lett. **67**, 3812 (1991); and Phys. Rev. B **45**, 3507 (1992)
3.169 R. Cingolani, K. Ploog, L. Baldassarre, M. Ferrara, M. Lugara, C.Moro: Appl. Phys. A **50**, (1990)
3.170 J. Feldmann, R. Sattmann, E.O. Göbel, J. Kuhl, J. Hebling, K. Ploog, R. Muralidharan, P. Dawson, C.T. Foxon: Phys. Rev. Lett. **62**, 1892 (1989)
3.171 D.J. Wolford, W.Y. Hsu, J.D. Dow, B.G. Streetman: J. Lumin. **18/19**, 863 (1978)
3.172 H.M. Gibbs: *Optical Bistability: Controlling Light with Light* (Academic, New York 1985)
3.173 H. Kalt, A.L. Smirl, T.F. Boggess: Phys. Status Solidi (b) **150**, 895 (1988)
3.174 J. Feldmann, E. Göbel, K. Ploog: Appl. Phys. Lett. **57**, 1520 (1990)
3.175 J. Feldmann: Kurzzeit Dynamik optischer Nichtlinearitäten und elektronischer Anregungen in Typ-II-AlGaAs/AlAs Halbleiterstrukturen. Disseratation, Universität Marburg (1990)
3.176 G.R. Olbright, W.S. Fu, A. Owyoung, J.F. Klem, R. Binder, I. Galbraith, S.W. Koch: Phys. Rev. Lett. **66**, 1158 (1991)
G.Olbright, W.S. Fu, J.F. Klem, H.M. Gibbs, G. Khitrova, R. Pon, B. Fluegel, K. Meissner, N. Peyghambarian, R. Binder, I. Galbraith, S.W. Koch: Phys. Rev. B **44**, 3043 (1991)
3.177 R. Binder, I. Galbraith, S.W. Koch: Phys. Rev. B **44**, 3031 (1991)

Chapter 4

4.1 For a recent review, see J. Shah: Superlattices and Microstr. **6**, 293 (1989)
4.2 T. Elsässer: Adv. Solid-State Physics **32**, 131 (Vieweg, Braunschweig 1992)
4.3 S. Zollner, S. Gopalan, M. Garriga, J. Humicek, L. Viña, M. Cardona: Appl. Phys. Lett. **57**, 2838 (1990)
4.4 D.Y. Oberli, D.R. Wake, M.V. Klein, J. Klem, T. Henderson, H. Morkoc: Phys. Rev. Lett. **59**, 696 (1987)
4.5 A. Seilmeier, H.J. Hübner, G. Abstreiter, G. Weimann, W. Schlapp: Phys. Rev. Lett. **59**, 1354 (1987)
4.6 W.W.Rühle: In *Proc. 20th Int'l Conf. on the Physics of Semiconductors*, ed. by E.M.Anastassakis, J.D.Joannoupulos (World Scientific, Singapore 1990) p.1226
4.7 B.R. Nag: *Electron Transport in Compound Semiconductors*, Springer Ser. Solid-State Sci., Vol.11 (Springer, Berlin, Heidelberg 1980)
4.8 E.M. Conwell, M.O. Vassell: Phys. Rev. **166**, 797 (1968)
4.9 L. Regiani: In *Hot-Electron Transport in Semiconductors*, ed. by L.Regiani, Topics Appl. Phys., Vol.58 (Springer, Berlin, Heidelberg 1985) p.60.
4.10 J.L. Birman, M. Lax, R. Loudon: Phys. Rev. **145**, 620 (1966)
4.11 S. Zollner, S. Gopalan, M. Cardona: J. Appl. Phys. **68**, 1682 (1990)
4.12 A.N. Pikhtin: Fiz. Tekh. Poluprov. **11**, 425 (1977) [Sov. Phys. – Semicond. **11**, 245 (1977)
4.13 C. Grein, S. Zollner, M. Cardona: Phys. Rev. B **44**, 12761 (1991)
4.14 H.Brooks: Unpublished results, as discussed, e.g., inJ.J. Tietjen, L.R. Weisberg: Appl. Phys. Lett. **7**, 261 (1965)
4.15 J.W. Harrison, J.R. Hauser: Phys. Rev. B **9**, 5347 (1976)

4.16 M.A. Littlejohn, J.R. Hauser, T.H. Glisson, D.K. Ferry, J.W. Harrison: Solid State Electron. **21**, 107 (1978)
4.17 D.K. Ferry: Phys. Rev. B **17**, 912 (1978)
4.18 A. Chandra, L.F. Eastman: J. Appl. Phys. **51**, 2669 (1980)
4.19 H.J. Lee, L.Y. Juravel, J.C. Wooley, A.J. Spring Thorpe: Phys. Rev. B **21**, 659 (1980)
4.20 A.K. Saxena: Phys. Rev. B **24**, 3295 (1981)
4.21 D.L. Rode, P.A. Fedders: J. Appl. Phys. **54**, 6425 (1983)
4.22 P.K. Bhattacharya, U. Das, M.J. Ludowise: Phys. Rev. B **29**, 6623 (1984)
4.23 T.J. Drummond, H.P. Hjalmarson: Appl. Phys. Lett. **48**, 1144 (1986)
4.24 H. Kalt, W.W. Rühle, K. Reimann, M. Rinker, E. Bauser: Phys. Rev. B **43**, 12364 (1991)
4.25 S.E. Güncer, D.K. Ferry: Phys. Rev. B **48**, 17072 (1993)
4.26 F. Oosaka, T. Sugano, Y. Okabe, Y. Okada: Jpn. J. Appl. Phys. **15**, 2371 (1976)
4.27 H. Kalt, A.L. Smirl, K. Bohnert, T.F. Boggess: SPIE Proc. **942**, 195 (1988)
4.28 J. Feldmann, R. Sattmann, E.O. Göbel, J. Kuhl, J. Hebling, K. Ploog, R. Muralidharan, P. Dawson, C.T. Foxon: Phys. Rev. Lett. **62**, 1892 (1989)
4.29 P. Saeta, J.F. Federici, R.J. Fischer, B.I. Greene, L. Pfeiffer, R.C. Spitzer, B.A. Wilson: Appl. Phys. Lett. **54**, 1681 (1989)
4.30 J. Feldmann, J. Nunnenkamp, G. Peter, E.O. Göbel, J. Kuhl, K. Ploog, P. Dawson, C.T. Foxon: Phys. Rev. B **42**, 5809 (1990)
4.31 J. Nunnenkamp, K. Reimann, J. Kuhl, K. Ploog: Phys. Rev. B **44**, 8129 (1991)
4.32 T. Ando, S. Wakahara, H. Akera: Phys. Rev. B **40**, 11609 (1989)
4.33 N.J. Pulsford, R.J. Nicholas, P. Dawson, K.J. Moore, G. Duggan, T.C. Foxon: Phys. Rev. Lett. **63**, 2284 (1989)
4.34 J.-B. Xia: Phys. Rev. B **41**, 3117 (1990)
4.35 H. Sakaki, T. Noda, K. Hirakawa, M. Tanaka, T. Matsusue: Appl. Phys. Lett. **51**, 1943 (1987)
4.36 K.J. Moore, G. Duggan, P. Dawson, T.C. Foxon: Phys. Rev. B **38**, 5535 (1988)
4.37 H.W. van Kesteren, E.C. Cosman, P. Dawson, K.J. Moore, C.T. Foxon: Phys. Rev. **39**, 14426 (1989)
4.38 P. Dawson, C.T. Foxon, H.W. van Kesteren: Semicond. Sci. Technol. **5**, 54 (1990)
4.39 D.Z.-Y. Ting, Y.-C. Chang: Phys. Rev. B **36**, 4359 (1987)
4.40 Weikun Ge, M.D. Sturge, W.D. Schmidt, L.N. Pfeiffer, K.W. West: Appl. Phys. Lett. **57**, 55 (1990)
4.41 S. Gopalan, N.E. Christensen, M. Cardona: Phys. Rev. B **39**, 5165 (1987)
4.42 J. Ihm: Appl. Phys. Lett. **50**, 1068 (1987)
4.43 P.C. Becker, H.L. Fragnito, C.H. Brito Cruz, J. Shah, R.L. Fork, J.E. Cunningham, J.E. Henry, C.V. Shank: Appl. Phys. Lett. **53**, 2089 (1988)
4.44 G. Noll, U. Siegner, S. Shevel, E.O. Göbel: Phys. Rev. Lett. **64**, 792 (1990)
4.45 H. Schwab, V. Lyssenko, J.M. Hvam, C. Klingshirn: Phys. Rev. B **44**, 3413 (1991)
4.46 E.O. Göbel: *Adv. Solid-State Phys.* **30**, 269 (Vieweg, Braunschweig 1990)
4.47 J. Kuhl, A. Honold, L. Schultheis, C.W. Tu: *Adv. Solid-State Phys.* **29**, 157 (Vieweg, Braunschweig 1989)
4.48 R. Zimmermann: *Adv. Solid-State Phys.* **30**, 295 (Vieweg, Braunschweig 1990)

4.49 H. Stolz: *Adv. Solid-State Phys.* **31**, 219 (Vieweg, Braunschweig 1991)
4.50 K. Leo: *Adv. Solid-State Phys.* **32**, 97 (Vieweg, Braunschweig 1992)
4.51 J. Feldmann: *Adv. Solid-State Phys.* **32**, 81 (Vieweg, Braunschweig 1992)
4.52 W. Kuett: *Adv. Solid-State Phys.* **32**, 113 (Vieweg, Braunschweig 1992)
4.53 D. Bennhardt, P. Thomas, A. Weller, M. Lindberg, S.W. Koch: Phys. Rev. B **43**, 8934 (1991)
4.54 W.-Z. Lin, R.W. Schoenlein, J.G. Fujimoto, E.P. Ippen: IEEE QE-**24**, 267 (1988)
4.55 W.W. Rühle, H.-J. Polland: Phys. Rev. B **36**, 1683 (1987)
4.56 See, e.g., Proc. Int'l Conf. on Hot Carriers in Semiconductors published biannually in Solid-State Electronics
4.57 C.L. Collins, P.Y. Yu: Phys. Rev. **27**, 2602 (1983)
4.58 C.L. Collins, P.Y. Yu: Phys. Rev. **30**, 4501 (1984)
4.59 J.A. Kash, J.H. Hvam, J.C. Tsang: Phys. Rev. Lett. **54**, 2151 (1985)
4.60 D. von der Linde, J. Kuhl, H. Klingenburg: Phys. Rev. Lett. **44**, 1505 (1980)
4.61 J. Shah, B. Deveaud, T.C. Damen, W.T. Tsang, A.C. Gossard, P. Lugli: Phys. Rev. Lett. **59**, 2222 (1987)
4.62 D.S. Kim, P.Y. Yu: Phys. Rev. Lett. **64**, 946 (1990)
4.63 D.S. Kim, P.Y. Yu: Phys. Rev. B **43**, 4158 (1991)
4.64 C.L. Tang, D.J. Erskine: Phys. Rev. Lett. **51**, 840 (1983)
4.65 D.J. Erskine, A.J. Taylor, C.L. Tang: Appl. Phys. Lett. **45**, 54 (1984)
4.66 A.J. Taylor, D.J. Erskine, C.L. Tang: J. Opt. Soc. Am. **2**, 663 (1985)
4.67 M.J. Rosker, F.W. Wise, C.L. Tang: Appl. Phys. Lett. **49**, 1726 (1986)
4.68 D.W. Bailey, C.J. Stanton, M.A. Artaki, K. Hess, F.W. Wise, C.L. Tang: Solid State Electron. **31**, 467 (1988)
4.69 W.Z. Lin, J.G. Fujimoto, E.P. Ippen, R.A. Logan: Appl. Phys. Lett. **51**, 161 (1987)
4.70 W.Z. Lin, R.W. Schoenlein, J.G. Fujimoto, E.P. Ippen: IEEE J. QE-**24**, 267 (1988)
4.71 C.L. Tang, I.A. Walmsley, F.W. Wise: Appl. Phys. Lett. **52**, 850 (1988)
4.72 G. Boehne, T. Sure, R.G. Ulbrich, W. Schäfer: Phys. Rev. B **41**, 7549 (1990)
4.73 T. Elsässer, J. Shah, L. Rota, P. Lugli: Phys. Rev. Lett. **66**, 1757 (1991)
4.74 X.Q. Zhou, G.C. Cho, U. Lemmer, W. Kütt, K. Wolter, H. Kurz: Solid State Electron. **32**, 1591 (1989)
4.75 M.C. Nuss, D.H. Auston, F. Capasso: Phys. Rev. Lett. **58**, 2355 (1987)
4.76 D.Y. Oberli, J. Shah, T.C. Damen: Phys. Rev. B **40**, 1323 (1989)
4.77 J. Shah, T.C. Damen, B. Deveaud, D. Block: Appl. Phys. Lett. **50**, 1307 (1987)
4.78 A. Katz, R.R. Alfano: Appl. Phys. Lett. **53**, 1065 (1988)
4.79 S. Zollner, S. Gopalan, M. Cardona: Appl. Phys. Lett. **54**, 614 (1989)
S. Zollner, J. Kircher, M. Cardona, S. Gopalan: Solid State Electron. **32**, 1585 (1989)
4.80 D.N. Mirlin, I.Ya. Karlik, L.P. Nikitin, I.I. Reshina, V.F. Sapega: Solid State Commun. **37**, 757 (1981)
4.81 R.G. Ulbrich, J.A. Kash, J.C. Tsang: Phys. Rev. Lett. **62**, 949 (1989)
4.82 D.W. Snoke, W.W. Rühle, Y.-C. Lu, E. Bauser: Phys. Rev. Lett. **68**, 990 (1992); Phys. Rev. B **45**, 10979 (1992)
4.83 G. Fasol, H.P. Hughes: Phys. Rev. B **33**, 2953 (1986)
4.84 D.N. Mirlin, I.Ya. Karlik, V.F. Sapega: Sol. State Commun. **65**, 171 (1988)
4.85 J.A. Kash: Phys. Rev. B **40**, 3455 (1989)

4.86 W. Hackenberg, G. Fasol: Appl. Phys. Lett. **57**, 174 (1990)
4.87 G. Fasol, W. Hackenberg, H.P. Hughes, K. Ploog, E. Bauser, H. Kano: Phys. Rev. B **41**, 1461 (1990)
4.88 S. Zollner, S. Gopalan, M. Cardona: SPIE Proc. **1282**, 78 (1990)
4.89 A.R. Göni, A. Cantarero, K. Syassen, M. Cardona: Phys. Rev. B **41**, 10111 (1990)
4.90 S. Satpathy, M. Chandrasekhar, H.R. Chandrasekhar, U. Venkateswaran: Phys. Rev. B **44**, 11339 (1991)
4.91 B. Monemar, K.K. Shih, G.P. Petit: J. Appl. Phys. **47**, 2604 (1976)
4.92 D.Z.-Y. Ting, Y.-C. Chang: Phys. Rev. B **30**, 3309 (1984)
4.93 M.D. Sturge, E. Cohen, R.A. Logan: Phys. Rev. B **27**, 2362 (1983)
4.94 H. Kalt, K. Bohnert, D.P. Norwood, T.F. Boggess, A.L. Smirl, I.J. D'Haenens: J. Appl. Phys. **62**, 4187 (1987)
4.95 R. Sarfaty, A. Ron, E. Cohen, R.A. Logan: J. Appl. Phys. **59**, 780 (1986)
4.96 H. Kalt, A.L. Smirl, T.F. Boggess: J. Appl. Phys. **65**, 294 (1989)
4.97 M. Rinker, H. Kalt, K. Köhler: Appl. Phys. Lett. **57**, 584 (1990)
4.98 M. Rinker, H. Kalt, Y.-C. Lu, E. Bauser, P. Ganser, K. Köhler: Appl. Phys. Lett. **59**, 1102 (1991)
4.99 A.K. Saxena: J. Appl. Phys. **52**, 5643 (1981)
4.100 F.W. Wise, I.A. Walmsley, C.L. Tang: Appl. Phys. Lett. **51**, 605 (1987)
4.101 A. Jayaraman: Rev. Mod. Phys. **55**, 65 (1983)
4.102 K. Bohnert, H. Kalt, A.L. Smirl, D.P. Norwood, T.F. Boggess, I.J. D'Haenens: Phys. Rev. Lett. **60**, 37 (1988)
4.103 H. Kalt, M. Rinker: Phys. Rev. B **45**, 1139 (1992)
4.104 H. Kalt: *Adv. Solid-State Phys.* **32**, 145 (Vieweg, Braunschweig 1992)
4.105 E.F. Schubert, E.O. Göbel, Y. Horikoshi, K. Ploog, H.J. Queisser: Phys.Rev. B **30**, 813 (1984)
4.106 H. Kalt, K. Reimann, W.W. Rühle, M. Rinker, E. Bauser: Phys. Rev. B **42**, 7058 (1990)
4.107 R.J. Elliott, J.A. Krumhansl, P.L. Leath: Rev. Mod. Phys. **46**, 465 (1974)
4.108 J.A. Kash, S.S. Jha, J.C. Tsang: Phys. Rev. Lett. **58**, 1869 (1987)
4.109 K.J. Nash, M.S. Skolnick: Phys. Rev. Lett. **60**, 863 (1988)
4.110 S. Baroni, S. de Gironcoli, P. Giannozzi: Phys. Rev. Lett. **65**, 84 (1990)
4.111 M.V. Klein, M.D. Sturge, E. Cohen: Phys. Rev. B **25**, 4331 (1982)
4.112 D.C. Reynolds, K.K. Bajaj, C.W. Litton, P.W. Yu, J. Klem, C.K. Peng, H. Morkoc, J. Singh: Appl. Phys. Lett. **48**, 727 (1986)
4.113 H. Mariette, D.J. Wolford, J.A. Bradley: Phys. Rev. B **33**, 8373 (1986)
4.114 D.J. Wolford, J.A. Bradley: Solid State Commun. **53**, 1069 (1985)
4.115 M. Chandrasekhar, U. Venkateswaran, H.R. Chandrasekhar, B.A. Vojak, F.A. Cambers, J.M. Meese: *Proc. 18th Int'l Conf. on the Physics of Semiconductors*, ed. by O.Engström (World Scientific, Singapore 1986) p.943
4.116 W.W. Rühle, K. Leo, E. Bauser: Phys. Rev. B **40**, 1756 (1989)
4.117 R.W. Martin, H.L. Störmer: Solid State Commun. **22**, 523 (1977)
4.118 H. Kalt, W.W. Rühle, K. Reimann: Solid State Electron. **32**, 1819 (1989)
4.119 A. Zrenner: *Adv. Solid-State Phys.* **32**, 61 (Vieweg, Braunschweig 1992)
4.120 M.-H. Meynadier, R.E. Nahory, J.M. Worlock, M.C. Tamargo, J.L. de Miguel, M.D. Sturge: Phys. Rev. Lett. **60**, 1338 (1988)
4.121 M.S. Skolnick, G.W. Smith, I.L. Spain, C.R. Whitehouse, D.C. Herbert, D.M. Whittaker, L.J. Reed: Phys. Rev. B **39**, 11191 (1989)

4.122 B.A. Wilson, C.E. Bonner, R.C. Spitzer, R. Fischer, P. Dawson, K.J. Moore, C.T. Foxon, G.W. 't Hooft: Phys. Rev. B **40** 1825 (1989)
4.123 S.M. Sze: *Physics of Semiconductor Devices* (Wiley, New York 1981)
4.124 H.C. Casey, M.B. Panish: *Heterostructure Lasers* Pts. A and B (Academic, New York 1978)
4.125 H. Kressel, J.K. Butler: *Semiconductor Lasers and Heterojunction LED's* (Academic, New York 1977)
4.126 J. Nishizawa, M. Koike, C.C. Jin: J. Appl. Phys. **54**, 2807 (1983)
4.127 N. Holonyak Jr., D.R. Scifres, H.M. Macksey, R.D. Dupuis: Appl. Phys. Lett. **20**, 11 (1972)
4.128 D.R. Scifres, N. Holonyak Jr., H.M. Macksey, R.D. Dupuis, G.W. Zack, M.G. Craford, W.O. Groves, D.L. Keune: J. Appl. Phys. **43**, 2368 (1972)
4.129 W.P. Dumke: Phys. Rev. **127**, 1559 (1962)
4.130 R. Westphäling, A. Wörner, H. Kalt, K. Köhler: Appl. Phys. Lett., submitted
4.131 M. Rinker, H. Kalt, Y.-C. Lu, E. Bauser, K. Köhler, P. Ganser: Appl. Phys. A **53**, 198 (1991)
4.132 M.A. Haase, J. Qiu, J.M. DePuydt, H. Cheng: Appl. Phys. Lett. **59**, 1272 (1991)
4.133 H. Jeon, J. Ding, W. Patterson, A.V. Nurmikko, W. Xie, D.C. Grillo, M. Kobayashi, R.L. Gunshor: Appl. Phys. Lett. **59**, 3619 (1991)
4.134 J.M. Dallesasse, D.W. Nam, D.G. Deppe, N. Holonyak Jr., R.M. Fletcher, C.P. Kuo, T.D. Osentowski, M.G. Craford: Appl. Phys. Lett. **53**, 1826 (1988)

Chapter 5

5.1 H.C. Casey, M.B. Panish: *Heterostructure Lasers*, Pts. A and B (Academic, New York 1978)
5.2 D.J. Wolford, W.Y. Hsu, J.D. Dow, B.G. Streetman: J. Lumin. **18/19**, 863 (1978)
5.3 P. Lawaetz: Phys. Rev. B **4**, 3460 (1971)
5.4 J.S. Blakemore: J. Appl. Phys. **53**, R123 (1982)
5.5 E. Hess, I. Topol, K.R. Schulze, H. Neumann, K. Unger: Phys. Status Solidi (b) **55**, 187 (1973)
5.6 B. Reinlaender, H. Neumann, P. Fischer, G. Kühn: Phys. Status Solidi (b) **48**, K167 (1972)
5.7 S. Adachi: J. Appl. Phys. **58**, R1 (1985)

Index

Absorption bleaching 120–124, 158–161
– blue shift 123
– , induced 120–124
– tail 144, 145
Adiabatic approximation 1
AlAs 6–16
$Al_xGa_{1-x}As$ 12–16, 19–36, 45, 56–72, 102–112, 119–122, 128–134, 138, 139, 144–158, 166–172
– , material parameters of 177
Alloy disorder 23, 29, 30, 102–112, 128–130, 144–158
– – factor 130
– – potential 130, 144–158
Anticrossing 163
APW method 5

Band-acceptor luminescence 45, 46
Band alignment, type-I 36
– – , type-II 36–40
Band bending 96, 98, 101
Band filling 81–83, 119–124, 138
Band gap, direct 7
– – egineering 124
– – , fundamental 7, 11
– – , indirect 7
– – narrowing/renormalization 15, 42, 109–112
– – – , differential 15, 48, 65–77, 156, 160, 170
– – – in bulk 42, 47–72
– – – in one-component plasmas 83–84
– – – in 1D 45, 81–83
– – – in 2D 45, 72–80
– – – , multivalley model for 55–64
– – – , transient 75–77
– – – , universal formula of 47, 56–64, 72, 73
– – – , universality in 2D 73, 78
– – offset 33

Band structure 1–16, 125, 129–132
– – calculations 5, 6
– – effect 21–24
– – , many-valley 9
– – , multi-valley 9, 11–177
– – of AlAs 7
– – of GaAs 7–11
– – of III-V semiconductors 6–11
– – tuning 16, 145
Bloch waves 3–6
Blue shift of Fabry-Perot fringes 120, 121
Bose condensation 43
Bragg reflection 3
Brillouin zone 3–6
– – , center of 5
– – , edge of 3, 4
– – folding 131, 132, 165
– – , mini 131, 132
– – of the fcc lattice 6
Broadening, homogeneous 18, 24, 84, 92, 125, 143, 144, 152, 154–158
– , inhomogeneous 18, 84, 91, 152
– , Landsberg 52–54

Carrier cooling 134–144, 160, 161
– lifetime 125
CdS 101
CdSe 46
Center-of-mass motion 18
Charge separation 96–98
– transfer 131, 132
Classes (of space-group elements) 8
Coherent excitation of electrons 157
Coherent potential approximation 130
Condensation seeds 108, 118
Conduction band 6
– – minima 7–16
– – – , nonequivalent 47–77
Confinement energy 33

Conwell's formula 127, 142, 143, 161
Correlation effects 42, 55, 56, 79, 84, 94–101
– enhancement 80, 97
Corrugation 38, 118
Coulomb-hole term 47, 56
Coulomb interaction 2, 3, 17–19, 36, 41–47, 91, 94, 96
–– between carriers and ionized impurities 84, 99–101
Critical density for droplet formation 105–107
– temperature 101–107
Crossing of Γ and L minima 69–71
Crossover composition 19, 20, 67
– , direct-to-indirect 13, 14, 19–24
–––– , composition-induced 13, 14, 19, 20, 103, 104, 166–172
–––– , density-induced 15, 67–70
–––– in 2D and 1D 36–40
–––– , pressure-induced 13, 14, 21, 22, 24, 26, 27, 38, 39, 61, 67, 103, 104, 143–158
– , type-I to type-II 36–40, 68, 159–166
Cu_2O 43

Degeneracy (of energy bands) 8, 9
Dephasing 134–136
– time 45
Dielectric function 18
Differential transmission 44, 45, 122, 158–161
Dispersion of excitons 18
– of free electrons 3
– of nearly free electrons 3, 4
– , parabolic 4, 52
–– , deviations from 5, 9, 10, 52
Doped semiconductors 83–101
Drift velocity 12, 13

Effective mass 4, 10, 11
–– approximation 4
–– , density of states 11
–– , longitudinal 10, 11
–– , optical 11
–– renormalization 80
–– , transverse 10, 11
Electro-optic sampling 139, 140
Electron-hole clusters 102
–– droplets 52, 101–119, 144–158
––– , growth of 101, 107–110
––– , quantum-confined 112–119
––– , surface effects of 104, 109, 110, 116, 117
–– liquid 43, 52, 101–119, 144–158
––– binding energy 105–107, 117
––– ground-state density 106
––––– energy 105–107
––– phase diagram 102–119
–––– separation 104–108
–– plasma 42, 49–77, 110–122
––– in magnetic fields 76, 77
––– in 1D 81–83
––– in 2D 72–80
––– luminescence 49–83, 101–119, 144–158, 166–172
––– , self-confinement of 111, 112
Envelope function 17
Equal-pulse optical correlation technique 138
Exchange-correlation energy 55–58, 106, 107
Exchange interaction 2, 3, 42, 45, 48, 55, 56, 79, 80, 84
–– , electron 58–64
–– , intersubband 79, 80
Exciton 17–40
– Bohr radius 18
– , bound 18, 20–23, 30–33, 153, 154
–– , lifetime of 21, 22
– dispersion 18
– dynamics 25–33
– eigenenergy 18, 33
– eigenfunction 17
– , free 18, 23–33
– gas 101–119, 148, 156
– , heavy-hole 34–36
– , light-hole 34–36
– , localized 28, 29, 105, 135, 145, 152
– , low-dimensional 33–36
––– binding energy 34
––––– , effective 74, 75, 77, 78
––– radius 34
– , Mahan 42, 85–101, 123
– in Type-II SPSL 38, 112–119
– oscillator strength 119–124
– Rydberg energy 18
– , thermal reemission of 30–33
– , three-dimensional 17–19
– trapping 30–33
– wave vector 17
– , X-point 25–33, 65
– , Γ-point 25–33, 65
Excitonic absorption 18, 35, 43, 44, 143, 144, 152

– enhancement 42, 87–91
– luminescence 18, 21–33, 101–119, 143–158, 161–166

Femtosecond pump-probe measurements 138, 139
Fermi-Dirac integrals 52
– -edge singularity 42, 85–101, 123
– energy, quasi- 51, 52
– functions 51, 52
– 's golden rule 125–132
Final-state damping 52–54, 82, 92
Forbidden gap 4–6

GaAs 6–16, 19–24, 42–47, 56, 61, 72, 78, 99, 101–103, 134–145, 151–158, 170
GaAs/AlAs type-II heterostructures/superlattices 102, 122–124, 131, 132, 158–166
–– quantum-well wire superlattices 112–119
GaAs/AlGaAs quantum wells 34–40, 44–47, 72–80, 102, 138
–––– , center doped 98–101
–––– , modulation doped 87–98
GaAs/AlGaAs quantum wires 45, 81–83
$GaAs_xP_{1-x}$ 12, 22, 62, 166, 167
$GaIn_xP_{1-x}$ 22
Gain spectroscopy 74, 168–172
GaP 7, 19, 24
GaSb/AlSb quantum wells 73
GaSe 63
Ge 56, 59, 101–103, 167
Ge/SiGe quantum wells 102
Group theory 8–11, 131, 132
Group velocity 4
Gunn oscillator 12

Hartree equation 2
Hartree-Fock approximation 2
–– equation 2, 3
Haynes' rule 18
High-current-filament formation 13
High-index surface 38
Hot (e,A^0) emission 141–143
Hot electrons/carriers relaxation 15, 44–47, 53, 126, 134–144
–– mobility 139, 140
–– transfer device 13

Impurities 84
InAs 7
$In_y(Ga_xAl_{1-x})_{1-y}P$ 172
InGaAs/InP quantum wells 73, 77–80
–––– , modulation doped 87–98
$In_xGa_{1-x}P$ 166, 167
InP 7, 19, 140
Interface disorder/roughness 131, 132, 161–166
– mixing 127, 163–166
Intersubband transitions 126
Intervalence-band transitions 126
Intervalley coupling 21–24, 125–172
–– , alloy-disorder induced 144–158, 165–172
–– , optical spectroscopy of 134–166
–– potential, disorder-induced 144–158
Intervalley deformation potential (IDP) 127, 128, 136–144, 148, 151
– transfer/scattering 12–16, 24, 27, 30, 53, 119–124, 125–172
–– assisted by superperiodicity 12, 122, 131, 132, 158–166
–– , disorder-assisted 7, 12, 30, 128–130, 144–158, 161–166
–– , phonon-assisted 7, 9, 12, 127, 128, 136–144, 159–166
–– rates/times 126–130, 151, 166
Intravalley scattering 14, 128–130, 138, 144, 152, 153, 156
Isoelectronic traps 167

KKR method 5
k-linear terms 9, 10
$\mathbf{k} \cdot \mathbf{p}$ method 5, 10

Laser, optically pumped 171, 172
Lattice potential, periodic 1–6
–– clusters 129, 130
–– fluctuations 23, 126–134, 152
––– , length scales of 126, 127
– translations 3
LCAO method 5
Light-emitting diode (LED) 14, 15, 22
Lineshape analysis 49–54, 67, 68, 72, 104, 105, 147, 148, 157
–– of 1D luminescence 81–83
–– of 2D luminescence 73, 74, 114–116
Localization of holes 87–89, 98–101
Luminescence up-conversion 45, 140

Many-particle/body effects 15, 41–124
–– system 2

Metal-insulator transition 83
Minibands 161
Mixing of wavefunctions 125, 144, 159–166
– potential 163–165
Mobility, Hall 13, 14
– , in alloys 129
– , negative differential 12, 13
Modulation doping 84
Modulation function 17
Momentum conservation 126–134
Mott transition 42, 56, 83, 98, 99, 102
Multiplication table 8

Nearly-free-electron approximation (NFE) 5
Negative differential mobility 12, 13
– – resistance (NDR) 12, 13
Normalized interparticle distance 56, 72

One-component plasma 73, 79, 83–101, 123
– – – , dyamical effects in 94, 97
One-electron approximation 1, 2
Optical nonlinearities 119–124
– transitions, dipole-allowed 9
– – , direct 7
– – , indirect 21–24, 37–40, 49–54, 69–72, 112–119, 125, 133, 134
– – involving virtual states 125, 133–135, 166–172
OPW method 5

Passive mode locking 123
Pauli principle 2, 42, 44, 47, 56
Phase-space filling 43, 44, 122, 123, 159–161
Phonons 1
– , nonequilibrium (hot) 136, 137
– spectral function 128
– , zone-edge 23, 148–158, 163–166
Photoluminescence excitation spectroscopy (PLE) 25, 35–39, 90–101
– intensity profile 51–54
– , timeresolved 25–33, 49–54, 103–119, 138, 140, 144–158
Point group 4
Pseudopotential 5

Quantum dots 33–36
– efficiency 14, 15
– number 18
– wells 33–36
– – , anti-modulation doped 98–101
– – , center doped 85, 98–101
– – , modulation-doped (MDQW) 73, 79, 84–89
– – – – absorption 86
– – – – luminescence 86–98
– – – – , photoluminecence exitation of 89–98
– – – – , single-side 96–98
– -well wire superlattice 38–40
– – – – , type-II 38–40, 158–166
– – – – absorption 38–40
– – – – luminescence 38–40
– wire 33–36
Quasi-momentum 4

Raman spectroscopy 136, 137
Random-phase approximation (RPA) 47, 54–56, 62, 72, 73, 77, 79
Real-space transfer 158–166
Recombination, direct in indirect semicond. 53, 54, 65–67, 154–158
– , disorder-assisted 23, 24, 50–54, 69–72, 144–158, 166–172
– , indirect 49–54, 134–136, 144–158
– of non-equilibrium electrons 141–143
– , phonon-assisted 23, 24, 37–40, 50–54, 112–119, 144–158
– , spatially indirect 36–40, 161–166
– , zero-phonon 21–24, 37–40, 50–54, 69–72, 112–119, 144–172
Renormalized chemical potential 55
Representation 8, 9
– , irreducuble 8
– – , dimension of 8
Rigid pseudo-ion model 128

Scattering 19
– , alloy disorder 30, 127–130, 144–158
– – – , intraband 128–130
– , carrier-carrier 45, 46, 92, 93, 135, 138, 139, 157
– , carrier-phonon 45
– , deformation potential 127, 128, 136–144
– , electron-hole 46
– , electron-phonon 127, 128
– , exciton-exciton 45
– , exciton-free carrier 45
– Hamiltonian 126–134
– , hole-hole 92
– , interface disorder 127

– , limit of weak 125, 128
– potentials 126-132, 144–158
– , selection rules for 128, 165
Schrödinger equation 2
Screened-exchange term 47, 56
Screening (of the Coulomb interaction) 5, 41–47, 55, 59, 77, 120
– in bulk 41–43
– in one-component plasmas 83–101
– in 1D 45
– , intersubband 79, 80, 95–98
– in 2D 43–45, 72, 79, 80, 119, 123, 159–161
Second-order perturbation theory 133, 134, 168
Self energy 55, 56, 94, 130
Semiconductor lasers 14, 166–172
Shake-up process 86, 94, 97
Si 6–16, 56, 78, 89, 101–112, 167
Single-particle energy 55
Slater determinant 2
Space-charge instabilities 13
Space group 8
–– T_d 6–11
Spatial overlap 132, 134, 159–161
Spectral hole burning 44, 138
Spin 2, 6
– -orbit interaction/splitting 9, 52
Stark effect 161–163
–– , optical 46
Stimulated emission 50, 68–72
–– , indirect 50, 69–72, 144, 149, 166–172
–– in 2D 74–77
–– threshold 69–72, 166–172
Subband 33–36
– renormalization 72–80
–– , rigid 78, 79
Superlattice (SL) 33–36
– , short period (SPSL) 16, 36–40, 158–166
––– , type-II 36–40, 131–134, 158–166
––––– , absorption of 37, 38
––––– , luminescence of 37, 38
– , points of high 6–9, 126–134
––––– , minima ordering in 164
Superperiodicity 37, 131, 132, 158–166
Symmetry, crystal 3–6
– operations 8
– , point 7–9
– , time reversal 4
– , translational 3–6

Thermalization 45, 46, 53, 134–139
Tight-binding approximation 5
Timescales of carrier dynamics 134–136
Transfer between real states 125–132, 134, 144
Transient gratings 140
Tunnelling 126

Ultrafast laser spectroscopy 15, 134–136, 158–161

Valence band 6
–– , heavy-hole 8–11, 33–36
–– , light-hole 8–11, 33–36
–– , maxima of 6
–– , split-off 8–11
Valence electrons 1
Valley anisotropy 58
– , central 12
– degeneracy factor 58
– , equivalent 11, 12
– , nonequivalent 12
– , side 12
Variable-stripe-length method 168–172
Vertex corrections 94
Virtual crystal approximation 130
Virtual intermediate states 133, 134

Warping 9, 10

Zincblende structure 6

Springer Series in Solid-State Sciences

Editors: M. Cardona P. Fulde K. von Klitzing H.-J. Queisser

48 **Magnetic Phase Transitions**
Editors: M. Ausloos and R. J. Elliott

49 **Organic Molecular Aggregates**
Electronic Excitation and Interaction Processes
Editors: P. Reineker, H. Haken, and H. C. Wolf

50 **Multiple Diffraction of X-Rays in Crystals**
By Shih-Lin Chang

51 **Phonon Scattering in Condensed Matter**
Editors: W. Eisenmenger, K. Laßmann, and S. Döttinger

52 **Superconductivity in Magnetic and Exotic Materials** Editors: T. Matsubara and A. Kotani

53 **Two-Dimensional Systems, Heterostructures, and Superlattices**
Editors: G. Bauer, F. Kuchar, and H. Heinrich

54 **Magnetic Excitations and Fluctuations**
Editors: S. W. Lovesey, U. Balucani, F. Borsa, and V. Tognetti

55 **The Theory of Magnetism II** Thermodynamics and Statistical Mechanics By D. C. Mattis

56 **Spin Fluctuations in Itinerant Electron Magnetism** By T. Moriya

57 **Polycrystalline Semiconductors**
Physical Properties and Applications
Editor: G. Harbeke

58 **The Recursion Method and Its Applications**
Editors: D. G. Pettifor and D. L. Weaire

59 **Dynamical Processes and Ordering on Solid Surfaces** Editors: A. Yoshimori and M. Tsukada

60 **Excitonic Processes in Solids**
By M. Ueta, H. Kanzaki, K. Kobayashi, Y. Toyozawa, and E. Hanamura

61 **Localization, Interaction, and Transport Phenomena** Editors: B. Kramer, G. Bergmann, and Y. Bruynseraede

62 **Theory of Heavy Fermions and Valence Fluctuations** Editors: T. Kasuya and T. Saso

63 **Electronic Properties of Polymers and Related Compounds**
Editors: H. Kuzmany, M. Mehring, and S. Roth

64 **Symmetries in Physics** Group Theory Applied to Physical Problems 2nd Edition
By W. Ludwig and C. Falter

65 **Phonons: Theory and Experiments II**
Experiments and Interpretation of Experimental Results By P. Brüesch

66 **Phonons: Theory and Experiments III**
Phenomena Related to Phonons
By P. Brüesch

67 **Two-Dimensional Systems: Physics and New Devices**
Editors: G. Bauer, F. Kuchar, and H. Heinrich

68 **Phonon Scattering in Condensed Matter V**
Editors: A. C. Anderson and J. P. Wolfe

69 **Nonlinearity in Condensed Matter**
Editors: A. R. Bishop, D. K. Campbell, P. Kumar, and S. E. Trullinger

70 **From Hamiltonians to Phase Diagrams**
The Electronic and Statistical-Mechanical Theory of sp-Bonded Metals and Alloys By J. Hafner

71 **High Magnetic Fields in Semiconductor Physics**
Editor: G. Landwehr

72 **One-Dimensional Conductors**
By S. Kagoshima, H. Nagasawa, and T. Sambongi

73 **Quantum Solid-State Physics**
Editors: S. V. Vonsovsky and M. I. Katsnelson

74 **Quantum Monte Carlo Methods in Equilibrium and Nonequilibrium Systems** Editor: M. Suzuki

75 **Electronic Structure and Optical Properties of Semiconductors** 2nd Edition
By M. L. Cohen and J. R. Chelikowsky

76 **Electronic Properties of Conjugated Polymers**
Editors: H. Kuzmany, M. Mehring, and S. Roth

77 **Fermi Surface Effects**
Editors: J. Kondo and A. Yoshimori

78 **Group Theory and Its Applications in Physics**
2nd Edition
By T. Inui, Y. Tanabe, and Y. Onodera

79 **Elementary Excitations in Quantum Fluids**
Editors: K. Ohbayashi and M. Watabe

80 **Monte Carlo Simulation in Statistical Physics**
An Introduction 2nd Edition
By K. Binder and D. W. Heermann

81 **Core-Level Spectroscopy in Condensed Systems**
Editors: J. Kanamori and A. Kotani

82 **Photoelectron Spectroscopy**
Principle and Applications
By S. Hüfner

83 **Physics and Technology of Submicron Structures**
Editors: H. Heinrich, G. Bauer, and F. Kuchar

84 **Beyond the Crystalline State** An Emerging Perspective By G. Venkataraman, D. Sahoo, and V. Balakrishnan

85 **The Quantum Hall Effects**
Fractional and Integral 2nd Edition
By T. Chakraborty and P. Pietiläinen

86 **The Quantum Statistics of Dynamic Processes**
By E. Fick and G. Sauermann

87 **High Magnetic Fields in Semiconductor Physics II**
Transport and Optics Editor: G. Landwehr

88 **Organic Superconductors**
By T. Ishiguro and K. Yamaji

89 **Strong Correlation and Superconductivity**
Editors: H. Fukuyama, S. Maekawa, and A. P. Malozemoff